CRANFIELD UNIVERSITY

SHATHA S. ALKUBRAGYI

A New Supervisory Energy Management Control Strategy of a Modified D-STATCOM Configuration with Dual DC Source in Distribution Grids

SCHOOL OF WATER, ENERGY, AND ENVIRONMENT

Phd Thesis

Thesis Submitted for the Degree of Doctor of Philosophy
Academic Year: 2018

Supervisor: Prof Patrick Chi-Kwong Luk
Dr John Economou

CRANFIELD UNIVERSITY

SCHOOL OF WATER, ENERGY, AND ENVIRONMENT

Phd Thesis

Academic Year 2018

SHATHA S. ALKUBRAGYI

A new Supervisory Energy Management Control Strategy of a Modified D-STATCOM Configuration with Dual DC Source in Smart Distribution Grids

Supervisor: Prof Patrick Chi-Kwong Luk
Dr John Economou

This thesis is submitted in partial fulfilment of the requirements for the degree of Ph.D

© Cranfield University 2018. All rights reserved. No part of this publication may be reproduced without the written permission of the copyright owner.

ABSTRACT

A microgrid is a state-of-the-art, next generation of electric distribution grid that provides a fundamental paradigm shift from passive grid networks to active networks. Power electronic technologies play a vital role in enabling microgrids to meet their system level requirements of power quality, reliability and demand response capability. A conventional distribution static compensator (D-STATCOM) is a power electronic converter which acts as a reactive power compensator and voltage controller at the point of common coupling in a grid system. However, these devices have limited ability to mitigate voltage fluctuations caused by active power disturbances. By integrating energy storage into the DC link of a D-STATCOM, controllable active power from the storage device can result in enhanced voltage compensating capability. The active and reactive power control between the D-STATCOM and AC power point is achieved by suitable tuning of the phase and magnitude of the output voltage of the D-STATCOM's converter.

Recent advances and innovations in energy storage systems such as super-capacitors and batteries allow the combination of battery-supercapacitor hybrid energy storage systems to act as an effective solution for energy management in smart grid operation. However, the concept and control of the hybridisation of energy storage are relatively new, and there are great challenges to the development of control management systems, for example, reduce battery current stresses.

This study presents a novel approach in applying a fuzzy-PI controller to a D-STATCOM based energy storage unit to provide enhanced power quality and voltage stability in distribution grids. Full information is provided concerning the implementation of the system, and the dynamic controls devised during the research programme.

A second novel approach is the use of sugeno fuzzy logic controller based decision making for power management of the D-STATCOM based HESS to achieve a robust and superior performance for voltage regulation. Recent

developments in this field have tended to converge on intelligent control as the best approach to achieve an effective strategy for power sharing with HESSs by using a high-power storage unit (supercapacitor) and high energy storage unit (battery) in combination with the D-STATCOM to avoid the drawbacks of a single storage unit. This development is considered one of the main ways to upgrade energy storage technology, with gains of faster voltage regulation and decreased battery current peak value.

Verification of the control designs has been achieved through simulation using MATLAB/SIMULINK based on the derived analytical model in state-space form. Comprehensive simulation results show that the proposed fuzzy controller demonstrates significant improvements over conventional controllers in supporting voltage stability in distribution networks.

Keywords:

Voltage stability, D-STATCOM, energy storage system, fuzzy logic.

ACKNOWLEDGEMENTS

All Praise to the Almighty God for enabling me to complete this thesis.

I would like to express my deep gratitude to my supervisors Professor Patrick Luk and Dr John Economou for their support, encouragement and suggestions throughout the work. I would like to offer my special thanks to the Ministry of Higher Education and Scientific Research of Iraq for offering me the funding to running this research.

I would also like to express my sincere gratitude to Dr Maciej Bendyk who helps me, Dr Akram Bati for their valuable assistance and a special thank you goes out to Sam Skears.

I would like to express my very great appreciation to my husband Ahmed for his constant support, his ongoing patience, inspiration, and encouragement throughout my study. In addition, my heartfelt appreciation goes out to my daughter Dania and my son Mohamed for their love, encouragement, and unfailing support.

My deepest thanks and love to my family who encouraged me to do this research: my mum, my sisters and my brothers

Finally, I would like to extend my thanks and gratitude to all who had ever assisted me during the period of this research.

TABLE OF CONTENTS

ABSTRACT i
ACKNOWLEDGEMENTS iii
LIST OF FIGURES ix
LIST OF TABLES xvii
LIST OF EQUATIONS xix
LIST OF ABBREVIATIONS xxv
NOMENCLATURE xxix
1 Chapter One: Introduction 1
1.1 Background 1
1.2 Power quality challenges. 4
1.3 Traditional Mitigation Methods for Voltage Regulation 6
1.3.1 Voltage Regulation 7
1.3.2 Reactive Power Compensation 7
1.4 Flexible AC Transmission System (FACTS) Devices Based Mitigation Methods for Voltage Issues 8
1.5 Research Motivation 9
1.6 Research Aim and Objectives 10
1.7 Contributions to Knowledge 11
1.8 Thesis Overview 12
1.9 Associated Published Work 14
2 Chapter Two: Literature Review 17
2.1 Introduction 17
2.2 Smart grid and micro grid concept 17
2.3 Energy storage technology 22
2.4 The role of the power electronics in power systems operation 25
2.5 Distributed static synchronous compensators (D-STATCOM) 30
2.6 Principle of D-STATCOM operation 31
2.7 Control Algorithms and approaches of D-STATCOM 33
2.7.1 Phase shift control. 34
2.7.2 Instantaneous (p-q) Theory. 35
2.7.3 Synchronous rotating frame method. 37
2.7.4 Nonlinear controllers. 39
2.8 D-STATCOM application 41
2.8.1 Application of D-STATCOM for load compensation 41
2.8.2 Application of D-STATCOM for dynamic and transient stability 42
2.9 Summary 45
3 Chapter Three: Modelling of D-STATCOM in Distribution Systems 47
3.1 Introduction 47
3.2 Modelling of Distribution Grid 47

3.2.1 Modelling and Steady State Analysis of The Distribution System Based DSTATCOM 50
3.2.2 abc to dq Reference Frame 51
3.2.3 Steady State Analysis of D-STATCOM Based Distribution System . 53
3.3 Design of D-STATCOM Rating 67
3.4 Summary 68
4 Chapter Four: Design of D-STATCOM Control 71
4.1 Introduction 71
4.2 Grid connected power converters 72
4.3 Two –level three phase power convert 73
4.4 Modelling of D-STATCOM 74
4.5 Steady state analysis of the D-STATCOM 78
4.6 Control design of D-STATCOM 83
4.6.1 Current control loop 84
4.6.2 VPCC voltage control loop 86
4.6.3 DC–link voltage control loop 87
4.6.4 DC –link voltage control loop based on fuzzy logic 89
4.7 Simulation of a distribution system with a sudden load change 97
4.7.1 Simulation without D-STATCOM 97
4.7.2 Simulation with D-STATCOM. 99
4.8 Simulation of a distribution system with a three-phase fault applied at load point 105
4.9 Summary 108
5 Chapter Five: D-STATCOM Battery Based Energy Storage System 111
5.1 Introduction 111
5.2 D-STATCOM based battery energy storage 111
5.3 Modelling and control design of D-STATCOM based BESS 113
5.3.1 Two level three phase D-STATCOM controller 116
5.3.2 Battery modelling 120
5.3.3 Two level DC to DC controller 121
5.4 Simulation of D-STATCOM based battery energy storage 127
5.4.1 Simulation of a distribution system with a sudden load change 127
5.4.2 Comparison between fuzzy-tuned PI controller and the PI controller (with a sudden load change) 131
5.4.3 Simulation of a distribution system with a three-phase fault applied at load point 135
5.4.4 Comparison between fuzzy-tuned PI controller and the standard PI controller (faults applied) 138
5.5 Summary 145
6 Chapter Six: D-STATCOM Based Hybrid Energy Storage System (HESS) 147
6.1 Introduction 147
6.2 Configurations and modelling of the HESS 148

6.2.1 Configurations 148
6.2.2 Modelling of HESS topology 150
6.3 Standard HESS control strategy 155
6.3.1 Constraint conditions 157
6.3.2 Control loops design for HESS 158
6.4 Fuzzy logic design of controller for HESS 161
6.4.1 The general scheme of power management 161
6.4.2 The structure of FLC 163
6.5 Simulation of D-STATCOM based hybrid energy storage 172
6.5.1 Simulation of a distribution system with a sudden load change 174
6.5.2 Simulation of a distribution system with a three-phase fault applied at load point 181
6.6 Summary 188
7 Chapter Seven: Experiment Design and Implementation of Real-Time Controller for a Battery-Supercapacitor Hybrid Energy Storage System 191
7.1 Introduction 191
7.2 Prototype Hardware Description 191
7.2.1 The Load of Platform 193
7.2.2 Modified cascade inverter 193
7.2.3 Switch drive circuit of the inverter 194
7.2.4 Battery bank 195
7.2.5 Supercapacitor storage unit 196
7.2.6 Control platform 197
7.2.7 Optoisolated digital signal interface 198
7.2.8 Optoisolated voltage and current sensing circuit 198
7.3 Experimental Setup 200
7.4 Summary 216
8 Chapter Eight: Conclusions and Future Work 217
8.1 Discussion and Conclusions 217
8.2 Suggestion for future work 223
REFERENCES 225
Appendix A Small Signal Modelling of the PCC Control loop design 251
Appendix B State equation for buck and boost controller 255
Appendix C Graphic Description of the Laboratory setup 259

LIST OF FIGURES

Figure 1-1 (a) Conventional electrical network,(b) Future electrical network [15]3

Figure 1-2 V-I characteristic of fixed Capacitor/Inductor [33]..... 8

Figure 2-1 General configuration of smart microgrid [52]. 21

Figure 2-2 Energy Storage Technologies 23

Figure 2-3 Classification of energy storage technologies 24

Figure 2-4 Power electronic scheme for electrical power system [59]..... 26

Figure 2-5 three kinds of the SVC, (a) Thyristor Switched Capacitor (TSC), (b) Thyristor Controlled Reactor (TCR), (c) TSC-TCR (figure is adapted based on [72]) 29

Figure 2-6 D-STATCOM connected to the AC distribution grid 30

Figure 2-7 V-I operating characteristics of SVC and D-STATCOM [figure is adapted based on 35]. 31

Figure 2-8 Single line diagram of D-STATCOM connected to the AC grid 32

Figure 2-9 PWM switching technique 34

Figure 2-10 Phase shift Controller [87]..... 35

Figure 2-11 Block diagram of the controller using p-q theory (figure is adapted based on [91] ,[92])..... 37

Figure 2-12 Basic block diagram of PLL [95]..... 38

Figure 2-13 Block diagram of the controller using SRF [76] 39

Figure 3-1 Modelling circuit for D-STATCOM with distribution grid [155] 48

Figure 3-2 Equivalent circuit of power distribution system with D-STATCOM [155] 50

Figure 3-3 d-axis equivalent circuit..... 51

Figure 3-4 q-axis equivalent circuit..... 51

Figure 3-5 Orientation of d-q transformation 52

Figure 3-6 Load active power as a function of Ls at constant value of Ts..... 57

Figure 3-7 Load active power as a function of Ts at constant value of Ls..... 57

Figure 3-8 Load active power as a function of Ls and Vs..... 58

Figure 3-9 Load active power as a function of Ts and Vs 58

Figure 3-10Source voltage Vs as a function of Ls at constant value of Ts 59

Figure 3-11 Source voltage as a function of Ts at constant value of Ls 59

Figure 3-12 Voltage source as a function of Ls and Pl 60

Figure 3-13 Voltage source as a function of Ts and Pl 60

Figure 3-14 $SD-STATCOM$as a function of Ls and Vs with power factor of the load of unity and source time constant 3.14 62

Figure 3-15 $SD-STATCOM$as a function of Ts and Vs with power factor of the load of unity 62

Figure 3-16 $SD-STATCOM$as function of Ls and $Vs$with lagging power factor of the load of 0.9 63

Figure 3-17 $SD-STATCOM$as function of Ts and Vs at with lagging power factor of the load of 0.9 63

Figure 3-18 $SD-STATCOM$as function of Ls and Pl with power factor of the load of unity 65

Figure 3-19 $SD-STATCOM$as function of Ts and $Pl$with power factor of the load of unity 65

Figure 3-20 $SD-STATCOM$as function of Ls and Pl with lagging power factor of the load of 0.9 66

Figure 3-21 $SD-STATCOM$as function of Ts and Pl with lagging power factor of the load of 0.9 66

Figure 4-1 Three-phase, two-level converter [166] 74

Figure 4-2 Detailed model of D-STATCOM 75

Figure 4-3 the equivalent diagram of DSTATCOM 75

Figure 4-4 The steady state response of the D-STATCOM variables Id Iq and Vdc 81

Figure 4-5 Surface plots of the active current (I_d), reactive current (I_q) and DC voltage (V_{dc}) with u_d and u_q 82

Figure 4-6 The overall control scheme for the D-STATCOM 83

Figure 4-7 closed current control loop 86

Figure 4-8 V_{PCC} control loop 87

Figure 4-9 closed voltage control loop 88

Figure 4-10 Structural design of the fuzzy -PI controller based DC voltage side 89

Figure 4-11 (a) Membership functions for error input signal. (b) Membership functions for deviation in error signal 92

Figure 4-12 Rules Surface..... 95
Figure 4-13 System structure of simulation model 97
Figure 4-14 Simulation results without D-STATCOM 98
Figure 4-15 Voltage magnitude at PCC..... 98
Figure 4-16 Voltage at PCC with P controller..... 101
Figure 4-17 DC side voltage with P controller 101
Figure 4-18 Voltage at PCC with PI controller..... 102
Figure 4-19 DC side voltage with PI controller 102
Figure 4-20 Voltage at PCC with fuzzy controller..... 102
Figure 4-21 DC-side voltage with fuzzy controller 103
Figure 4-22 Simulation results with D-STATCOM only..... 104
Figure 4-23 Supply current (simulation of the system with D-STATCOM only) 104
Figure 4-24 d and q components of the support current (simulation of the system with D-STATCOM only) 105
Figure 4-25 Circuit diagram of simulated system with a fault 106
Figure 4-26 Voltage magnitude at PCC for the fault condition lasting 10 cycles 106
Figure 4-27 d and q components of the support current for fault condition lasting 10 cycles..... 107
Figure 4-28 Voltage magnitude at PCC for fault condition lasting 5 cycles 107
Figure 4-29 d and q components of the support current for fault condition lasting 5 cycles..... 108
Figure 5-1 Configuration of the D-STATCOM with BESS..... 113
Figure 5-2 Detailed model of D-STATCOM based BESS..... 114
Figure 5-3 The control scheme for the D-STATCOM /BESS..... 118
Figure 5-4 ESS scheme 120
Figure 5-5 DC to DC Circuit Diagram [47] 122
Figure 5-6 BESS in buck mode [47] 123
Figure 5-7 BESS boost mode circuit [47] 124
Figure 5-8 (a) the structure diagram of DC -DC controller (b) control signal of model switching 126

Figure 5-9 The buck control diagram 126

Figure 5-10 The boost control diagram 127

Figure 5-11 Simulation results for the case with D-STATCOM based BESS with PI controller 128

Figure 5-12 Voltage magnitude at PCC point results for the case with D-STATCOM based BESS with PI controller 129

Figure 5-13 Supply current (simulation of the system with D-STATCOM based BESS) 130

Figure 5-14 d and q components of the support current (simulation of the system with D-STATCOM based battery) 131

Figure 5-15 The current and voltage magnitude of the battery storage 131

Figure 5-16 Voltage magnitude at PCC point 132

Figure 5-17 Simulation results for the case with D-STATCOM based BESS with fuzzy - tuned PI controller 133

Figure 5-18 DC-side voltage 134

Figure 5-19 Voltage magnitude at PCC for the fault condition lasting 10 cycles 136

Figure 5-20 DC side voltage during the fault condition for 10 cycles 137

Figure 5-21 Comparison of d components of the support current 137

Figure 5-22 Comparison of q components of the support current 138

Figure 5-23 The current and voltage magnitude of the battery storage 138

Figure 5-24 Voltage magnitude at PCC point 140

Figure 5-25 DC side voltage 141

Figure 5-26 Comparison of d components of the support current 142

Figure 5-27 Comparison of q components of the support current 142

Figure 5-28 Voltage magnitude at PCC point 143

Figure 5-29 DC side voltage 144

Figure 6-1 HESS topologies 149

Figure 6-2 D-STATCOM with HESS configuration 150

Figure 6-3 The equivalent circuit of supercapacitor 151

Figure 6-4 Equivalent circuit of HESS 153

Figure 6-5 Equivalent circuit of HESS in time-average model [201] 153

Figure 6-6 HESS controller 156
Figure 6-7 Overall control strategy of HESS 157
Figure 6-8 Current control loop of supercapacitor 160
Figure 6-9 Voltage control loop of HESS 160
Figure 6-10 Current control loop of battery 161
Figure 6-11 Detailed model of D-STATCOM based HESS 163
Figure 6-12 Control diagram of HESS 164
Figure 6-13 Membership functions of input variables 166
Figure 6-14 Surface plots 171
Figure 6-15 Surface description 172
Figure 6-16 System structure of simulation model 173
Figure 6-17 Voltage magnitude at PCC point 175
Figure 6-18 Simulation results for standard HESS management 175
Figure 6-19 Voltage magnitude at PCC 177
Figure 6-20 DC-side voltage 177
Figure 6-21 Voltage magnitude at PCC 179
Figure 6-22 Simulation results for HESS with FLC management 179
Figure 6-23 Comparison of the voltage magnitudes at PCC 180
Figure 6-24 Comparison of the DC-side voltage 180
Figure 6-25 Voltage magnitude at PCC 181
Figure 6-26 Simulation results for standard HESS management system with fault 183
Figure 6-27 Comparison of the voltage magnitude at PCC 183
Figure 6-28 Comparison of the DC-side voltages 184
Figure 6-29 Voltage magnitude at PCC 186
Figure 6-30 Simulation results for HESS with FLC management with fault 186
Figure 6-31 Comparison of the voltage magnitude at PCC 187
Figure 6-32 Comparison of the DC-side voltage 187
Figure 7-1: Overall schematic of experimental system 192
Figure 7-2 The load platform 193

Figure 7-3 Photo showing details of inverter 194

Figure 7-4 The battery voltage source..... 195

Figure 7-5 Capacitor bank and modelling circuit 196

Figure 7-6: Architecture of the CompactRIO system [208] 197

Figure 7-7 The NI Compact RIO system with input/output allocation 198

Figure 7-8: The hardware structure of the experimental rig..... 199

Figure 7-9 Waveforms of the three-phase bridge at output voltage 40 V (experimental results), (a) Channel 1 (yellow) voltage of inverter at line AB, channel 2 (green) voltage of inverter at line BC, channel 3 (purple) voltage of inverter at line CA, channel 4 (blue) phase current of inverter, (b) Battery current (A)..... 202

Figure 7-10 Waveforms of the three-phase bridge at output voltage 40 V (simulation results), (a) voltage waveforms of three-phase bridge, (b) three phase current of inverter, (c) Battery current (A) 203

Figure 7-11 Waveforms of the three-phase bridge at output voltage 50 V (experimental results), (a) Channel 1 (yellow) voltage of inverter at line AB, channel 2 (green) voltage of inverter at line BC, channel 3 (purple) voltage of inverter at line CA, channel 4 (blue) phase current of inverter, (b) Battery current (A)..... 204

Figure 7-12 Waveforms of the three-phase bridge at output voltage 50 V (simulation results), (a) volt-age waveforms of three-phase bridge, (b) three phase current of inverter, (c) Battery cur-rent (A) 205

Figure 7-13 Waveforms of the three-phase bridge at output voltage 60 V (experimental results), (a) Channel 1 (yellow) voltage of inverter at line AB, channel 2 (green) voltage of inverter at line BC, channel 3 (purple) voltage of inverter at line CA, channel 4 (blue) phase current of inverter, (b) Battery current (A)..... 206

Figure 7-14 Waveforms of the three-phase bridge at output voltage 60 V (simulation results), (a) voltage waveforms of three-phase bridge, (b) three phase current of inverter, (c) Battery current (A) 207

Figure 7-15 Waveforms of the inverter based battery and SC at output voltage 40 V (experimental results), (a) Channel 1 (yellow) voltage of inverter at line AB, channel 2 (green) voltage of inverter at line BC, channel 3 (purple) voltage of inverter at line CA, channel 4 (blue) phase current of inverter, (b) channel 1 (yellow) Battery current (A), channel 2 (green) SC current (A) 209

Figure 7-16 Waveforms of the inverter based battery and SC at output voltage 40 V, (simulation results), (a) voltage waveforms of three-phase bridge, (b) three phase current of inverter, (c) channel 1 (blue) Battery current (A), channel 2 (red) SC current (A) 210

Figure 7-17 Waveforms of the inverter based battery and SC at output voltage 50 V (experimental results), (a) Channel 1 (yellow) voltage of inverter at line AB, channel 2 (green) voltage of inverter at line BC, channel 3 (purple) voltage of inverter at line CA, channel 4 (blue) phase current of inverter,(b) channel 1 (yellow) Battery current (A), channel 2 (green) SC current (A) 211

Figure 7-18 Waveforms of the inverter based battery and SC at output voltage 50 V, (simulation results), (a) voltage waveforms of three-phase bridge, (b) three phase current of inverter, (c) channel 1 (blue) Battery current (A), channel 2 (red) SC current (A) 212

Figure 7-19 Waveforms of the inverter based battery and SC at output voltage 60 V (experimental results), (a) Channel 1 (yellow) voltage of inverter at line AB, channel 2 (green) voltage of inverter at line BC, channel 3 (purple) voltage of inverter at line CA, channel 4 (blue) phase current of inverter,(b) channel 1 (yellow) Battery current (A), channel 2 (green) SC current (A) 213

Figure 7-20 Waveforms of the inverter based battery and SC at output voltage 60 V, (simulation results), (a) voltage waveforms of three-phase bridge, (b) three phase current of inverter, (c) channel 1 (blue) Battery current (A), channel 2 (red) SC current (A) 214

Figure 7-21 Phase waveforms of the inverter at output voltage 40 V 215

Figure 7-22 phase waveforms of the inverter at output voltage 50 V 215

Figure 7-23 Phase waveforms of the inverter at output voltage 60 V 215

Figure A-1 Modelling circuit for D-STATCOM with AC grid 251

Figure B 1 Inductor current during one sample for DC-DC converter topology 255

Figure B 1 Inductor current during one sample for DC-DC converter topology 255

Figure C- 1 Schematic diagram of input LC_filter for induction motor 259

Figure C- 2 Modified cascade inverter with switch drive circuits..... 260

Figure C- 3 Simplified diagram of the HCPL2601 optocoupler..... 260

Figure C- 4 Schematic diagram of analogue optoisolator..... 261

Figure C- 5 Schematic diagram of voltage measurement interface..... 261

Figure C- 6 Schematic diagram of including voltage and current sensing 262
Figure C- 7 : Compact RIO cRIO-9012 configuration 264
Figure C-8 : CRIO chassis connection to CRIO controller 265
Figure C- 9 : NI 9425 model configuration 265
Figure C-10: NI 9476 model configuration 266
Figure C-11: NI 9474 model configuration 266
Figure C-12: NI 9402 model configuration 266
Figure C-13: NI 9201 model configuration 266

LIST OF TABLES

Table 2-1 A comparison of battery, ultracapacitor and conventional capacitors performance [57][58] 25

Table 3-1 Parameters of the distribution power system [158]..... 56

Table 3-2 Reactive power for source voltage sags..... 67

Table 3-3 Reactive power for different loads. 67

Table 4-1 D-STATCOM parameters [158]. 80

Table 4-2 Rule base for the deviation in Kp 94

Table 4-3 Rule base for the deviation in Ki 94

Table 4-4 System parameters of simulation model 97

Table 4-5 Required reactive power for different sources..... 99

Table 4-6 Required reactive power for different loads..... 99

Table 5-1 Comparison of the system performance..... 134

Table 5-2 Comparison of the system performance..... 141

Table 5-3 Comparison of system performance for fuzzy-tuned PI and standard PI controller..... 145

Table 6-1 The variables names of membership functions 166

Table 6-2 System parameters 173

Table 6-3 Comparison of system performances. 180

Table 6-4 Comparison of system performances. 188

Table C- 1 Induction motor parameters..... 259

LIST OF EQUATIONS

(2-1)..... 32
(2-2)..... 32
(2-3)..... 35
(2-4)..... 36
(2-5)..... 36
(2-6)..... 36
(2-7)..... 36
(2-8)..... 36
(2-9)..... 36
(2-10)..... 38
(2-11)..... 38
(3-1)..... 48
(3-2)..... 49
(3-3)..... 49
(3-4)..... 49
(3-5)..... 49
(3-6)..... 49
(3-7)..... 49
(3-8)..... 49
(3-9)..... 50
(3-10)..... 50
(3-11)..... 50
(3-12)..... 51
(3-13)..... 51
(3-14)..... 51
(3-15)..... 52
(3-16)..... 52
(3-17)..... 52

(3-18)..... 52
(3-19)..... 52
(3-20)..... 52
(3-21)..... 52
(3-22)..... 53
(3-23)..... 53
(3-24)..... 53
(3-25)..... 53
(3-26)..... 53
(3-27)..... 53
(3-28)..... 53
(3-29)..... 54
(3-30)..... 54
(3-31)..... 54
(3-32)..... 54
(3-33)..... 54
(3-34)..... 54
(3-35)..... 55
(3-36)..... 55
(3-37)..... 55
(3-38)..... 55
(3-39)..... 55
(3-40)..... 56
(3-41)..... 68
(3-42)..... 68
(4-1)..... 76
(4-2)..... 76
(4-3)..... 76
(4-4)..... 76

(4-5)..... 76
(4-6)..... 77
(4-7)..... 77
(4-8)..... 77
(4-9)..... 77
(4-10)..... 79
(4-11)..... 79
(4-12)..... 79
(4-13)..... 79
(4-14)..... 84
(4-15)..... 85
(4-16)..... 85
(4-17)..... 85
(4-18)..... 85
(4-19)..... 85
(4-20)..... 86
(4-21)..... 87
(4-22)..... 87
(4-23)..... 88
(4-24)..... 88
(4-25)..... 88
(4-26)..... 88
(4-27)..... 88
(4-28)..... 90
(4-29)..... 90
(4-30)..... 90
(4-31)..... 90
(4-32)..... 93
(4-33)..... 93

(4-34)..... 93
(4-35)..... 94
(4-36)..... 96
(5-1)..... 114
(5-2)..... 114
(5-3)..... 114
(5-4)..... 114
(5-5)..... 115
(5-6)..... 116
(5-7)..... 116
(5-8)..... 117
(5-9)..... 117
(5-10)..... 119
(5-11)..... 119
(5-12)..... 119
(5-13)..... 121
(5-14)..... 121
(5-15)..... 121
(5-16)..... 123
(5-17)..... 123
(6-1)..... 152
(6-2)..... 152
(6-3)..... 152
(6-4)..... 152
(6-5)..... 152
(6-6)..... 152
(6-7)..... 153
(6-8)..... 153
(6-9)..... 153

(6-10) 154
(6-11) 154
(6-12) 155
(6-13) 155
(6-14) 156
(6-15) 156
(6-16) 156
(6-17) 157
(6-18) 158
(6-19) 158
(6-20) 158
(6-21) 158
(6-22) 158
(6-23) 159
(6-24) 160
(6-25) 160
(6-26) 160
(6-27) 161
(6-28) 161
(6-29) 167
(6-30) 167
(6-31) 168

(A-1) 251
(A-2) 252
(A-3) 252
(A-4) 252
(A-5) 252
(A-6) 252

(A-7) 252
(A-8) 252
(A-9) 253
(A-10) 253
(A-11) 253
(A-12) 253
(A-13) 253
(B-1) 255
(B-2) 255
(B-3) 255
(B-4) 255
(B-5) 256
(B-6) 256
(B-7) 256
(B-8) 256
(B-9) 256
(B-10) 256
(B-11) 256
(B-12) 256
(B-13) 257
(B-14) 257
(B-15) 257
(B-16) 257
(B-17) 257
(B-18) 257
(B-19) 257

LIST OF ABBREVIATIONS

AC	Alternating current
ANN	Artificial Neural Network
APC	active power control
BESS	Battery energy storage system
CCL	current control loops
CMC	Cascaded Multilevel Converter
COG	Centre of Gravity
CSC	current source converter
DC	Direct current
DESS	Distributed energy storage systems
DGs	Distributed Generators
DSP	digital signal processors
D-STATCOM	Distribution static synchronous compensator
DVR	Dynamic Voltage Restorer
ESR	equivalent series resistance
ESS	Energy storage systems
FACTS	Flexible AC Transmission System
FLC	Fuzzy logic controller
FPGAs	field programmable gate arrays
GA	genetic algorithm
GTO	Gate-Turn-Off
HESS	Hybrid energy storage system
ICT	Internet and communication technologies
IGBT	Insulated Gate Bipolar Transistors
IPFC	interline power flow controller
IRP	Instantaneous reactive power
Li-Ion	Lithium -Ion
LPF	low pass filters

MC	micro controllers
MG	Microgrid
MOSFETs	metal-oxide-semiconductor field effect transistors
NiCad	Nickel Cadmium
NiMH	Nickel Metal Hydride
NPC	Neutral Point Clamped
OLTC	on load tap changer
PCC	Points of common connection
PCS	power conversion system
PEVs	plug-in electric vehicles
PHEVs	plug-in hybrid electrical vehicles
PI	Proportional-Integral
PID	Proportional Integral Derivative
PLL	phase locked loop
PQ	Power quality
PSO	particle swarm optimization
PVs	Photovoltaics
PWM	Pulse width modulation
rms	root mean square
RPC	reactive power compensator
SC	Supercapacitor
SHE	selected harmonic elimination
SMES	superconducting magnetic energy storage
SRF	synchronous rotating frame
SSSC	static synchronous series compensator
STATCOM	static synchronous compensator
SVC	static var compensator
SVC	Static VAR compensators
SVM	space vector modulation

SVPWM	space vector pulse-width modulation
TCPS	Thyristor-controlled phase shifters
TCSC	Thyristor-controlled series capacitors
UPFC	unified power flow controller
VSC	Voltage source converter

NOMENCLATURE

A	exponential zone amplitude (V)
B	exponential zone time constant inverse (*Ah*)−1
C_{dc}	the capacitor of the DC link of D-STATCOM
C_f	coupling capacitor
D	the duty cycle
$Derror(i)$	the deviation in the error
d_B	the duty cycle of the battery converter
$d_B^{\sim}$	small changes in the duty cycle of the battery
d_{sc}	the duty cycle of the SC converter
$d_{sc}^{\sim}$	small changes in the duty cycle of the supercapacitor
D_B	the linearised value of d_B
D_{sc}	the linearised value of d_{sc}
ΔI_q	the variations of the reactive current component passing in the line.
ΔV_{PCC}	the change in the voltage at PCC,
ΔK_p and ΔK_i	the deviation in the proportional and integral parameters
$error(i)$	the error signal between the actual and reference value
E_0	Battery constant voltage (V)
E	no-load voltage (V)
f	the frequency of the system
f_{sw}	Switching frequency
I_f	the injection current by the D-STATCOM
I_s	the source current
$\overline{I_l}$	the load current
I_{sc}	the current of the supercapacitor
i_{La}, i_{Lb}, i_{Lc}	phase load current
i_B	actual battery current
$i_B^{\sim}$	small changes in battery current

i_B^*	reference battery current
i_{DC}	the total current required by the ESS
i_d	d component of Line current
i_q	q component of Line current
i_{sc}	actual supercapacitor current
$i_{sc}^{\sim}$	small changes in the supercapacitor current
i_{sc}^*	reference supercapacitor current
i_α	current in α plane
i_β	current in β plane
K	polarisation voltage (V)
K_p and K_i	proportional and integral parameters
K_{pref} and K_{iref}	the normal values of proportional and integral parameters
L	coupling reactor
L_b	the buck/boost inductor
L_B	the buck/boost inductor of the battery converter
L_l	the load inductor
L_s	the source inductance
L_{sc}	the buck/boost inductor of the supercapacitor converter
m	modulation index
P	the active power
P_B	the actual power of the battery
P_{Bmin} and P_{Bmax}	the lower and higher power boundaries of the battery
P_{ESS}	the power of the energy storage system
P_l	the power on the load side
P_{load}	the load power
P_{sc}	the actual power of the supercapacitor
P_{scmin} and P_{scmax}	the lower and higher power boundaries of the supercapacitor
P_{source}	the power of the main supply in the grid

P_{uncomp}	uncompensated battery power
p_{ac}	the instantaneous power of the AC side of the converter
p_{dc}	the instantaneous power of the DC- link of D-STATCOM
Q	Battery capacity (Ah)
Q	the reactive power
R	internal resistance of the coupling reactor
Rc	represents losses in the converter.
R_b	internal resistance of the battery (Ω)
R_l	the load resistance
R_s	the source resistance
SOC	state of the charge
SOC_B	the state of the charge of the battery
SOC_{Bmin}, SOC_{Bmax}	the lower and higher SOC boundaries of the battery
SOC_{sc}	the state of the charge of the supercapacitor
SOC_{scmin}, SOC_{scmax}	the lower and higher SOC boundaries of the supercapacitor
δ	the phase difference between the output voltage of the D-STATCOM and the grid voltage
T_l	the time constant of the load
T_s	the time constant of supply
V_{DC_error}	the error signal of the DC side voltage
V_G	the rms voltage of the main grid
V_{PCC}	the voltage at the point of common coupling
V_{PCC}^*	the reference voltage at the point of common coupling
V_{STAT}	the output AC voltage of the D-STATCOM
V_{dc}	actual value of the DC side voltage
V_{dc_ref}	reference value of the DC side voltage
V_s	the source voltage
$V_{sc,0}$	the voltage for a fully charged supercapacitor
V_{sc}	the actual voltage of the supercapacitor

V_{sd}	d component of supply voltage
V_{sq}	q component of supply voltage
$V_{st\ ,abc}$	the D-STATCOM's AC voltage
$V_{st,d}$	d component of DSTATCOM output voltage
$V_{st,q}$	q component of DSTATCOM output voltage
V_{td}	desired load voltage magnitude
V_B	Battery voltage (V)
v_a, v_b, v_c	phase voltages
v_d	voltage in d axis
v_q	voltagein q axis
v_α	voltage in α plane
v_β	voltage in β plane
ω_s	angular speed of the infinite bus
ω	angular frequency of the rotating reference frame
X_L	the leakage reactance
$Z_{th}\angle\beta$	the feeder impedance between the source and load

1 Chapter One: Introduction

1.1 Background

Over the last century, large power stations have centralised electrical power generation, delivering the electricity produced into an interconnected network to provide electricity to the customer. Basically, the entire power network has been divided into three significant sectors: generating stations, transmission networks and distribution grids. The main source of electricity generation depends on the fuel used in the centralized power stations. e.g., fossil fuel that produces greenhouse gases. The electric energy produced is transported through the distribution grids and interconnected transmission networks, see Figure 1.1 (a). As a result, most control functions are performed in the central power stations or at the substations which form part of the transmission system [1].

The electric power industry is moving toward a new design of power grid which satisfies increasing consumer demands, while reducing fuel costs and minimizing emissions. In December 1997, the Kyoto protocol was established. This is an international agreement with the goal of decreasing climate change by reducing greenhouse gases (CO2, NOx, SOx etc.) in the atmosphere. The United Kingdom is one of the participating countries [2]. The UK Energy Agency supports the minimization of carbon dioxide emission and other gases. To achieve this, the UK goal is to develop a renewable energy sector to meet about 15 % of consumption demand in 2020 in a sustainable and economical way, in order to reach the second target of reducing 80% of greenhouse emission by 2050 [2], [3].

Thus, conventional centralized energy generation based on fossil fuels is no longer considered as having a long-term future in the electricity sector [4]. As a result, more renewable energy sources “such as wind and solar photovoltaics (PVs), solar thermal power, hydropower, bioenergy, and ocean power” [4], [5] will be required to supply power to the grids. These renewable power sources are usually distributed in the form of small generators known as distributed generators (DGs) and their contributions to the centralized power grids managed at the distribution level, as presented in Figure 1-1 (b).

The future network structures, “microgrids” are expected to be active grids which interface between generators/loads and the main utility grid to make a flexible, manageable and sustainable electricity system. The microgrids can work in either grid-connected or grid-independent (islanded) mode [6], [7]. The distribution grids are likely to become a more important part of the overall system, while the transmission networks will become less important. According to the Institute of Engineering and Technology [8], in the UK the number of generators providing grid control (all connected to the transmission system) are expected to rise from 10-15 recently to more than 600,000 (transmission and distribution linked) by 2030. Also, it is predicted that the number of voltage regulation devices could rise from 10,000 to 900,000 by 2030. Figure 1.1 (a and b) presents a simplified representation of the differences that could happen to the production and distribution of electrical power. Figure 1.1 (a) shows conventional power production and distribution while Figure 1.1 (b) shows a possible new power plant power production and distribution system operating with bidirectional power flow. The number of the power sources will increase by connected a number of DGs at the distribution level each of which could operate with bidirectional power flow.

It can be anticipated that the essential changes that are going to happen over the coming years are:

- A number of distributed energy storage systems (DESS) and various kinds of DGs will be researched, developed and marketed [9].
- Future power grids will require a substantial increase in power electronic devices to control the active and reactive power flows between the grids and the storage units [10], [11].
- An increase in the number of islanded grids, where part of the grid operates separately from the main grid, using small local sources which will need to be managed and controlled [12].

However, the structural changes resulting from high penetrations of renewable energy sources (and other forms of distributed resources) into the grid system also create new challenges, in particular voltage stability and power quality issues to the grid due to the intrinsic low inertia and intermittency of these new energy

sources. Subsequently new and innovative measures are needed to support voltage regulation at the points of common connection (PCC) of these sources with the power grid at the distribution levels [13] [14].

This research work aims to extend existing work on microgrids by investigating voltage control for electrical distribution systems, which will be an important issue in future smart distribution power grids.

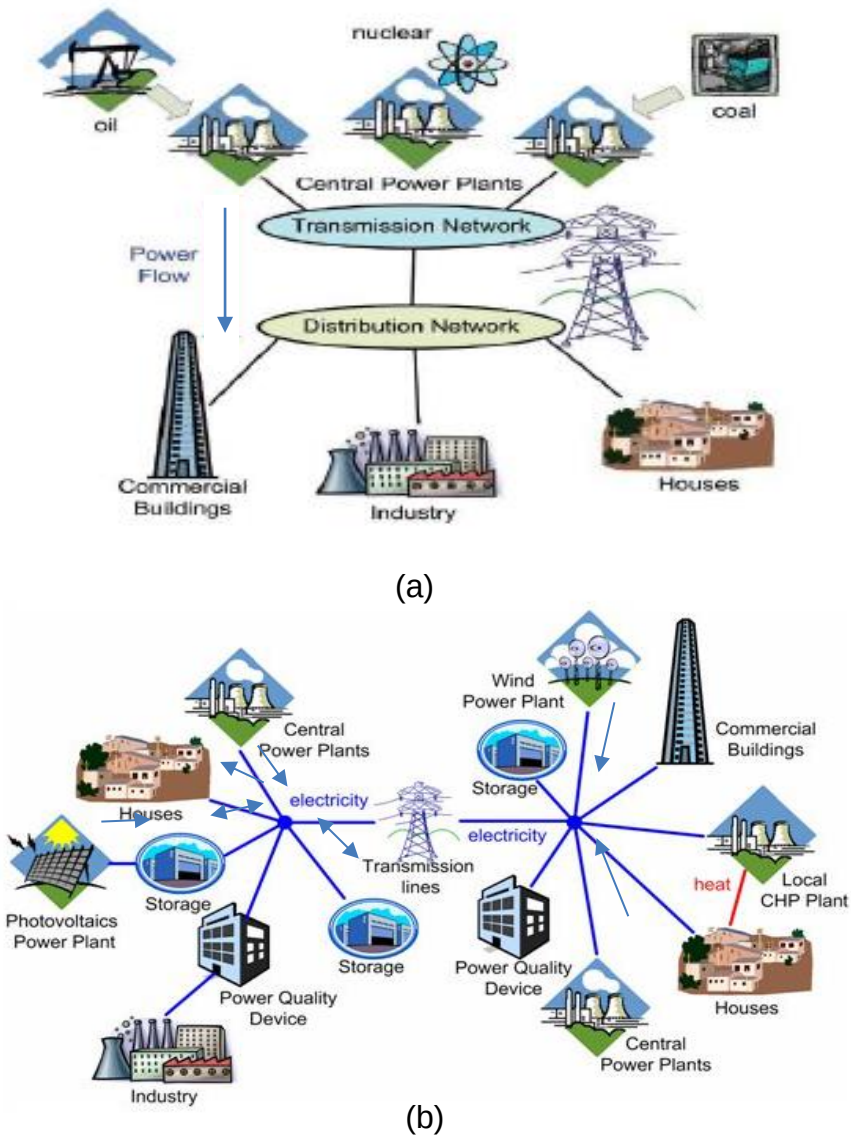

Figure 1-1 (a) Conventional electrical network,(b) Future electrical network [15]

1.2 Power quality challenges.

The power quality (PQ) concept includes all the variational issues related to the voltage and current waveforms in the power grids including; magnitude, phase and frequency [16] [17]. PQ problems are taken seriously in industrial and commercial utilities. In particular, the modern power system is expected to work smartly using Information and Communication Technology (ICT) and power electronic loads [18], [19], and needs a higher PQ performance level because it is so sensitive to power system disturbances. Poor PQ is often the consequence of transient conditions and load disturbances in the power grids.

Variations in the steady state and transient voltage problems which are common PQ issues are explain next. In general, the PQ problems related to voltage can be categorised as [20]:

- Transients
- Long-Duration Voltage Variations
- Short-Duration Voltage Variations
- Voltage Imbalance
- Waveform Distortion
- Voltage Fluctuation

Transients can be a destructive form of power disturbance and are normally classified into two types: impulsive and oscillatory. Impulsive transients can be defined as a sudden sharp peak (either positive or negative) of the voltage and/or current from the steady state values, for a duration of less than 50 ns [17]. For example, an electrostatic discharge can produce a positive impulsive transient of this kind. Surge arresters are an effective means of suppressing such impulsive transients. Oscillatory transients occur through a sudden variation in the steady state condition of voltage and/or current at the system frequency. Typically, the response duration of the oscillatory transient is much slower compared to the impulsive transients, but it will decay to zero within one cycle. Transient overvoltage results from the oscillatory transient and can lead to break-down in the power feeder insulators.

Long-term voltage variation is any variation in the root mean square (rms) value of the voltage for more than one minute at the setting value of the system frequency. This PQ category includes under-voltage and over-voltage deviations: under-voltage is a voltage reduction *below* 90% of the *reference voltage* for *more than one minute*, and over-voltage is a voltage increase of 10% or more above the reference voltage for a period exceeding one minute [17], [20].

All deviations in the voltage waveform for a period less than one minute are known as short-term voltage variations. Short-term variations address voltage sags and swells. The voltage sag is a drop in the rms voltage to between the reference value and 90% of the reference value for time periods from one half-cycle to one minute and is known to be one of the most frequent power quality problem related to voltage disturbances influencing the industrial user and utilities [21]. Voltage sags are usually caused by the tuning of the large inductive loads of industrial end-users [17] but may be due to faults that occur in the power systems themselves [22], [21]. Normally, the common cause of voltage sags are faults occurring in the power distribution system and sudden inductive load increases [23]. Voltage sags can cause loss of production in automated processes since the voltage sag can trip a motor or cause its controller to malfunction. Voltage sags can also damage data processing systems and computers. For semiconductor manufacturing industries such a loss can be substantial [20].

A voltage swell is an increase in the rms voltage to between the reference value and 10% more than the reference value for one half-cycle to one minute [19]. Voltage swells could damage computers and other home devices. However, short- term voltage variations have less impact than long-term voltage variations [24].

The condition of inequality in the relative amplitudes of the three phases of the voltage supply is defined as voltage imbalance. “Furthermore, they may not even be equally displaced in time. The voltage imbalance can cause temperature rise in motors and can even cause a large motor to trip” [20] .

Generally, the voltage distortions are due to three factors: DC offset, harmonics and notching. All generate a variation in the steady state voltage or current waveform from an ideal sine wave. DC offset is when the average value of the voltage over a cycle is not zero, this can cause deterioration of performance or even damage the core of a power transformer. Harmonics can lead to losses and heat generation in transformers and failure of the control system. Notching is a voltage distortion that occurs with the same periodicity as the voltage, and is due to the normal operation of power electronic devices when the current is commutated from one phase to another. Although the magnitude of the notch may be relatively small the rate of change of voltage can be high and this can damage capacitive components connected as shunts.

Voltage fluctuation (flicker) is systematic variation in the voltage waveform that occurs in a fast and random manner. Voltage flicker can occur due to large start-up currents flowing in the system, such as when an arc furnace is connected as load. This causes a dip in the voltage of the bus to which the furnace is connected and other customers supplied by the same feed face a severe voltage drop unless the supply bus is very stiff. Flicker is known to reduce the life span of electronic equipment [20].

1.3 Traditional Mitigation Methods for Voltage Regulation

The main function of power distribution operators is to maintain the supply voltage at a steady state level within acceptable boundaries despite system variations. Voltage regulation and reactive power compensation devices are the most commonly used devices to keep the voltage within permitted limits in power distribution systems. The devices include: “on load tap changer (OLTC) transformers” [25], [26], “switched shunt capacitors” [27] and “steps voltage regulator” [28]. The basic operational concept of these devices is based on power flow theory in conventional power distribution networks where the power flows from the main substation toward the customer. Consequently, the voltage reduces along the feeder buses.

1.3.1 Voltage Regulation

Voltage regulation is obtained by placing voltage regulators at appropriate points in the power grid. The voltage regulators can be categorised as one of two types: linear or switching. Most of these devices are suited to traditional distribution grids where the power flow is unidirectional; from the substation to the customer [29]. The penetration of DGs make the assumption of unidirectional power flow no longer valid. A DG might increase the voltage at the feeder-end so that it is higher than the voltage at the source [30]. Adaptations have been suggested for upstream line voltage regulators if DGs are connected to the system. Multiple line drop compensation based voltage regulators are effective for regulating the system voltage even with high penetration of DGs [31]. Hence, the grid voltage in conventional distribution network is maintained by installing voltage regulators, with reactive power compensation placed at the customer's end. The bus voltages not allowed to be regulated by the DGs themselves.

1.3.2 Reactive Power Compensation

Reactive power compensation is known to be an important issue in alternating electric power networks, and in distribution and transmission networks is usually achieved by shunt compensation devices. Both conventional reactors and capacitors are connecting in parallel at the buses of the loads according to requirements [32]. The voltage of the system can be increased to acceptable limits by using shunt capacitors while the shunt reactors are typically employed to reduce the system voltage when it is increased under conditions of light load and load rejection. The V-I characteristics of fixed capacitive and inductive compensation is shown in Figure 1-2 [33].

When the variability of new distribution grids due to the installation of DGs, the power flow and the voltage profiles are affected as well as the system is no longer passive but active make traditional devices no longer applicable or effective in adjusting voltage variation [34]. Synchronous condensers can be used to provide a continuously controlled reactive power output from inductive to capacitive region [35]. However, such devices tend to have a slow response and high cost, and so are not commonly used in distribution systems.

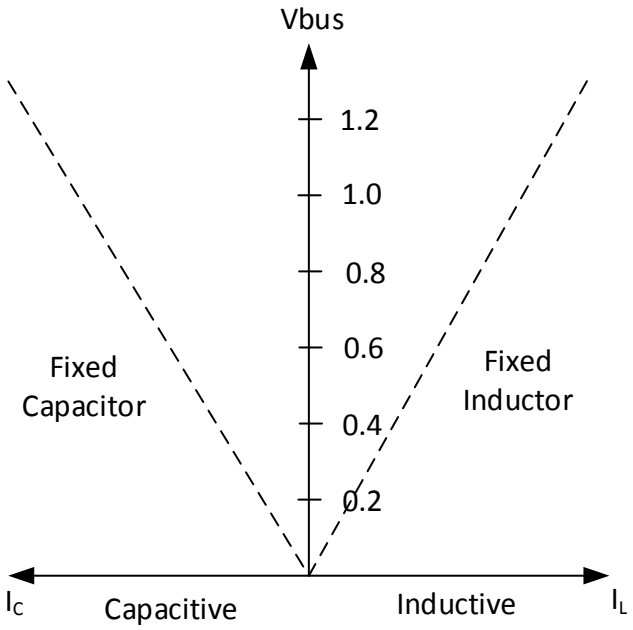

Figure 1-2 V-I characteristic of fixed Capacitor/Inductor [33]

1.4 Flexible AC Transmission System (FACTS) Devices Based Mitigation Methods for Voltage Issues

Recently, electrical power grids have accommodated a number of changes due to the inclusion of distribution generation and renewable power sources. The control operation and management of these new grids requires a new technology to maintain and improve the stability and reliability of power systems in a fast and efficient manner. Power-electronic technologies make an essential contribution in smart grid and electrical grid integration of renewable energy sources. They are widely used and their use is rapidly expanding as their application becomes more integrated with grid-based systems [36], [14], [37].

Flexible AC-Transmission System (FACTS) devices are one of applications of power electronics based on the use of semiconductor device and other static controllers. The cost-effective availability of high power semiconductor devices such as Gate-Turn-Off (GTO) thyristors and Insulated Gate Bipolar Transistors (IGBTs) has made FACTS technology possible and it has now emerged as a practical solution to improve voltage stability in transmission and distribution systems.

FACTS devices have a number of significant benefits when applied to power systems, including [33]:

- Providing reactive power compensation
- Providing voltage regulation
- Enhancing steady-state and transient voltage stability
- Eliminating power system oscillations
- Increasing power transfer capability

The static synchronous compensator (STATCOM), Dynamic Voltage Restorer (DVR), unified power flow controller (UPFC) and static var compensator (SVC) are examples of FACTS devices [35], [38]. FACTS devices are known as D-FACTS when used with electrical distribution grids. The D-STATCOM (distribution static synchronous compensator) has been combined with smart grid technologies to improve voltage stability of distribution networks [6], [39], [40]. Amongst FACTS devices D-STATCOM has attracted great attention as a power device for improving voltage stability.

1.5 Research Motivation

The modern power system is employed to work smartly using DGs. The interaction of DGs with the traditional distribution grids are forcing these grids to operate with bidirectional power flow. The DGs have significant benefits including being environmentally friendly power sources, minimizing grid loss, and enhancing system reliability. In general, DGs will be connected with the main utility grid at distribution levels with loads at the PCC. The DGs will have a negative influence on the dynamic performance, power stability and power quality of the power system with voltage variation which is the main concern with this kind of connection. The ability of the system to regulate the voltage at the PCC with the electrical system is key for the successful operation of microgrids.

As advanced bidirectional power paradigms, microgrids are a challenge that has not yet been fully addressed. Microgrids require an instantaneous online voltage controller to work jointly with the main utility grid and provide a reliable service. Generally, microgrids have utilized distributed energy storage systems such as batteries, flywheels, fuel cells and supercapacitors for efficient performance in smart grid operation [21], [41]. On the other hand, due to its ability to maintain power quality, even with voltage sag, D-STATCOM has been increasingly used in recent power systems [24] [42] [43].

To date, there have been limited studies in the area of intelligent control and analysis of D-STATCOM, which has the quality of both absorbing and/or delivering reactive power to a power system . Nor, and in particular, has there been much research into exploiting the reactive and active power of energy storage systems (ESS) as additional resources to support the grid's voltage stability.

The motivation of this study is to configure ESSs using D-STATCOM as active and reactive power devices in order to improve the reliability and power quality of distribution grids, identifying predefined control algorithms, and the extent to which they have been used. It then proposes a new control approach based on a Sugeno fuzzy logic supervisor to ensure a fast and consistent voltage response under different operating conditions. It also focuses on determining the effectiveness of Sugeno fuzzy supervisor control management of the ESS in exploiting the active power of the ESS more efficiently, in addition to the D-STATCOM's reactive power, to support the grid's voltage stability.

1.6 Research Aim and Objectives

The main aim of this research is to improve the reliability and power quality of the distribution grids by controlling the voltage at the PCC. In order to achieve this there is a need to develop a voltage control for a distribution network using reactive power compensation, by combining the use of D-STATCOM with energy storage technology. To meet this, aim the following objectives were identified:

1. To derive and develop a mathematical model of the D-STATCOM connected with a distribution system and its control in a rotating synchronous frame.
2. To design a new control approach with a Proportional-Integral (PI) based Sugeno fuzzy logic supervisor to provide superior performance over varying operating conditions.
3. To develop the D-STATCOM functionality by integrating energy storage into the DC side to produce controllable active power.
4. To modify the D-STATCOM converter, supplied by a dual DC source (battery and supercapacitor) to enhance grid steady state and transient voltage stability.
5. To demonstrate the effectiveness of the D-STATCOM based hybrid energy storage system (HESS) in providing voltage control during short-term voltage stability.
6. To develop a novel approach based on a new fuzzy control strategy for HESS management to provide an intelligent real-time energy management controller.
7. To validate and implement the proposed algorithms based on simulation results.

1.7 Contributions to Knowledge

The main contributions of this study to knowledge can be listed as:

1. This work contributes to a better understanding of the smart distribution grid by modelling D-STATCOM with a HESS for voltage stability enhancement in distribution power grids.
2. This work investigates the viability of an improved standard PI controller of the DC side of the D-STATCOM controller and establishes that adjusting the proportional and integral coefficients of a Sugeno - PI-fuzzy controller during critical transients such as a load disturbance improves controller efficiency. To overcome the sub-optimal operation of existing methods which are based on optimization of a single operating point during steady state operation, requires intelligent control implementation using fuzzy

control in a nonlinear model

3. a new Sugeno - PI-fuzzy controller which exploits the DC storage capability of the D-STATCOM is designed to improve the voltage stability of the distribution grid. The approach employs d-q control theory to obtain in real-time the active and reactive currents from the energy storage under different operating conditions.
4. This project develops a modified voltage control strategy for D-STATCOM with HESS to support the distribution power network during short-term voltage stability. Where, voltage control, steady state and transient stability have been discussed in the literature with different control and configuration of D-STATCOM. However, there has been relatively little prior work on the integration of D-STATCOM and HESS related to short-term voltage stability. The main advantages of a modified D-STATCOM configuration with dual DC source (battery and supercapacitor) are faster voltage regulation and battery current stresses are reduced.
5. Finally, this project develops a new approach to supervisory control strategy to be realised through the design of a HESS based on Sugeno fuzzy rules. This is the first time such a design has been applied in a D-STATCOM/HESS controller. In the design, the advantage of a high-power storage unit (supercapacitor) and high energy storage unit (battery) have been combined with the D-STATCOM configuration to avoid the drawbacks of a single, specific storage unit and facilitate overall power sharing directly between the battery and supercapacitor (which is considered one of the main features for the future of energy storage technology in smart grids). Its real-time performance will provide superior output current response for both battery and supercapacitor.

1.8 Thesis Overview

This thesis has been arranged in eight chapters with abstract, references and appendices. A general outline of the chapters is as follows:

Chapter One introduces power quality problems, especially voltage sags and dips, and discusses their importance in distribution systems. FACT based

mitigation methods for voltage issues are introduced as are the motivation, aim and objectives of the study.

Chapter Two provides a review of current works on microgrids including distributed generators. A short review of energy storage system technology is also presented. The issues of distribution systems and integrated distributed generators are discussed with mitigation measures for voltage problems. The D-STATCOM operation is described briefly, including the basic configuration and working principle of the D-STATCOM. The different applications of D-STATCOM devices in distribution systems are also explained in this chapter.

Chapter Three explains the mathematical model of the distribution system which is proposed based on the synchronously rotating reference frame. Steady-state characteristics are obtained from the state equation of the distribution system with the D-STATCOM, which leads to an analysis of the steady state performance. The designed component rating of the D-STATCOM for voltage regulation is computed in this chapter.

Chapter Four gives a brief review of the power converters connected to the grid. In particular, the two-level, three-phase power converter is described. The modelling of the D-STATCOM is presented in this chapter. The conventional D-STATCOM operation and design are explained in detail. Dynamic equations of the D-STATCOM model and the vector control strategy of D-STATCOM based on the d-q theory are presented, including current control, DC-link voltage control, the external loop control design and the design of the new Sugeno PI fuzzy controller to enhance the performance of the standard D-STATCOM. Finally, the simulation of the model and control design of the conventional D-STATCOM is demonstrated using MATLAB/SIMULINK.

Chapter Five presents the modified D-STATCOM configuration based on a battery energy storage system (BESS). The modelling and its control algorithm are described in greater detail including the DC-to-DC bidirectional power converter which is used as the main control device in BESS. At the end of this chapter, a simulation study to investigate the D-STATCOM based BESS

capabilities to support the grid with active and reactive power is carried out under load disturbances and fault condition.

Chapter Six addresses a detailed analysis of a novel approach on a modified D-STATCOM converter based HESS (battery and supercapacitor). Firstly, the modelling and the configurations of general types of HESS topologies are presented. Then, two control strategies, a standard controller with low pass filter and a new Sugeno fuzzy control strategy are proposed and tested for HESS management. Finally, results and discussions of the simulation are reported.

Chapter Seven describes the experimental hardware prototype, the overall schematic of the experimental rig and the output results to verify the effectiveness of the proposed energy management configurations described in Chapters 5 and 6 using National Instruments Compact RIO Real-Time control platform and Lab VIEW software

Chapter Eight presents the thesis discussion, conclusions and future work sections.

1.9 Associated Published Work

1. Shatha Al kubragyi, Patrick C. K. Luk, J. Economou, Mohammed. K. Al-Saadi “Battery energy storage based on D-STATCOM device in distribution grid systems,” In Proceedings of the Conference of Cranfield Science for a Circular Economy. How to tackle the Water, Energy, Food nexus, Bedford, UK, 16 June 2017.
2. Shatha Al kubragyi, Patrick C. K. Luk, J. Economou, Mohammed. K. Al-Saadi, “D-STATCOM Based on Energy Storage for Fault Ride through in Distribution Grids,” In Proceedings of the Conference of Cranfield Science for a Circular Economy. How to tackle the Water, Energy, Food nexus, Bedford, UK, 16 June 2017.
3. Shatha Al kubragyi, Patrick C. K. Luk, J. Economou “ Sugeno - PI Fuzzy Controller for Battery Bidirectional Charging in the Electric Vehicle to Support Voltage Stability in V2G Distribution Grids ” 7th International

Conference on Power Electronics Systems and Applications - Smart Mobility, Power Transfer & Security (PESA), Hong Kong, China, 12-14 December 2017.

4. Mohammed. K. Al-Saadi, Patrick C. K. Luk, J. Economou, Shatha Al kubragyi, Hayder A. Abdulrahem, “Impacts of Storage Battery on the Economic Operation of the Microgrids with Considering the Battery Degradation Cost,” In Proceedings of the Conference of Cranfield Science for a Circular Economy. How to tackle the Water, Energy, Food nexus, Bedford, UK, 16 June 2017.

5. Mohammed. K. Al-Saadi, Patrick C. K. Luk, J. Economou, Shatha Al kubragyi, “Multi-Period Scenario-Based Stochastic Combined Dynamic Economic Emission Dispatch of the Microgrids”, In Proceedings of the Conference of Cranfield Science for a Circular Economy. How to tackle the Water, Energy, Food nexus, Bedford, UK, 16 June 2017.
6. Shatha Al kubragyi, Patrick C. K. Luk, J. Economou, “Supervisory Controller for D-STATCOM based Battery Energy Storage to Improve Power Quality in Distribution Grids”, Journal IET Renewable Power Generation .
7. Shatha Al kubragyi, Patrick C. K. Luk, J. Economou, “A new Supervisory Energy Management Control Strategy of a modified D-STATCOM Configuration with Dual DC Source in smart distribution grids”, Journal IET Renewable Power Generation .

2 Chapter Two: Literature Review

2.1 Introduction

An effective voltage control scheme for advanced power distribution grids is the main issue faced in this study. Conventional power grid structures have centralised electrical power generation using large power stations, delivering the electricity produced into a transmission and distribution network to deliver electrical power to the customer. In this context, to be realised, new and effective grid structures intended to increase the consumption of electrical energy must show some significant improvement, for example, a low carbon footprint. This chapter starts with a description of emerging grid structures including smart grids and microgrids. However, there are a number of important issues related to the use of smart grids and microgrids, in particular voltage stability. This chapter summarizes energy storage technology and the role of power electronics in the operation of emerging power systems including their role in attaining voltage stability.

As a representation of the electronic power controller, D-STATCOM is a promising device for voltage control. The basic configuration and principle operation of the D-STATCOM are explained in this chapter. The core of the D-STATCOM device is the control system, which will be different for different applications. The improvements made to the control algorithms and applications of D-STATCOM, and its useful application in power distribution, are reviewed in this chapter.

2.2 Smart grid and microgrid concept

Recently, there have been renewed interests in distributed generation (DG) due to incentivised commitments as well as regulatory requirements of renewable portfolio standards by electricity generation operators worldwide. In countries such as Germany and Denmark, there has been a particularly high rate of DG penetrations to support wind and solar energy generation as a result of their respective national policies [44]. In addition to supporting the integration of renewables to the grid, DG is also known to have distinctive advantages such as

reduction of transmission losses and energy security. Indeed, advances in internet and communication technologies (ICT) have enabled the modern power plants to gradually evolve into the ‘smart grid’, capable of highly sophisticated functions including advanced metering, health monitoring, demand side management, big data analytics, and other ancillary services [45]. The emerging grid structures, known as “smart grids” are expected to change conventional existing passive networks to intelligent operation with bidirectional power flow using distributed generators, including power electronic and energy storage units [18] [41] .

Different descriptions of the smart grid have been provided across the world and no single global united definition has yet been agreed. Generally, future electrical power grids will require the up-dating and up-grading of existing networks to meet the challenges of changes in patterns of behaviour of energy customers, of providing new services, while transitioning to a maintainable low carbon economy [46].

A general model has already been provided for the smart grid, describing the use of a set of technologies, topologies and approaches that will change the hierarchical structure of conventional power grids, including generation, transmission and distribution, to work smartly with end users in a fully clean environment. The smart grid will operate with bidirectional power flow that will allow automatic management of distributed energy sharing between the myriad of interconnected elements that form the electric power grid [47].

Internationally, the electrical power sector is facing a time of unprecedented advances, driven by the change from centralized conventional transmission and distribution networks into active power supply grids. In turn, this requires replacement of centralized power units based on fossil fuels by distributed generators, especially renewable energy sources (wind, solar, biomass and hydro). In this way, the electrical grid will ensure low emissions of carbon gases and become even more reliable and secure [46] [48]. The conversion of the current power grid structure came about due to aggressive investment in the generation and supply of electrical power by the companies in the electrical power

sector [48] . As a result, a new layer of authorized power generators, such as individual homeowners, have arisen.

DG's with automation, communication and information technology systems that can provide the capability for two-way power and information flows forms a major part in the smart grid paradigm shift, from the conventional centralised fossil based 'passive' network into a modern decentralised renewables-based 'active' network. DG has the possibility of providing cost-effective, and reliable, alternative sources of premium power for homes and businesses. There is as no commonly agreed definition of DG as the term includes many technologies and their applications. It is referred to variously as "embedded generation", "dispersed generation" or "decentralized generation".

The above definition does not specify any criterion or classification of DG based on their capacity. Although, there is no generally accepted rule or standard, there are different definitions are used in different countries and situations. For example, the Department of Energy (DOE) considers distributed power systems to typically range from less than a kilowatt (kW) to tens of megawatts (MW) in size as DG unit. while, In the English and Welsh power markets, a power plant with a capacity less than 100 MW is not centrally dispatched. Therefore, in this market, DG is referred to any generating unit under 100 MW [49].

In general, DG can be defined as a group of power generating units, small in comparison to conventional power units, joined within the main power grid to supply the electrical power at a point near the consumer [50] . DG is used as substitute energy sources to support the distribution grids. As DG uses local generators to provide the power delivered to the consumer, transmission and distribution losses are reduced, as is the cost of the overall power system. Consequently, consumers are provided with efficient energy usage management and the possibility of selecting the most economically viable electrical power provision, through smart grids which improve security and reliability of the overall power supply using automatic control systems. Also, the emerging grid structures are energized by alternative sources more friendly to the environment, including renewable power sources and distributed storage [41] [4]. With distributed

generators (including renewable sources) and other energy storage units now included as key ‘players’ in the next generation of electric grids at the distribution level, there is a fundamental paradigm shift from being passive grid networks to active networks. The microgrid is a key element in the emerging smart grid structure at the low voltage distribution level. It is assumed this new grid paradigm allows a cluster of loads and small sources including DG and distributed energy storages to operate as one controllable system, at a point close at consumer. MGs also offer great possibilities for power distribution control processes [51]. In this way, the power transmission grid stresses will be reduced and system reliability increased as electrical power can be produced close the load [47] [51]. A MG can be worked in either grid-connected or grid-independent (island) modes. The MG is isolated from the main grid at the point of common contact (PCC) as illustrated in Figure 2-1. In the grid-connected mode, the main power grid typically has additional backup power from the MG to meet the load requirements. In the island mode, the balance between the supply and demand requirements are managed by the MG only [52]. This proposed distribution grid is being developed to allow integration of renewable energy sources (with all their limitations - especially the irregular and intermittent production of power, and the present lack of electrical infrastructure at their usual locations), and also to allow for the additional connection of plug-in electric vehicles (PEVs) and plug-in hybrid electric vehicles (PHEVs)[41] . Figure 2-1 shows the general configuration of a MG integrating renewable and other distributed sources.

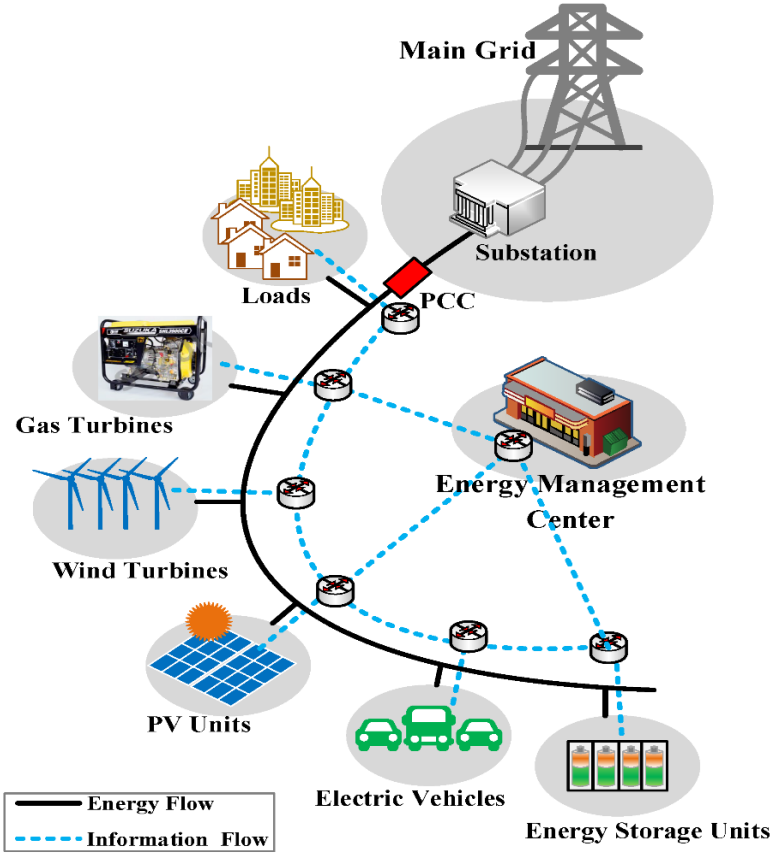

Figure 2-1 General configuration of smart microgrid [52]**.**

Renewable energy such as wind turbines and solar units have attracted great attention in smart distribution grids, as a form a DG which supports grid stability by adding generation capacity. However, the fluctuating nature of these renewable sources leads to power variation that can significantly influence the performance of the power grid. The voltage stability of distribution grids is considerably affected by increasing proliferation of these generators, especially at start-up of the unit and certain operating conditions. For example, some wind turbines depend on induction generators which are not grid supporting because they consume reactive power from the grid at the beginning of their operation [13].

To reduce these challenges, energy storage systems (ESS) based on power-electronic technologies have been suggested which can compensate any mismatch in the power between the sources and the loads in smart grids [41] [53]. A good controller for these advanced ESS, would achieve simultaneous and

instantaneous control of the active and reactive powers between the ESS and the AC power grid. As a result, it would provide the required security level for the power supply. a general overview of the different ESS technologies is explained below.

2.3 Energy storage technology

Nowadays, various kinds of energy storage technologies have been advanced and exploited for power system applications. Energy storage systems, involving either conventional or advanced energy storage devices, have significantly changed the level of ability to meet power system requirements, particularly active power compensation in the smart grids [54].

Energy storage application with AC power systems provides a potential solution to minimizing power demand fluctuation by exchanging electrical energy with the power grid for suitable periods of time. Active power regulation has long been known to be essential in power systems, presently the main challenge to the application of energy storage in power system is to reduce the cost [53].

The exchange process for electrical energy is dependent on the requirements of the AC power grids. At high load demand either the storage unit discharges or, for a period of time, the power supply cannot fully meet the demands of the load. Energy storage technologies can relieve power congestion, provide voltage control and damp oscillations and thus can improve power quality for the end costumer and the generation side. Additionally, from the economic viewpoint, the investment costs of installing reserve generation units could be reduced. Using energy storage with power grids could minimize the overall cost of the generation system as the power rate would be lowered when the peak demand decreased [53].

Energy storage technologies are categorised according to the type of stored energy. For example, mechanical (pumped hydro), thermal (molten salt), electrochemical (supercapacitors), and chemical (hydrogen) [55]. Selected examples of each type of energy storage are presented in Figure 2-2.

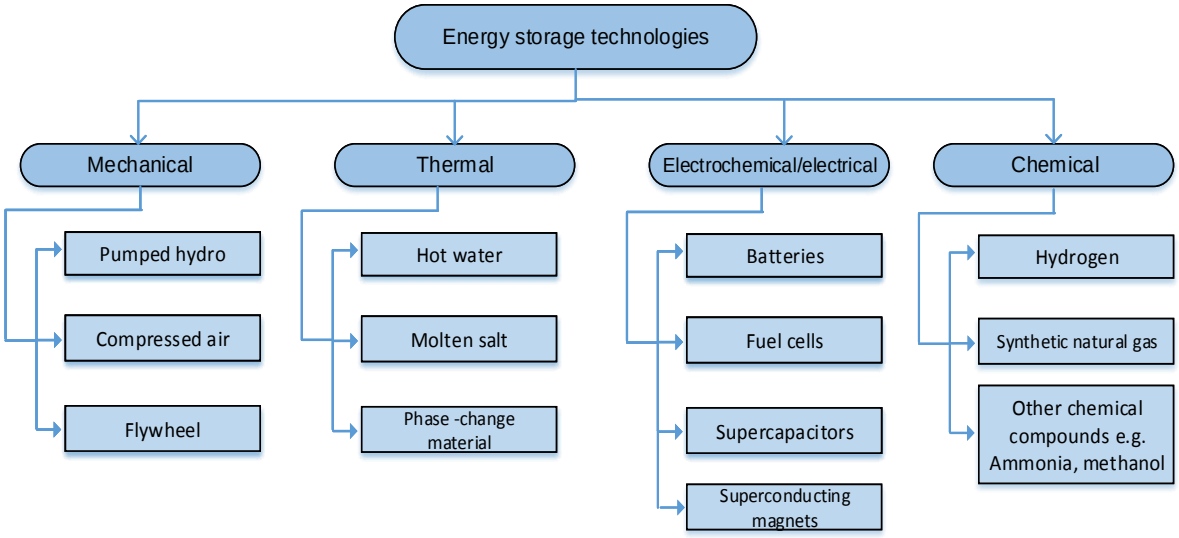

Figure 2-2 Energy Storage Technologies

Energy storage units also can be classified according to the response time, power rating and energy capabilities; i.e., into short-term (several seconds or minutes) and long-term storage (many minutes or hours) as illustrated Figure 2-3. Normally, short-term energy storage units are employed to support power grids during transient conditions, specifically to maintain the voltage and frequency within acceptable limits, such as supercapacitor, flywheel and superconducting magnetic energy storage (SMES). Long-term energy storage units such as battery, fuel cell and pumped hydro have been used to manage grid congestion for a longer times for both steady state and dynamic conditions [56]. Each of the energy storage units depicted in Figure 2-2 is limited in their application due to practical physics based reasons, depending on the advantages and disadvantages of each storage method. For instance, mechanical storage units such as flywheels, compressed air and pumped hydro have low energy capabilities. Furthermore, pumped hydro units operate on the principle of a hydro-electric power plant. Thus, their storage capacity is dependent only on the size of the water reservoir. Also, compressed air energy storage requires a large volume of compressed air to operate for extended periods of time. Therefore, using these storages, for example, there would be difficulties in meeting short storage

demands.

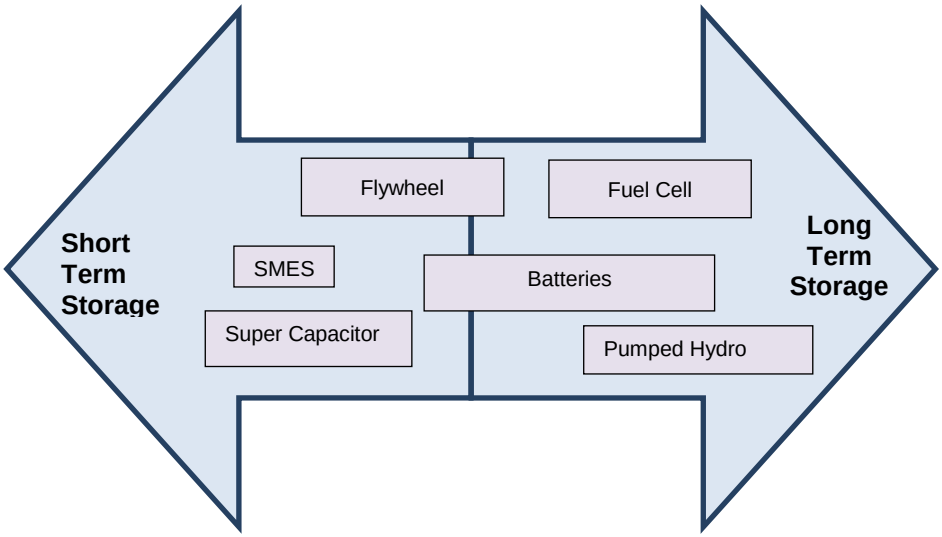

Figure 2-3 Classification of energy storage technologies

"These technologies are also restricted by geological and geographical requirements, high investment costs and long construction times"[55]. Conversely, electrochemical and electrical storage units have a relatively short response time and energy rating and so are likely to be widely deployed in short-term applications. The target application would also affect the choice of storage system. The electrochemical/electrical energy storage technology presents some benefits compared to the other energy storage technologies [9]. Batteries are a generic application of the electrochemical energy storage technology which have the ability to readily convert the stored energy into electrical energy. They can be installed in any place without geographical considerations because they are mobile devices and often quite small. Batteries can be either non-rechargeable (primary) or rechargeable (secondary), only rechargeable batteries are of interest for large-scale energy storage such as Lead acid and Lithium ion batteries [57]. whereas, the electrical energy storage technology included (capacitors and supercapacitors). Usually, capacitors represent within two plates employed to store the energy as an electric charge within an amount of a capacitance. They have the ability of a rapid charge and discharge. These characteristics enable the capacitors to be used for some power quality applications, such as voltage power correction. Nevertheless, they have limited capacity and relatively low energy

density in comparison to the batteries. The recent capacitor technology with double-layer capacitors known as a supercapacitor, included two conductors electrodes [9]. Due to their structures, the energy is stored in the form of static charge on the surfaces between the electrolyte and the two conductor electrodes. The supercapacitors with high-performance are based on nano materials to increase electrode surface area for enhancing the capacitance in comparison to the traditional capacitors [9]. A general comparison between the batteries, supercapacitor and conventional capacitors is given in Table 2-1

Table 2-1 A comparison of battery, ultracapacitor and conventional capacitors performance [57][58]

Available features	Lithium-ion (general)	Supercapacitor	Conventional Capacitor
Charging time	10- 60 minutes	0.3 to 30 second	10^{-3} to 10^{-6} second
Energy (Kw/kg)	120 to 240	1 to 10	<0.1
Cycle life	>10 000	>500 000	>500 000
Specific power w/kg	1000 to 3000	Up to 10 000	<100 000
Charge/Discharge efficiency	0.6 to 0.8	0.85 to 0.98	>0.95

2.4 The role of the power electronics in power systems operation

Recently, power electronics is widely known as the enabling technology that forms the key part of the solutions in connecting a greater range of renewable sources to conventional power grids which is necessary to transform the power grids to low-carbon emission grids [59] [60]. In general, the function of power electronics is to control electrical power flow and process the power from one form to another (AC to DC, DC to AC, AC to AC and DC to DC) to meet load demands. A general scheme for a power electronic circuit in a power system is given in Figure 2-4. The main part, that does the power converting is known as a “converter”. Also, the power conversion system (PCS), will include certain

essential components such as the control unit, semiconductor switches, and additional storage (capacitors, transformer and inductors) that process the conversion function [61] [62]. In this way; “Power electronics may be defined as the application of solid-state power semiconductor devices for the control and conversion of electric power [61].

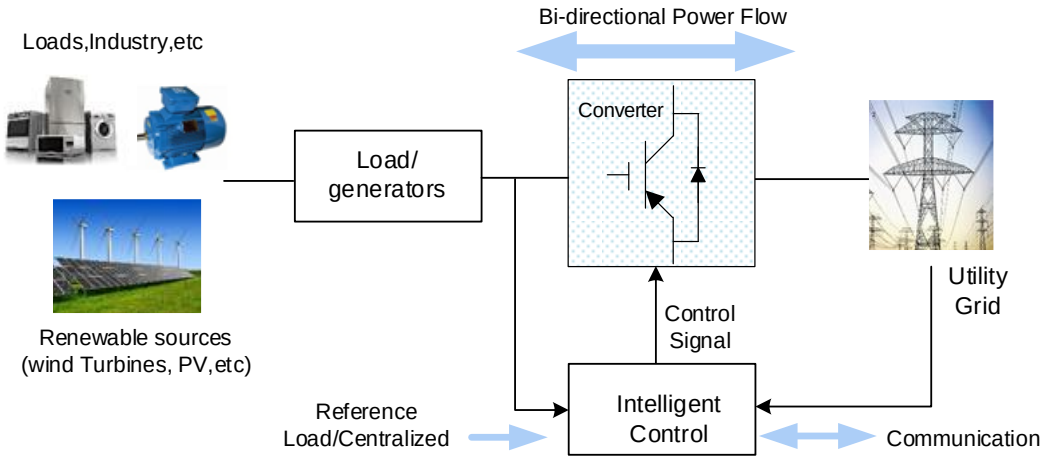

Figure 2-4 Power electronic scheme for electrical power system [59]

Power electronics technology forms a vital part of emerging power systems including renewable sources, and is considered a key element in conversion of power from renewable units such as wind turbines and solar cell panels. It must provide an efficient and extremely reliable performance to be capable of transmitting the power from the renewable units to the utility grid with a fast response, and to support the power system in specific conditions such as "low voltage ride through" with reactive power compensation [59]. The “friendly environment” based energies could be highly controllable using power electronics technology. However, power electronics systems can help meet the demands of the “distribution/ transmission operators" and additional loads of the end users, when controlled by an intelligent strategy. This will be even more true if the required demand profiles are known and advanced intelligent power devices are used.

One of the power electronics applications for power systems is the “Flexible AC Transmission System (FACTS)” devices. The IEEE Working Group has

described FACTS as: "Alternating current transmission systems incorporating power electronic-based and other static controllers to enhance controllability and increase power transfer capability” [63] [64]. In general, the FACTS devices are employed for controlling and regulating the power flow in transmission networks to enhance voltage stability at critical buses [65] [66] [67]. The power electronics based FACTS regulator devices can be classified into two categories: the first one uses the conventional thyristor as a switching device which offers only one option of switch operation. With a thyristor, only the switch ON status underpinned while the switch OFF status is achieved normally when the current through the switch is zero. “Thyristor-controlled series capacitors (TCSC), static VAR compensators (SVC), and the thyristor-controlled phase shifters (TCPS) are examples of the first category” [67].

The second category includes, “insulated gate bipolar transistors (IGBTs), gate turn-off (GTO) thyristor-switches and metal-oxide-semiconductor field effect transistors (MOSFETs) used as switching devices” [67]. The second category includes commercial products: "unified power flow controller (UPFC), static synchronous compensator (STATCOM), static synchronous series compensator (SSSC) and the interline power flow controller (IPFC)" [66] [67].

Recently, several of the FACTS devices have been considered for controlling the distribution voltage level [68]. The distributed SVC (D-SVC) and distributed STATCOM (D-STATCOM) are the most important of the shunt connected devices for controlling the distribution network. These are connected directly to low voltage distribution grids without any ancillary components. However, these devices are still being studied, and the trend for new designs is to use these devices in distribution systems to improve the quality of the voltage. This is because, in addition to their other advantaged, their cost has fallen due to the decreasing cost of power semiconductor switches [69]. The implementation of the SVC in a distribution grid is explained in [70]. The SVC is a FACTS device and typically consists of a capacitor element with a thyristor switch, or an inductor element with a thyristor switch, or a combination of both, as illustrated in Figure 2-5. In this context, manipulation of the three elements (inductor, capacitor and

switch), enables production of diversified types of SVC [71] [72]. Generally, the main function of the SVC is to compensate the reactive power and provide voltage control. In [70], the authors concluded that voltage control was obtained more quickly in comparison to the conventional device, an "on load tap changer (OLTC)" transformer.

The design of the D-SVC to regulate voltage fluctuations caused by renewable generation sources on distribution grids is presented in [73]. The use of the D-SVC to regulate the voltage variations was modelled in different ways. The authors confirmed the justification for using the FACTS devices in distribution grids, particularly the D-SVC [70]. In [74], the SVC was discussed in a detail and considered for reactive power compensation and voltage control in an electrical distribution network connected to non-linear loads. The authors explained specific design rules for the use of SVCs with non-linear loads. In addition, the paper described features of SVC and included typical SVC performance.

The above studies showed that the SVC can be used as an effective reactive power compensator for controlling voltage at distribution voltage level. However, as the thyristors are employed as switching devices in the SVC, there are some non-negligible drawbacks, mainly the injection of current harmonics which would likely require additional filtering devices [24], Also these switches, provide only one degree of freedom. It should be noted that resonance phenomena may be produced.

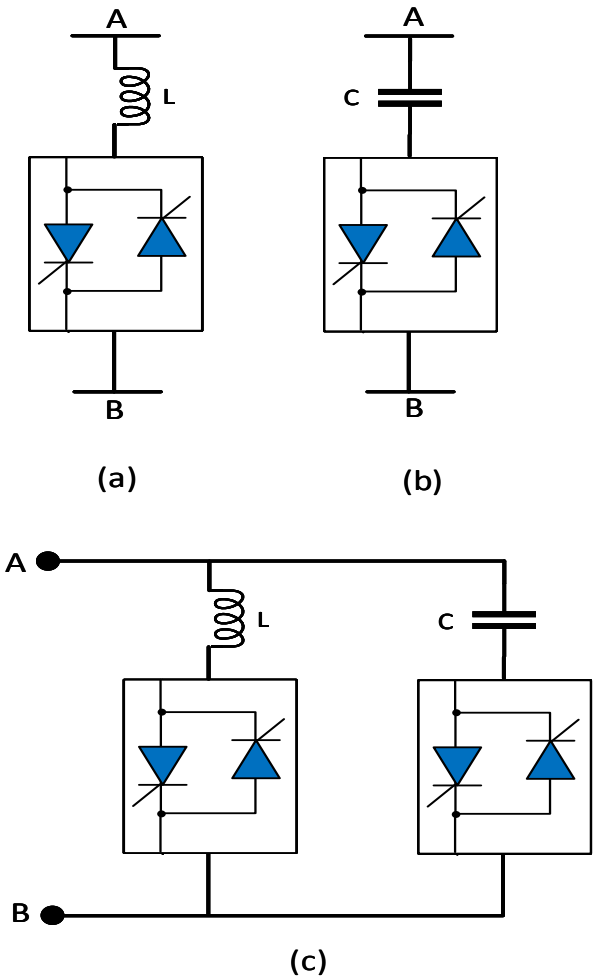

Figure 2-5 three kinds of the SVC, (a) Thyristor Switched Capacitor (TSC), (b) Thyristor Controlled Reactor (TCR), (c) TSC-TCR (figure is adapted based on [72]**)**

The STATCOM is a shunt connected static compensator which presents a number of solutions to the shortcomings of the SVC. STATCOM is a reactive power compensator based on a voltage source converter (VSC). Unlike the SVC which is based on thyristor switches, the VSC is basically constructed from semiconductor switching devices such as GTO, IGBT and MOSFET (with higher costs). However, the STATCOM has several technical advantages over a SVC [24] [75]:

- It has a faster response than other FACTS devices because it uses semiconductor devices as switching gates and lacks any rotating mass.
- Passive elements such as the reactor have been removed.

- It is compact, modular and relocatable.
- Active power control can be achieved in addition to reactive power control by adding a power storage unit such as a battery, fuel cell or supercapacitor to the STATCOM.

2.5 Distributed static synchronous compensators (D-STATCOM)

The Distributed STATCOM is a Fact-based device connected in parallel with AC distribution power grids. A functional representation of the D-STATCOM describing its main parts is given in Figure 2-6. It includes a VSC connected to the AC distribution bus through a coupling transformer and an energy storage unit such as a capacitor, on the DC side of the converter[76], [39], [23]. The firing pulses to the switches gates of the VSC are provided by using pulse width modulation (PWM) to obtain the active and reactive power from the D-STATCOM.

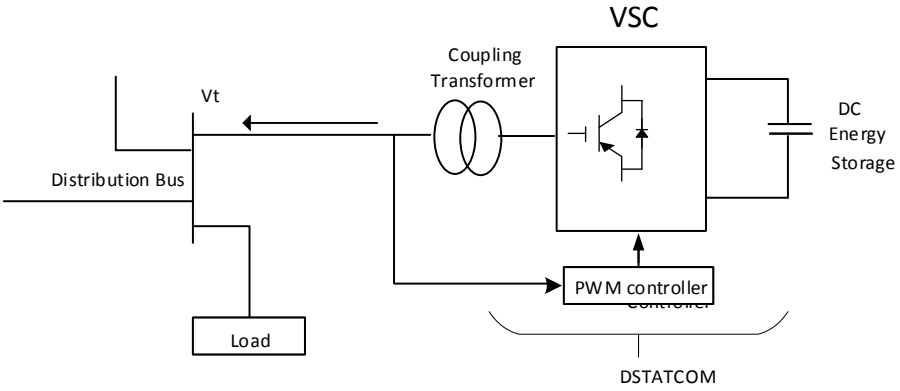

Figure 2-6 D-STATCOM connected to the AC distribution grid

The main function of the VSC is to generate a controllable three-phase sinusoidal voltage at the PCC from the DC storage device. These voltages are in phase and coupled with the AC system through the reactance of the coupling transformer [77]. Thus, the D-STATCOM can be represented as a reactive power source to control the buses' voltage and to improve the stability in the power distribution networks by providing /absorbing reactive power with a fast switching time.

The V-I operating features of a D-STATCOM are shown in Figure 2-7 along with the V-I operating characteristics of a SVC. It can be seen that the D-STATCOM

output current to provide or absorb power does not depend on the grid voltage[35]. Thus, even when the bus voltage is very low, the STATCOM will work at full capacity. This is quite different from the SVC, the performance of which declines the lower the bus voltage. Thus, the use of STATCOM is to be preferred to the SVC where the voltage is expected to drop to a low value or drops very fast and a fast response is required.

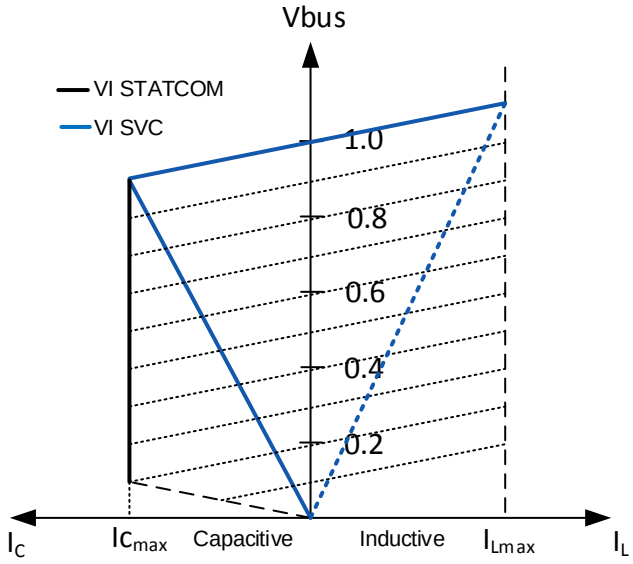

Figure 2-7 V-I operating characteristics of SVC and D-STATCOM [figure is adapted based on 35].

2.6 Principle of D-STATCOM operation

A typical representation of a simple, single line diagram of the D-STATCOM connected to the grid is shown in Figure 2-8. Generally, a DC capacitor acting as a DC voltage source is placed on the input side of the VSC which normally generates a balanced three-phase voltage, almost in a sinusoidal waveform [35][78]. The active and reactive power control between the D-STATCOM and AC power point can be achieved by suitable tuning of the phase and magnitude of D-STATCOM output voltage [79]. The active and reactive powers are given by.

$$\mathrm{P} = \frac{V_G . V_{STAT}}{X_L} . \sin(\delta) \quad \textbf{(2-1)}$$

$$\mathrm{Q} = \frac{V_{STAT}^2 - V_G . V_{STAT} . \cos(\delta)}{X_L} \quad \textbf{(2-2)}$$

Where P is the active power, Q is the reactive power, V_G is the rms voltage of the main grid, V_{STAT} is the output AC voltage of the D-STATCOM, X_L is the leakage reactance =$2\pi fL$, L is the leakage inductance, f is the frequency of the system and δ the power angle between V_G and V_{STAT}.

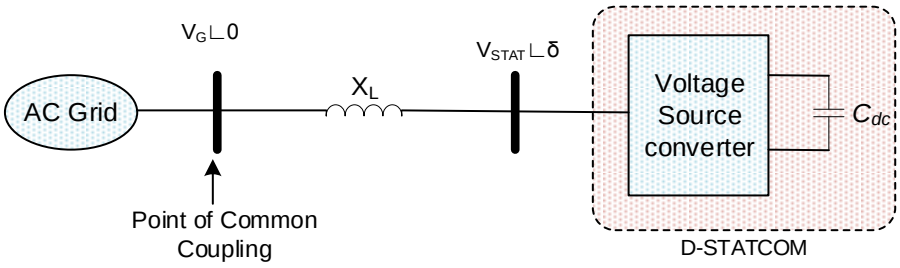

Figure 2-8 Single line diagram of D-STATCOM connected to the AC grid

It is clear from Equation (2-1) that the active power exchange is a function of the phase angle δ between the D-STATCOM terminal voltage and grid terminal voltage for nominal values of voltage magnitudes. Likewise, it is noted from Equation (2-2) that the reactive power is computed according to the difference between the voltage magnitude of the D-STATCOM AC terminal side and AC grid side. As the D-STATCOM has the possibility for active power exchange, by adding an energy storage device, such as supercapacitor or battery, to the DC side [80], [81].

The basic function of the D-STATCOM in providing reactive power depends on the reactive power exchange between the AC grid and the D-STATCOM. Typically, when the D-STATCOM voltage amplitude (V_{STAT}) is more than grid voltage (V_G), reactive power is injected into grid (the D-STATCOM operates in a capacitive mode). In contrast, if V_{STAT} is less than V_G, the D-STATCOM operates in an inductive mode by absorbing reactive power from the grid. Finally, if the D-

STATCOM voltage (V_{STAT}) is equal to the voltage grid (V_G) there is no reactive power exchanged [82],[79]. In the same way, when the power angle is positive, the real active power flows from D-STATCOM to the grid side, When the power angle is negative the D-STATCOM absorbs active power from the grid.

2.7 Control Algorithms and approaches of D-STATCOM

The D-STATCOM device consists of a VSC connected to the AC distribution bus through a coupling transformer and an energy storage unit such as a capacitor with appropriate measurements and a suitable controller. The functionality of the D-STATCOM compensator is determined by the implemented control algorithm. The control algorithm for any system should be flexible, simple and robust as well as optimizing multi-functions. Here, the desired control performance is obtained by tuning the control parameters according to the system configuration and application requirements. Normally, the control strategies of the D-STATCOM control circuit are determined according to several main steps.

Firstly, the measurement of voltage and current from source and load points to provide information concerning the dynamic condition of both the system and the load. Secondly, techniques such as “synchronous rotating reference frame (d-q)” [83] and “stationary reference frame transformations” [84] are used to synthesize the information measurements. Thirdly, a reference signal for the voltage and current is computed. After which, the D-STATCOM's compensating current is determined and the AC output voltage of the D-STATCOM is coordinated with the AC grid voltage. Finally, the load current is compared with the compensating current from the D-STATCOM to generate triggering pulses to the converter’s IGBT switches to determine the required compensating current.

Using the proper technique to generate the pulse signals for the IGBTs gates is very important to obtain optimal implementation of the control process. For this purpose, different modulation schemes have been introduced and reported in the literature. These include “sinusoidal pulse width modulation (PWM), space vector modulation (SVM) and selected harmonic elimination (SHE)” which are commonly used with high powers [85], [24], [86]. In fact, PWM is a common technique used to produce a series of high frequency gating pulses with different

width by comparing the sinusoidal waveform control signals which are 120° out of phase (known modulation signal) with triangular higher frequency signal (carrier signal) [86] as presented in the Figure 2-9. Vao, Vbo and Vco represent the phase voltage. The difference in the width of the pulses represents the magnitude of the voltage that is related to the sinusoidal modulation signal. The output current signal of the D-STATCOM is controlled using different control algorithms as have been proposed in the literature. The most common methods used are: the phase shift control, the instantaneous (p-q) theory (the Instantaneous reactive power theory) and synchronous rotating frame method (SRF).

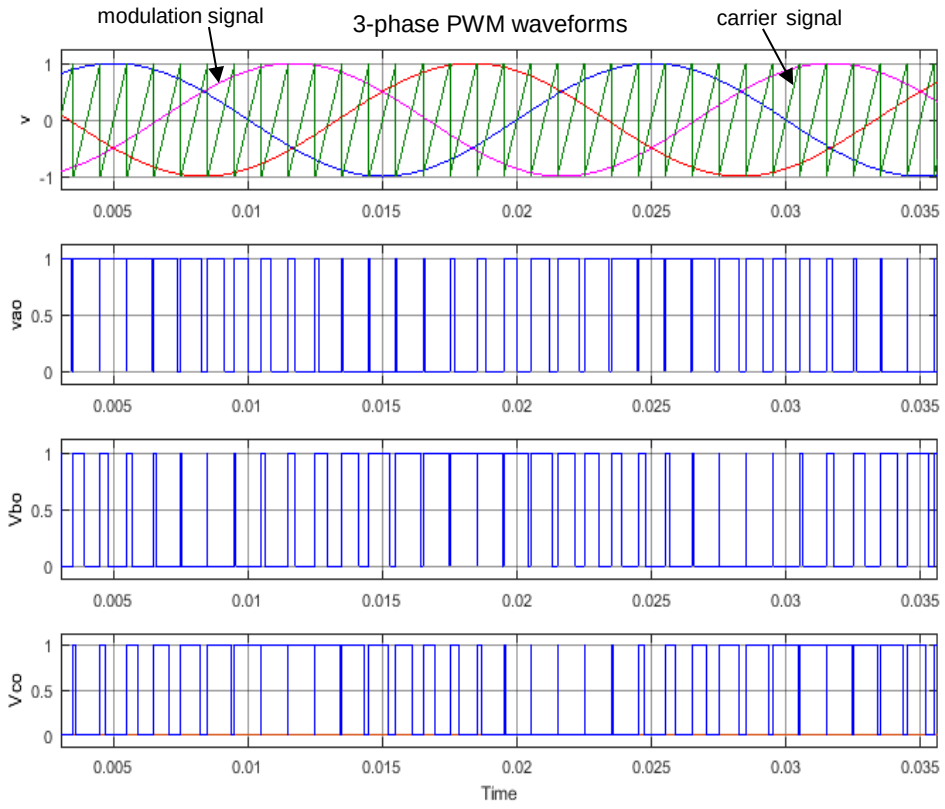

Figure 2-9 PWM switching technique

2.7.1 Phase shift control.

The main part of this control method is based on a simple PI controller as indicated in Figure 2-10. The compensation objective of the control is to regulate the PCC voltage at the required value. The error signal is produced by comparing

the measured voltage value (rms) of the PCC with a PCC reference voltage. The error is input to the PI control which produces the required phase shift between the VSC output and PCC voltage. The pulsing signals for the IGBT's switches of the VSC are based on a sinusoidal PWM technique. In this control, an independent DC source is used to keep the DC voltage terminal at a certain voltage. Although the control scheme is simple to implement, robust, and does not require any reactive current measurements, it has some negative aspects. It is a linear method, it does not solve the problem of undesired harmonics with non-linear loads, and it only partially supports the reactive power requirements [87], [88], [89].

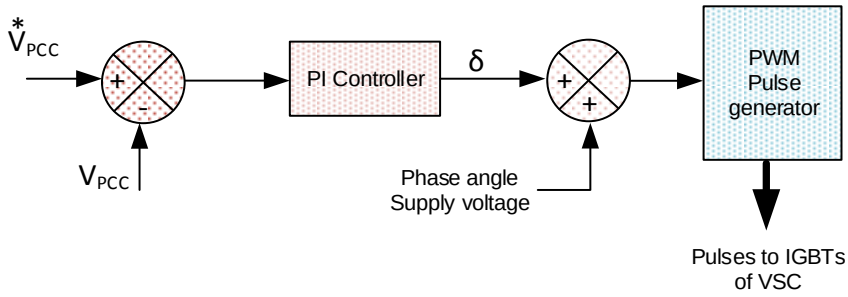

Figure 2-10 Phase shift Controller [87]

2.7.2 Instantaneous (p-q) Theory.

The instantaneous (p-q) control theory depends on the "Instantaneous reactive power (IRP) theory for a balanced three phase, three wire system with no zero-sequence active power component" [24]. This was first suggested by Akagi [86]. It uses the Clark transformation to convert the instantaneous measured value of the three-phase load current (i_{La}, i_{Lb}, i_{Lc}) and grid voltage (v_a, v_b, v_c) to the ($\alpha - \beta$) stationary frame without the zero sequence components as follows:

$$\begin{bmatrix} i_\alpha \\ i_\beta \end{bmatrix} = \sqrt{\frac{2}{3}} \begin{bmatrix} 1 & -1/2 & -1/2 \\ 0 & \sqrt{3}/2 & -\sqrt{3}/2 \end{bmatrix} \begin{bmatrix} i_{La} \\ i_{Lb} \\ i_{Lc} \end{bmatrix} \quad \textbf{(2-3)}$$

$$\begin{bmatrix} v_\alpha \\ v_\beta \end{bmatrix} = \sqrt{\frac{2}{3}} \begin{bmatrix} 1 & -1/2 & -1/2 \\ 0 & \sqrt{3}/2 & -\sqrt{3}/2 \end{bmatrix} \begin{bmatrix} v_a \\ v_b \\ v_c \end{bmatrix} \quad \textbf{(2-4)}$$

Then the instantaneous active and reactive power is calculated as[90] :

$$\begin{bmatrix} p \\ q \end{bmatrix} = \begin{bmatrix} v_\alpha & v_\beta \\ -v_\beta & v_\alpha \end{bmatrix} \begin{bmatrix} i_\alpha \\ i_\beta \end{bmatrix} \quad \textbf{(2-5)}$$

Each power (p and q) in the above formula has a DC (average) and an AC (oscillatory) component as:

$$p = \bar{p} + \tilde{p} \quad \textbf{(2-6)}$$

$$q = \bar{q} + \tilde{q} \quad \textbf{(2-7)}$$

The reactive power and oscillatory component of the active power are used as a reference value for reactive and harmonic compensation. So, only the DC part of the active power is transmitted by the source. Therefore, the $\alpha - \beta$ reference source current components are computed as:

$$\begin{bmatrix} i^*_{s\alpha} \\ i^*_{s\beta} \end{bmatrix} = \frac{1}{v_\alpha^2 + v_\beta^2} \begin{bmatrix} v_\alpha & -v_\beta \\ v_\beta & v_\alpha \end{bmatrix} \begin{bmatrix} p \\ 0 \end{bmatrix} \quad \textbf{(2-8)}$$

The inverse Clark transformation can be used to obtain a-b-c reference current component as:

$$\begin{bmatrix} i^*_{sa} \\ i^*_{sb} \\ i^*_{sc} \end{bmatrix} = \sqrt{\frac{2}{3}} \begin{bmatrix} 1/\sqrt{2} & 1 & 0 \\ 1/\sqrt{2} & -1/2 & \sqrt{3}/2 \\ 1/\sqrt{2} & -1/2 & -\sqrt{3}/2 \end{bmatrix} \begin{bmatrix} i^*_0 \\ i^*_{s\alpha} \\ i^*_{s\beta} \end{bmatrix} \quad \textbf{(2-9)}$$

where i^*_0 is the zero sequence component, which is zero in three-phase three-wire system [91].

This method is considered relatively not difficult to implement and gives an acceptable performance of load balancing. However, the disadvantages of this approach are that it is difficult to implement in a three phase four wire system and does not provide fully satisfactory power factor correction. Nor can it be applied to a single–phase grid because, it is naturally suited to sinusoidal three-

phase balanced networks with cancellation of zero sequence power[24], [76], [91] ,[92], [93], [94]. Figure 2-11 shows the basic block diagram of the p-q control theory.

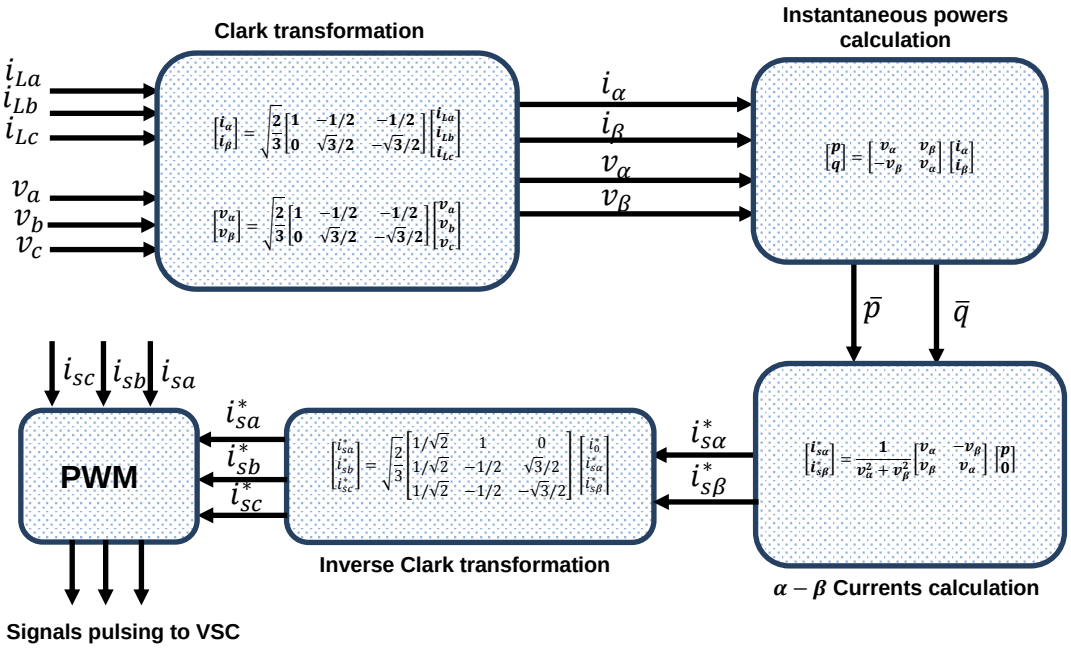

Figure 2-11 Block diagram of the controller using p-q theory (figure is adapted based on [91] **,**[92]**)**

2.7.3 Synchronous rotating frame method.

The synchronous rotating frame (SRF) theory relies on the transformation of the three-phase load currents to the d-q rotating coordinates by using Park's transformation. Firstly, i_{La}, i_{Lb}, i_{Lc} values are transformed to the α-β frame according to Equation (2-3) .Then the α-β axes are converted to a rotating frame by a vector rotation module to rotate with angle θ to track the d-q rotor axis. The SRF method is usually based on the phase locked loop (PLL) to obtain unit vector ($\cos\theta \ \ \sin\theta$) from the PCC voltage v_a, v_b, v_csignals, the basic block diagram of the PLL is shown in Figure 2-12. Thus, the currents rotate orthogonally and are defined as:

$$\begin{bmatrix} i_d \\ i_q \end{bmatrix} = \begin{bmatrix} \cos\theta & \sin\theta \\ -\sin\theta & \cos\theta \end{bmatrix} \begin{bmatrix} i_\alpha \\ i_\beta \end{bmatrix} \quad \textbf{(2-10)}$$

Here i_d and i_q are passed through low pass filters (LPF) to obtain the DC component i_{d_dc} and i_{q_dc}. The DC current components are transformed to α-β coordinates by a reverse Park transformation and then are transformed to a-b-c coordinates by Clark's transformation according to Equation (2-9).

$$\begin{bmatrix} i_{\alpha dc} \\ i_{\beta dc} \end{bmatrix} = \begin{bmatrix} \cos\theta & -\sin\theta \\ \sin\theta & \cos\theta \end{bmatrix} \begin{bmatrix} i_{d_dc} \\ i_{q_dc} \end{bmatrix} \quad \textbf{(2-11)}$$

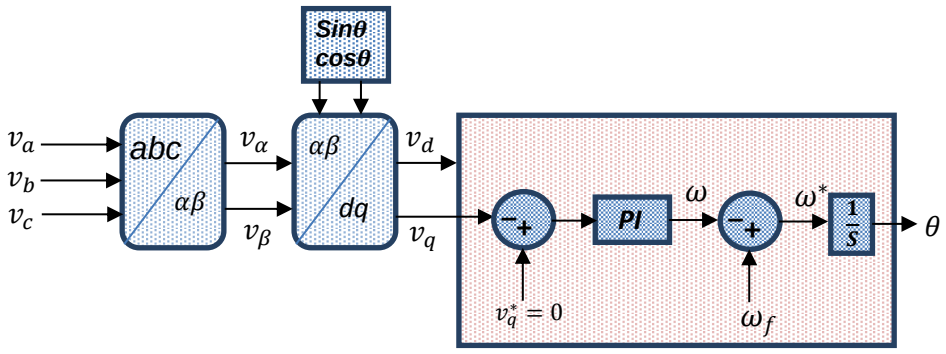

Figure 2-12 Basic block diagram of PLL [95]

Figure 2-13 illustrates the block diagram of a control scheme using SRF theory. In this method, the rotating orthogonal d-q representation of the three phase balance vector will be constant with time. The transformation angle is a function of time and is responsive to distortion and unbalanced source voltage. Thus, this control method gives a satisfactory and uncomplex performance, controlling the active and reactive power by dealing with i_d and i_q components. This is in addition to harmonic mitigation for linear and unbalanced non-linear loads [87], [91],[93], [94].

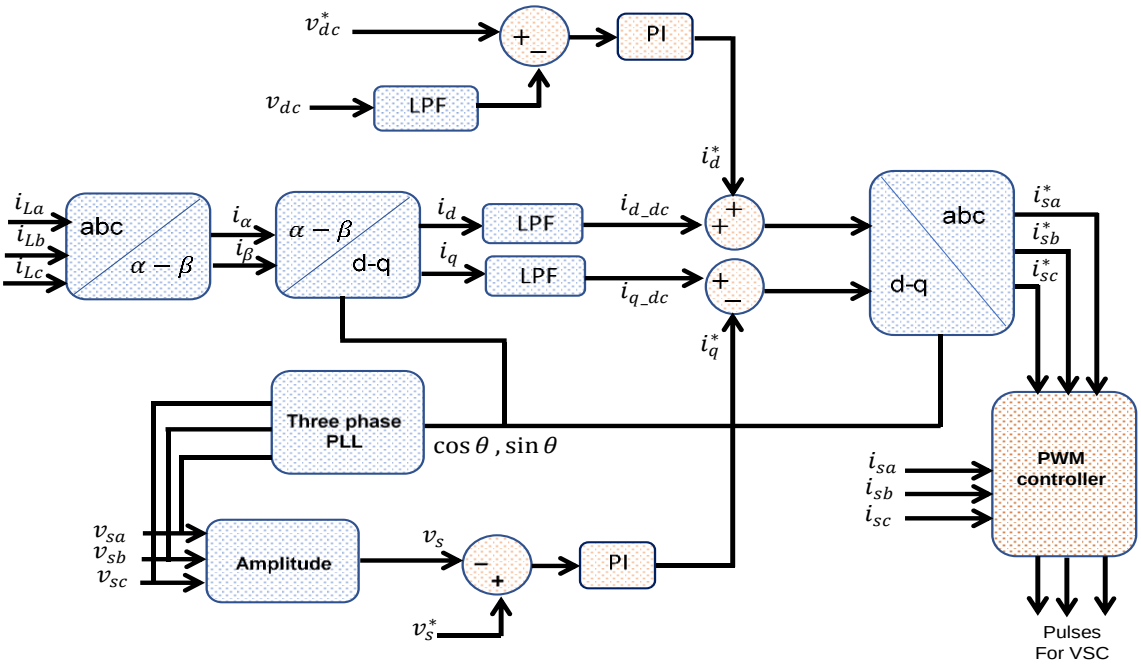

Figure 2-13 Block diagram of the controller using SRF [76]

2.7.4 Nonlinear controllers.

Proportional Integral (PI), and Proportional Integral Derivative(PID) controllers are conventionally used in D-STATCOM controllers. However, “The conventional controller has a limited application in some cases because of its non-adaptive parameters and linearity” [96]. To improve the operational performance of STATCOMs in different systems and for a range of conditions, new algorithms and non-linear control strategies have also been proposed. In these controllers, the desired switching signals can be generated directly to control the converter of the D-STATCOM. Controllers based on non-linear approaches can provide a fast control response [97]. Artificial Neural Network (ANN) controllers [98], fuzzy controllers [99], [100] and hysteresis controllers [87], [101] are examples of non-linear types. Generally, there are difficulties in the practical operation of these controllers.

The hysteresis technique is suitable for multi-functions such as harmonic suppression, load balancing, and voltage regulation as well as power factor improvement. The fast switching of this controller is produced by measuring the difference between the continuously measured STATCOM current and reference sinusoidal signals. The error signals are compared with “a fixed width hysteresis

band". The hysteresis controller is uncomplicated, robust and a commonly used closed loop scheme. However, it has some negative aspects, such as irregular switching frequency which leads to switching losses[101].

To overcome this limitation some researchers [102] have proposed a modified band hysteresis controller, adjusting the hysteresis band with the DC side voltage to obtain a constant modulation frequency. Unfortunately, such a proposal means the hysteresis scheme loses its simplicity.

Recently intelligent optimization techniques have found a way of improving the controller to obtain a fast and satisfactory response. An ANN has been applied, and in [103], [98] an ANN controller was designed and used instead of the PI controller to generate suitable switching patterns of the D-STATCOM inverter. The DC side voltage continued to be regulated by the traditional PI controller. The parameters of the PI controller in the D-STATCOM were modified using an ANN algorithm in [104]. but many examples of the latest evolutionary optimization algorithms such as the genetic algorithm (GA) and particle swarm optimization (PSO) are now readily available in the literature [105], [106], [107] & [108] to use and obtain optimal parameters for PI and PID controllers. In [109] a PID controller was combined with a fuzzy controller to improve inverter operation. Moon in [110] implemented predictive current control based on a space vector pulse-width modulation (SVPWM) approach to the D-STATCOM, to regulate reactive power transfer. This control is a non-linear type that gives better results with low switching losses. However, to generate the firing pulses it requires an external modulator and that means increasing the complexity of the control hardware. Non-linear controllers have been used but have the undesirable requirement of needing a fast pulsing rate to obtain a satisfactory control response. Recently, non-linear controllers have been implemented in real systems due to the rapid development of digital control devices such as "micro controllers (MC), digital signal processors (DSP), and field programmable gate arrays (FPGAs)" [111].

DSPs are used to implement discrete-time control schemes based on D-STATCOM [112], [113]. In [114] a closed loop hysteresis controller was implemented in prototype hardware based FPGA for reactive power

improvement.In addition to the implementation of digital non-linear controllers, the linear controller can be employed in digital devices. For example, PI controllers based on a rotating frame (d-q transformation) [115], [116].

2.8 D-STATCOM application

D-STATCOM technology has been employed for multi-dimensional implementations at the distribution grids to control grid parameters under steady state and abnormal conditions. Applications of D-STATCOM in distribution grids to improve power quality are reported in many references. Many reports have described various controller schemes using a D-STATCOM device, according on the power system factor to be controlled:

2.8.1 Application of D-STATCOM for load compensation

Referring to load compensation, it includes “harmonics reduction, power factor correction, reactive power compensation and load balancing”. The likely major applications of D-STATCOM will include load compensation, specifically reactive power compensation to improve voltage stability [40], [82]. In [117], [118] and [119] the researchers discussed the effect of using a D-STATCOM device to improve the buses voltage for a distribution network that integrated distributed wind turbines in order to enhance the voltage stability of the system. The authors in [13] investigated the size and location of the D-STATCOM using static and dynamic voltage analysis of distribution generation under different load models. A sensitivity index was used to identify weak buses in the system in order to determine the best location of the D-STATCOM and the shunt capacitor bank. These studies analysed the dynamic characteristics of distribution networks for various load configurations which impacted on the transient voltage recovery phenomenon. In [120] the aim was to identify the location and size of the D-STATCOM and DGs by using a heuristic algorithm to improve voltage buses and minimize losses in the radial distribution system.

In [87], [91], [93] a D-STATCOM was proposed for load compensation that included a reactive power requirement and unbalance mitigation under different loads. Different control algorithms were proposed to evaluate the operation of the

D-STATCOM. These algorithms were synchronous frame theory, instantaneous reactive power theory and a daline theory. In addition to these algorithm other approaches with the same goal are phase shift control, described in [89] and hysteresis control in [101], [121]. In [102] a modified band hysteresis controller was suggested. In [122], [123] a cascaded multilevel converter based D-STATCOM was described to manage the reactive power and reduce the harmonics drawn by non-linear loads. The D-STATCOM with SVPWM scheme controller was implemented in instantaneous p-q reactive theory reference. Another “closed-loop SVPWM technique” for the D-STATCOM controller was introduced in [124] to mitigate the harmonics generated in a MG. The D-STATCOM is a promising device that has been used not only for reactive power compensation and harmonic elimination but as a solution of other power quality problems such as power factor correction, as in [125] [126]. In [113] a DSP controller was used to eliminate the harmonics present in the load current. In [114] [115] [116] DSP and FPGA digital hardware provided a platform base for a D-STATCOM controller for reactive power improvement.

2.8.2 Application of D-STATCOM for dynamic and transient stability

Amongst the various FACTS devices, the D-STATCOM has attracted great attention as a means for improving system stability. The application of the D-STATCOM to a distributed system connecting wind generated power sources had the capability of improving the transient stability margins, and so increasing the system stability. The system was tested under symmetrical faults and different wind rates [127], [128]& [129]. However, the dynamic analyses of the wind turbines were not considered in these works. As in [130] the D-STATCOM operation was assessed under asymmetrical faults (line–ground fault) and load disturbance. A relative reduction for swell/sag problems in the phase voltages was indicated in the results. However, the voltage was still indicated as swell more than sag. The d-q-0 rotating transformation based PWM switching technique was implemented as a control algorithm with unmodified controller parameters for the different cases. In [131] a pole placement controller was

successfully used instead of PI controller for the D-STATCOM to mitigate the unbalanced faults effects.

However, the D-STATCOM has limited ability to mitigate voltage fluctuations caused by active power disturbances. By integrating energy storage into the DC link of a D-STATCOM, controllable active power from the storage device can be extracted to provide enhanced voltage compensating capability. Various kinds of energy storage technologies have been advanced and are being exploited for power system purposes. Energy storage, involving conventional and advanced energy storage systems have significantly changed the level of ability to meet power system requirements for active power, particularly in electrical microgrids [132] [133]. Therefore, in order to improve the D-STATCOM performance, the DC bus of the D-STATCOM can be integrated with different types of advanced energy storage, such as supercapacitor, flywheel storage and battery energy, as proposed by [134] [135] . A D-STATCOM coupled with a supercapacitor storage device has been proposed in many references [136],[137],[138],[139],[140],[141]. The power controls for a smart distribution system with supercapacitor was discussed under symmetrical and asymmetrical faults by [134]. The active and reactive power controls of smart distribution systems were discussed under symmetrical and asymmetrical faults in [142]. A supercapacitor storage unit has a high power density that enables it to deliver or store high power levels over short time periods. However, it has low capabilities of energy storage.

Recently, a battery energy storage system (BESS) has been adopted for use in power system applications to improve power quality problems in distribution power grids due to its high energy density compared to other storage types [132] [143], [133] [144]. A study presented in [145] and [146] included wind turbine operation in an isolated microgrid system with D-STATCOM based BESS. The D-STATCOM was operated as a voltage regulator at the PCC when the wind generation was fluctuating. The D-STATCOM absorbed the additional power generated from the wind turbine and providing voltage support. The simulation results demonstrated how using such a D-STACOM with energy storage makes it possible to control the power production of a renewable generation unit. In [147]

a D-STATCOM based BESS was tested under different conditions to enhance the dynamic stability of linear and non-linear loads.

In [81] and [148] the voltage and transient stability of a grid integrating STATCOM with battery storage was studied. D-STATCOM based BESS performances give better results than the traditional D-STATCOM. The main advantage of BESS is its high energy density but at the same time it has low dynamic response characteristic.

The ability of the D-STATCOM based BESS in providing a given amount of active power seems to be a distinctive advantage in improving voltage stability in steady state and transient conditions of the power grid. Remarkably, there appears no comprehensive study in using intelligent control in exploiting the potentials of the D-STATCOM with battery storage. To improve performance further, a fuzzy logic control (FLC) as a versatile tool has been employed in the controllers with complex structure grids. Several studies have been presented under the name of fuzzy-PI control in smart power systems. A new fuzzy logic controller (FLC) has been applied to the conventional D-STATCOM to meet load demand during the peak period [149]. Further research work on using fuzzy logic controllers in the conventional D-STATCOM to improve the damping of a power system has been reported in [150] [151]. To date, there have been limited studies in the area of intelligent control and analysis of the D-STATCOM based BESS and, in particular, in exploiting the reactive and active power of the D-STATCOM, as additional resources to support the grid's voltage stability.

The combination of supercapacitor and battery storages has been investigated to improve power quality of distribution networks [152]. Research on the D-STATCOM based using a hybrid energy storage system (HESS) to regulate the fluctuation of the output power of wind turbine units is discussed in [153] . Although energy storage technologies are getting significant interest in the electrical engineering sector, as one of the more promising options that will enable AC power grids to transfer power in a more efficient and flexible way, limited research has been carried out on D-STATCOM based energy technologies in the area of custom FACTS devices.

2.9 Summary

Microgrids, included distributed generators, in general, have had a positive impact on the stability and reliability of distribution grids and are considered as an important new research area in electrical science. Investigation of this new concept has been gaining more attention from scholars and the power communities. However, there are gaps in MG research. The literature survey reveals no accepted definition amongst the research community of what constitutes a microgrid. This is a serious gap in present knowledge. An accepted understanding of the concept of a microgrid will make it easier to identify its characteristics and thus contribute more effectively to solving the associated problems. A microgrid is a bidirectional power grid that allows for a cluster of loads and small sources, including DG and distributed energy storages, to operate as a single controllable system at a point close to the end consumer.

The review literature has revealed concerns about the voltage stability of MGs, in terms of both the steady state and transient performance of the distribution grids. This is particularly true when the small local sources are energized to supply part of the demand on the grid. Basically, the voltage at the distribution level has been regulated using conventional devices which include “on load tap changer (OLTC) transformers [25] [26], switched shunt capacitors [27] and step voltage regulator [28] [29]” . However. the variability of new distribution grids due to the number and distribution of connected generators make these traditional devices no longer applicable or effective in controlling voltage variations produced by DGs.

Advanced voltage control methods need to be used at the distribution level. Power electronics based D-FACT regulators have been used for controlling and regulating the power flow in distribution network to enhance voltage stability at critical buses. Recently, to fully exploit the potential of the D-FACT technology, energy storage technology has been combined with D-FACT to support the grid with reactive and active power. D-STATCOM among the D-FACT devices has long been regarded a preferred option for transient conditions due to its superior performance. Referring to the D-STATCOM’s application, the main factor in the D-STATCOM’s performance is the control algorithm.

Standard PI controllers are widely used in the D-STATCOM in all the above applications. However, the D-STATCOM is now being used with intelligent control strategies, including fuzzy and ANN controls. However, the details of how to determine and adjust the D-STATCOM controller parameters using these intelligent algorithms are lacking. There is a dearth of analysis and discussion by researchers, especially in how to exploit the reactive and active power of the D-STATCOM, as additional resources to support the grid's voltage stability. The battery and supercapacitor as long-term and short-term storage appear the most suitable for power application. However, the available open literature has not yet fully addressed these trends in combinations of energy storage devices with D-STATCOM.

To address these gaps, this study will carry out an investigation of intelligent supervisory energy management of the D-STATCOM based on dual energy storage to provide a faster voltage regulation in the distribution grid.

3 Chapter Three: Modelling of D-STATCOM in Distribution Systems

3.1 Introduction

To improve voltage stability of power distribution grids, FACTS devices were introduced as power electronic compensators. The D-STATCOM is one of the FACTS devices and acts as a reactive power source to control the bus voltage and to improve the stability in power distribution networks [78] [67] [154]

The mathematical modelling of an ideal D-STATCOM based on the distribution system is detailed in this chapter. The D-STATCOM device is represented as a controllable current source. As it is easier to design control loops of the system based on the d-q components, the equivalent circuit of the distribution system is transformed and derived in d-q components rotating reference frame, see Section 3.2. Additionally, in this section the ability of the D-STATCOM to provide reactive power compensation, to regulate the load voltage at both maximum load power and minimum supply voltage is identified and discussed. Moreover, the size of the D-STATCOM as a function of the system parameters is verified. The rating power of D-STATCOM according to the source voltage and load demand variation is calculated in Section 3.3. Finally, the chapter summary is given in Section 3.4

3.2 Modelling of Distribution Grid

The electrical power distribution system here can be represented with a simple grid of two buses (voltage source bus and load bus PCC) as Figure 3-1. The D-STATCOM is represented as an ideal current source connected with load parallelly to regulate voltage and compensate the power at the PCC of the distribution feeder.

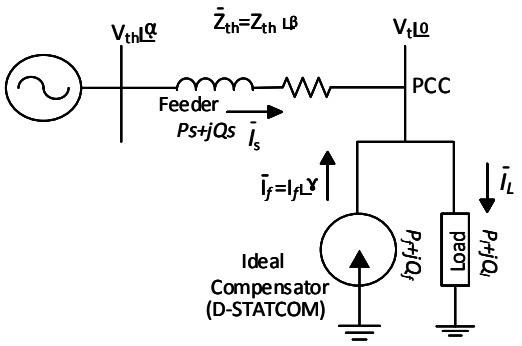

Figure 3-1 Modelling circuit for D-STATCOM with distribution grid [155]

The current injection of D-STATCOM to regulate the voltage by compensating the voltage drop across the feeder impedance of the system (Z_{th}) is given by:

$$\overline{I_f} = \overline{I_l} - \overline{I_s}$$

$$\overline{I_f} = \overline{I_l} - \frac{\overline{V_{th}} - \overline{V_t}}{\overline{Z_{th}}}$$

If $\overline{I_f} = I_f\angle\gamma, \overline{I_l} = I_l\angle-\theta, \overline{V_{th}} = V_{th}\angle\alpha, \overline{V_t} = V_t\angle 0, \overline{Z_{th}} = Z_{th}\angle\beta,$

Where $V_{th}\angle\alpha$ and $V_t\angle 0$ are the voltage of source and PCC, $Z_{th}\angle\beta$ is the feeder impedance between the source and load buses, $\overline{I_l} = I_l\angle-\theta$ is the load current, $I_f\angle\gamma$ is the injection current by the D-STATCOM, $\overline{I_s}$ is the source current, for simplicity the angle of voltage V_t is assumed to be zero.

Then,

$$I_f\angle\gamma = I_l\angle-\theta \quad - \frac{V_{th}\angle(\alpha-\beta)}{Z_{th}} + \frac{V_t\angle-\beta}{Z_{th}} \qquad \textbf{(3-1)}$$

It may be mentioned here that the effectiveness of the D-STATCOM in regulating voltage depends on the value of Z_{th}. When the injected current I_f is kept in quadrature with V_t, the desired voltage regulation can again be achieved without injecting any active power into the system. On the other hand, when the value of I_f is minimized, the same voltage correction can be achieved with minimum apparent power injection into the system. In this case, the entire load active power

P_l must be provided by the system. The active power flow through Z_{th} shown in Figure 3-1 on the load side is [156] [157]:

$$P_l = \frac{V_{th}V_t}{Z_{th}}\cos(\beta - \alpha) - \frac{V_t^2}{Z_{th}}\cos\beta \quad \textbf{(3-2)}$$

The angle α can be derived from (3-2) as:

$$\alpha = \beta - \cos^{-1}\left[\frac{V_t}{V_{th}}\cos\beta + \frac{Z_{th}P_l}{V_{th}V_t}\right] \quad \textbf{(3-3)}$$

The second term in brackets in Eq. (3-3) must be less than unity for $\cos^{-1}$ to have a real value.

$$\frac{V_t}{V_{th}}\cos\beta + \frac{Z_{th}P_l}{V_{th}V_t} \leq 1 \quad \textbf{(3-4)}$$

The above equation can be re-ordered as:

$$V_{th} \geq V_l\cos\beta + \frac{Z_{th}P_l}{V_t} \quad \textbf{(3-5)}$$

So, when the voltage source as in (3-5) the D-STATCOM can regulate the voltage without injecting any power into the system. However, the D-STATCOM can inject minimum apparent power to regulate the voltage. The equation of complex power flow injection of the D-STATCOM can be defined as:

$$\overline{S_f} = \overline{V_t}\overline{I_f^*} \quad \textbf{(3-6)}$$

Where * represents conjugate of complex variable.

The minimum power injection is subjected to the condition [157]:

$$\frac{\partial \overline{I_f}}{\partial \alpha} = 0 \quad \textbf{(3-7)}$$

$\overline{I_f}$ can be found from Eq. (3-1) and the solution of Eq. (3-7) gives the following:

$$\alpha = \tan^{-1}\left[\frac{Z_{th}I_l\sin(\beta - \theta)}{V_t + Z_{th}I_l\cos(\beta - \theta)}\right] \quad \textbf{(3-8)}$$

Thus, for a given load the value of α can be found from Eq. (3-8). Thus, the complex current and the apparent power of the D-STATCOM can be calculated from Eqs. (3-1) and (3-6) [157].

3.2.1 Modelling and Steady State Analysis of The Distribution System Based D-STATCOM

The power distribution system shown in Figure 3-1 can be represented by its equivalent circuit, as shown in Figure 3-2. It is assumed to be a balanced system; the system voltage is modelled as source bus with inductance L_s and resistance R_s connected in series with an inductor L_l and R_l as load, and a controllable current source i_f with parallel capacitor C_f as the D-STATCOM [158].

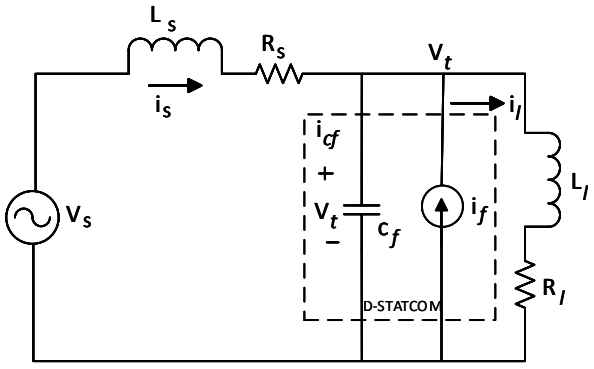

Figure 3-2 Equivalent circuit of power distribution system with D-STATCOM [155]

The dynamic differential equations of the system are:

$$L_s \frac{di_{s,abc}}{dt} = -R_s i_{s,abc} - v_{t,abc} + v_{s,abc} \quad \textbf{(3-9)}$$

$$C_f \frac{dv_{t,abc}}{dt} = i_{s,abc} + i_{f,abc} - i_{l,abc} \quad \textbf{(3-10)}$$

$$L_l \frac{di_{l,abc}}{dt} = v_{t,abc} - R_l i_{l,abc} \quad \textbf{(3-11)}$$

Here, $i_{s,abc}$, $i_{f,abc}$, $v_{s,abc}$ and $v_{t,abc}$ are vectors consisting of individual phase quantities denoted in Figure 3-2.

The d-q transformation analysis applied to above equations, gives:

$$L_s \frac{di_{s,dq}}{dt} = -(R_s + j\omega L_s) i_{s,dq} - v_{t,dq} + v_{s,dq} \quad \textbf{(3-12)}$$

$$C_f \frac{dv_{t,dq}}{dt} = -\left(j\omega C_f\right) v_{t,dq} + i_{s,dq} + i_{f,dq} - i_{l,dq} \quad \textbf{(3-13)}$$

$$L_l \frac{di_{l,dq}}{dt} = -(R_l + j\omega L_l) i_{l,dq} + v_{t,dq} \quad \textbf{(3-14)}$$

Where the $\omega = \frac{d\theta}{dt}$ is the rotating speed of the d-q axis in space. The equivalent diagram of the system for the d-q analysis is shown in Figure 3-3 and Figure 3-4.

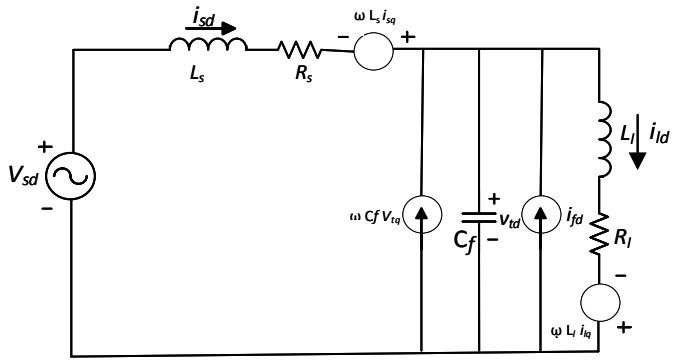

Figure 3-3 d-axis equivalent circuit

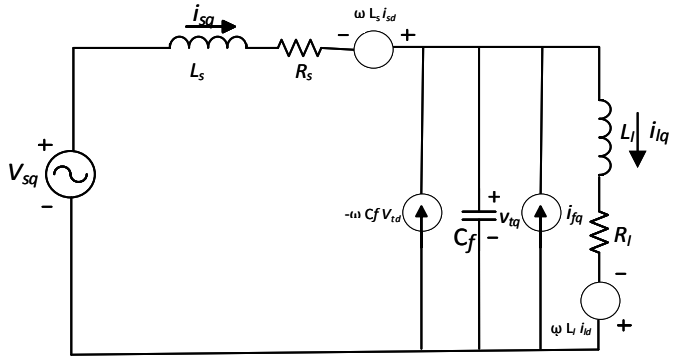

Figure 3-4 q-axis equivalent circuit

3.2.2 abc to dq Reference Frame

The vector representation of the *abc* to dq transformation is shown in Figure 3-5, where θ is the instantaneous angle between the x-axis and d-axis.

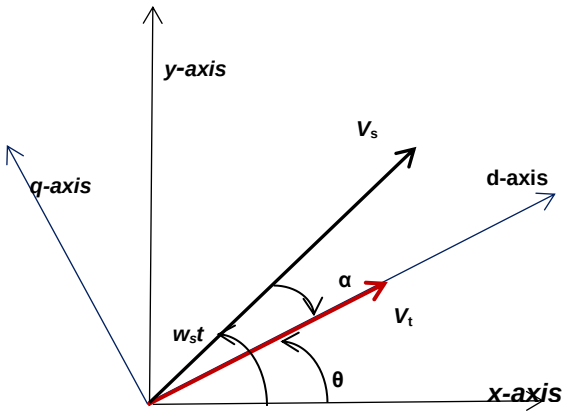

Figure 3-5 Orientation of d-q transformation

Thus, $\boldsymbol{\alpha = \theta - \omega_s t}$

where ω_s is the angular speed of the infinite bus voltage.

If the d-component is aligned to the supply source voltage, $v_{tq=0}$, the d-q equations of the system can be rewritten as:

$$\frac{di_{sd}}{dt} = -\frac{1}{T_s} i_{sd} + \omega i_{sq} - \frac{1}{L_s} v_{td} + \frac{v_s}{L_s} \cos\alpha \quad \textbf{(3-15)}$$

$$\frac{di_{sq}}{dt} = -\frac{1}{T_s} i_{sq} - \omega i_{sd} - \frac{v_s}{L_s} \sin\alpha \quad \textbf{(3-16)}$$

$$\frac{dv_{td}}{dt} = -\frac{1}{C_f} i_{ld} + \frac{1}{C_f} i_{sd} + \frac{1}{C_f} i_{fd} \quad \textbf{(3-17)}$$

$$\frac{dt_{ld}}{dt} = -\frac{1}{T_l} i_{ld} + \omega i_{lq} + \frac{1}{L_l} v_{td} \quad \textbf{(3-18)}$$

$$\frac{di_{lq}}{dt} = -\frac{1}{T_l} i_{lq} - \omega i_{ld} \quad \textbf{(3-19)}$$

$$\frac{d\alpha}{dt} = \omega - \omega_s \quad \textbf{(3-20)}$$

$$\omega = \frac{-i_{lq} + \quad i_{sq} + \quad i_{fq}}{C_f \quad v_{td}} \quad \textbf{(3-21)}$$

Where $T_s = \frac{L_s}{R_s}$ is the time constant of supply and line. $T_l = \frac{L_l}{R_l}$ is the time constant of the load.

3.2.3 Steady State Analysis of D-STATCOM Based Distribution System

The steady state equations of the system can be easily obtained by making all the derivative terms of dynamic Eqs. (3-15) - (3-20) equal zero as follows [158]:

$$0 = -\frac{1}{T_s} I_{sd} + \omega I_{sq} - \frac{1}{L_s} v_{td} + \frac{v_s}{L_s} \cos\alpha \quad \textbf{(3-22)}$$

$$0 = -\frac{1}{T_s} I_{sq} - \omega I_{sd} - \frac{v_s}{L_s} \sin\alpha \quad \textbf{(3-23)}$$

$$0 = -\frac{1}{C_f} I_{ld} + \frac{1}{C_f} I_{sd} + \frac{1}{C_f} I_{fd} \quad \textbf{(3-24)}$$

$$0 = -\frac{1}{T_l} I_{ld} + \omega I_{lq} + \frac{1}{L_l} V_{td} \quad \textbf{(3-25)}$$

$$0 = -\frac{1}{T_l} I_{lq} - \omega I_{ld} \quad \textbf{(3-26)}$$

$$0 = \omega - \omega_s \quad \textbf{(3-27)}$$

$$\omega = \frac{-I_{lq} + \quad I_{sq} + \quad I_{fq}}{C_f \quad V_{td}} \quad \textbf{(3-28)}$$

Where: $i_{sd} = I_{sd}$, $i_{sq} = I_{sq}$, $v_{td} = V_{td}$, $i_{ld} = I_{ld}$, $i_{lq} = I_{lq}$ (after the quantities have been transformed into the d-q reference frame), V_{td} is the magnitude of the load voltage.

The D-STATCOM can regulate the system by supplying both active and reactive power. However, in this part the investigation of D-STATCOM is sized to inject only the reactive power and the load active power requirements are supplied by the source [159].

Thus,

$$P_l = V_{td} I_{ld} = V_{td} I_{sd} \quad \textbf{(3-29)}$$

If the D-STATCOM supports the grid with reactive power only, the active current of the load is equal the active current of the supply ($I_{ld} = I_{sd}$). By solving Eqs. (3-22) and (3-23), the supply active current is derived as:

$$I_{sd} = \frac{-R_s}{R_s^2 + \omega_s^2 L_s^2}(V_{td} - V_s \cos\alpha) - \frac{\omega_s L_s}{R_s^2 + \omega_s^2 L_s^2} V_s \sin\alpha \quad \textbf{(3-30)}$$

From Eqs. (3-29) and (3-30) the P_l can be obtained as:

$$P_l = \frac{V_{td} V_s}{\sqrt{R_s^2 + \omega_s^2 L_s^2}} \left\{ \frac{R_s}{\sqrt{R_s^2 + \omega_s^2 L_s^2}} \cos\alpha - \frac{\omega_s L_s}{\sqrt{R_s^2 + \omega_s^2}} \sin\alpha \right\} - \frac{V_{td}^2 R_s}{R_s^2 + \omega_s^2 L_s^2} \quad \textbf{(3-31)}$$

If $\frac{R_s}{\sqrt{R_s^2+\omega_s^2 L_s^2}} = \cos\beta$ & $\frac{\omega_s L_s}{\sqrt{R_s^2+\omega_s^2 L_s^2}} = \sin\beta$ (β is the supply impedance angle.)

$$P_l = \frac{V_{td} V_s}{\sqrt{R_s^2 + \omega_s^2 L_s^2}} \{\cos\beta \cos\alpha - \sin\beta \sin\alpha\} - \frac{V_{td}^2 R_s}{R_s^2 + \omega_s^2 L_s^2} \quad \textbf{(3-32)}$$

$$P_l = \frac{V_{td} V_s}{\sqrt{R_s^2 + \omega_s^2 L_s^2}} (\cos(\beta - \alpha)) - \frac{V_{td}^2 R_s}{R_s^2 + \omega_s^2 L_s^2} \quad \textbf{(3-33)}$$

From Eq. (3-33) the supply voltage's phase angle can be written as:

$$\alpha = \beta - \cos^{-1}\left\{ \frac{V_{td}}{V_s} \frac{R_s}{\sqrt{R_s^2 + \omega_s^2 L_s^2}} + \frac{P_l \sqrt{R_s^2 + \omega_s^2 L_s^2}}{V_{td} V_s} \right\} \quad \textbf{(3-34)}$$

The term in brackets in Eq. (3-34) must be less or equal to unity for $\cos^{-1}$ to have a real value.

$$\frac{V_{td}}{V_s}\frac{R_s}{\sqrt{R_s^2+\omega_s^2L_s^2}}+\frac{P_l\sqrt{R_s^2+\omega_s^2L_s^2}}{V_{td}V_s}\leq 1 \quad \textbf{(3-35)}$$

In Eq. (3-35), if the magnitude of the load voltage is regulated at the desired value $V_{td,desired}$ with D-STATCOM, the load active power, $P_{l,desired}$, at the desired load voltage can be expressed as in Eq. (3-36) and the source voltage, V_s, as in Eq. (3-37).

$$P_{l,desired}\leq\left\{\frac{V_s\sqrt{R_s^2+\omega_s^2L_s^2}-V_{td,desired}R_s}{R_s^2+\omega_s^2L_s^2}\right\}V_{td,desired} \quad \textbf{(3-36)}$$

$$V_s\geq V_{td,desired}\frac{R_s}{\sqrt{R_s^2+\omega_s^2L_s^2}}+\frac{P_{l,desired}\sqrt{R_s^2+\omega_s^2L_s^2}}{V_{td,desired}} \quad \textbf{(3-37)}$$

From Eqs. (3-36) and (3-37) $P_{l,desired}$ and V_s are each a function of the resistance R_s and inductance L_s when the $V_{t,desired}$ is kept constant.

Regarding the D-STATCOM's application to control the load voltage, the power model is generally used to determine the loads in the power distribution grids. Thus, the values of R_l and L_l are found by solving Eqs. (3-38) and (3-39).

$$V_{td,desired}^2\frac{R_l}{R_l^2+\omega_s^2L_l^2}-P_{l,desired}=0 \quad \textbf{(3-38)}$$

$$V_{td,desired}^2\frac{\omega_sL_l}{R_l^2+\omega_s^2L_l^2}-Q_{l,desired}=0 \quad \textbf{(3-39)}$$

If we now assume the D-STATCOM is lossless and injecting only reactive power (the active current of the D-STATCOM $I_{fd}=0$), then the reactive current of the

D-STATCOM can be derived from Eqs. (3-22)-(3-28). The reactive power support provided by D-STATCOM may be written as:

$$S_{DSTATCOM} = Q_{DSTATCOM} = V_{td} I_{fq} \quad \textbf{(3-40)}$$

Where:$V_{td} = V_{td,desired}$

As indicated in Eqs (36) and (37) the amount of active power, $P_{l,desired}$, and the desired voltage magnitude of the system, V_s, are a function of Rs and Ls when $V_{td,desired}$ is kept constant. The system parameters in Table 3-1 have been chosen to study the impact of system parameter on maximum load active power and the magnitude of the supply system voltage, $V_{s,min}$.

Table 3-1 Parameters of the distribution power system [159]**.**

Parameters	Values
Nominal source voltage	12.1 kV
Desired load voltage magnitude, V_{td}	11.00 kV
R_s and L_s	10 Ω, 10 mH
Nominal load power P_l and Q_l	12.0 MW and 0 MVar
System frequency	50 Hz
Coupling capacitor	50 µf

Figure 3-6 and Figure 3-7 show the plots of maximum desired load power $P_{l,desired}$ with the system parameters R_s and L_s at a various values of source voltage. Figure 3-6 shows the maximum load power as a function of system inductance, Ls, with time constant of the supply, T_s, kept constant at 3.14 and $V_{td,}$ maintained at 11.00 kV. It shows that the maximum value of the load power decreases as the system inductance increases. Figure 3-7 shows the maximum load power $P_{l,desired}$ as a function of T_s, with L_s kept constant at 10.00 mH. It can be seen that the load power $P_{l,desired}$ increases as the source time constant, T_s, increases.

Figure 3-8 and Figure 3-9 show surface plots of maximum load power, $P_{l,desired}$ as a function of L_s and V_s, and T_s and Vs respectively. These figures show that $P_{l,desired}$ increases linearly with source voltage V_s.

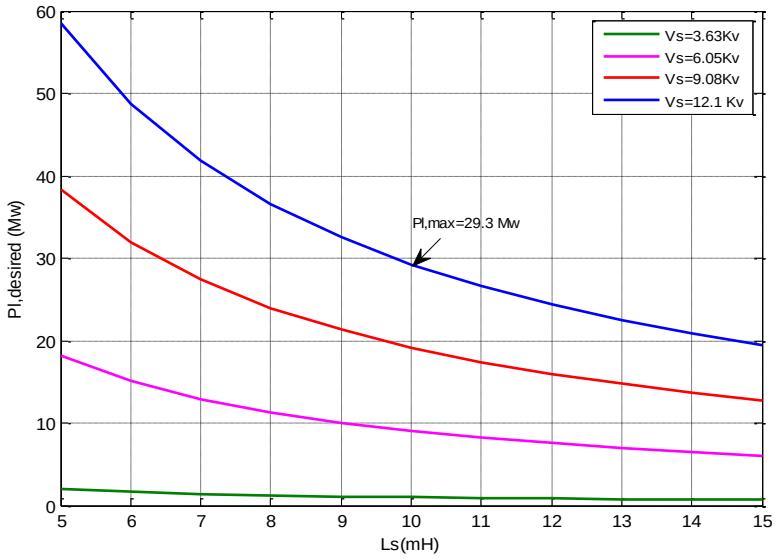

Figure 3-6 Load active power as a function of L_s at constant value of T_s

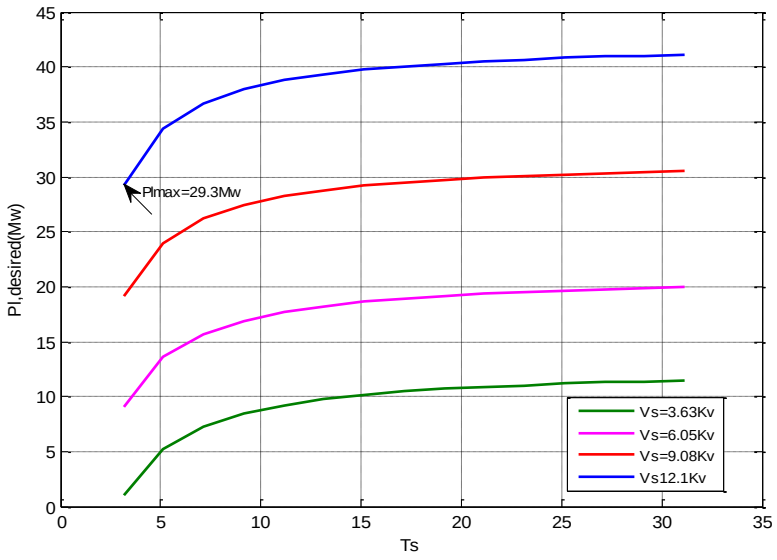

Figure 3-7 Load active power as a function of T_s at constant value of L_s

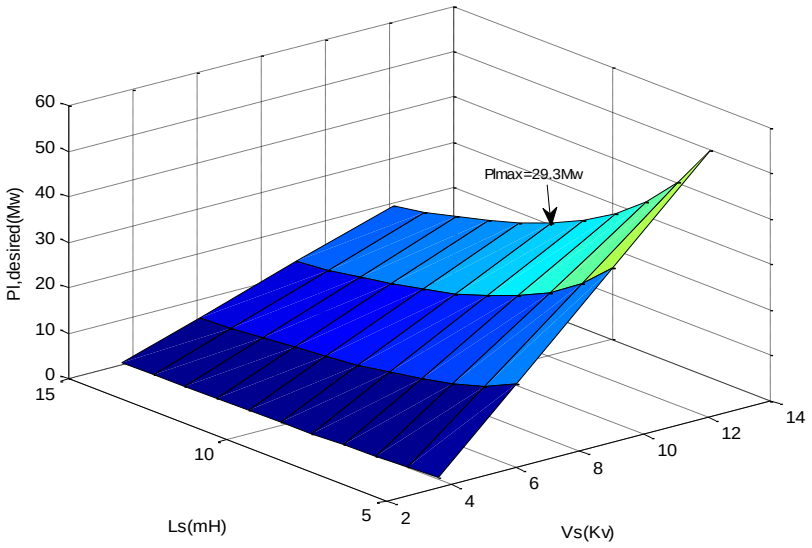

Figure 3-8 Load active power as a function of L_s and V_s

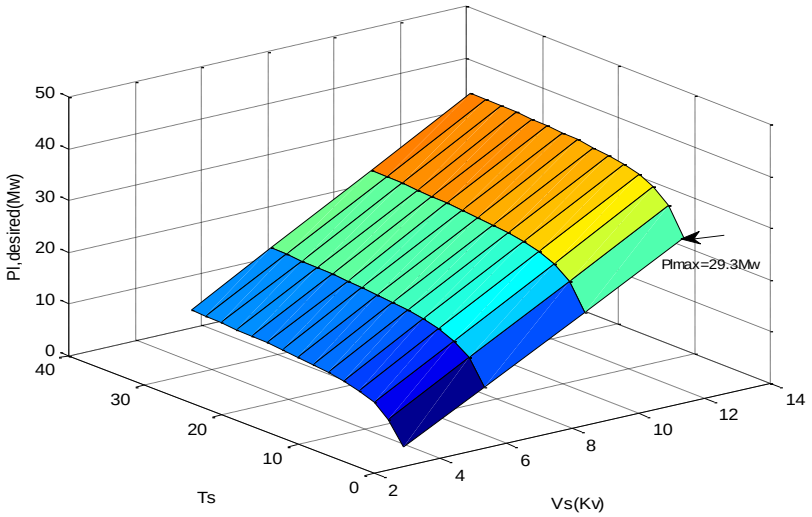

Figure 3-9 Load active power as a function of T_s and V_s

Figure 3-10 and Figure 3-11 show the source voltage ($V_{s,min}$) plots as a function of system inductance, $L_s$and source time constant, T_s, with various levels of the active power of the load (P_l). In Figure 3-10, T_s and load voltage $V_{td}$are kept constant at 3.14 and 11.00 kV respectively. It can be seen from this figure that $V_{s,min}$ increases with increase in L_s. The source voltage as a function of T_s is

shown in Figure 3-11. The L_s was constant at 10.00 mH. It can be seen that $V_{s,min}$decreases as the time constant T_s increases.

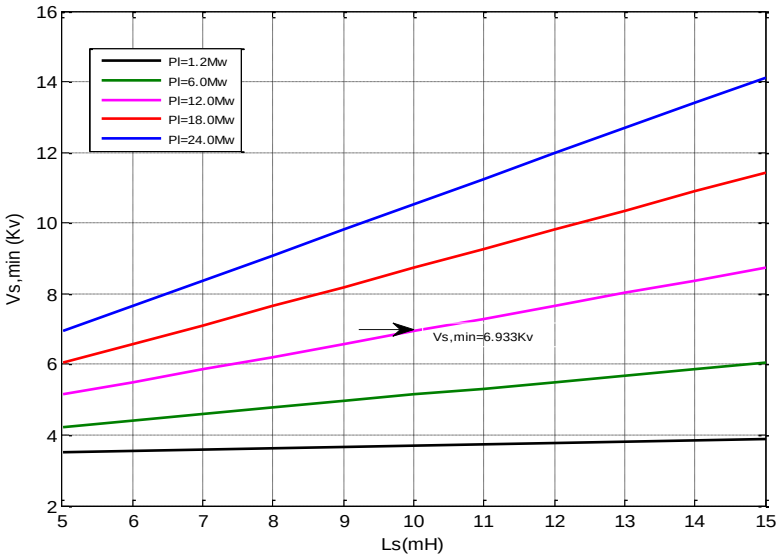

Figure 3-10Source voltage V_s as a function of L_s at constant value of T_s

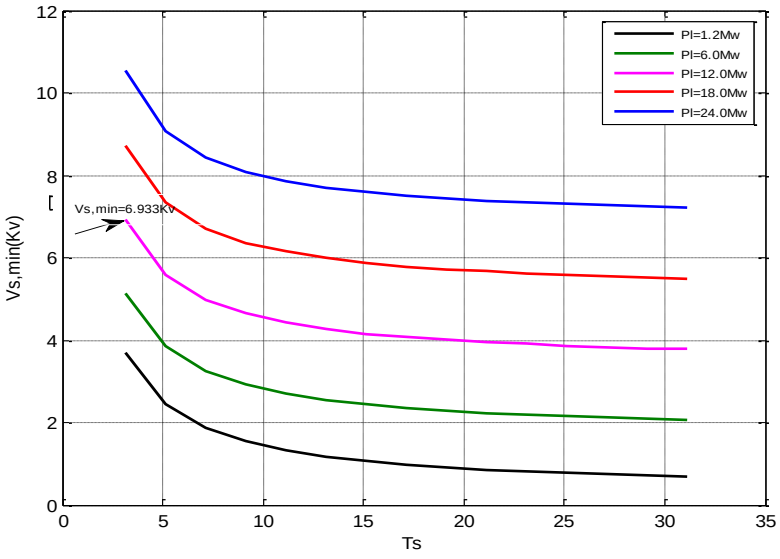

Figure 3-11 Source voltage as a function of T_s at constant value of L_s

Figure 3-12 and Figure 3-13 show the surface plots of source voltage, $V_{s,min}$ as a function of load power (P_l) and $L_s$and T_s respectively. These figures show that

$V_{s,min}$ increases linearly with load power, for example line AB in the figures, which relates to P_l=12.00 MW in both Figure 3-10 and Figure 3-11.

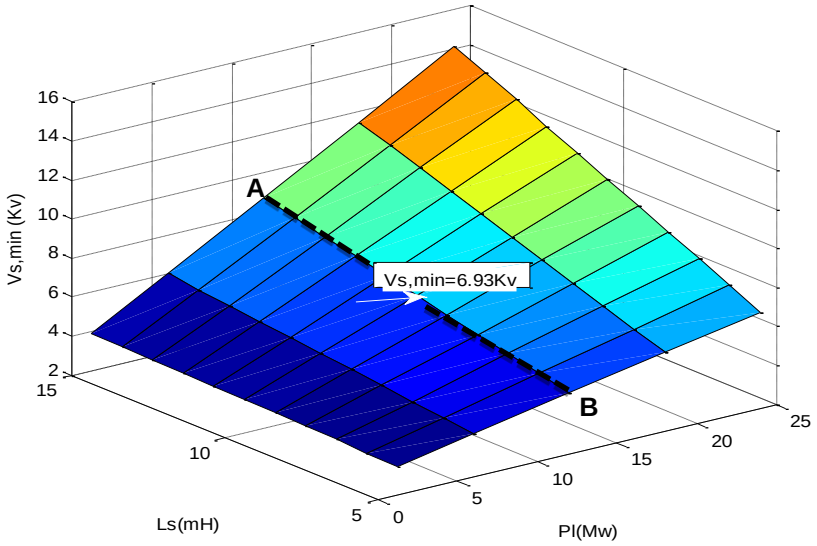

Figure 3-12 Voltage source as a function of L_s and P_l

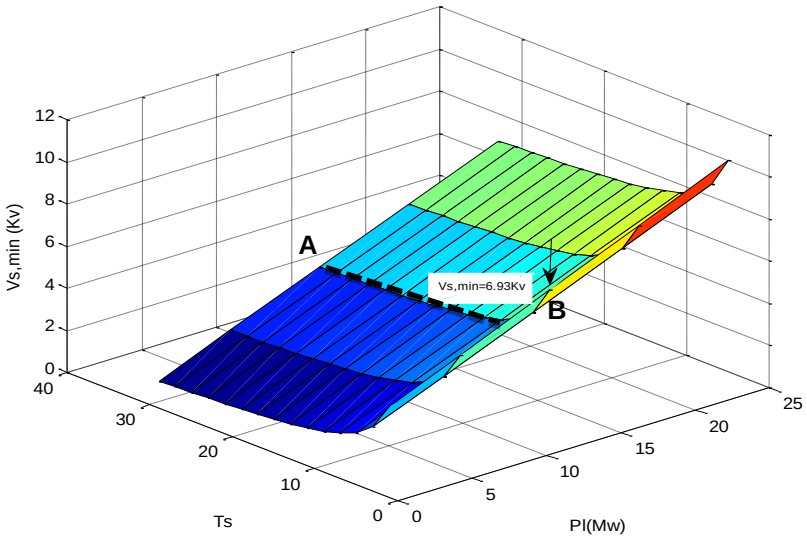

Figure 3-13 Voltage source as a function of T_s and P_l

The rating of the D-STATCOM ($S_{D-STATCOM}$) is affected by the system parameters: i.e. L_s, R_s, V_s, and P_l. The inductance L_s and time constant T_s of the source were changed to evaluate the impact of the system parameters on the

rating of the D-STATCOM. Figure 3-14 and Figure 3-15 show the surface plot of $S_{D-STATCOM}$ as a function of L_s and T_s, when the load power factor is unity (Q_l=0) as the source voltage decreased from 14.00 to 6.00 kV.

In Figure 3-14, the source inductance was varied from 5 to 20 mH for different levels of source voltage up to 12.1 kV. The time constant and V_{td} were kept constant at 3.14 and 11.00 kV. It is seen in Figure 3-14 at the normal system parameters (L_s= 10.00 mH and V_s =12.1 kV), the voltage of the load bus is at the required value (11.00 kV), the DSTATCOM does not support the grid with any power ($S_{D-STATCOM}$ = 0). D-STATCOM regulated the load voltage by injecting/absorbing power. So, at the nominal case (V_s=12.1 kV), the D-STATCOM absorbs power to control the load voltage at the rated value when load voltage increased. The negative value of $S_{D-STATCOM}$ corresponds to a load voltage more than 11.00 kV.

The effect of the source time constant T_s on the required power of D-STATCOM is indicated in Figure 3-15. The source time constant is changed between 3.14 and 31.5 with source voltage sags from 6.96 to 12.1 kV. Here V_{td} and L_s remained constant at 11.00 kV and 10.00 mH respectively.

At T_s=3.14, a reduction in source voltage from 12.1 to 6.96 kV, leads to a drop in the load voltage from 11.00 to 6.6 kV. Thus, the voltage of the load needed to be regulated by injecting reactive power when the source voltage dropped from 12.1 to 6.96 kV. When the T_s was more than 3.14, the load voltage V_{td} was reduced from 11 kV because the source voltage changed from 12.1 to 6.69 kV. In this case, D-STATCOM regulated the load voltage by injecting or absorbing power. However, for the normal case the D-STATCOM absorbed the reactive power when the load voltage is more than the required value (11.00 kV) that related to the negative value of $S_{D-STATCOM}$.

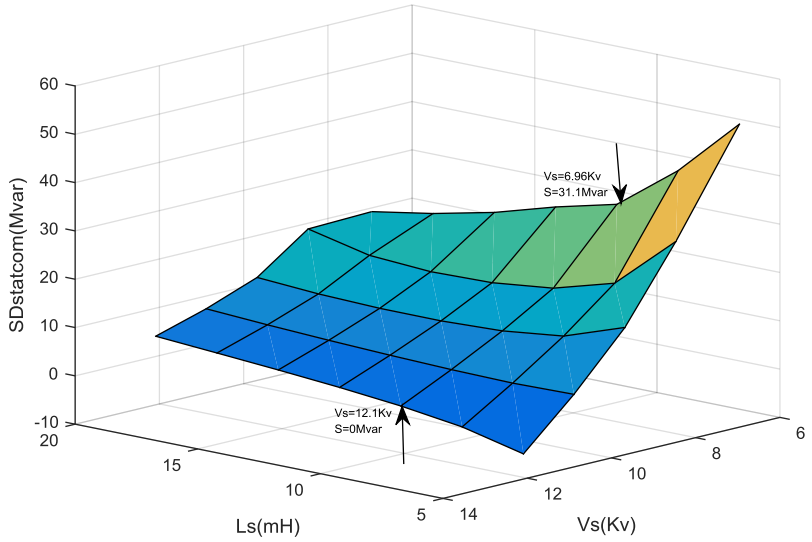

Figure 3-14 $S_{D-STATCOM}$ as a function of L_s and V_s with power factor of the load of unity and source time constant 3.14

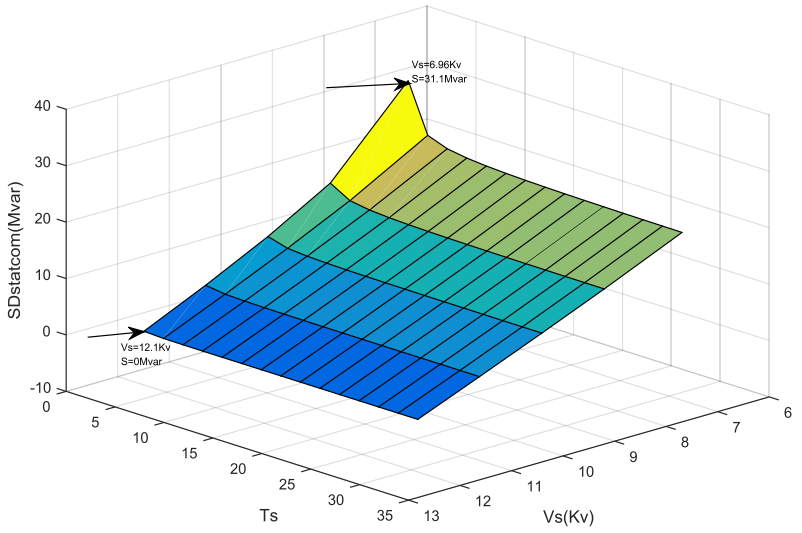

Figure 3-15 $S_{D-STATCOM}$ as a function of T_s and V_s with power factor of the load of unity

Figure 3-16 and Figure 3-17 show the surface plot of $S_{D-STATCOM}$ with lagging load power factor of 0.9 (lagging because load is inductive), as a function of inductance and time constant of the source at different levels of the system voltage. As indicated in the figures, the load demand at a power factor of 0.9 influences the load voltage only, whereas the minimum source voltage remained

the same in the case of power factor of unity. For example, at nominal system voltage (12.1 kV) the load voltage is 11.00 kV at unity power factor, but at a power factor of 0.9 the load voltage is 9.83 kV for the same source voltage variations. Thus, the rating of the D-STATCOM input to regulate the load voltage at 0.9 load power factor is more than for a power factor of unity.

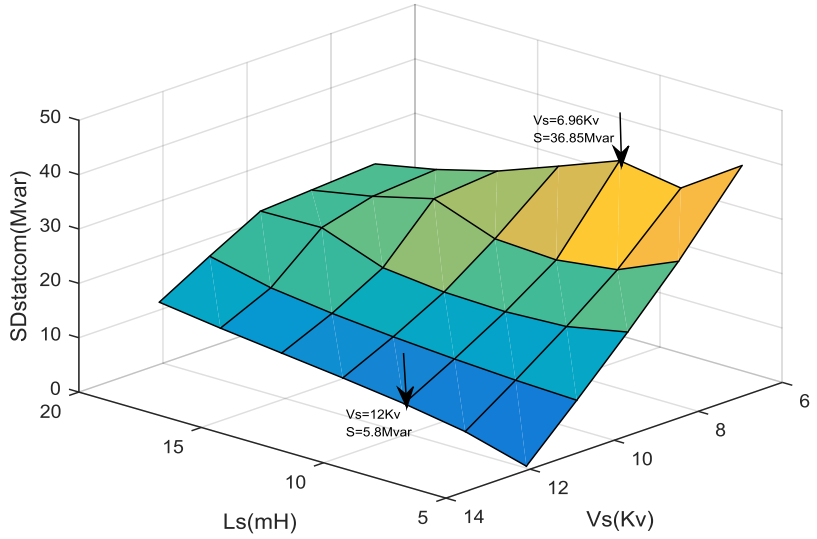

Figure 3-16 $S_{D-STATCOM}$as function of L_s and $V_s$with lagging power factor of the load of 0.9

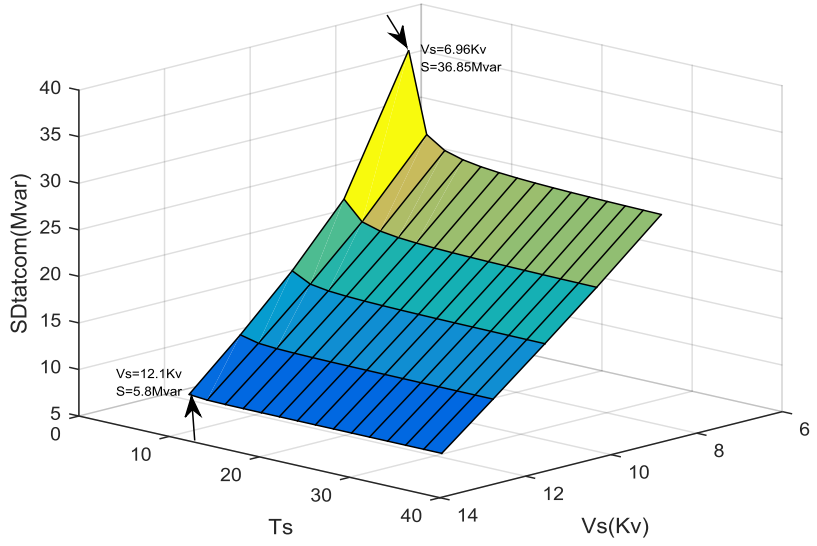

Figure 3-17 $S_{D-STATCOM}$as function of T_s and V_s at with lagging power factor of the load of 0.9

To study the effect of variation in load power on the magnitude of the D-STATCOM, Figure 3-18 and Figure 3-19 show the surface plots of $S_{D-STATCOM}$ as a function of load power level, P_l, and L_s, and P_l and T_s respectively, for a load power factor of unity (Q_l=0). The voltage of the source remained constant at 12.1 kV.

Figure 3-20 and Figure 3-21 show the surface plots of $S_{D-STATCOM}$ as a function of load power level, P_l, and L_s, andP_l and T_s respectively, for a lagging load power factor of 0.9.

Figure 3-18 shows the results obtained as the load power changed from 10 to 50 MW and the source inductance changed from 20 to 5 mH, for constant load voltage of 11.00 kV and time constant of 3.14. As previously, the D-STATCOM does not add any reactive power to the grid at the nominal case when L_s= 10.00 mH, P_l=12.00 MW and V_{td}=11.00 kV.

The maximum load power for which the D-STATCOM can compensate the load voltage can be computed from Eq. (3-36), which shows $P_{l,desired}$ = 29.3 MW. When the load power was raised to 29.3 MW it caused a reduction of the load terminal voltage from 11.00 kV to 8.51 kV. So, the D-STATCOM injected reactive power to regulate the load voltage. On the other hand, when the power of the load is less than 12.00 MW, the load voltage becomes more than 11.00 kV and the D-STATCOM absorbs the reactive power from the system to regulate load voltage and that corresponds to a negative value of $S_{D-STATCOM}$.

Figure 3-19 shows the surface plot of $S_{D-STATCOM}$as a function of T_s and P_l. The source inductance and load voltage were kept at 10 mH and 11.00 kV, respectively. T_s was increased from 3.14 and 31.5.

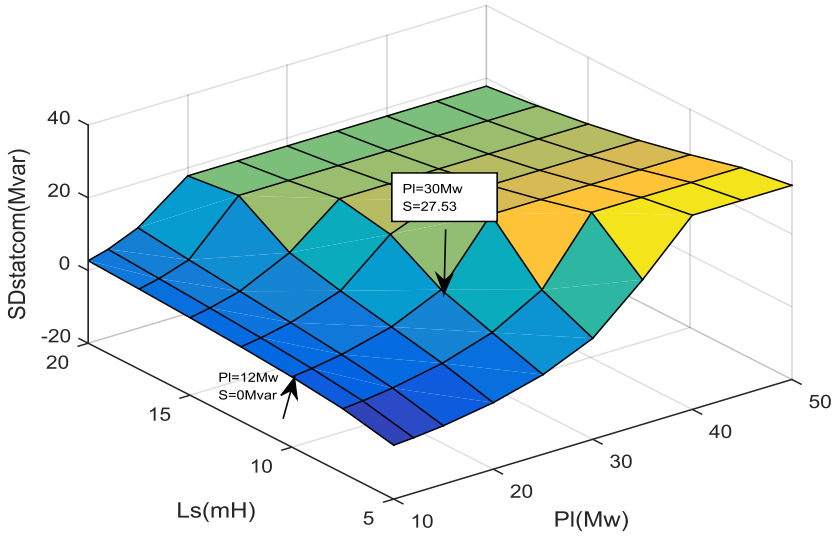

Figure 3-18 $S_{D-STATCOM}$ as function of L_s and P_l with power factor of the load of unity

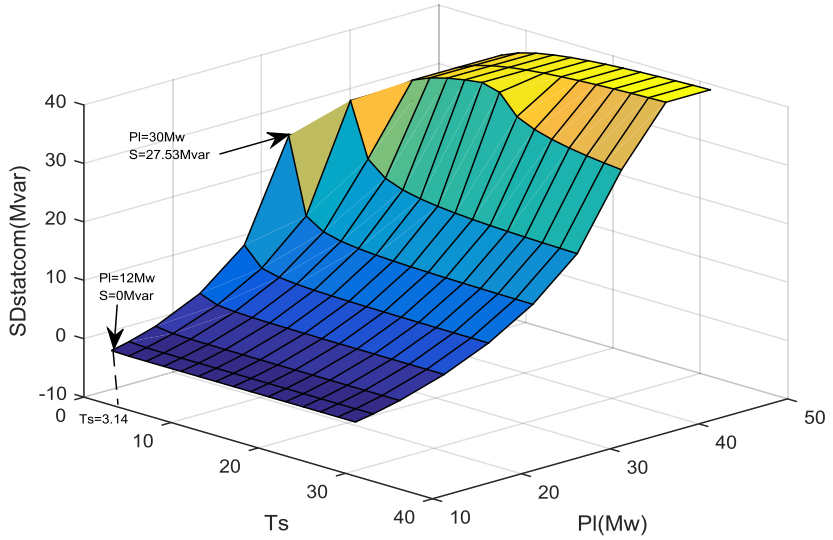

Figure 3-19 $S_{D-STATCOM}$ as function of T_s and P_l with power factor of the load of unity

For the case of a load power factor of 0.9, Figures (3-20) and (3-21) show surface plots of $S_{D-STATCOM}$ with respect to the inductance and time constant of the source for different power loads. As indicated in the Figures, the load demand with a power factor of 0.9 affected the load voltage, whereas the maximum load power

remained the same as in the case of a power factor of unity. For example, at nominal load of 12.1 MW the load voltage was 11.00 kV at unity power factor, while for power factor of 0.9 was 9.83 kV for the same load power variations. So, the rating of the D-STATCOM to regulate the load voltage at 0.9 load power factor is greater than for load power factor of unity.

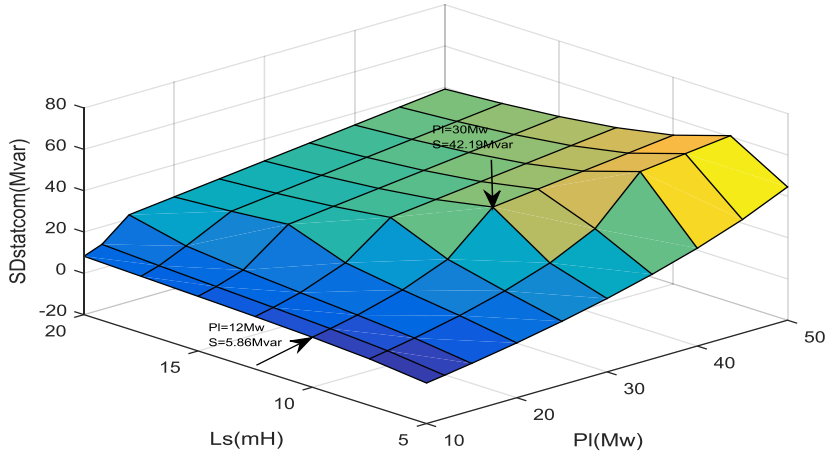

Figure 3-20 $S_{D-STATCOM}$ as function of L_s and P_l with lagging power factor of the load of 0.9

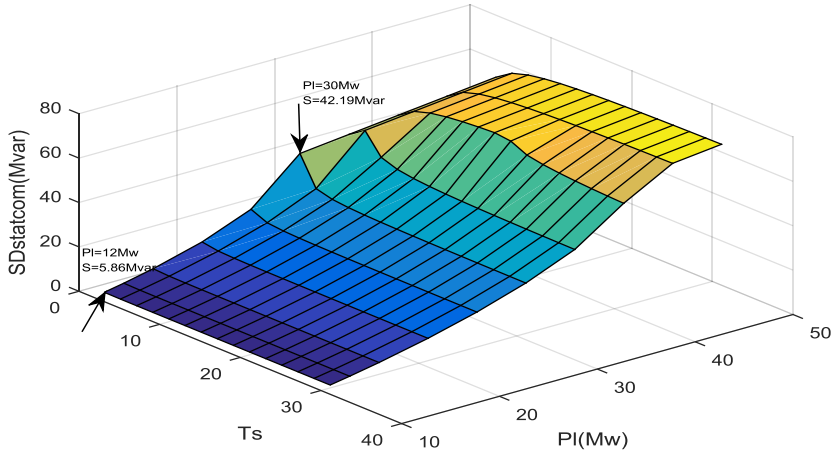

Figure 3-21 $S_{D-STATCOM}$ as function of T_s and P_l with lagging power factor of the load of 0.9

3.3 Design of D-STATCOM Rating

Essentially, the D-STATCOM is constructed from switching devices based on insulated gate bipolar transistors (IGBTs) or metal-oxide-semiconductor field effect transistors (MOSFETs), a capacitor unit and a coupling inductor. The rating power of the D-STATCOM can be decided according to the source voltage and variation in load demand. The system parameters as shown in Table 3-1 are taken as an example design to demonstrate how to determine the component rating. Figure 3-14 and Figure 3-16 depict the reactive power supply with variation of source voltage at power factors of unity and 0.9 lag respectively. Figure 3-18 and Figure 3-20 illustrate the supplied reactive power with different levels of load power again for power factors of unity and 0.9 lag respectively. Table 3-2 and Table 3-3 give the required reactive power for source voltage sags and various loads respectively.

Table 3-2 Reactive power for source voltage sags.

Source Voltage (kV)	Required reactive power (MVar) Load power factor=1	Required reactive power (MVar) Load power factor=0.9 lag
12.10	0.00	5.80
10.89	5.05	10.82
9.68	10.53	16.30
8.50	16.83	22.61

Table 3-3 Reactive power for different loads.

Active power load (MW)	Required reactive power (MVar) Load power factor=1	Required reactive power (MVar) Load power factor=0.9 lag
12.00	0.00	5.80
14.00	1.36	7.70
16.00	4.84	9.74
20.00	10.97	14.62

If the converter is lossless, the current rating of the D-STATCOM is determined from the following equation [160]:

$$Q_{D-STATCOM} = \sqrt{3} V_{td} I_f \quad \textbf{(3-41)}$$

As an example, we use Table (3-2) where the source voltage dips to 8.50 kV with a lagging power factor of 0.9. The required reactive power of D-STATCOM is 22.61 MVar ($Q_{D-STATCOM}$= 22.61 MVar) and load voltage, V_{td}, is 11.00 kV. The value of the D-STATCOM current, I_f, is 1.19 kA from Eq. (3-41).

When the desired voltage of the load terminal is 11.00 kV, the DC side voltage of the D-STATCOM can be calculated from [160]:

$$V_{dc} = \frac{2 * \sqrt{2} \left(\frac{V_t}{\sqrt{3}} \right)}{m} \quad \textbf{(3-42)}$$

Where m is the modulation index which ranges between 0 and 1. If it is assumed m = 0.5, the voltage of the DC side is:

$V_{dc} = 35.93585\ kV\ \approx 36\ kV$

3.4 Summary

This chapter presented the modelling circuit for D-STATCOM with a distribution grid. The system voltage was modelled as a source bus with impedance, the load was modelled as a resistance connected in series with an inductor, and the D-STATCOM modelled as a controllable current source with parallel capacitor. The dynamic differential equations of the distribution system were given and applied in the d-q transformation analysis. A set of steady state equations were obtained from the dynamic equations.

The D-STATCOM capabilities to control the load voltage at the maximum load power and the minimum source voltage were considered and discussed in this chapter. It was found that the maximum load power, $P_{l,(max)}$ decreased as the source inductance *(L_s)* increased, whereas increasing the time constant of the source (T_s) resulted in an increase of the maximum load power. The effects of

change in inductance of the source and time constant on the source voltage were discussed; decrease in source time constant (T_s) resulted in an increase of the minimum source voltage ($V_{s,min}$) while the voltage of the source increased linearly with increase in source inductance.

This chapter also addressed, the ability of the D-STATCOM ($S_{D-STATCOM}$) as a voltage regulator corresponding to the system parameters for different levels of the source voltage and a range of values of the load power. The rating of the output of the $S_{D-STATCOM}$was found to be a function of the system parameters e.g. source resistance (R_s) and source inductance (L_s).

4 Chapter Four: Design of D-STATCOM Control

4.1 Introduction

As stated previously, voltage stability is enhanced in power systems by controlling the voltage and reactive power flow at all points in the system within acceptable limits. Real power may have to be injected to support the power grid at the setting frequency.

Different types of compensation devices have been used in distribution systems to ensure the system meets the demand for reactive power and to avoid any voltage disturbance in the system [161].

In recent time, compensator-based power electronic devices have been employed as reactive power sources in AC power systems to maintain voltage stability [62]. A D-STATCOM power electronic device is fast-acting and can produce or absorb reactive power more rapidly than other classical reactive power compensators such as capacitor banks and SVCs [161].

The main aim of this chapter is to adopt and improve the performance of the D-STATCOM device to provide enhanced power quality and voltage stability in distribution grids. To ensure a fast and consistent voltage response during a load change, a novel approach that decouples the d-q power components has been developed; applying a Sugeno fuzzy PI controller to a D-STATCOM. Based on this strategy, the error signal of the DC side voltage is reduced significantly because the proportional and integral coefficients of PI based fuzzy logic controller have been adjusted almost instantaneously during the transients as a result of changes in load and operating conditions. The resultant excellent performance is verified by comprehensive MATLAB/SIMULINK models

The chapter is organized as follows. Section 4.2 explains grid connected power converters. The two–level, three phase power converter is detailed in Section 4.3. The modelling and steady state analysis of D-STATCOM are described in Sections 4.4 and 4.5. Section 4.6 describes the design of the D-STATCOM control loops built using a voltage source power converter, and the design of the new Sugeno PI fuzzy controller to enhance the performance of the standard D-

STATCOM. Sections 4.7 and 4.8 present the simulation of a distribution system with a sudden load change and during fault condition, showing the benefits of using a D-STATCOM. Furthermore, a performance comparison of the system has been carried out for the fuzzy-tuned PI and the standard PI controllers under load disturbance. At the end, Section 4.9 makes some concluding remarks on the current work.

4.2 Grid connected power converters

Previously, industrial, domestic and information technology applications depended mainly on power-electronic converters. However, in the last two decades, due to advancements in semi-conductor and electronic technologies, the benefits of their use in power systems have become more significant. Thus, the number of commercial and industrial companies including active power filtering and compensation in equipment based on power electronics is increasing rapidly [162].

The accurate control of the active and reactive power flow is the main objective of most power distribution systems designed to maintain the system voltage stable [163]. Thus, electronic converters are employed as the main part of the control system due to their ability to convert power from AC to DC or vice versa. There are mainly two types of AC to DC converters: voltage source converters (VSC) and current source converters (CSC) depending on the source type used on DC side of the converter. In the VSC a voltage source such as a capacitor is used in the DC side while a current source, for example, a reactor is utilised in CSCs. The VSC has a number of advantages over the CSC; including autonomous reactive and active power conversions and unlimited reactive power [47].

The configuration of a three-phase VSC can be described based on the number of levels [162]. In general, the VSC configuration is classified into two or multilevel converters. Cascaded Multilevel Converter (CMC) [122], Cascaded Multilevel H-Bridge converter [123], Neutral Point Clamped (NPC) and Flying Capacitor Multilevel converter [85] are different applications of the multilevel converter. These converter structures increase the ability of IGBT devices to control the

voltage of IGBT devices and meet the needs of high power grids. However, to use CMCs in high and medium-voltage power amplifiers necessitates employing transformers to deliver the required active dc sources that are electrically isolated [164]. To build multilevel inverters, complex control and isolated power sources are required at each stage [165]. This increases costs and energy losses and adds to the complexity of the power circuit.

The modular multilevel converter is attractive for use in medium and high voltage applications because of its modularity which makes it feasible to adapt it to multiple levels without the problem of having to balance the capacitor voltage [164] [166] However, such applications can require the addition of a number of semiconductors and large capacitors which may adversely affect the losses and footprint of the convertor [164].. Thus, the two level (six pulse) three phase VSC configuration has been selected for this work, which is appropriate for medium and low power grids.

4.3 Two –level three phase power converter

The two-level converter has been widely used for a many application at different power levels. “A VSC uses composite self-commutated switching devices such as the insulated gate bipolar transistor (IGBT) and anti-parallel diodes” as shown in Figure 4-1“to enable bi-directional current flow in each phase-leg, hence bidirectional power flow between AC and DC sides.”[167]. The three- phase two-level VSC schematic diagram is presented in Figure 4-1. The converter is a two-level converter because the AC voltage level of the converter at phase a, b and c can be produced from only two discrete voltage levels, ½ V_{dc} and −½ V_{dc}, based on the supply mid-point (0). The converter consists of three legs, two controllable switches in each leg connecting in series (a total of 6 switches) [47] [167]. In any one phase-leg the switches are complementarily. When the top switch in a phase is switched on, the ½V_{dc} voltage potential is supplied to the converter, conversely, the -½V_{dc} voltage is produced when the lower switch in the same phase is turned on. So, the two switches in the same leg should never work simultaneously, as this would produce an undesirable current through the DC side with the risk that the converter switching units would be destroyed.

Thus, maintaining the successful operation of the converter in any real system is achieved by operating one switching device at a time. A delay is introduced between the switching gates to avoid any failure in converter operations by ensuring both switches in the same lag are never on simultaneously.

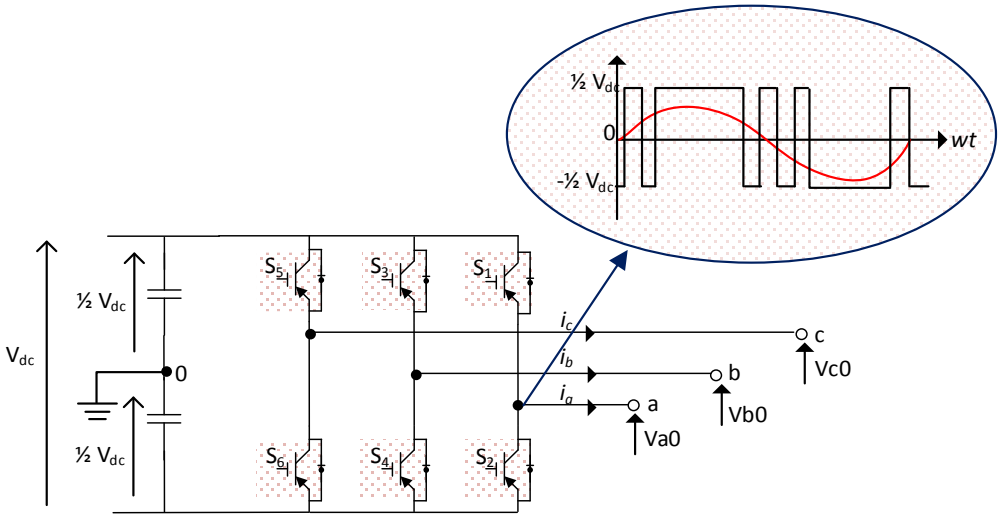

Figure 4-1 Three-phase, two-level converter [167]

4.4 Modelling of D-STATCOM

In this study the voltage source converter is employed as the core of the D-STATCOM device [163].

The detailed model of the D-STATCOM with a 2-level three phase converter and its control are shown in Figure 4-2. For the purpose of deriving equations describing the workings of the D-STATCOM device, a simplified equivalent circuit is first obtained. A simplified, equivalent VSC is assumed to be connected to the electric system. It is also assumed that the inverter operates under ideal, balanced conditions, that it produces an ideal sinusoidal voltage at a fundamental frequency. See Figure 4-3. The necessary equations can now be derived relatively easily from consideration of Figure 4-3.

In this figure, each switch represents a power semiconductor device and anti-parallel diode combination. V_{sa}, V_{sb}, and V_{sc} represent the AC grid voltages. $V_{st,a}$, $V_{st,b}$, and $V_{st,c}$ represent the converter voltages. i_a, i_b, and i_c are the line currents flowing through the coupling reactor, L. The converter is integrated into the AC grid through a coupling transformer and inductor. The inductor also acts as filter

unit to eliminate the harmonic components of the output currents. The inductance, L, in this figure represents the leakage inductance of the transformer and the interfacing inductors. The copper loss of the connecting transformer and loss of the interfacing inductor is represented by a resistance R.

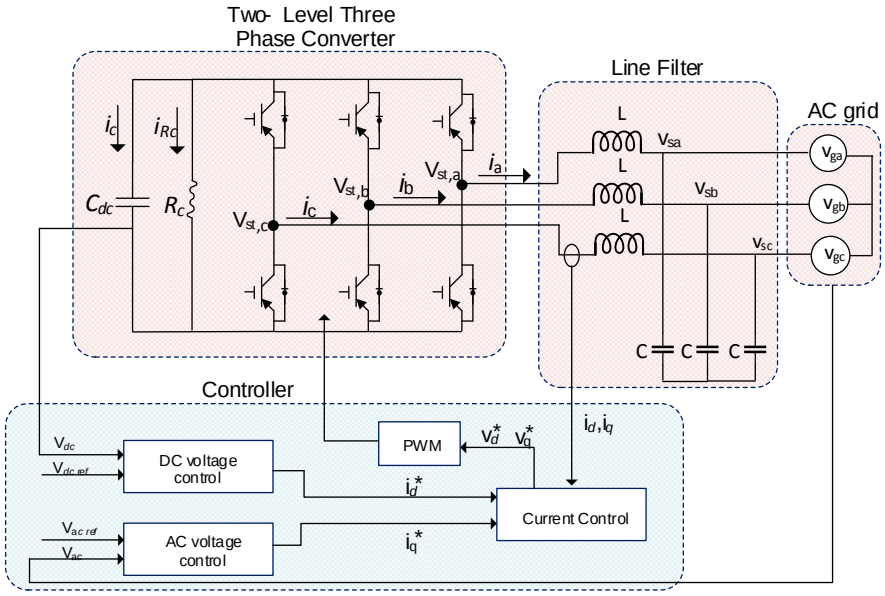

Figure 4-2 Detailed model of D-STATCOM

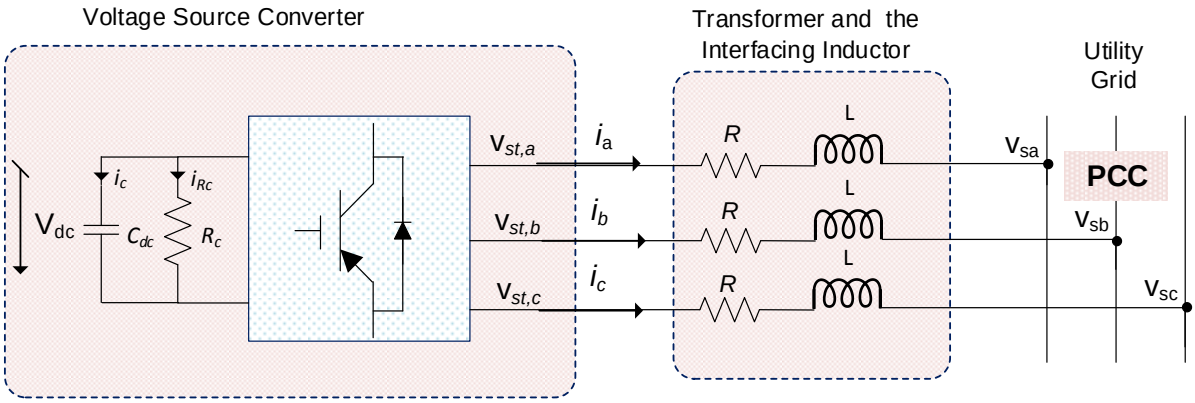

Figure 4-3 the equivalent diagram of DSTATCOM

According to Figure 4-3, $V_{st,abc}$ represents the D-STATCOM's AC voltage and thus the three-phase dynamic differential equations of AC system may be expressed as:

$$L\frac{di_a}{dt} = -Ri_a - v_{s,a} + v_{st,a}$$

$$L\frac{di_b}{dt} = -Ri_b - v_{s,b} + v_{st,b} \quad \textbf{(4-1)}$$

$$L\frac{di_c}{dt} = -Ri_c - v_{s,c} + v_{st,c}$$

Referring to the DC side in Figure 4-3, the DC link of D-STATCOM is represented by capacitor C_{dc} . The DC current flows through the capacitor C_{dc} and resister Rc which represents losses in the converter. (To represent both the power losses in the capacitor, C_{dc}, and the switching losses in the inverter, a shunt resistance Rc is placed across the capacitor). The power balance equation of the convertor and the instantaneous power of the DC- link can be expressed as

$$p_{dc} = v_{dc}i_{dc} = v_{dc}(i_c + i_{Rc}) = p_{ac} = v_{st,abc}^T i_{abc} \quad \textbf{(4-2)}$$

According to Figure 4-3, the DC current may be described as

$$i_{dc} = C_{dc}\frac{dv_{dc}}{dt} + \frac{v_{dc}}{R_c} \quad \textbf{(4-3)}$$

From Equations (4-2) and (4-3), the relation between DC and AC power can be expressed as:

$$v_{dc}\left\{C_{dc}\frac{dv_{dc}}{dt} + \frac{v_{dc}}{R_c}\right\} = -\left(v_{st,abc}^T, i_{,abc}\right) \quad \textbf{(4-4)}$$

The vector representation of the abc to dq transformation in Chapter Three is applied to analyse the above equations. Thus, the dynamic equation of the D-STATCOM in a d-q reference frame can be represented as:

$$\frac{di_d}{dt} = -\frac{R}{L}i_d + \omega i_q - \frac{1}{L}v_{sd} + \frac{1}{L}m\cos\delta\, v_{dc} \quad \textbf{(4-5)}$$

$$\frac{di_q}{dt} = -\frac{R}{L} i_q - \omega i_d + \frac{1}{L} m \sin\delta \, v_{dc} \quad \textbf{(4-6)}$$

$$\frac{dv_{dc}}{dt} = -\frac{v_{dc}}{C_{dc} R_c} - \frac{3}{2}\frac{1}{C_{dc}} m \cos\delta \, i_d - \frac{3}{2}\frac{1}{C_{dc}} m \sin\delta \, i_q \quad \textbf{(4-7)}$$

From Equations (4-5), (4-6) and (4-7) the state equation will have the general form:

$\dot{x}(t) = Ax(t) + Bu(t)$

$y(t) = Cx(t) + Du(t),$ (D=0)

After substituting the D-STATCOM parameters, and with C= [1 1 1], the following is obtained:

$$\frac{d}{dt}\begin{bmatrix} i_d(t) \\ i_q(t) \\ v_{dc}(t) \end{bmatrix} = \begin{bmatrix} -\frac{R}{L} & \omega & \frac{1}{L} m \cos\delta \\ -\omega & -\frac{R}{L} & \frac{1}{L} m \sin\delta \\ -\frac{3}{2}\frac{m}{C_{dc}} \cos\delta & -\frac{3}{2}\frac{m}{c_{dc}} \sin\delta & -\frac{1}{C_{dc} R_c} \end{bmatrix} \begin{bmatrix} i_d(t) \\ i_q(t) \\ v_{dc}(t) \end{bmatrix} + \begin{bmatrix} -\frac{1}{L} \\ 0 \\ 0 \end{bmatrix} [v_{sd}] \quad \textbf{(4-8)}$$

$$\frac{d}{dt}\begin{bmatrix} i_d \\ i_q \\ v_{dc} \end{bmatrix} = \begin{bmatrix} -\frac{R}{L} & \omega & \frac{1}{L} m \cos\delta \\ -\omega & -\frac{R}{L} & \frac{1}{L} m \sin\delta \\ -\frac{3}{2}\frac{m}{C_{dc}} \cos\delta & -\frac{3}{2}\frac{m}{c_{dc}} \sin\delta & -\frac{1}{C_{dc} R_c} \end{bmatrix} \begin{bmatrix} i_d \\ i_q \\ v_{dc} \end{bmatrix} + \begin{bmatrix} -\frac{1}{L} \\ 0 \\ 0 \end{bmatrix} [v_{sd}] \quad \textbf{(4-9)}$$

The Linear and Time Invariant dynamic matrix is:

$$A = \begin{bmatrix} -\frac{R}{L} & \omega & \frac{1}{L} m \cos\delta \\ -\omega & -\frac{R}{L} & \frac{1}{L} m \sin\delta \\ -\frac{3}{2}\frac{m}{C_{dc}}\cos\delta & -\frac{3}{2}\frac{m}{C_{dc}}\sin\delta & -\frac{1}{C_{dc}R_c} \end{bmatrix}$$

And the corresponding input matrix $B = \begin{bmatrix} -\frac{1}{L} \\ 0 \\ 0 \end{bmatrix}$ and the state vector $x^T = \begin{bmatrix} i_d \\ i_q \\ v_{dc} \end{bmatrix}$

where: ω is angular frequency of the rotating reference frame, *m* is the modulation index of the converter and δ is the phase difference between the output voltage of the D-STATCOM and the grid voltage, i_d and i_q are the direct axis and quadrature axis components of the line currents v_{sd} *i*s the AC voltages of the system on d-axis.

This mathematical model describes the averaged continuous state-space; it represents the steady-state behaviour of an ideal D-STATCOM referred to the d-q reference frame. This is the model that will be used as the basis for the design of the proposed inner control loop scheme. [56] has reported that greater accuracy can be obtained when static inverters are modelled using an orthogonal rotating, synchronised d-q reference frame, instead of a stationary coordinate system. Moreover, such a system simplifies the design of the control system compared to using abc or αβ

4.5 Steady state analysis of the D-STATCOM

Equation (4-8) is a set of dynamic equations of the D-STATCOM. The steady state equations for the D-STATCOM can be easily obtained by making the derivative terms of Equation (4-8) equal to zero. If it is assumed that the output AC voltages of the D-STATCOM ($m\cos\delta\, v_{dc}$) and ($m\sin\delta\, v_{dc}$) on d-axis and q-axis are represented by mu_dV_{dc} and mu_qV_{dc} respectively, then i_d, i_q and V_{dc} are the state variables of D-STATCOM and thus u_d and u_q represent the inputs signals to the D-STATCOM [168]. After the voltage and current are transformed into DC quantities, obtained by applying d-q frame reference ($v_{sd} = V_{sd}$, $v_{dc} =$

V_{dc}, $i_d = I_d$, $i_q = I_q$) the D-STATCOM steady state equations are obtained as follows:

$$\begin{bmatrix} -R & X & mu_d \\ -X & -R & mu_q \\ -3mu_d & -3mu_q & -\frac{2}{R_c} \end{bmatrix} \begin{bmatrix} I_d \\ I_q \\ V_{dc} \end{bmatrix} = \begin{bmatrix} V_{sd} \\ 0 \\ 0 \end{bmatrix} \quad \textbf{(4-10)}$$

From Equation (4-9) the solutions of I_d, I_q and V_{dc} are:

$$I_d = -\frac{R + \frac{3}{2}m^2 u_q^2 R_c}{R^2 + X^2 + \frac{3}{2}m^2 R R_c\left(u_d^2 + u_q^2\right)} v_{sd} \quad \textbf{(4-11)}$$

$$I_q = -\frac{R + \frac{3}{2}m^2 u_d u_q R_c}{R^2 + X^2 + \frac{3}{2}m^2 R R_c\left(u_d^2 + u_q^2\right)} v_{sd} \quad \textbf{(4-12)}$$

$$V_{dc} = -\frac{\frac{3}{2}m R_c\left(u_d R - u_q X\right)}{R^2 + X^2 + \frac{3}{2}m^2 R R_c\left(u_d^2 + u_q^2\right)} v_{sd} \quad \textbf{(4-13)}$$

Where $X\ is\ \omega L$

It seems from the steady state Equations (4-10) to (4-12), that I_d, I_q and V_{dc} do not include the magnitude of the capacitor of the DC link. The steady state performance of the system does not appear to depend on the DC capacitor size. However, The DC capacitor is used to maintain the DC voltage level on the DC side of converter.

The D-STATCOM parameters in Table 4-1 [159] were used to evaluate the steady state performance of the system according to Equations (4-10) - (4-12). The steady state response of the D-STATCOM variables I_d I_q and V_{dc} against AC voltage component based *q*-axis, u_q, at different values of the AC voltage

component based *d*-axis, u_d, are presented in Figure 4-4 (a), (b) and (c) respectively, with m =0.5

Table 4-1 D-STATCOM parameters [159].

D-STATCOM parameters	Values
Interfacing resistance and inductance	0.01 Ω 5.07 mH
DC capacitor	150 μF
The resistance of DC side R_C	61.273 kΩ
Switching frequency	5 kHz

As indicated from Figure 4-4 (b), generally, the reactive current I_q varies linearly with the AC voltage component u_q over the range of values $-1*10^{-3} < u_q < 1*10^{-3}$. The D-STATCOM provides the reactive current to the grid when the u_q has positive values, which means the D-STATCOM device is in a capacitive mode. When the u_q has negative values the D-STATCOM device is in an inducative mode, which mean it absorbs reactive current from the grid .

The DC side voltage V_{dc} decreases linearly as a function of AC voltage u_q (Figure 4-4 (c)). Relative to reactive current, there is very little change in the active current with change the AC voltage component u_q (Figure 4-4 (a)). This is because it acts only to regulate the DC voltage side at the required level and to offset converter losses.

Figure 4-5 shows the surface plots of the active current (I_d), reactive current (I_q) and DC voltage (V_{dc}) as a function of the AC voltage component on the q-axis (u_q) for different values of the AC voltage component on the d-axis (u_d). The Figures show that the surface trends of the active current, reactive current and DC voltage all show a slight change at high values of the AC voltage component based d-axis (u_d). where there are dramatic changes at low values of AC voltage commands on the d-axis (u_d) with respect to the AC voltage component based q-axis (u_q).

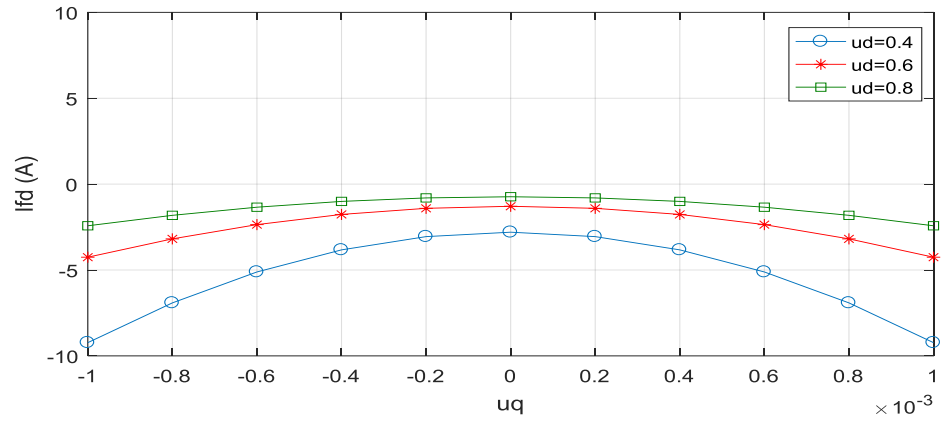

(a)

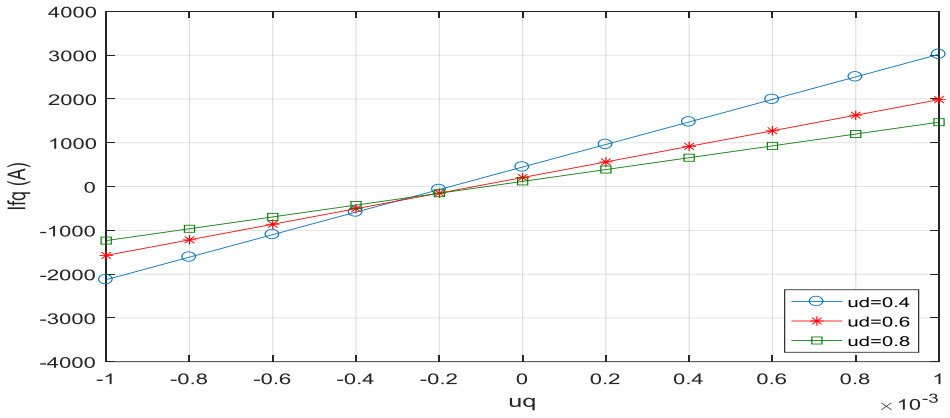

(b)

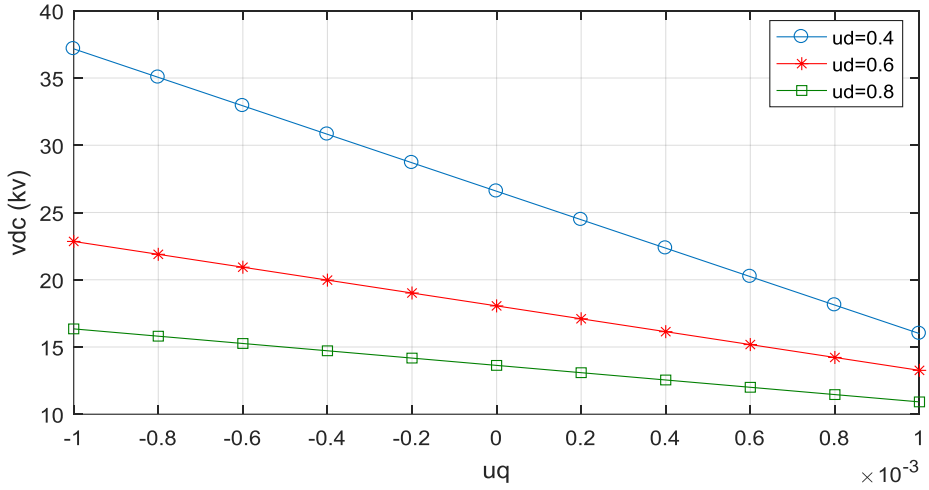

(c)

Figure 4-4 The steady state response of the D-STATCOM variables I_d I_q and V_{dc}

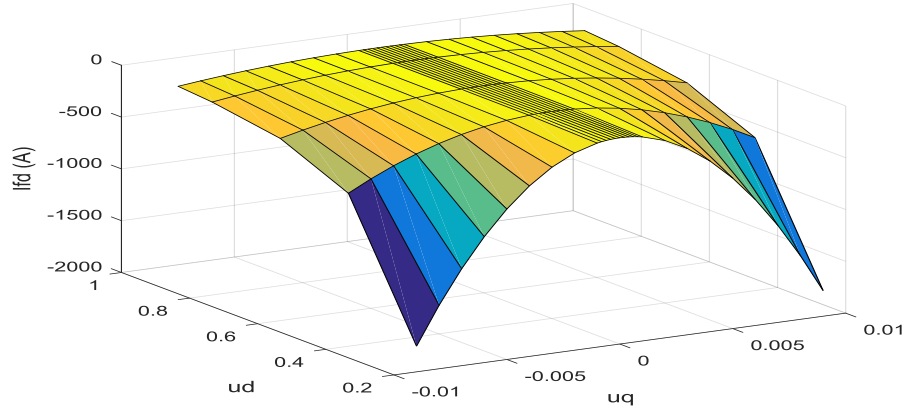

(a)

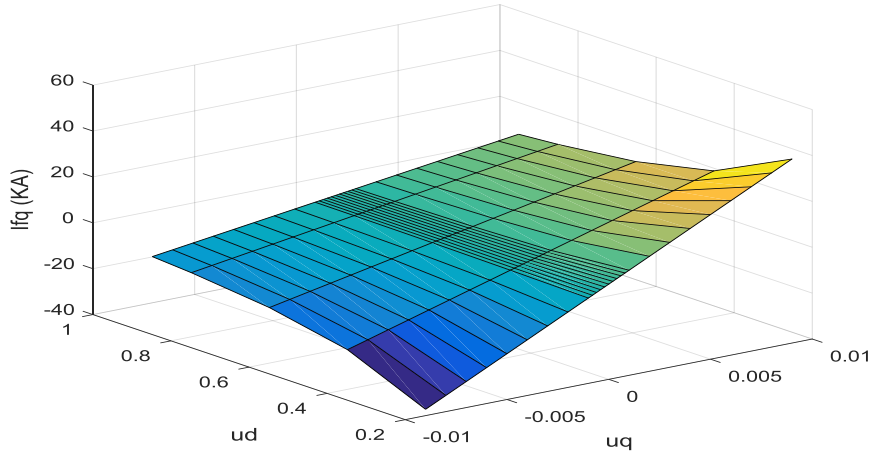

(b)

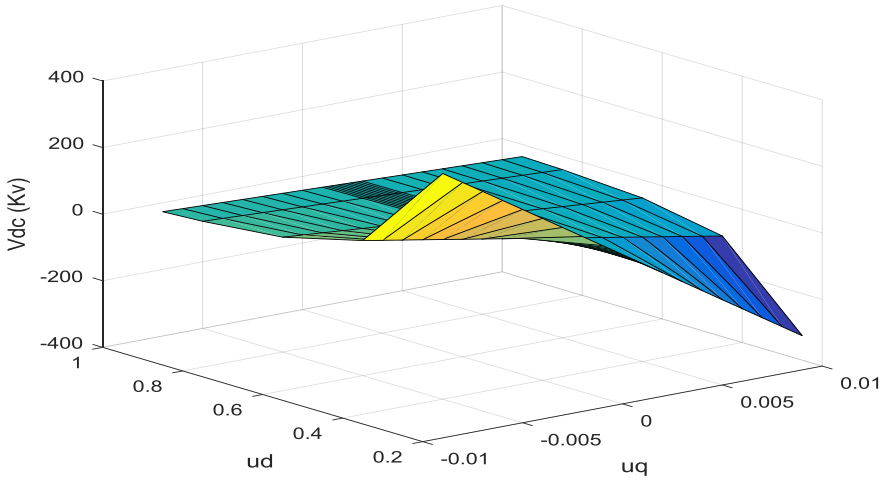

(c)

Figure 4-5 Surface plots of the active current (I_d), reactive current (I_q) and DC voltage (V_{dc}) with u_d and u_q

4.6 Control design of D-STATCOM

A vector control algorithm [169] based on a rotating reference theory of the (d-q) components has been adopted in this controller. The overall control scheme for the D-STATCOM controller is illustrated in Figure 4-6.

Firstly, the instantaneous measured grid voltage and current in a-b-c stationary components are transformed to the α-β reference frame. The angle θ for the rotating transformation of the voltage at the PCC is obtained from the voltage transformation (α-β) to carry out the synchronization with the system voltage. Then, another transformation is done from α-β to d-q, which rotates at the same speed as the AC grid quantities. The D-STATCOM controller is designed in three loops, the inner control loop, outer voltage control loop of the DC- link and the V_{PCC} control loop. The inner loop is the main current loop which will adapt to adjust I_d and I_q corresponding to the required active and reactive power demands. The output signal is used to calculate the reference voltage of the PWM (modulating voltage). Then, the modulating voltage is compared with the carrier signal to generate the required pulses of the IGBT switches. The DC-link voltage loop is needed to regulate the DC side voltage for proper performance of the D-STATCOM, and to set the flowing active current between the VSC and the AC grid. The V_{PCC} controller loop controls the grid voltage by adjusting the flowing reactive current between the VSC and the AC grid.

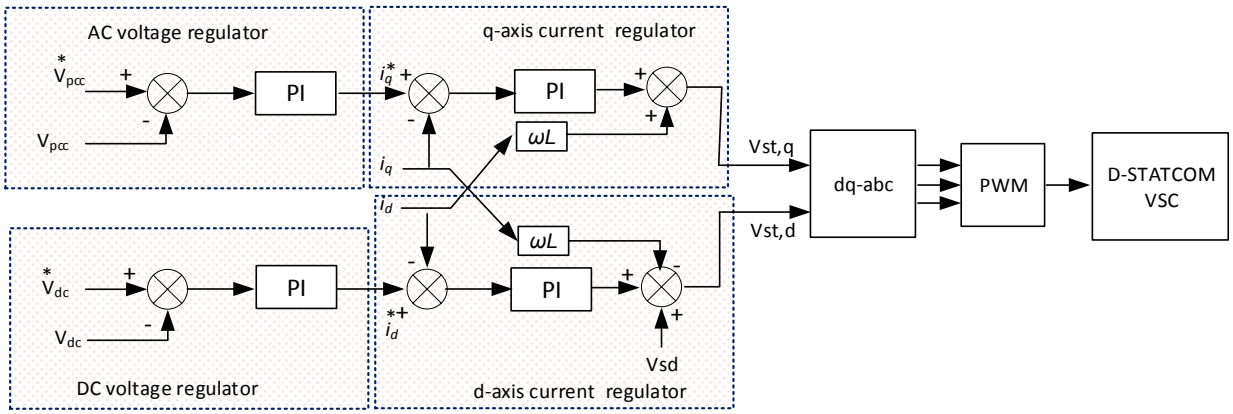

Figure 4-6 The overall control scheme for the D-STATCOM

4.6.1 Current control loop

The current control loop of the D-STATCOM controller can be designed from the dynamic equation of the D-STATCOM. The three phase dynamic differential equations of DSTATCOM are expressed in Equations (4-5) to (4-7).

Equations (4-5) to (4-7) demonstrate that the output currents of the D-STATCOM are due to the modulation of its output voltage. Nevertheless, the power converter in the (d-q) synchronously rotating reference frame controls the current via a two-output, two-input system which has cross-coupling between the reactive and active currents. To decouple the control and eliminate interaction between i_d and i_q, Equations (4-5) and (4-6) are written as:

$$v_{sd} = -\left(Ri_d + L\frac{di_d}{dt}\right) + \omega L i_q + v_{st,d}$$

$$v_{sq} = -\left(Ri_q + L\frac{di_q}{dt}\right) - \omega L i_d + v_{st,q} \qquad \textbf{(4-14)}$$

Where:

V_{sd} d component of supply voltage

V_{sq} q component of supply voltage

i_d d component of Line current

i_q q component of Line current

$V_{st,d}$ d component of DSTATCOM output voltage

$V_{st,q}$ q component of DSTATCOM output voltage

R internal resistance of the coupling reactor

L coupling reactor

ω angular frequency of the rotating reference frame

The i_d component is used to regulate the DC- voltage loop while the reactive demand and PCC voltage loop is controlled by the i_q component. The PI controller to be used to control the D-STATCOM currents is based on these considerations,

If the d-component is aligned to the supply source, voltage $V_{sq=0}$, Equation (4-14) can be rewritten as:

$$v_{sd} = -\left(Ri_d + L\frac{di_d}{dt}\right) + \omega Li_q + v_{st,d}$$

$$0 = -\left(Ri_q + L\frac{di_q}{dt}\right) - \omega Li_d + v_{st,q} \quad \textbf{(4-15)}$$

To control the d and q axis currents, the D-STATCOM has to produce associated output voltages according to the reference voltage signals determined from Equation (4-15). The associated output voltages are given as:

$$V^*_{st,d} = V'_d + (-\omega Li_q + V_{sd})$$

$$V^*_{st,q} = V'_q + (\omega Li_d) \quad \textbf{(4-16)}$$

Where,

$$V'_d = Ri_d + L\frac{di_d}{dt}$$

$$V'_q = Ri_q + L\frac{di_q}{dt} \quad \textbf{(4-17)}$$

The Laplace transformation applied to Equation (4-17), gives:

$$V'_d(s) = Ri_d(s) + SLi_d(s)$$

$$V'_q(s) = Ri_q(s) + SLi_q(s) \quad \textbf{(4-18)}$$

V'_d and V'_q will calculated from the current control as applied in Equation (4-16) to compute the reference voltages of the PWM. The current control loop can be designed according to:

$$\mathrm{G}(S) = \frac{i_d(S)}{V'_d(S)} = \frac{i_q(S)}{V'_q(S)} = \frac{1}{SL+R} \quad \textbf{(4-19)}$$

The control loop design is illustrated in Figure 4-7. A connecting inductor L=10.00 mH with R=0.1 ohm were used to design the PI controller, where *I* in the figure represents the current on the d and q axis and V' represents the voltage reference on the d and q axis. An anti-aliasing filter with a cut-off frequency of 1500 Hz was used to remove the high frequency switching noise. A 5-kHz switching frequency was used and this was also used as the sampling frequency.

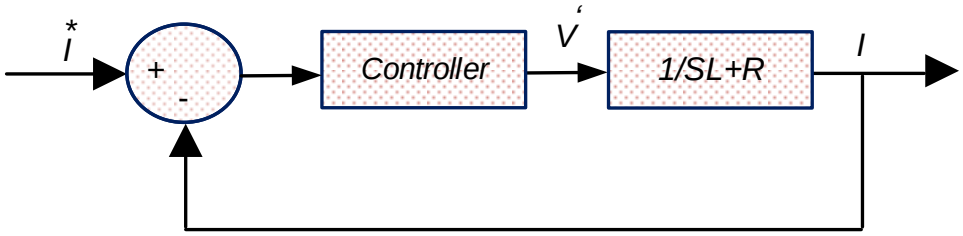

Figure 4-7 closed current control loop

The design of the control loop was carried out using standard procedure: MATLAB SISO tool box with 110 Hz bandwidth.

4.6.2 V_{PCC} voltage control loop

The D-STATCOM should produce the desired amount of the reactive power to the AC grid to control the voltage magnitude at the PCC as in the power grid shown in Figure 4-13. As the change in the voltage at PCC is based on the variations of the current flowing from source to PCC point, the control loop design of the V_{PCC} is derived using the small signal model which is detailed in Appendix A and presented in Equation (4-20) [170].

$$\frac{\Delta V_{PCC}}{\Delta I_q} = \omega . L \qquad \textbf{(4-20)}$$

where, ω is the angular frequency of the rotating reference farm, ΔV_{PCC} is the change in the voltage at PCC, ΔI_q is the variations of the reactive current component passing in the line.

As in the current control loop, the low pass filter (anti-aliasing filter) was used in the loop design of the Figure 4-9 with a cut-off frequency of 1500 Hz. The design of the control loop was carried out using standard procedure: MATLAB SISO tool box with 10 Hz bandwidth.

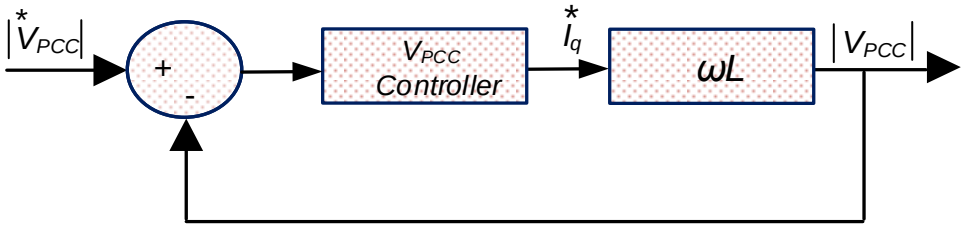

Figure 4-8 V_{PCC} control loop

4.6.3 DC–link voltage control loop

To design the voltage control loop of the DC-side, the D-STATCOM was represented as a current source, as explained in Chapter Three. The voltage of the DC-side was based on power flowing from source to convertor.

The current flowing from the current source was:

$$I_{dc} = 3\frac{V_d I_{d+}\, V_q I_q}{V_{dc}} = C_{dc}\frac{dV_{d.c}(t)}{dt} \qquad \textbf{(4-21)}$$

As stated earlier, if the d-component is aligned to the supply source voltage, $V_{q=0}$ and Equation (4-19) is written as:

$$I_{dc} = 3\frac{V_d I_d}{V_{dc}} = C_{dc}\frac{dV_{d.c}(t)}{dt} \qquad \textbf{(4-22)}$$

The modulation index (m) is defined as the ac voltage (rms value) of the converter to the DC-side voltage.

$$m = \frac{2\sqrt{2} \ . \ V_d}{V_{dc}} \quad \textbf{(4-23)}$$

$$V_d = \frac{m.V_{dc}}{2\sqrt{2}} \quad \textbf{(4-24)}$$

From Equations (4-22) and (4-24)

$$I_{dc} = 3\frac{m.I_d}{2\sqrt{2}} = C_{dc}\frac{dV_{dc}}{dt} \quad \textbf{(4-25)}$$

The Laplace transformation applied to Equation (4-25), gives:

$$I_{dc} = 3\frac{m.I_d(S)}{2\sqrt{2}} = SC_{dc}V_{dc}(S) \quad \textbf{(4-26)}$$

The voltage control loop can be designed according to:

$$\mathrm{G}(S) = \frac{V_{dc}(S)}{I_d(S)} = \frac{3m}{2\sqrt{2}.SC_{dc}} \quad \textbf{(4-27)}$$

The block diagram of the DC-side voltage loop design is shown in Figure 4-9. An anti-aliasing filter with a cut-off frequency of 120 Hz is used to remove the high frequency switching noise. The cut-off frequency is chosen as a compromise between the speed of the dynamic response of the controller and the filtering of high frequency switching noise. A capacitor with C_{dc}=1000 µF was used in the design of the PI controller for the voltage control loop.

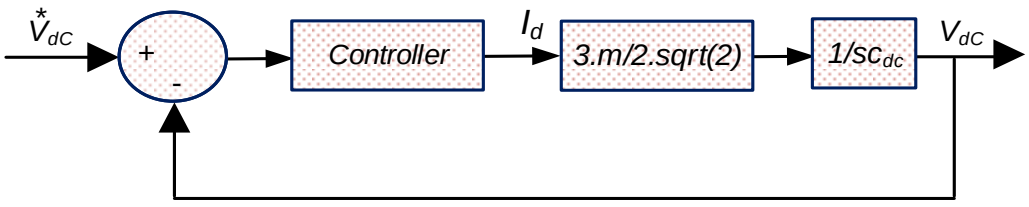

Figure 4-9 closed voltage control loop

The design of the control loop was carried out using standard procedures: MATLAB SISO tool box with 10 Hz bandwidth.

4.6.4 DC –link voltage control loop based on fuzzy logic

The performance of the VSC of the D-STATCOM is directly affected by the DC-side voltage. Thus, for proper performance of the D-STATCOM, it is important to keep the DC voltage side close to the reference level. A conventional PI compensator may be used in the DC control loop to adjust the DC side voltage to the reference level by processing the error signal between the actual and reference values of the DC side voltage. In general, standard PI controllers will give a satisfactory response when the system parameters are pre-defined and subject to minimum disturbances. However, if the model's initial conditions vary, an adaptive PI controller which tunes the controller parameters may be essential for good performance. Fuzzy logic control is particularly conducive to more complex control structures, by using functional objectives and linguistic descriptions, rather than mathematical equations, to define the system's mission and the relationship between the input information and the output action [171][172]. The structural design of the DC side with a fuzzy-PI controller is illustrated in Figure 4-10. The scaling terms G1, G2, G3 and G4 are introduced here to normalize the input and output signals [173].

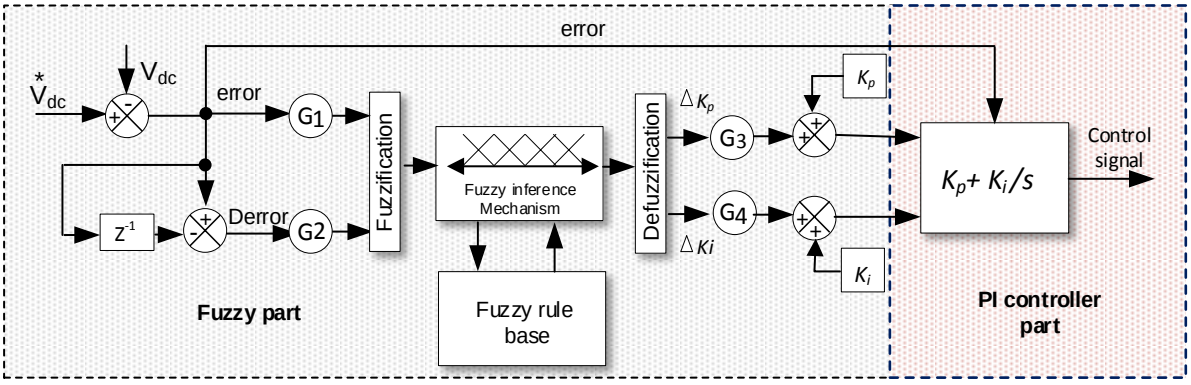

Figure 4-10 Structural design of the fuzzy -PI controller based DC voltage side

Fuzzy logic controller (FLC) has the following advantages over the conventional controllers:

- simplicity and flexibility in the design
- The problems can be handled with empirical and estimated data
- The nonlinear functions can be modelled of arbitrary complexity

- The fuzzy control model can be developed according to the system requirements.
- It can be covered a wider range of operating conditions
- A self-organizing fuzzy controller can automatically refine an initial approximate set of fuzzy rule

FLC involves four principal components: “a fuzzification interface, an inference mechanism, a rule base, and a defuzzification interface” [174]. The fuzzy logic controller design requires precise selection of suitable inputs and outputs for building each and every one of the four components of FLC. The four components of the fuzzy logic controller based on the DC voltage regulator will be explained in the next section. The strategy of the fuzzy-tuned PI controller is stimulated during the disturbance times and when the DC voltage amplitude is in the steady state, the PI compensator gains are kept at their original values. A more detailed explanation of the control design of the fuzzy logic is found in [174]. The error signal between the actual and reference value of the DC side voltage and the deviation in the error as a function of the input signals of the PI-fuzzy supervisor are:

$$error(i) = (V_{dc_ref} - V_{dc}) \quad \textbf{(4-28)}$$

$$Derror(i) = error(i) - error(i-1) \quad \textbf{(4-29)}$$

Where, $error(i)$ and $Derror(i)$ is the error and deviation in the i^{th} iteration. The output signal of the PI-fuzzy was the deviation in the controller gains (ΔK_p and ΔK_i).

$$K_p = K_{pref} + \Delta K_p \quad \textbf{(4-30)}$$

$$K_i = K_{iref} + \Delta K_i \quad \textbf{(4-31)}$$

K_{pref} and K_{iref} are the normal steady state values decided on, and tuned from the standard procedure by the MATLAB SISO tool box. A Sugeno fuzzy logic based supervisor control is designed to adjust the gain of the PI controller used

for the DC link voltage control. The fuzzy supervisor is designed in such a way that the gains ΔK_p and ΔK_i are the outputs of the fuzzy logic supervisor, which are added to the reference gains (K_{pref} and K_{iref}) during changes in load. Hence, the design process is intuitively stable and the system's response can be further enhanced and improved by the Sugeno/fuzzy controllers

ΔK_p and ΔK_i are normalised gain perturbations obtained directly from the Sugeno defuzzification process equations (Equations (4-32) and (4-34)). Thereafter the gain perturbations are scaled to suitable values which will generate the desired system response using the time invariant factors G_3 and G_4.

A. Fuzzification

Fuzzification is the first part in designing the FLC and includes the process of converting the real input signals into a linguistic variable. Each range of the input represents a membership function. There are a number kinds of membership functions: including triangular, trapezoidal, singleton, Gaussian and piecewise linear. It is decided to select five triangular membership functions for each input: Nlarge (Negative large), Nmedium (Negative medium), Z(Zero), Pmedium (Positive medium) and Plarge (Positive large). The triangular membership functions are very fast to run in real-time applications thus making them excellent candidates. The limits of the membership functions (i.e. LHS and RHS) are trapezoidal to retain the denominator in, i.e., Equations (4-33) and (4-35), thus retaining system stability. This allows the Sugeno fuzzy controller to have added value without large gain changes. The number of functions was empirically verified so that the minimum number of functions was used. The input membership functions have been tuned according to the system requirements and the membership values for each membership function ranged between (0-1). Figure 4-11 shows the membership functions for each error and the deviation of error signals. It is noticed that one or two membership functions will be initiated for each error or deviation in error signals.

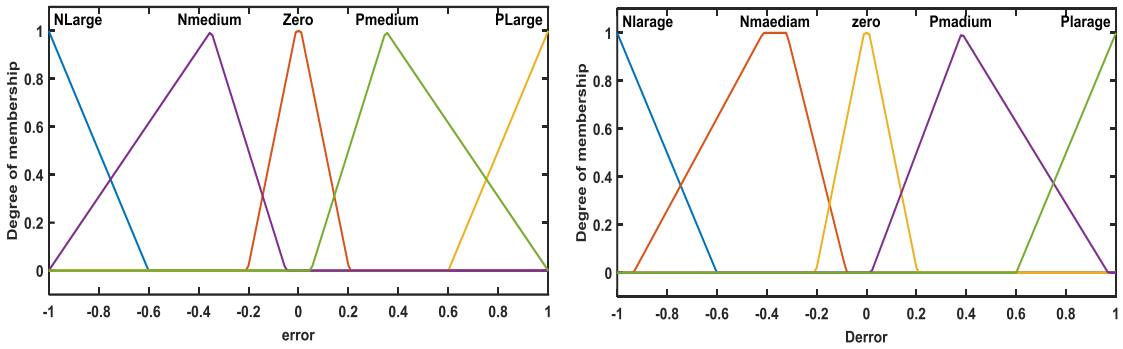

(a) (b)

Figure 4-11 (a) Membership functions for error input signal. (b) Membership functions for deviation in error signal

B. Inference Mechanism

The main task of the inference mechanism is to decide the appropriate rules for the status of the system dependent on the membership functions of the input signals. "*Once the rules are determined, the certainty of the control action is ascertained from the membership values*" [175] .This is known as the premise quantification.

Finally, after tis part, a set of linguistic control rules involving the necessary information would be ascertained as valid for the system. The database of the FLC which contains the rule data is the rule base. A real control action is activated from the output of the fuzzy inference mechanism. The rules data is normally described by the format of "(IF) and (THEN)" statements. For example:

The error is defined as $e(t)$ and the derivative of the error is defined as Derror $=e^*(t)$

For the ΔK_p every rule has the following form:

Rule 1: IF $e(t)$ is A_{11} AND $e^*(t)$ is B_{11}

then $\Delta K_{p1} = a_{11}.e(t) + b_{11}.e^*(t) + c_{11}$

Rule 2: IF $e(t)$ is A_{12} AND $e^*(t)$ is B_{12}

then $\Delta K_{p2} = a_{12}.e(t) + b_{12}.e^*(t) + c_{12}$

Rule k: IF $e(t)$ is A_{1k} AND $e^*(t)$ is B_{1k}

then $\Delta K_{pk} = a_{1k}.e(t) + b_{1k}.e^*(t) + c_{1k}$

So,

$$\Delta K_{p(e,e^*)} = \frac{\sum_{\sigma=1}^{k} \prod_{jq} A_{1j}(e).B_{1q}(e^*).\Delta K_{p\sigma}}{\sum_{\sigma=1}^{k} \prod_{jq} A_{1j}(e).B_{1q}(e^*)} \quad \textbf{(4-32)}$$

Subject to the constraint:

$$\sum_{\sigma=1} \prod_{jq} A_{1j}(e).B_{1q}(e^*) > \varepsilon_p \quad \textbf{(4-33)}$$

For the ΔK_i every rule has the following form:

Rule 1: IF $e(t)$ is A_{21} AND $e^*(t)$ is B_{21}

then $\Delta K_{i1} = a_{21}.e(t) + b_{21}.e^*(t) + c_{21}$

Rule 2: IF $e(t)$ is A_{22} AND $e^*(t)$ is B_{22}

then $\Delta K_{i2} = a_{22}.e(t) + b_{22}.e^*(t) + c_{22}$

Rule k: IF $e(t)$ is A_{2k} AND $e^*(t)$ is B_{2k}

then $\Delta K_{ik} = a_{2k}.e(t) + b_{2k}.e^*(t) + c_{2k}$

So ,

$$\Delta K_{i(e,e^*)} = \frac{\sum_{\sigma=1}^{k} \prod_{jq} A_{2j}(e).B_{2q}(e^*)\Delta K_{i\sigma}}{\sum_{\sigma=1}^{k} \prod_{jq} A_{2j}(e).B_{2q}(e^*)} \quad \textbf{(4-34)}$$

Subject to the constraint:

$$\sum_{\sigma=1} \prod_{jq} A_{2j}(e).B_{2q}(e^*) > \varepsilon_i \quad \textbf{(4-35)}$$

Where: $j, q \leq k$ also $\varepsilon_p > 0 \quad and \quad \varepsilon_i > 0$, and a, b and c are all constants.

C. The rule base

The importance part of the FLC design is forming the rule base. In a FLC, the rule base defines the dynamic behaviour of fuzzy control system in an expert way by a set of rules based on linguistic variables. Table 4-2 and Table 4-3 show a set of fuzzy rules applied, which describe the connection between the input signals ($error$ and $Derror$) and output signal (ΔK_p and ΔK_i) respectively. The surface viewers of the fuzzy control applied in the model are illustrated in Figure 4-12 (a) and (b) respectively.

Table 4-2 Rule base for the deviation in K_p

error / Derror	Nlarge (B_{15})	Nmedium (B_{14})	Zero (B_{11})	Pmedium (B_{12})	Plarge (B_{13})
Nlarge (A_{15})	High	High	Med	Low	Zero
Nmedium (A_{14})	High	High	Low	Zero	Low
Zero (A_{11})	Med	Zero	Zero	Zero	Med
Pmedium (A_{12})	Med	Zero	Low	High	High
Plarge (A_{13})	Zero	Low	Med	High	High

Table 4-3 Rule base for the deviation in K_i

error / Derror	Nlarge (B_{25})	Nmedium (B_{24})	Zero (B_{21})	Pmedium (B_{22})	Plarge (B_{23})
Nlarge (A_{25})	Low	Med	Zero	Zero	Zero
Nmedium(A_{24})	Low	Low	Zero	Zero	Zero
Zero (A_{21})	High	High	Zero	Med	High
Pmedium(A_{22})	Zero	Zero	Zero	Low	Low
Plarge (A_{23})	Zero	Zero	Zero	Med	Low

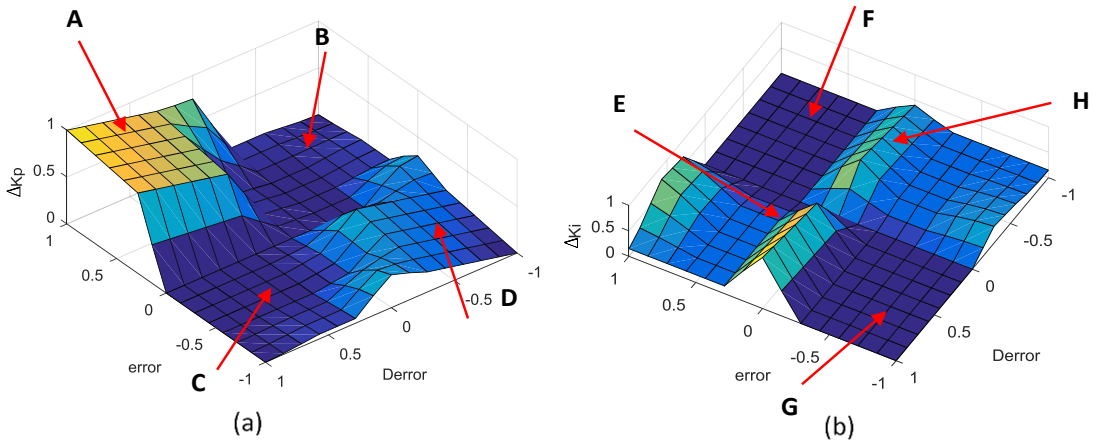

Figure 4-12 Rules Surface

According to the surface plots in Figure 4-12, the tuning of ΔK_p and ΔK_i are based on some important points.

- For large values of $error$ and $Derror$, then $\Delta K_p$is increased (area A) and vice versa, which mean the DC side voltage moves away from the target point.
- When the $error$ is negative in value and $Derror$ is positive, ΔK_p is set to zero and vice versa (areas B and C). which means approaching the steady state.
- When the $error$ and $Derror$ have big values, $\Delta K_i$is set to zero, which help to prevent control saturation. (Areas F and G).
- When the value of the $error$ approaching to zero, ΔK_i is active and $\Delta K_i$is increasing to minimize overshoot and to reduce steady-state error. (Areas E and H).

The main effect of applying a Sugeno fuzzy logic with PI inside the D-STATCOM controller is that by varying the parameters of the quantities contained in the fuzzy rules, the fuzzy control surface is improved. Consequently, the strength of the PI controller coefficients K_p and K_i can be adapted. For instance, Figure 4-12 (a) depicts the fuzzy control surface used to adjust the K_p parameter, the effect of the control parameter is changed to an extreme when error and Derror have large values, and decreased when error and Derror are near zero, approaching the

steady state. Furthermore, observe that the transition between the areas is done efficiently (area D), so that a kind of gain scheduling is accomplished. These points are confirmed clearly in the next section in the simulation results when system performances are compared.

The fuzzy inference can be accomplished with a variety of methods such as: “Mamdani method, Larsen method, Tsukamoto method, and the Sugeno style inference method” [176]. The Mamdanie and Sugeno have been widely used in FLCs, and the Sugeno method [177] has been chosen and applied in this thesis. The output memberships of the fuzzy controller are taken as constant and/or linear memberships and are represented as High, Med, Low and Zero for deviations in both K_p and K_i. Using information obtained from the rule base, the inference mechanism will determine both the rule and its level of certainty. Defuzzification is the name given to the method whereby the fuzzy results are converted into swift and decisive control actions, see next section.

D. Defuzzification

Defuzzification is the processing of the rule and converting the output linguistic constant’s memberships into crisp numerical data, such that “the fuzzy control action is transformed to a non-fuzzy control action” [175]. There are different algorithms for defuzzification operation. The commonly used operation is Centre of Gravity (COG) which has been used in this study.

$$\text{COG is defined as } = \frac{\sum_{\sigma=1}^{k}[u_i\mu_i]}{\sum_{\sigma=1}^{k}[\mu_i]} \qquad \textbf{(4-36)}$$

where u is the output variable, μ is the membership function after accumulation, i is index and k is the number of the output memberships.

4.7 Simulation of a distribution system with a sudden load change

4.7.1 Simulation without D-STATCOM

To illustrate the reactive power possibilities of the D-STATCOM, the performance of a simple circuit diagram without D-STATCOM Figure 4-13 is simulated. Figure 4-14 and Figure 4-15 show the simulation results obtained by SIMULINK/MATLAB. The circuit parameters are depicted in Table 4-4. The voltage at the PCC is indicated in first trace of Figure 4-14. The magnitude of the voltage sag at t = 0.15 s can be clearly observed in Figure 4-15. The initial value is very close to 1 p.u when carrying Load 1, at 0.15 second, Load 2 is turned on by connecting the circuit breaker (C.B1). A sudden drop in V_{PCC} from 0.988 p.u to 0.830 p.u occurs due to the increase in load. The supply current is raised as shown in the second trace of Figure 4-14.

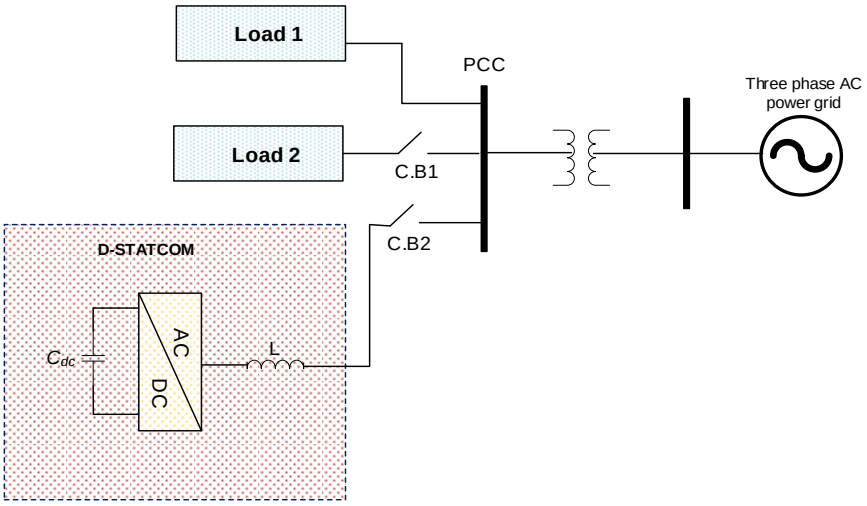

Figure 4-13 System structure of simulation model

Table 4-4 System parameters of simulation model

Parameters	Values
Supply voltage	20 kV, 50 Hz
Transformer	20 kV/380 V
Load1	380 V,50 Hz, 25 kW
Load 2	380 V,50 Hz, 15kW, 4.6 kVR

VSC	IGBTs based 3 arms 6 pulses, Carrier frequency =1.65kHz, Sample time =50μs
DC voltage	700 V
DC Capacitor	1000 μF

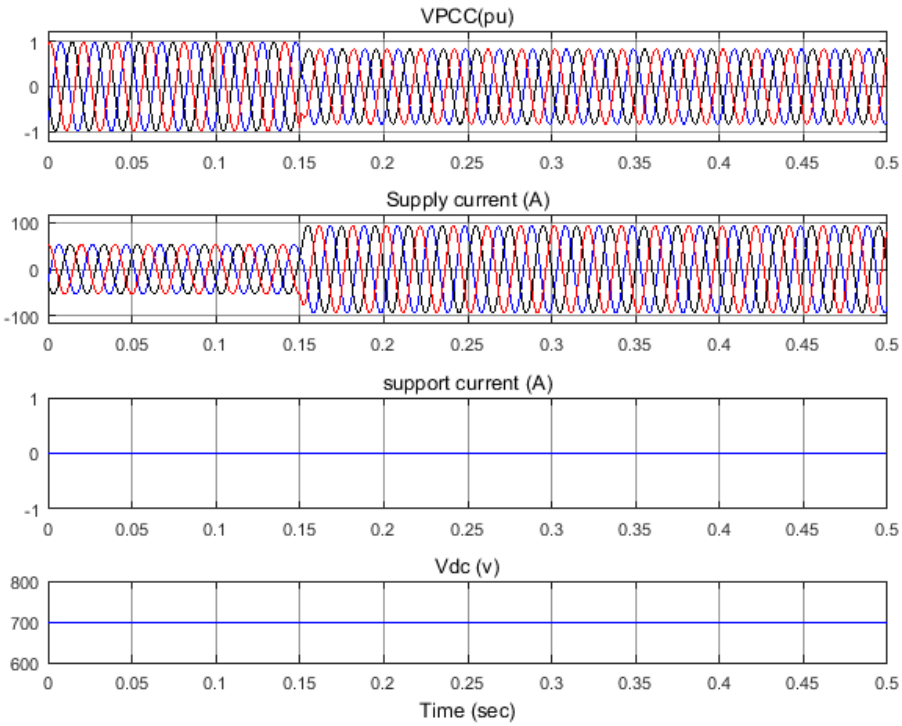

Figure 4-14 Simulation results without D-STATCOM

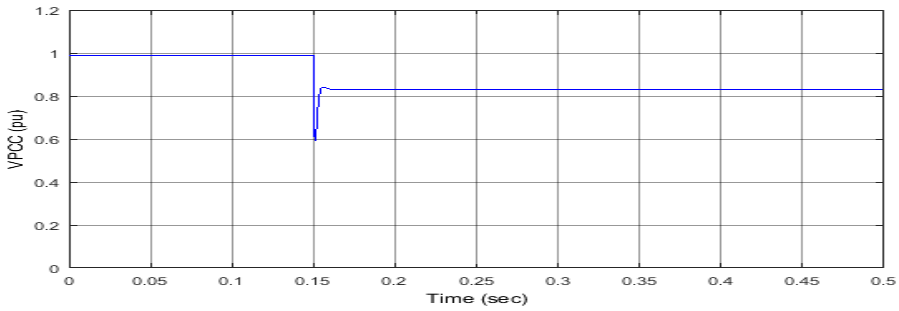

Figure 4-15 Voltage magnitude at PCC

4.7.2 Simulation with D-STATCOM.

According to Section 3.2.3 (Steady State Analysis of D-STATCOM based Distribution System), the maximum load active power ($P_{l,desired}$), and minimum source voltage ($V_{s,min}$) of the system with the given parameters in the Table 4-4 are 35.83 kW and 16.94 kV, respectively. ± 26.5 kVA D-STATCOM is chosen for load voltage compensation in this system. This D-STATCOM can regulate the load voltage as 380 V when the source voltage is more than 17.00 kV. In addition, it can be applied to regulate the voltage of the load as 380 kV when the load active power is more than 15 kW. The required reactive power for different source voltages is given in Table 4-5. Meanwhile, the required reactive power for different load power is given in Table 4-6.

Table 4-5 Required reactive power for different sources

Source voltage (kV)	Required reactive power (Kvar)	Required reactive power (Kvar)
	Unity power factor	0.9 power factor
27.00	-12.0855	4.8648
26.00	-8.7705	8.1798
25.00	-4.7370	12.2133
24.20	0.0022	16.9525
20.00	8.2346	25.1849
19.00	8.5321	25.4824
18.00	8.8295	25.7798
17.00	9.1270	26.0773

Table 4-6 Required reactive power for different loads

Load active Power (kV)	Required reactive power (Kvar)	Required reactive power (Kvar)
	Unity power factor	0.9 power factor
15	-22.6831	-15.3497
20	-20.9731	-11.1953
25	-18.1021	-5.8799

30	-13.4554	1.2113
35	-4.7278	12.3833

The reactive power possibilities of the D-STATCOM are demonstrated by simulating the circuit diagram (Figure 4-13), by connecting the conventional D-STATCOM (without energy storage at the DC side) at the PCC point by turning on the circuit breaker (C.B2). To examine the dynamic response of the proposed fuzzy-tuned PI with D-STATCOM controller, two test cases are performed and compared to conventional P and PI controllers with and without filter. The two cases have been examined with conventional D-STATCOM starting with the general structure of a vector control (Figure 4-6) as below:

Case 1: PI- controller with K_p tuned with fuzzy control and K_i parameter is fixed.

Case 2 : PI controller with both K_p and K_i tuned with fuzzy control.

After 0.15 second, the D-STATCOM is coupled to the system at the PCC, the voltage at the PCC and the DC side with P controller and P with added filter are compared as shown in Figure 4-16 and Figure 4-17 respectively. Although, the P controller with filter gives a better dynamic response, it gives higher overshoot in the voltage at the PCC and the DC side voltage is still uncontrolled and the DC side voltage of the D-STATCOM is actually higher than the reference voltage (700 Volt). However, this problem can be eliminated by using the PI controller. The voltage response from the PI controller at the PCC and DC side with and without filter are shown in Figure 4-18 and Figure 4-19 respectively. As can be seen in these figure, the DC side voltage response is not in excess of the reference value and it has a rather acceptable response but there are still oscillations and overshoots in the voltage. This may lead to instability of the power system. When the fuzzy controller with tuning of the K_p parameter, with the K_i parameter fixed, is applied, the voltage responses are as shown in Figure 4-20 and Figure 4-21 respectively. The fuzzy tuned PI can be seen to provide a good response. Similar observations with fewer dips, swells and oscillations are seen with the fuzzy tuned PI for both K_p and K_i in Figure 4-20 and Figure 4-21. It is

noticed that both fuzzy controllers (only tuning K_p and tuning both K_p and K_i) give a faster response of voltage at the PCC with a shorter settling time and oscillation against both P and PI controllers. Clearly the fuzzy tuned PI for both K_p and K_i offers a good response of the DC side voltage with no oscillation and ripple, and a faster response compared to fuzzy only tuning of K_p. Additionally, a clear reduction in the dip can be seen in the DC side voltage at the beginning and at time = 0.15 s.

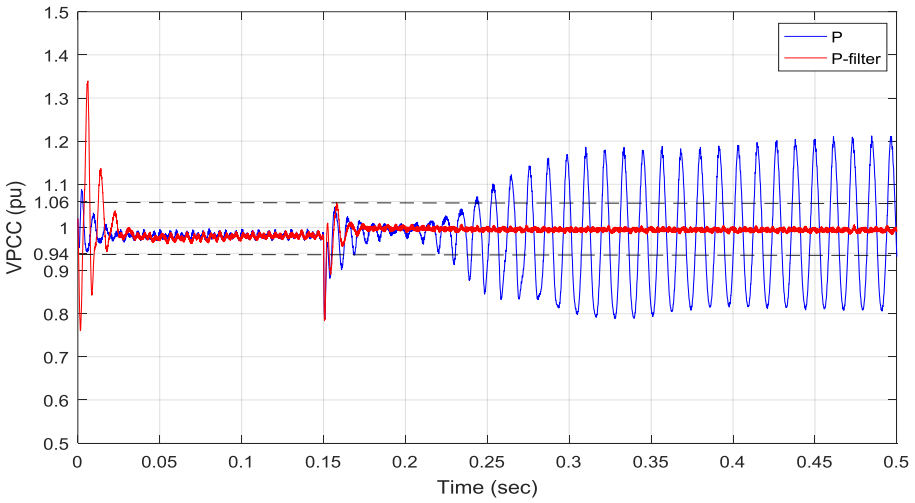

Figure 4-16 Voltage at PCC with P controller

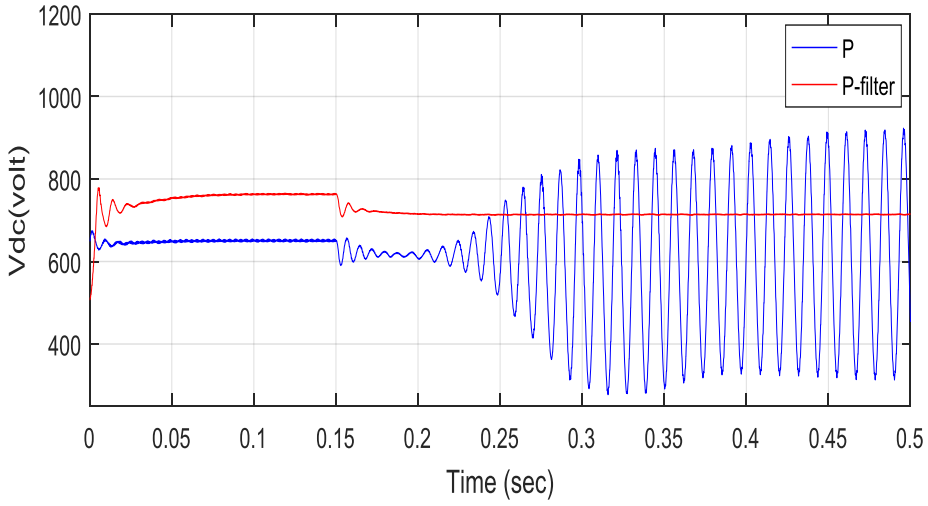

Figure 4-17 DC side voltage with P controller

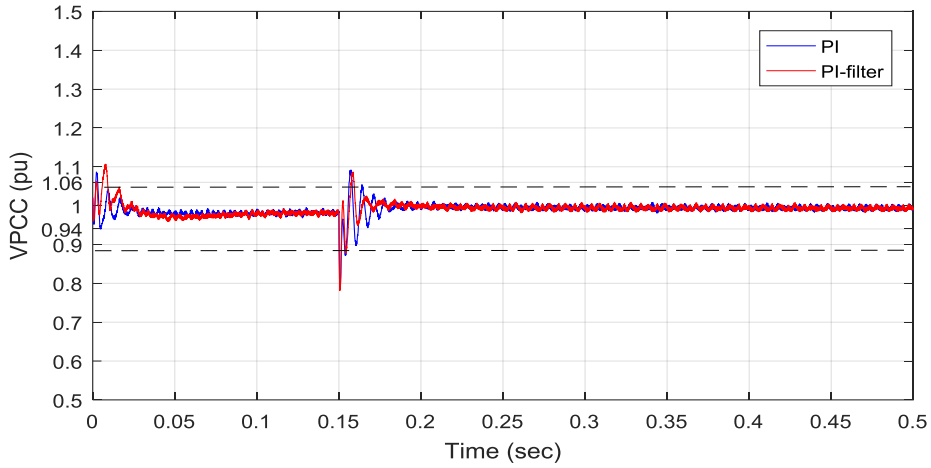

Figure 4-18 Voltage at PCC with PI controller

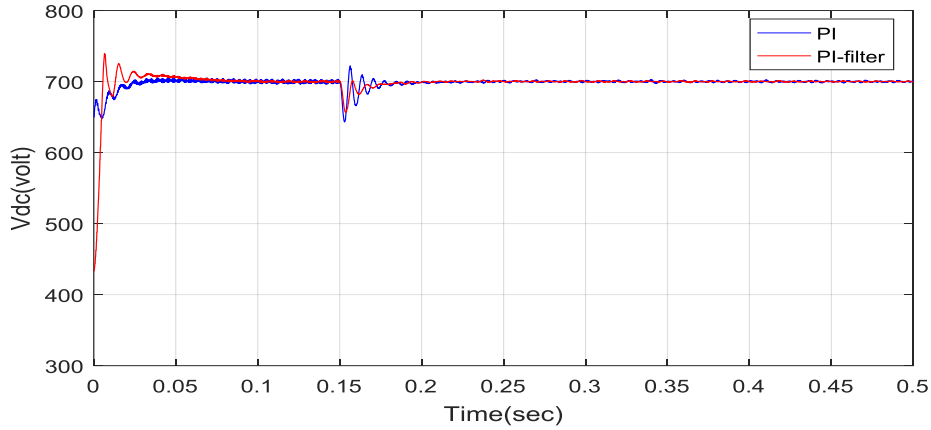

Figure 4-19 DC side voltage with PI controller

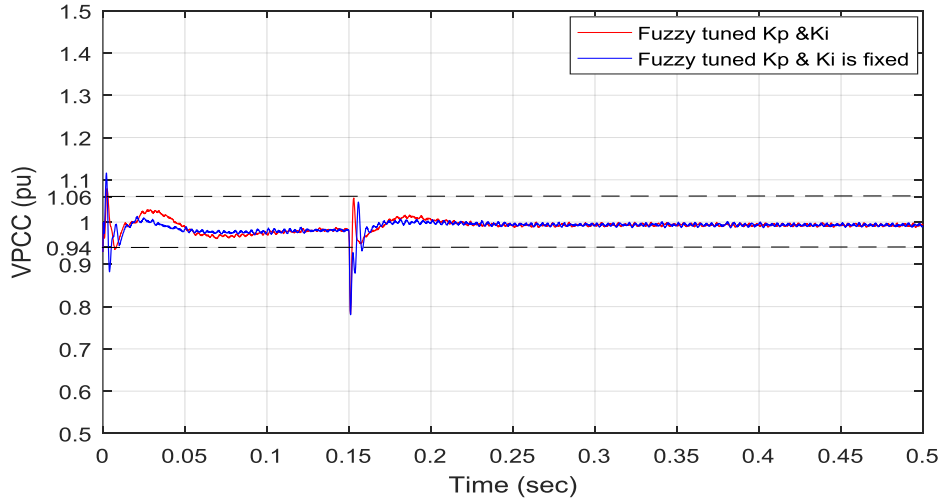

Figure 4-20 Voltage at PCC with fuzzy controller

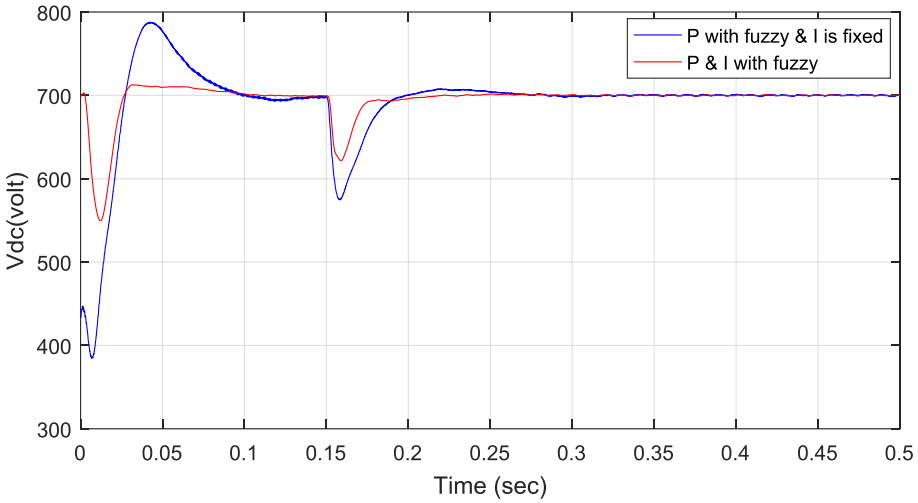

Figure 4-21 DC-side voltage with fuzzy controller

Although the linear PI controller gives a rather acceptable result under normal conditions, the point is that the fuzzy controller activates a control system that captures the nonlinearities of the Microgrid online. Thus, the nonlinear fuzzy controller is proposed for the D-STATCOM controller. The simulation results (Figure 4-22) with D-STATCOM support are achieved by using SIMULINK/MATLAB. After 0.15 second the D-STATCOM is coupled to the system, as a result, the voltage at the DC side displayed in the fourth trace (Figure 4-22) is controlled to the desired value of 700V. D-STATCOM reactive power is represented by the support current in the third trace of Figure 4-22. By comparing the voltage at the PCC obtained from the simulated circuit without D-STATCOM in Figure 4-15 to the voltage at PCC in Figure 4-20 (circuit with D-STATCOM), showed that the PCC voltage is improved when the D-STATCOM is linked to the circuit. The output voltage of the convertor (VSC) is shown in the fifth trace (Figure 4-22). The supply current of the source with D-STATCOM only can be clearly observed in Figure 4-23.

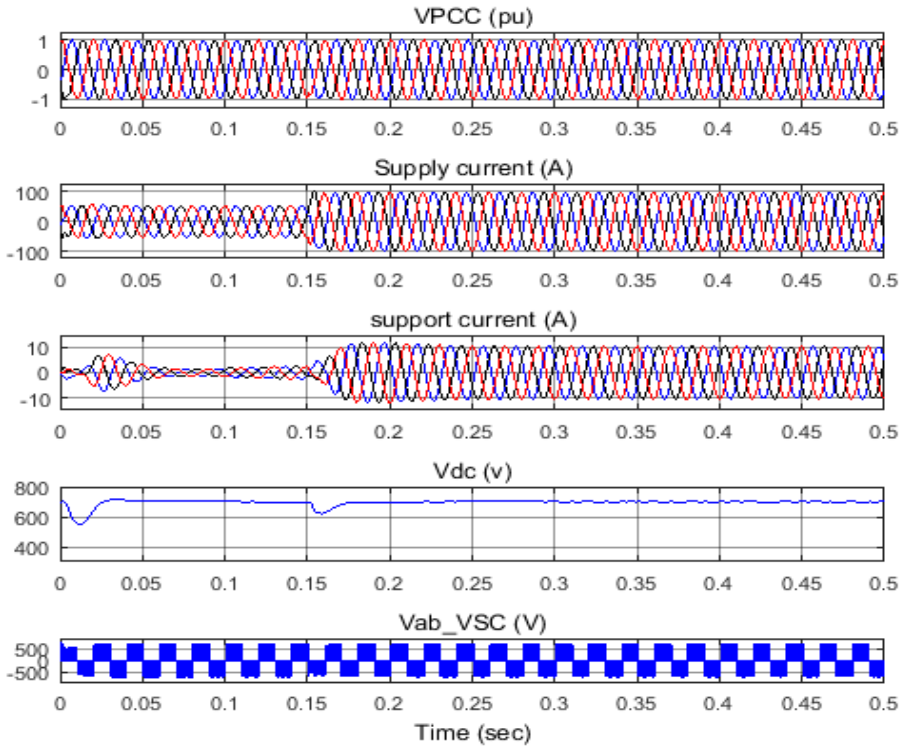

Figure 4-22 Simulation results with D-STATCOM only

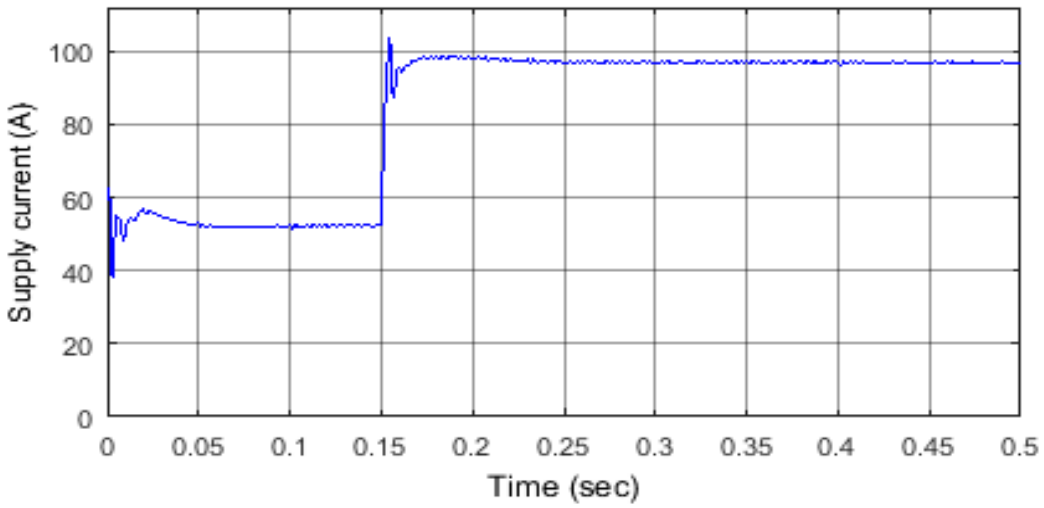

Figure 4-23 Supply current (simulation of the system with D-STATCOM only)

From the d and q components of D-STATCOM's current, shown in Figure 4-24, it can be seen, that the I_d current component is zero as indicated in the first trace. The I_q current component nearly reached -10 A when the second load was turned on, as seen in the second trace. The results show that the conventional D-STATCOM has a limited capability to support the voltage when exchanging only

reactive power with the system. However, D-STATCOM performance can be improved by adding an energy storage system device to D-STATCOM to support both active and reactive power.

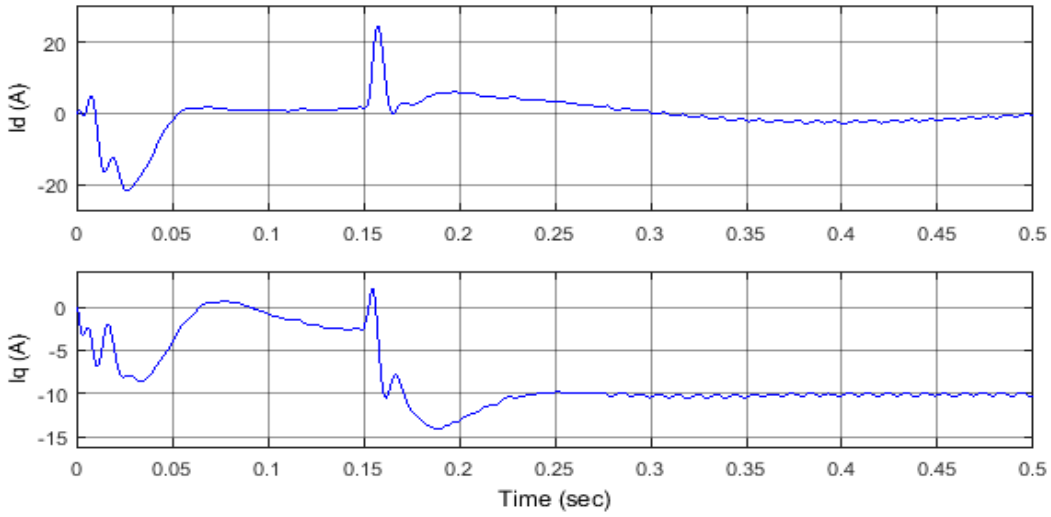

Figure 4-24 d and q components of the support current (simulation of the system with D-STATCOM only)

4.8 Simulation of a distribution system with a three-phase fault applied at load point

A symmetrical fault is applied at the PCC using a fault breaker in series with fault impedance (Figure 4-25). The value of the fault impedance has been programmed to produce a voltage dip 80% and 30% voltage sag at the PCC.

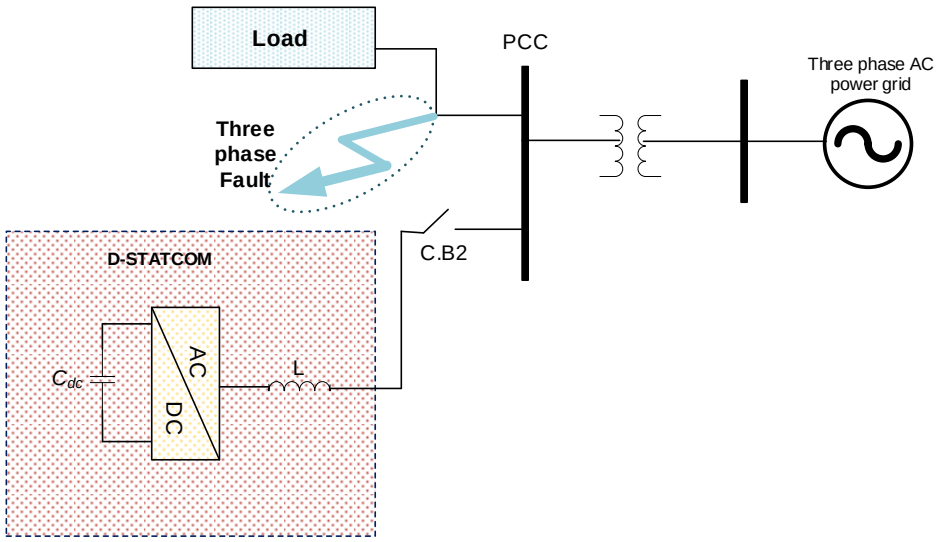

Figure 4-25 Circuit diagram of simulated system with a fault

The fault is assumed to be happen at t= 0.15 s under two conditions: for the duration of 10 and 5 cycles of a 50 Hz source. The system performance was evaluated without D-STATCOM and with D-STATCOM. A voltage sag more than 20% for more than 2 seconds and/or a voltage swell above 20% for more than 1 second will trip the generating units from the grid [178]. In addition, high voltage sag or voltage swell at the load bus due to a fault or load change, degrades the power quality. The use of the D-STATCOM device could improve the power quality in distribution systems.

Figure 4-26 shows the voltage at the PCC during the fault condition of a voltage sag for 10 cycles. The voltage sag at the PCC without any compensating device reaches almost 30%. With a conventional D-STATCOM device, the D-STATCOM is controlled to compensate for the amount of reactive power in the grid. When the control senses the fault, the D-STATCOM starts injecting reactive current into the grid and the system tries to compensate the voltage but with a high degree of oscillation and, in general, the system is disturbed because the conventional D-STATCOM has limited capability to support the voltage when exchanging only reactive power with the system. However, the D-STATCOM performance can be improved by adding an energy storage system (ESS) device to D-STATCOM which will explained clearly in the next chapter.

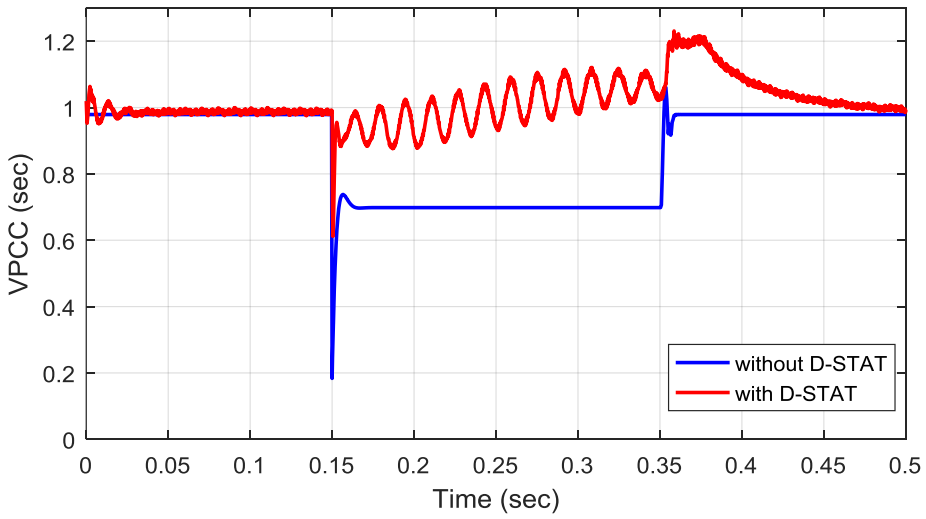

Figure 4-26 Voltage magnitude at PCC for the fault condition lasting 10 cycles

The d and q components of the D-STATCOM's current for the 10 cycles fault are shown in Figure 4-27. Figure 4-28 and Figure 4-29 show the voltage magnitude at PCC and support current during fault of duration 5 cycles.

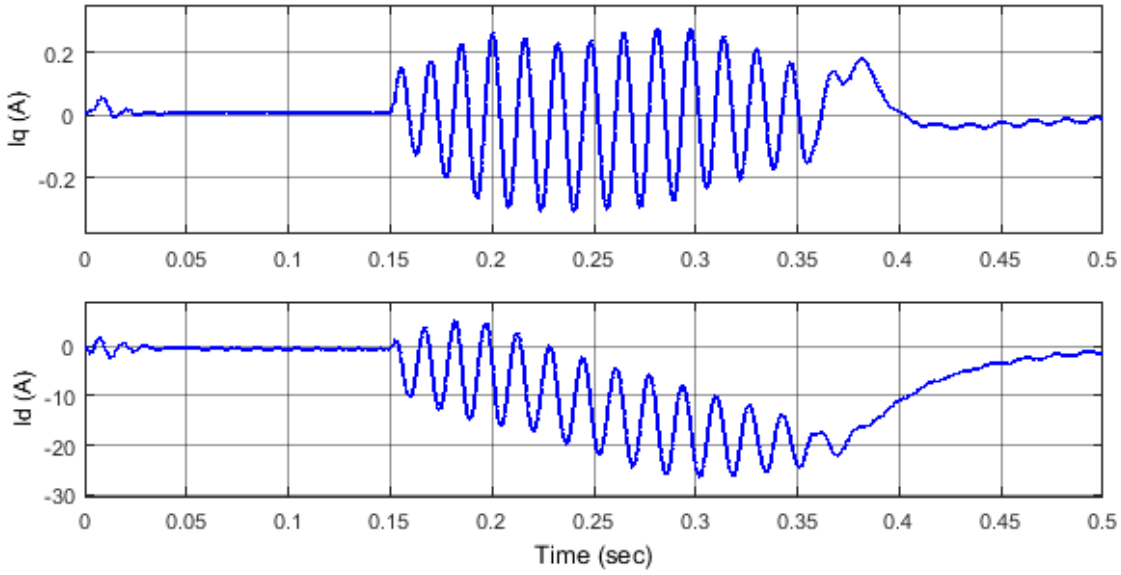

Figure 4-27 d and q components of the support current for fault condition lasting 10 cycles

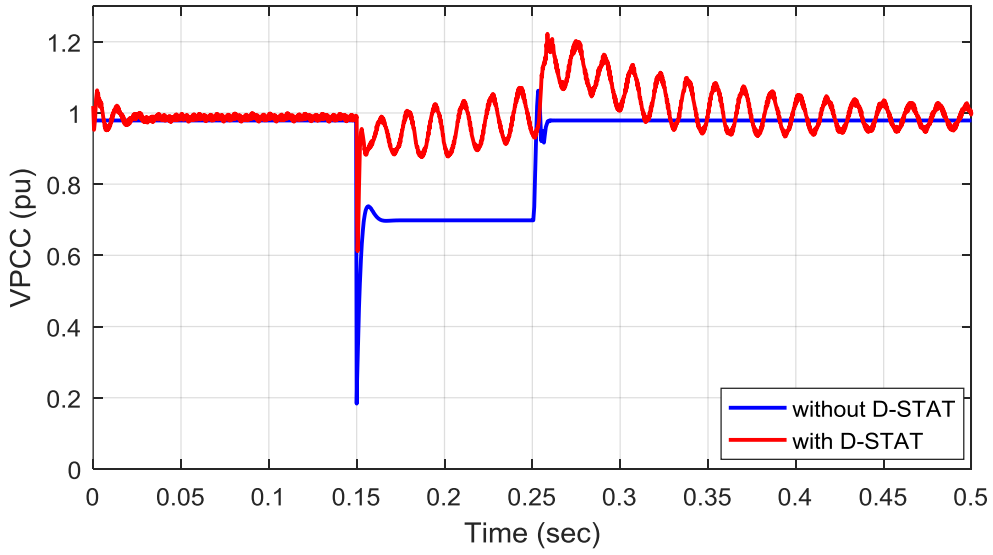

Figure 4-28 Voltage magnitude at PCC for fault condition lasting 5 cycles

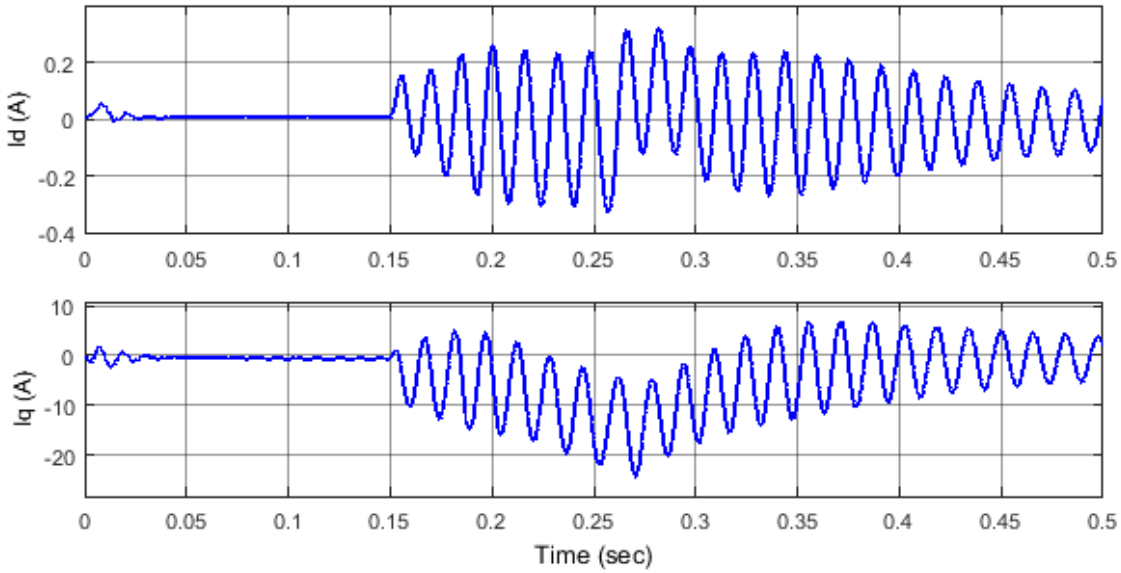

Figure 4-29 d and q components of the support current for fault condition lasting 5 cycles

4.9 Summary

D-STATCOM acted as a reactive power compensator and voltage controller at the point of common coupling. The voltage source converter is the core of the D-STATCOM device which basically operated in inductive and capacitive modes.

In this chapter, the modelling and the control loop designs for a D-STATCOM have been presented. The inner vector current control loop and the outer voltage/reactive power control loop, respectively, have been derived. Furthermore, the Sugeno-PI fuzzy controller approach has been applied to the structural design of DC side. The approach used the *d-q* control theory to obtain, in real-time, the active and reactive currents from the D-STATCOM during different operating conditions. To overcome the sub-optimal operation of existing methods which are based on optimization of a single operating point during steady state, the proposed method adjusted the proportional and integral coefficients based on the Sugeno PI fuzzy controller during critical transients such as a load disturbance. The performance of the system with voltage sag dip has been investigated using different controllers. Comprehensive simulation results show that the proposed fuzzy PI controller demonstrates significant

improvements over conventional PI controllers in supporting voltage stability in distribution networks.

The simulations clearly demonstrated that voltage sags due to sudden load change were compensated by including a conventional D-STATCOM but can be partially compensated for by including a conventional D-STATCOM in the distribution grid during the fault condition. However, the system did attempt to compensate for the voltage sag but introduced a high degree of oscillation because the conventional D-STATCOMs essentially act as a reactive power compensator and voltage controller at the point of common coupling in a grid system and they have limited ability to mitigate voltage fluctuations due to active power disturbances. However, by integrating energy storage innovatively with the D-STATCOM, active power from the storage device can be effectively harnessed to enhance voltage compensating capability. This will explain clearly in the following chapters.

5 Chapter Five: D-STATCOM Based Battery Energy Storage System

5.1 Introduction

AC power systems that employ distributed generation should be able to deliver and exchange active and reactive power to ensure stability of the power distribution grid [179]. The new renewable, distributed sources employ power electronics to meet system level requirements in terms of power quality, reliability and demand response capability [179][180]. The D-STATCOM is a power electronic converter widely used with reactive power device applications to enhance power system stability. However, it is limited in its application with respect to improving active power in the system. However, D-STATCOM functionality can be developed by integrating energy storage into the DC-side to produce controllable active power through the DC-to-DC converter. Active and reactive powers can be exchanged simultaneously with the grid by adjusting the magnitude and phase angle of the converter output voltage.

In this chapter, a modified D-STATCOM configuration based on a battery energy storage system (BESS) is explained in Section 5.2. Section 5.3 presents design and modelling of a D-STATCOM based BESS. In Section 5.4 the simulation of a distribution system with D-STATCOM plus energy storage under a sudden change in load and with a fault condition is presented with results. Further, a summary of the comparative performances of a fuzzy -tuned PI and the standard PI controller is reported. Finally, Section 5.5 provides a summary of the chapter.

5.2 D-STATCOM based battery energy storage

The advance of new power electronic strategies, particularly FACTS, is currently focusing attention on the integration of energy storage technologies to provide adequate support for electrical power grids during critical condition of the microgrid, allowing it to be managing in an isolated mode [181].

The D-STATCOM based power electronic controller is attracting significant interest among electrical engineers as one of the desired options that could enable AC power grids to provide power in a more efficient and flexible way [56][62]. D-STATCOM acts as a reactive power compensator and voltage controller at the point of common coupling (PCC) which produces or absorbs reactive power. The active power exchange can be accomplished by controlling the phase of the D-STATCOM voltage, if adding the energy storage device to the DC-side [182]. The action takes the form of a controlled current delivered between the utility grid and D-STATCOM through the coupling inductor. This enables the D-STATCOM to control the amplitude of the voltage at the PCC for such cases as sags, swells and transients. Moreover, it can use the active power capacity of the energy storage.

The capability of the D-STATCOM/BESS to provide active power permits the modification of its control objectives, reduction of transmission losses and improvement of voltage stability with steady state and transient demands on the power microgrid.

A modified configuration of D-STATCOM based battery energy storage for a three phase grid operating under load disturbance and balanced voltage sags is presented in this chapter. Figure 5-1 shows the structural model of the battery energy storage unit connected with the D-STATCOM for microgrid applications. The main part of the model consists of the voltage source converter (VSC) and battery energy storage connected in parallel to the DC-side of the D-STATCOM, and bidirectional interface controller, represented through the DC-to-DC converter.

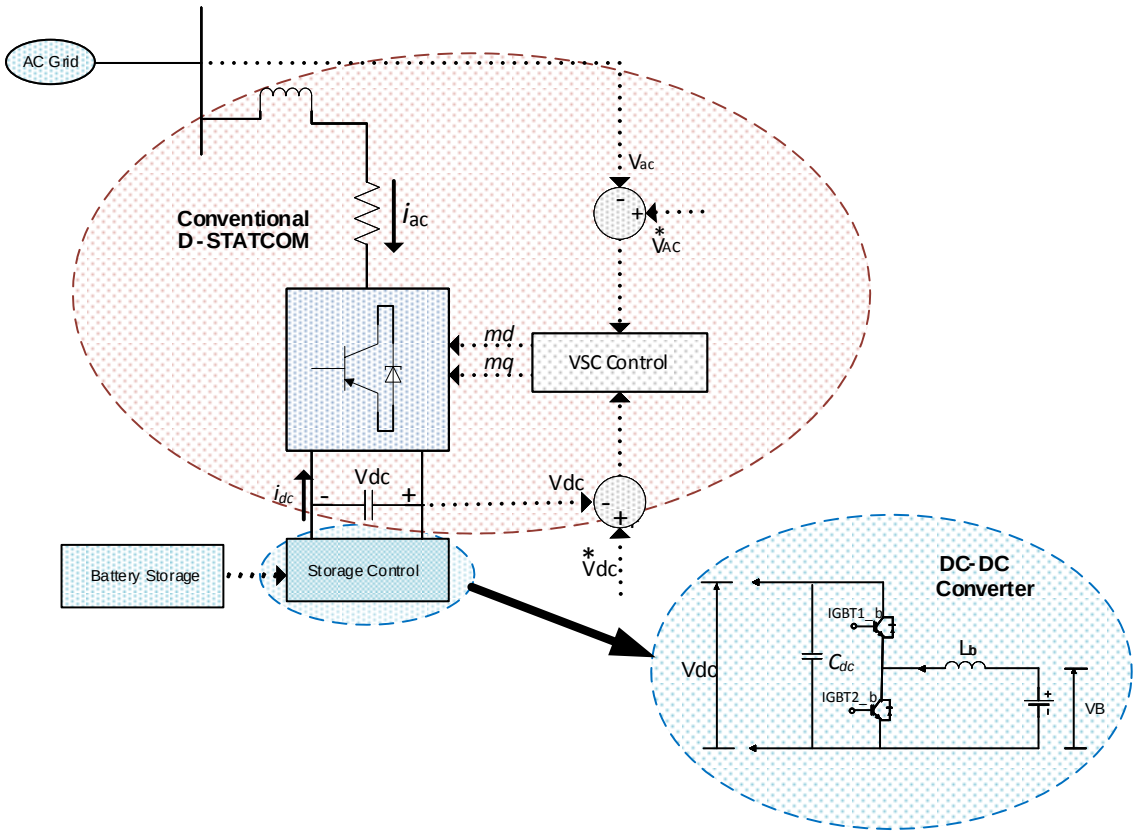

Figure 5-1 Configuration of the D-STATCOM with BESS

5.3 Modelling and control design of D-STATCOM based BESS

The battery energy storage unit is proposed as the energy storage device to be connected into the DC-side of the D-STATCOM. The general structure of the D-STATCOM based BESS is shown by the model in Figure 5-2. It includes a two-level, three-phase VSC connected to the battery storage unit through the DC-to-DC converter for application in the distribution grid. The control scheme of the D-STATCOM based on BESS consists of two controllers: a vector controller of a two-level, three phase AC-to-DC converter, is based on d-q rotating reference components; and a BESS controller which consists of DC-to-DC converters. The control objectives are simultaneous control of the amplitude of the voltage at the PCC and to utilize the active power capacity of the energy storage. To achieve that, the controller must ensure instantaneous energy balance between the grid and battery storage. Thus, the battery storage unit is controlled through the bidirectional (buck/boost) converter.

After transforming the three-phase equations to a rotating d-q frame, the dynamic equations of the AC side of the D-STATCOM, previously depicted in Equations (4-5)-(4-7) can be represented as [183]:

$$\frac{di_d}{dt} = -\frac{R}{L} i_d + \omega i_q - \frac{1}{L} v_{sd} + \frac{1}{L} m \cos\delta \, v_{dc} \tag{5-1}$$

$$\frac{di_q}{dt} = -\frac{R}{L} i_q - \omega i_d + \frac{1}{L} m \sin\delta \, v_{dc} \tag{5-2}$$

$$\frac{dv_{dc}}{dt} = -\frac{1}{c_{dc}} \left(\frac{R_b R_c}{R_c + R_b} \right) v_{dc} + \frac{v_B}{R_b c_{dc}} - \frac{3}{2} \frac{1}{C_{dc}} m \cos\delta \, i_d - \frac{3}{2} \frac{1}{C_{dc}} m \sin\delta \, i_q \tag{5-3}$$

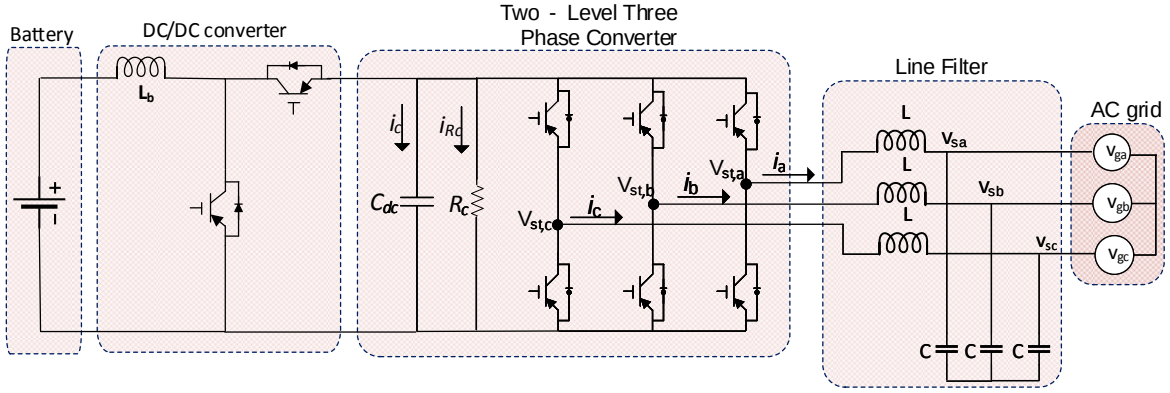

Figure 5-2 Detailed model of D-STATCOM based BESS

By combining the Equations (5-1) – (5-3), the dynamic model of the D-STATCOM based BESS can be expressed as:

$$\frac{d}{dt}\begin{bmatrix} i_d \\ i_q \\ v_{dc} \end{bmatrix} = \begin{bmatrix} \frac{-R}{L} & \omega & 0 \\ -\omega & \frac{-R}{L} & 0 \\ 0 & 0 & \frac{1}{c_{dc}} \left(\frac{R_b R_c}{R_c + R_b} \right) \end{bmatrix} \begin{bmatrix} i_d \\ i_q \\ v_{dc} \end{bmatrix} + \begin{bmatrix} \frac{m}{L} \cos\delta \, v_{dc} \\ \frac{m}{L} \sin\delta \, v_{dc} \\ -\frac{3}{2c_{dc}} m \cos\delta \, i_d - \frac{3}{2c_{dc}} m \sin\delta \, i_q \end{bmatrix} - \begin{bmatrix} \frac{v_{sd}}{L} \\ 0 \\ \frac{-v_B}{R_b c_{dc}} \end{bmatrix} \tag{5-4}$$

$$\text{where } [A] = \begin{bmatrix} \frac{-R}{L} & \omega & 0 \\ -\omega & \frac{-R}{L} & 0 \\ 0 & 0 & \frac{1}{c_{dc}}\left(\frac{R_b R_c}{R_c + R_b}\right) \end{bmatrix}$$

Equation (5-4) is the state equation of a nonlinear system. Such an equation may be subjected to linearization around an equilibrium operating point [183]. The linear equations of system thus obtained are:

$$\frac{d}{dt}\begin{bmatrix} \Delta i_d \\ \Delta_{iq} \\ \Delta v_{dc} \end{bmatrix} = [A_0]\begin{bmatrix} \Delta i_d \\ \Delta i_q \\ \Delta v_{dc} \end{bmatrix} + [B_0]\begin{bmatrix} \Delta m \\ \Delta\delta \end{bmatrix} \qquad \textbf{(5-5)}$$

$$\begin{bmatrix} \Delta i_d \\ \Delta_{iq} \\ \Delta v_{dc} \end{bmatrix} = \begin{bmatrix} i_d - i_{d0} \\ i_q - i_{q0} \\ v_{dc} - v_{dc0} \end{bmatrix}, \quad \begin{bmatrix} \Delta m \\ \Delta\delta \end{bmatrix} = \begin{bmatrix} m - m_0 \\ \delta - \delta_0 \end{bmatrix}$$

[A] is is now [A_o], where:

$$[A_0] = \begin{bmatrix} \frac{-R}{L} & \omega_0 & \frac{m_0 \cos\delta_0}{L} \\ -\omega_0 & \frac{-R}{L} & \frac{m_0 \sin\delta_0}{L} \\ -\frac{3}{2c_{dc}} m_0 \cos\delta_0 & -\frac{3}{2c_{dc}} m_0 \sin\delta_0 & \frac{-1}{c_{dc}}\left(\frac{R_b R_c}{R_c + R_b}\right) \end{bmatrix}$$

The corresponding matrix [B_o] is:

$$[B_0] = \begin{bmatrix} \frac{v_{dc0}\cos\delta_0}{L} & \frac{-v_{dc0}m_0\sin\delta_0}{L} \\ \frac{v_{dc0}\sin\delta_0}{L} & \frac{v_{dc0}m_0\cos\delta_0}{L} \\ \frac{-3}{2c_{dc}}\left(i_{d0}\cos\delta_0 + i_{q0}\sin\delta_0\right) & \frac{3m_0}{2c_{dc}}\left(i_{d0}\sin\delta_0 - i_{q0}\cos\delta_0\right) \end{bmatrix}$$

where $[\Delta i_d \quad \Delta i_q \quad \Delta v_{dc}]^T$ represent the state variable vectors, and $[\Delta m \quad \Delta\delta]^T$ are the control variables. All the characters with subscript $_0$ in Equation (5-5) represent system values at the equilibrium point.

5.3.1 Two level three phase D-STATCOM controller

The vector control algorithm based on the rotating reference theory for the d-q components has been adopted for the two-level, three phase D-STATCOM controller. The vector controller consists of the main inner current control loop, outer voltage control loop for DC- link and VPCC control loop as shown in Figure 5-3. The active and reactive power transfer between the DSTATCOM/BESS device and the utility grid is decided by the outer control loop which is outlined in Figure 5-3. The design adapted the D-STATCOM device to achieve two main power purposes; the reactive power compensator (RPC) to regulate the voltage at the PCC, and dynamic active power control (APC) to transfer power between the BESS and the utility grid. Decoupled power control theory is introduced for the two-level converter to give parallel control of active and reactive power. According to instantaneous reactive power theory [169], the active and reactive powers can be described as:

$$P = \frac{3}{2}\left(V_d i_d + V_q i_q\right) \quad \textbf{(5-6)}$$

$$Q = \frac{3}{2}\left(V_q i_d - V_d i_q\right) \quad \textbf{(5-7)}$$

The instantaneous measured grid voltage and current in a-b-c stationary components are transformed to d-q components, (V_d , V_q, and i_d i_q) respectively. Then, they are filtered to reject all undesirable components. As previously stated in Chapter Four, the d-component of the voltage, V_d, is usually aligned with the

instantaneous voltage vector, V. Therefore, V_q in Equations (5-6) and (5-7) is zero and the formula can be re-written as follows:

$$P = \frac{3}{2} |V_{d|} i_d \quad \textbf{(5-8)}$$

$$Q = \frac{3}{2} |V_{d|} i_q \quad \textbf{(5-9)}$$

As is obvious from Equations (5-8) and (5-9), the instantaneous active power P is specified by the d-component of the VSC current, whereas the instantaneous reactive power is represented through the q-component of the current. Furthermore, the actual active and reactive currents, $i_d \; and \; i_q$ respectively are calculated and filtered through the low pass filter and forwarded to the inner control loop. The angle θ for coordinate transformation of the voltage and current at the PCC from abc to d-q axes is obtained from a phase locked loop used to carry out the synchronization with system voltage and current. The dynamic response of the control loops designed in the d-q reference frame is more manageable than applying the stationary frame techniques.

The voltage regulator at the PCC is the main loop of the outer control loops, achieving compensation of the reactive power by adjusting the quadratic component of the D-STATCOM current. This control mode has provided good performance in conventional D-STATCOM controllers (for the case of no energy storage see Chapter Four). The second loop of the outer control loops is the APC. The APC controls the active power transfer from the utility grid to enhance the desired system response. Thus, the reference signal of the active current component of the D-STATCOM, i_d, is computed by comparing the reference active power value with actual power signals through the PI controller. Therefore, the active power transferring between the D-STATCOM/BESS and the utility grid is controlled by forcing the BESS to deliver active current when the active power signal is positive (discharging process), or to absorb active current when the active power signal is negative (charging process)

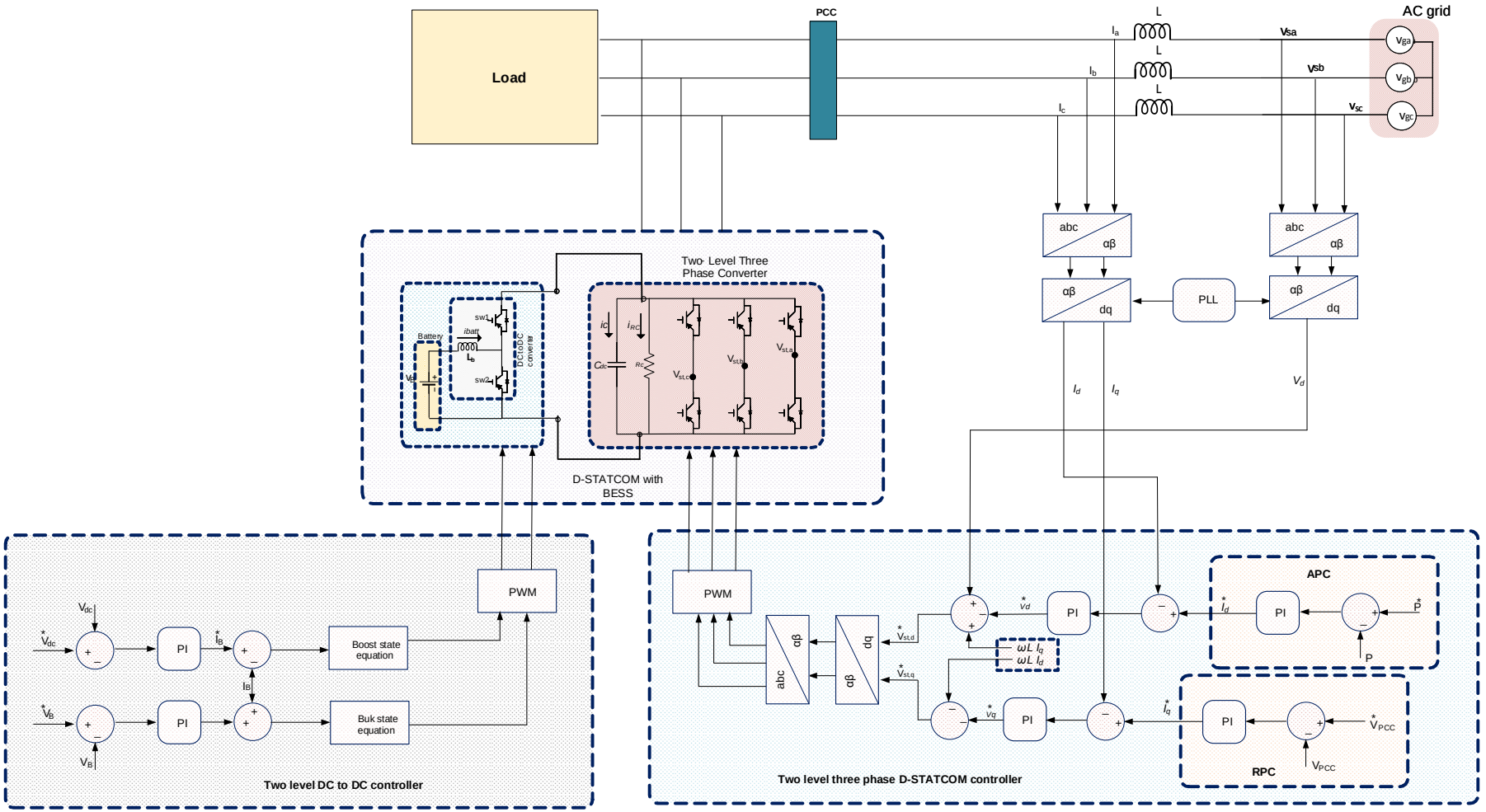

Figure 5-3 The control scheme for the D-STATCOM /BESS

The reference output signals produced from the outer loops is forwarded to the inner control loops to track expected output values. The control design of the inner loops is based on simplified state-space averaged model of the D-STATCOM/BESS in the rotating d-q reference frame, which is given in Equations (5-1) – (5-3). Inspection of Equations (5-1) to (5-3) indicates a cross-coupling of both components of the BESS output current through ω. To decouple active and reactive power control, all that is required is to decouple the control of i_d and i_q. At the equilibrium point, assume there is no exchange of active power between the grid and battery, i_{d0} and δ_0 equal zero. Therefore, A_0 and B_0 in Equation (5-5) can be formulated as:

$$[A_0] = \begin{bmatrix} \frac{-R}{L} & \omega_0 & \frac{m_0}{L} \\ -\omega_0 & \frac{-R}{L} & 0 \\ -\frac{3}{2c_{dc}} m_0 & 0 & \frac{-1}{c_{dc}}\left(\frac{R_b R_c}{R_c + R_b}\right) \end{bmatrix} \quad \textbf{(5-10)}$$

$$[B_0] = \begin{bmatrix} \frac{v_{dc0}}{L} & 0 \\ 0 & \frac{v_{dc0}}{L} \\ 0 & -\frac{3m_0}{2c_{dc}}(i_{q0}) \end{bmatrix}$$

If Equation (5-10) is substituted into Equation (5-5), the first two rows of equation (5-5) can be written as:

$$\frac{d}{dt}\begin{bmatrix} i_d \\ i_q \end{bmatrix} = \begin{bmatrix} \frac{-R}{L} & 0 \\ 0 & \frac{-R}{L} \end{bmatrix}\begin{bmatrix} \Delta i_d \\ \Delta i_q \end{bmatrix} + \begin{bmatrix} x_1 \\ x_2 \end{bmatrix} \quad \textbf{(5-11)}$$

$$\begin{bmatrix} x_1 \\ x_2 \end{bmatrix} = \begin{bmatrix} \omega_0 \Delta i_q + \frac{m_0}{L}\Delta v_{dc} + \frac{v_{dc0}}{L}\Delta m_0 \\ \frac{v_{dc0} m_0}{L}\Delta_\delta - \omega_0 \Delta i_d \end{bmatrix} \quad \textbf{(5-12)}$$

Where $[x_1 \quad x_2]^T$ is the new control variable vector, and i_d and i_q are active and reactive control current. The decoupling of the controls of the active and reactive

powers of the VSC is obtained by using standard PI controllers. The introduction of these new control signals yields a full AC side, VSC model reduced to two first-order functions, see Equation (5-11) (the control design of the inner loops was explained in Chapter Four).

According to Equation (5-3), there is another coupling of the derivative of DC voltage v_{dc} to i_d and i_q. Thus, the condition corresponding to Equation (5-3) must be satisfied to keep the DC-side voltage at an acceptably constant level, and eliminate variation of the steady state voltage, v_{dc}. Thus, another controller is used to solve the problem of fluctuation of the DC voltage. It is represented by a DC-to-DC converter connected between the ESS (battery) and the DC-side of the grid to maintain the DC voltage side of D-STATCOM constant. The DC-to-DC converter controls the flow of energy to/from the energy storage combination and grid through modulation of the duty cycle (*D)* of the DC/DC chopper. The state equations to determine the duty cycles of buck/boost are derived and explained in Appendix B.

5.3.2 Battery modelling

The Lithium-ion battery model is made up of an energy storage component and energy loss element, and the equivalent circuit of the battery model is shown in Figure 5-4) with “all the model parameters determined based on the discharge curve” [184]. It is represented as a voltage source E connected in series with resistance R_b. The voltage equation of the voltage source is computed using a non-linear equation with respect to the state of charge of the battery (SOC) in the following equations[184] [185].

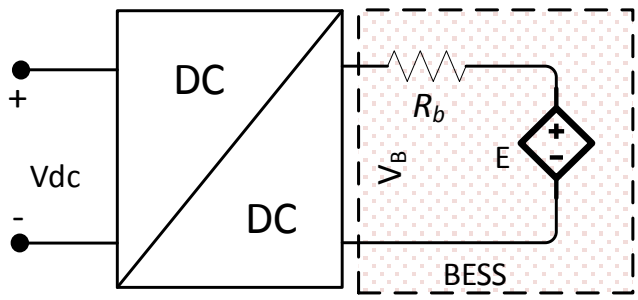

Figure 5-4 ESS scheme

$$E = E_0 - K\frac{Q}{Q - \int idt} i + Ae^{-B.\int_0^t idt} \quad \textbf{(5-13)}$$

And,

$$V_B = E - R_b.\ i \quad \textbf{(5-14)}$$

where

E = no-load voltage (V)

E_0 = battery constant voltage (V)

K = polarisation voltage (V)

Q = battery capacity (Ah)

idt = actual battery charge (Ah)

A = exponential zone amplitude (V)

B = exponential zone time constant inverse (*Ah*)−1

V_B = battery voltage (V)

R_b= internal resistance (Ω)

i = battery current (A)

The non-linear voltage in Equation (5-13) is based on the actual battery charge. The SOC may be taken as 100% for a completely charged battery, and fully discharged has SOC = 0%. This indicates that the totally discharged battery causes the voltage to approach zero. The state of charge is determined according to Coulomb-counting as:

$$SOC = 100\left\{1 - \frac{1}{Q}\int_0^t i(t)dt\right\} \quad \textbf{(5-15)}$$

where: t is the time of charging or discharging; $i(t)$ is the current charging or discharging.

5.3.3 Two level DC to DC controller

As formerly described, the conventional D-STATCOM has a limited capability to support the voltage by exchanging reactive power with the system. However, the D-STATCOM performance is improved by adding an energy storage system

device to D-STATCOM to support the grid with active and reactive power. On the other hand, directly connecting of the battery (energy storage) to the DC-side will influence the D-STATCOM operation during real power exchange.

A wide variation in voltage and current levels between the DC-side of the D-STATCOM and battery storage will occur due to the charging and discharging of power between the battery and the grid. For example, if the voltage level of the DC-side falls to a level less than the boundary limit of the AC side, the D-STATCOM operation will be ended. To avoid and solve this issue, a bidirectional DC-to-DC (buck/boost) controller is connected between the battery storage and the DC-side [56].

Figure 5-5 shows the basic circuit diagram of the combination of the energy storage (BESS) with DC-to-DC converter. As indicated in the circuit the converter consists of two high power, fast IGBT switches operating in two modes (boost/buck) in order to provide suitable control of the overall system. This bidirectional step-up and step-down converter provides the means of decreasing the overall power rating of the devices by controlling the current flow from the BESS to the D-STATCOM inverter, and vice versa.

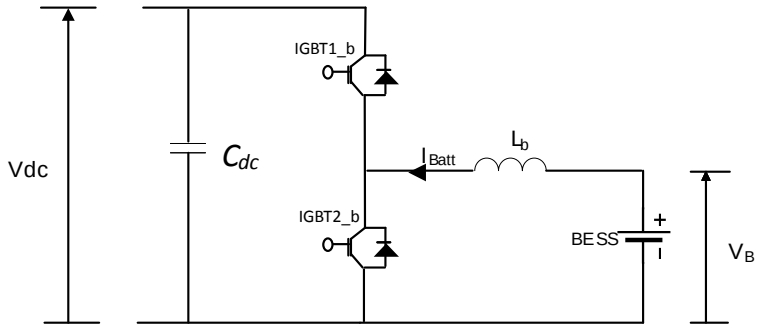

Figure 5-5 DC to DC Circuit Diagram [47]

Basically, the DC-to-DC converter operates in two modes (boost/buck). The boost mode operation, is when power is transferred from energy storage to AC grid (discharging mode), the buck mode is the transfer of power from the grid to storage mode (charging mode). The bidirectional power transfer is regulated

using the inductor, L_b. The buck/boost state equations used to generate the pulses for the buck/boost switches are:

$$d_{buck} = \frac{L\Delta I + V_B}{V_{dc}} \quad \textbf{(5-16)}$$

$$d_{boost} = 1 + \frac{L\Delta \mathrm{I} - V_B}{V_{dc}} \quad \textbf{(5-17)}$$

Where V_B is the battery voltage, ΔI_{on} is the inductor current during the on-period, ΔI_{off} is the inductor current during the off-period and ΔI is the inductor current changing across one sampling period [79]: $\Delta I = \Delta I_{on} - \Delta I_{off}$.

The D-STATCOM operation based energy storage can be categorized into three operating modes: D-STATCOM only mode, D-STATCOM with ESS boost mode and D-STATCOM with ESS buck mode. The overall D-STATCOM with BEES controller is shown in Figure 5-3.

In the case when BESS is not utilised, the D-STATCOM is used in standard D-STATCOM mode only. Referring to the circuit diagram in Figure 5-6 the converter is in buck mode (charging) when the upper switch (IGBT1_b) is turned on and when the DC bus voltage is regulated by injecting the energy from the grid into the battery storage.

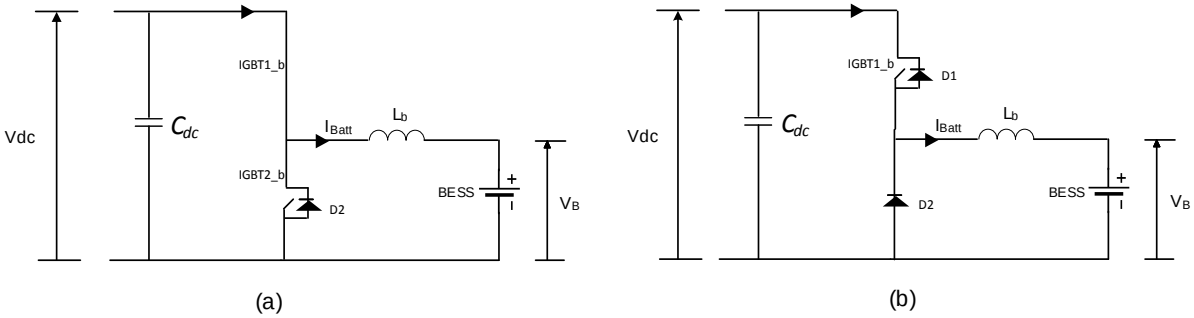

Figure 5-6 BESS in buck mode [47]

Once switch 1 (IGBT1_b) is closed as displayed in Figure 5-6 (a), energy is transmitted from the power grid to be stored as magnetic energy in buck/boost inductor (L_b); the battery current flowing is I_{Batt}. Whenever switch 1 (IGBT1_b) is

opened, see Figure 5-6 (b), the diode D2 conducts due to the induced back emf across L_b causing L_b to discharge the stored energy to battery storage. The process of energy transfer between the DC-side of D-STATCOM and the battery is managed through the duty cycle of IGBT1_b. During this cycling, the voltage of the battery is controlled, and the charging mode will stop when the battery voltage reaches the saturation rate. The converter is in boost mode when power is injected from the energy stored in the battery to the AC grid by closing and opening the lower switch (IGBT2_b) as shown in Figure 5-7 [47].

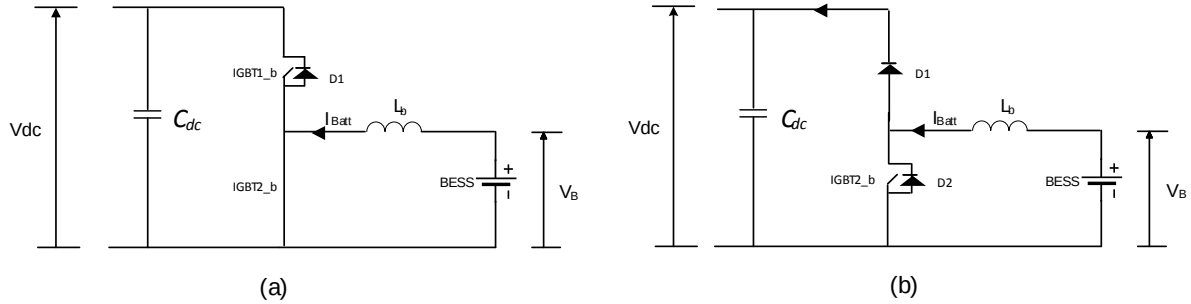

Figure 5-7 BESS boost mode circuit [47]

In the case that IGBT2_b is closed, see Figure 5-7 (a), energy is transmitted from the battery to be stored as magnetic energy in the buck/boost inductor (L_b); with battery current (I_{Batt}). When, the switch 2 (IGBT2_b) is opened as in Figure 5-7 (b), the diode D1 is conducting because of the induced back emf across L_b, causing L_b to discharge the stored energy to the DC-side capacitor and then to the grid. The process of energy transfer between the DC-side of D-STATCOM and the battery is controlled through the duty cycle of IGBT2_b. The voltage of the DC-side capacitor is regulated at setting value during the converter boost mode. This is suitable for real power injection where constant DC-link voltage is essential.

5.3.3.1 Control Strategies

The DC-to-DC controller includes two control loops, the outer voltage control loop and the inner current control loop. The voltage error signals are used in the voltage control loop to control the required energy to be absorbed or injected. The

battery voltage error is used in the buck operation mode to produce the appropriate pulsing of the IGBT switches. In the boost operation mode, the error signal of the DC-side voltage is used to produce the required pulsing signals for the IGBT switches. As mentioned above, the bidirectional power transfer between the battery and DC-side capacitor is regulated by using an inductor, L_b. Therefore, the reference control feedback current is obtained from the voltage control loop and fed forward to the inner control loop. This reference current signal is compared with the actual signal of the inductor current and the resulting error signal is used by the PI controller. The PWM duty cycle is produced by the controller and transmitted to the gate drive to provide the gate signals of IGBT1_b and IGBT2_b to generate the necessary output power.

Figure 5-8 (a) presents the structure diagram for the two controller modes (buck and boost). Depending on the mode of operation, only one IGBT switch of the DC to DC converter is needed to be switched. In order to select the proper IGBT switch, the battery reference current I_{batt} is given by the two controllers separately. Mode switching is controlled by the inductor actual current (I_{Batt}). The different control modes can be represented by the different current flow directions. In Figure 5-8 (b) if the charging current signal through the inductor in the buck controller is positive, the discharging current for the boost mode will be negative. Hence, the function of the converter, whether charging or discharging, is determined by the positive or negative sign of the inductor current. This effectively protects the converter against critical transient over-currents during mode exchange [186]. The control diagram of the buck mode loop is given in Figure 5-9. The outer voltage loop regulates the battery voltage whilst the internal current loop is employed to generate the duty cycle based on the buck state equations. The control diagram of the boost mode loop is presented in Figure 5-10 .The outer voltage loop regulates the DC-side voltage whilst the internal current loop is employed to control the inductor current necessary for operation of the boost mode.

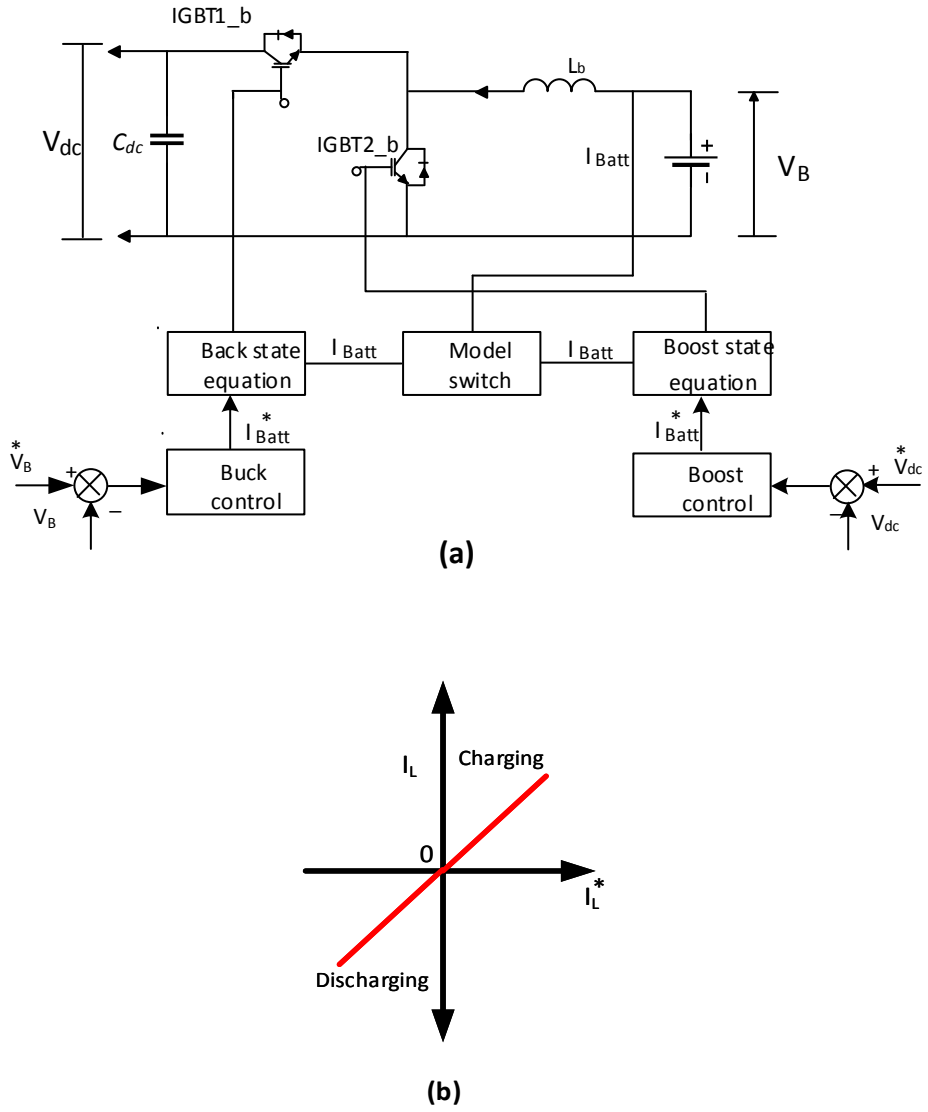

Figure 5-8 (a) the structure diagram of DC -DC controller (b) control signal of model switching

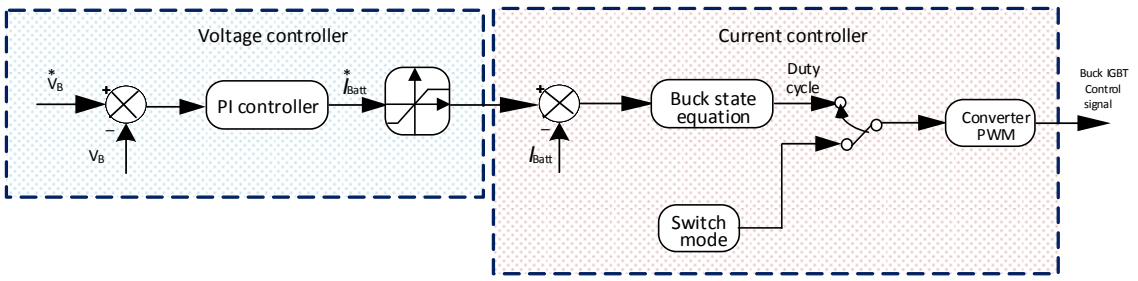

Figure 5-9 The buck control diagram

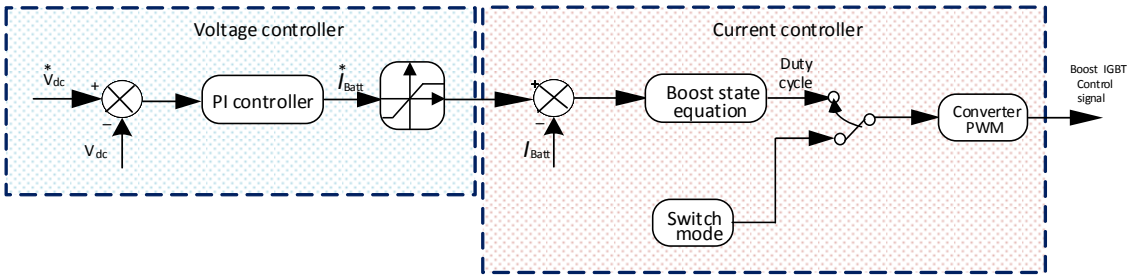

Figure 5-10 The boost control diagram

5.4 Simulation of D-STATCOM based battery energy storage

5.4.1 Simulation of a distribution system with a sudden load change

The capacity of the D-STATCOM to support the grid with active and reactive power is shown by adding the BESS to the DC-side of D-STATCOM. The battery rated at 400 V with a capacity of 60 Ah is connected to the DC-side of the D-STATCOM through the DC-to-DC converter with $\mathrm{L_b} = 10mH$. The simulation results of the D-STATCOM based BESS with PI controller are illustrated in Figure 5-11 and Figure 5-12. At time t=0.15 s, a sudden step change in the load current has occurred when a second load is switched on by closing the circuit breaker (C.B1), shown in Figure 4-13. The load current is measured and transformed to d-q components. The measured load current is then used to trigger the D-STATCOM with BESS. There is a consequent supply current change as shown in the second trace of Figure 5-11. The voltage at the DC-side displayed in the fourth trace of Figure 5-11 is regulated relatively to the desired value of 700 V. The supply source provides the real power demand by the second load briefly until the support current from the D-STATCOM based BESS unit takes full control.

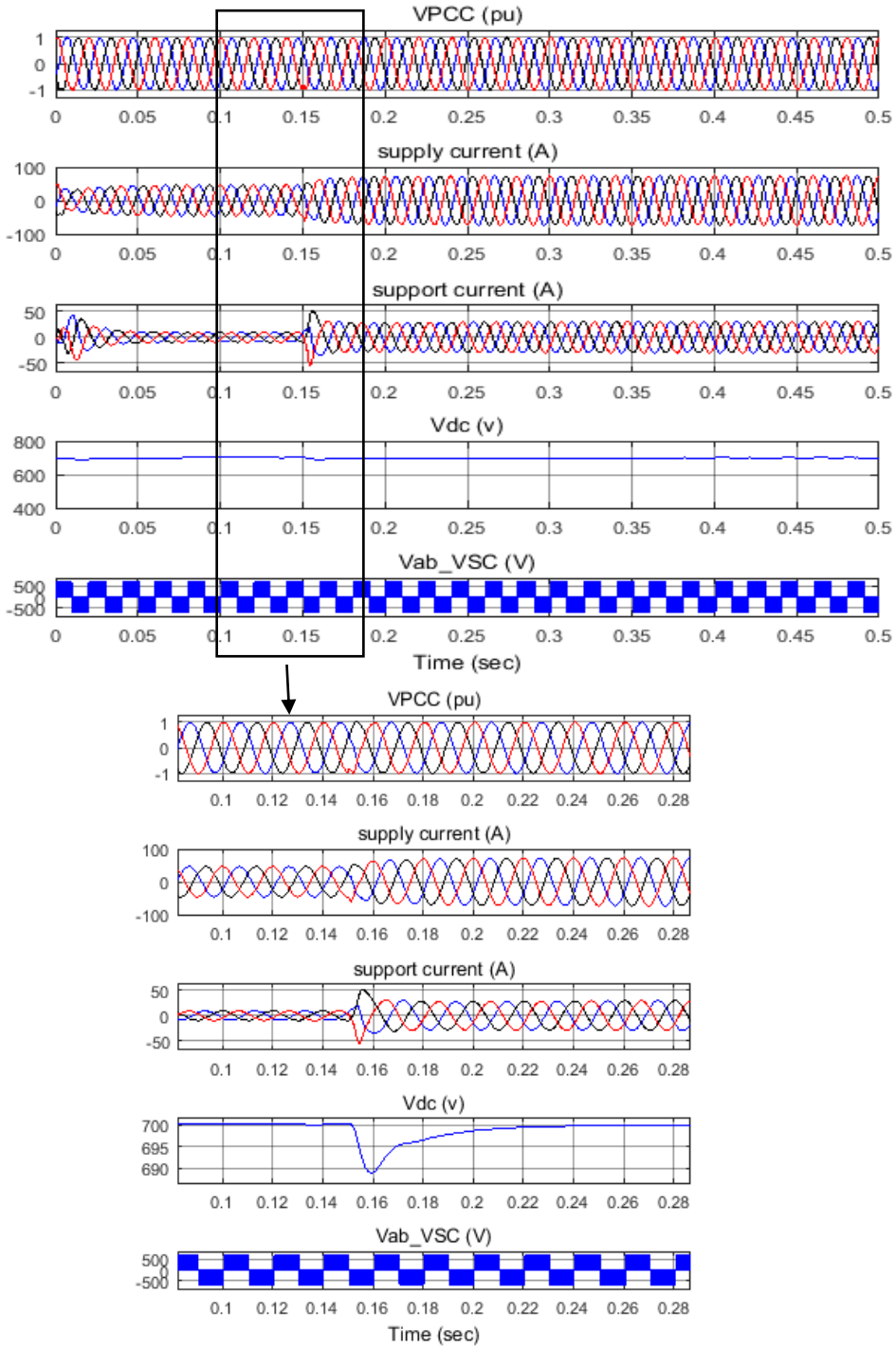

Figure 5-11 Simulation results for the case with D-STATCOM based BESS with PI controller

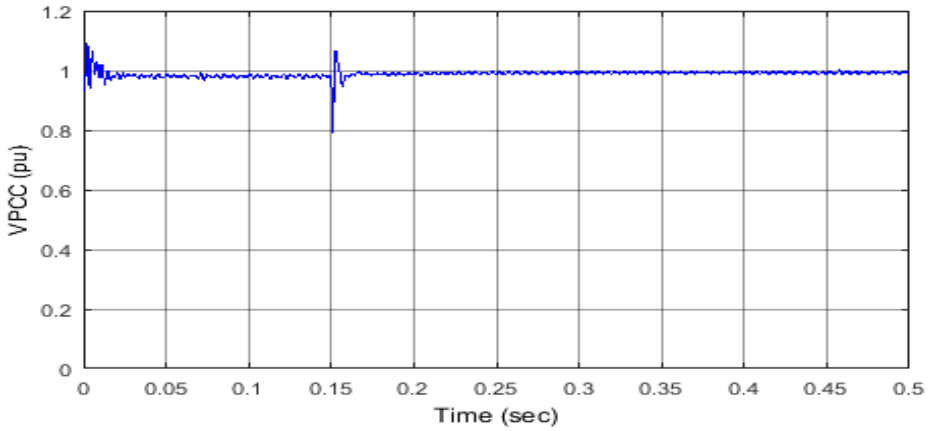

Figure 5-12 Voltage magnitude at PCC point results for the case with D-STATCOM based BESS with PI controller

The voltage response at the PCC is maintained reasonably constant at 1 pu as indicated in Figure 5-12. However, there is some oscillation in the voltage response during the system loading when compared to the voltage response of Figure 4-18. The oscillation in the system response occurred because the D-STATCOM takes energy from the DC-side until the BESS starts to operate in boost operating mode to provide the additional real power required by the second load. The export of power from the DC link created an oscillation in the voltage at the PCC. The active power possibilities of the D-STATCOM based BESS can be shown clearly by comparing second and third traces of Figure 4-22 (simulation of D-STATCOM without BESS) and Figure 5-11 (simulation of D-STATCOM based BESS). In Figure 4-22, the supply source provided the active power demanded by the system as illustrated in the second trace (supply current). The third trace represented the D-STATCOM's reactive current to compensate the voltage during the load change (support current). In Figure 5-11 , the support current shown on the third trace is more than the current shown in the third trace of Figure 4-22.The support current represents the active and reactive power requirements by the second load which are supported by D-STATCOM and BESS. Meanwhile the supply current in the second trace is less than the current shown in the second trace of Figure 4-22 . The supply current of the source with BESS can be clearly observed in Figure 5-13.

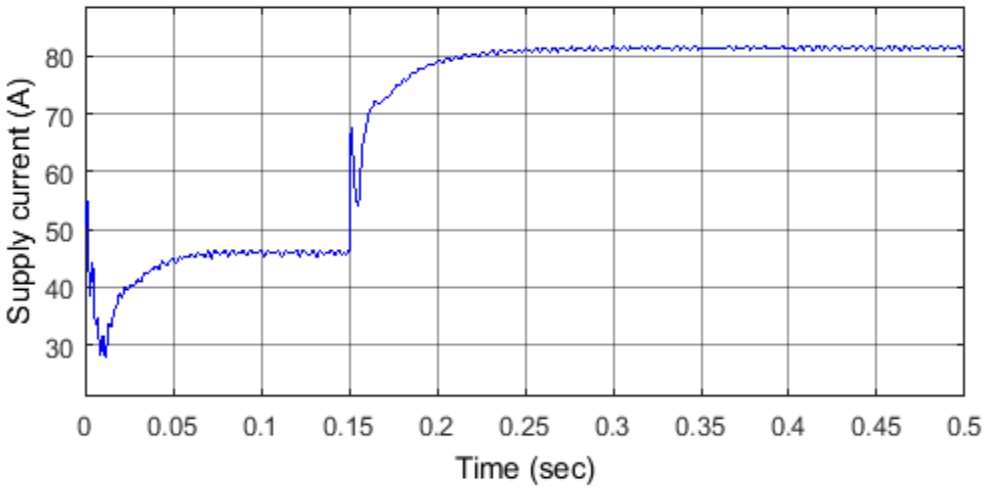

Figure 5-13 Supply current (simulation of the system with D-STATCOM based BESS)

The D-STATCOM with battery supported the grid with active and reactive power as can be confirmed by the d and q quantities of D-STATCOM's current.

From the d and q components of the D-STATCOM current without and with energy storage (Figure 4-24 and Figure 5-14,) it can be seen that the I_d current component is zero as indicated in the first trace (Figure 4-24). The I_q current component nearly reached -10 A when the second load was turned on, as seen in the second trace. As expected it is provided by D-STATCOM without energy storage to improve the voltage at the PCC. From Figure 5-14, the active current component is clearly indicated in the first trace with nearly -20 A provided by D-STATCOM with battery, to support the grid with active power when the second load was turned on. The reactive current I_q was injected by D-STATCOM to compensate the voltage at the PCC. The current and voltage magnitude of the battery storage are shown in Figure 5-15.

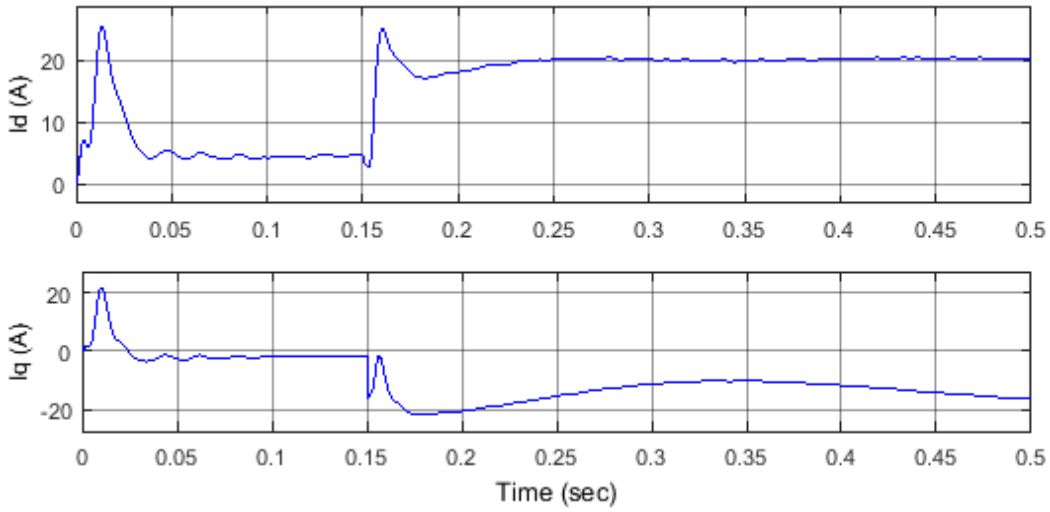

Figure 5-14 d and q components of the support current (simulation of the system with D-STATCOM based battery)

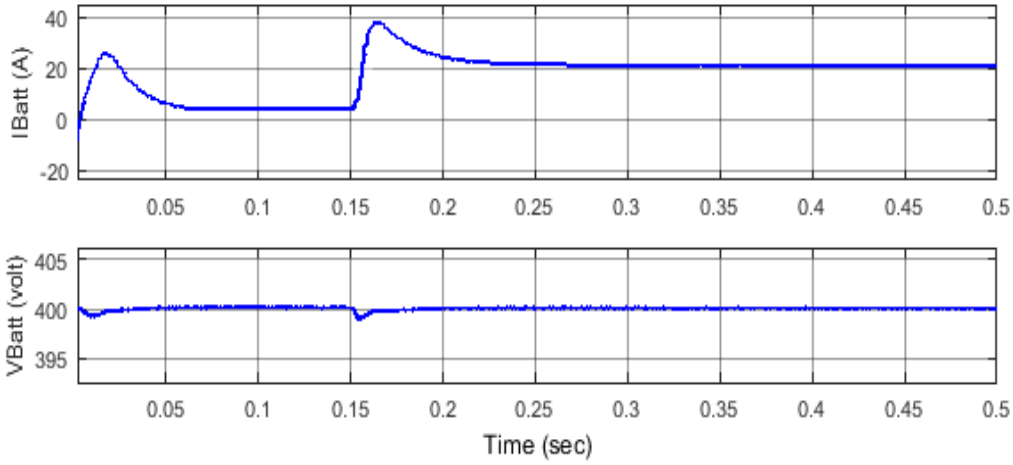

Figure 5-15 The current and voltage magnitude of the battery storage

5.4.2 Comparison between fuzzy-tuned PI controller and the PI controller (with a sudden load change)

the dynamic behaviour of the distribution grid (Figure 4-13) based on D-STATCOM integrated BESS is simulated with fuzzy-tuned PI controller and compared with standard PI controller in this section. Figure 5-16 shows the dynamic response of the voltage at the point of common coupling with both the D-STATCOM controllers. It can be noticed from Figure 5-16 that the dynamic response of the voltage at the PCC is much improved by adopting the PI-

controller with fuzzy logic. The voltage waveform in the case of the PI-controller with fuzzy logic (fuzzy- tuned PI) has a more consistent response. This particularly true during the system loading, whereas the voltage response when using the PI compensator shows much rougher behaviour. Figure 5-17 shows the simulation results of the system obtained by SIMULINK/MATLAB. It is observed that the rating of the support current at start up and at the change in load, as shown in the third trace of Figure 5-17 is less than third trace shown in Figure 5-11. A DC-side voltage comparison is presented in Figure 5-18. The voltage response has less steady state error in the case of applying a fuzzy logic controller; with a clear reduction in the value of the voltage dip during the load change at t= 0.15 s. A reduction of nearly reached 50% is noted. A summary of the performance comparison between the fuzzy-tuned PI and the standard PI controller is shown in Table 5-1.

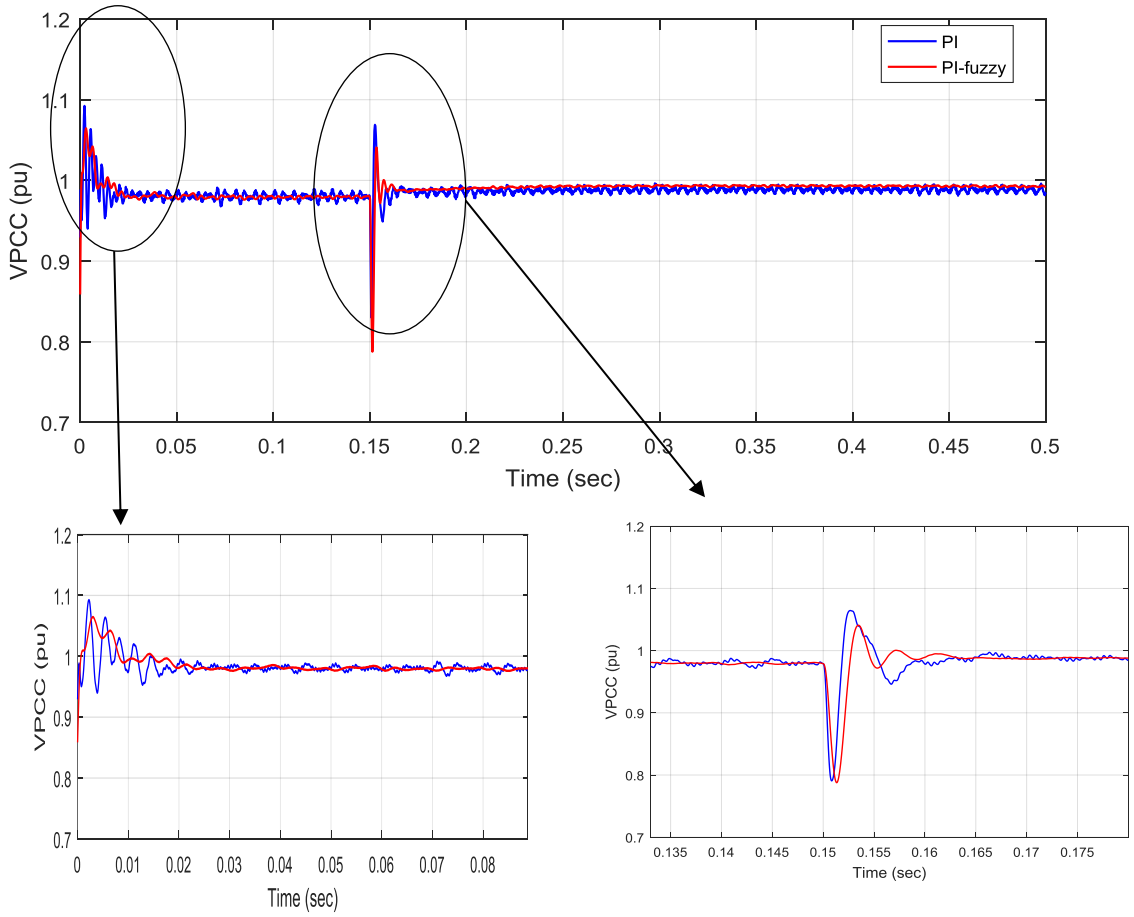

Figure 5-16 Voltage magnitude at PCC point

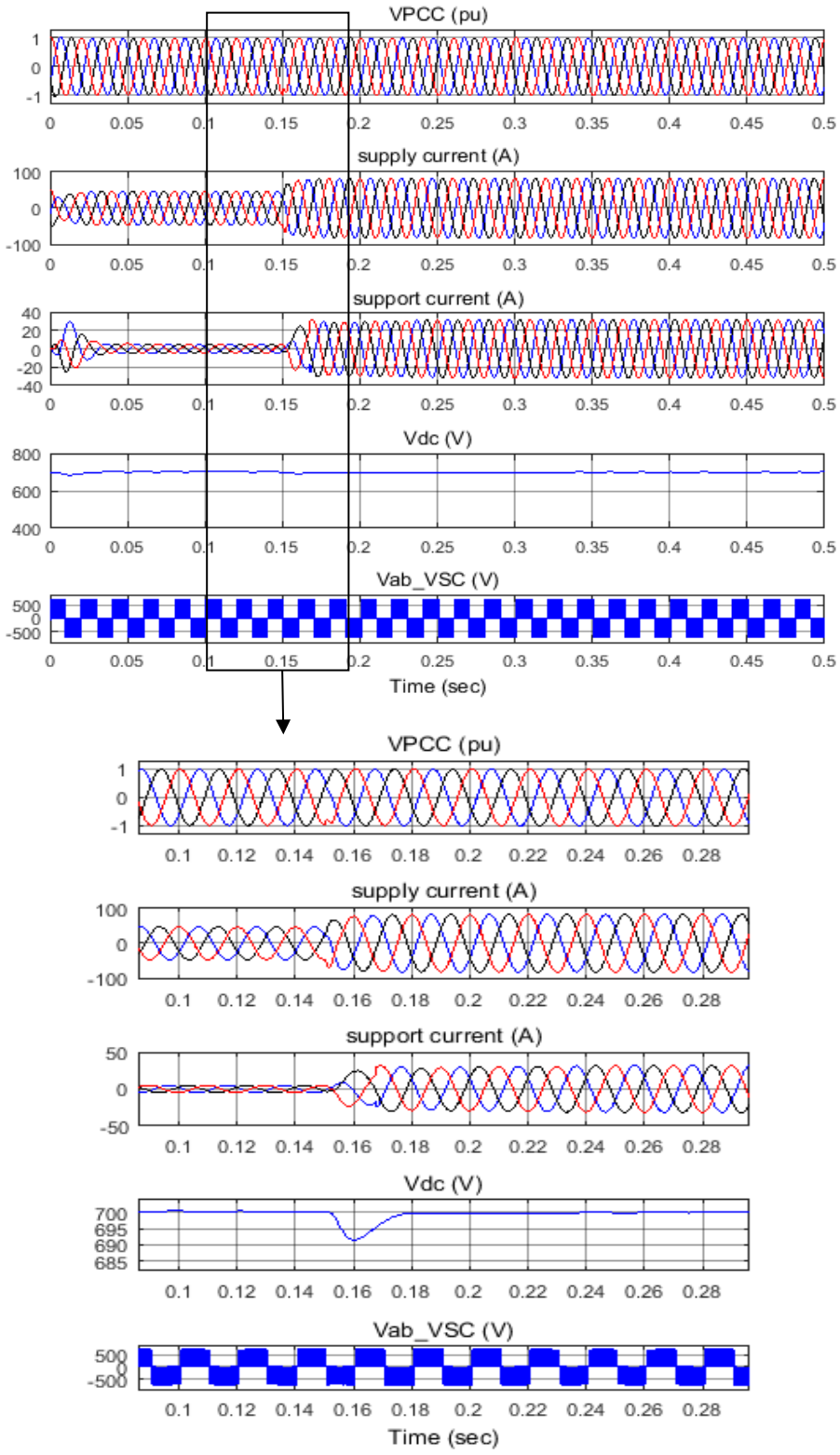

Figure 5-17 Simulation results for the case with D-STATCOM based BESS with fuzzy - tuned PI controller

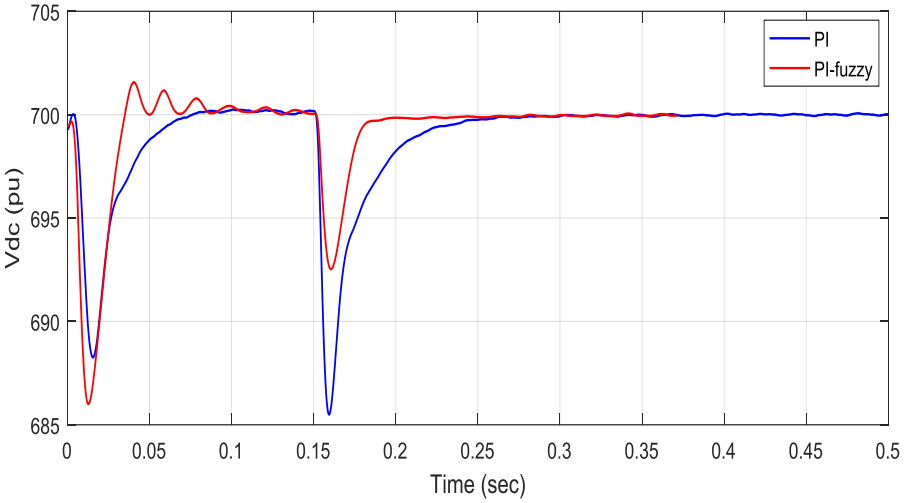

Figure 5-18 DC-side voltage

Table 5-1 Comparison of the system performance

System performance		Standard PI-controller		Fuzzy -tuned PI	
		VPCC (pu)	Vdc (volt)	VPCC (pu)	Vdc (volt)
at Start-up	Max peak	1.092	-----	1.06	701.5
	Min dip	0.94	688.5	≅ zero	686
	Settling time (msec)	20	80	10	50
at Load change at t =0.15 s	Max peak	1.065	------	1.04	-----
	Min dip	0.788	685.5	0.787	693
	Settling time (msec)	20	100	15	50

5.4.3 Simulation of a distribution system with a three-phase fault applied at load point

The effectiveness of the D-STATCOM based battery energy storage is shown by simulated a voltage dip of 80% followed by a sag of 30% for 10 cycles caused by a symmetrical fault (Figure 4-25). First, the simulation is carried out with a balanced three phase fault applied at time t = 0.15 s and cleared at t = 0.35 s, without coupling the D-STATCOM. The simulation results are shown in Figure 5-19. It can be observed that a voltage drop at the PCC resulted from the three phase fault action. Secondly, the model assumed that when the fault occurred the D-STATCOM is operating. In this case, the D-STATCOM compensation device is connected without the battery storage unit and it can be seen that the system's dynamic response is still unacceptable because the conventional D-STATCOM has only limited capacity, exchanging only reactive power, as discussed in Section 4.8. Finally, the model simulated a D-STATCOM with battery storage unit (BESS) linked with the system. The DC-to-DC converter is coupled between the battery and DC-side capacitor to control the power flowing between the battery and the grid.

The simulation results are shown in Figure 5-19 and Figure 5-20. It can be seen from Figure 5-19 that the voltage magnitude at the PCC is effectively regulated at 1 pu with the D-STATCOM based battery storage under the fault condition. The spikes that can be seen at the beginning and end of the voltage sag for this situation are due to the charging and discharging of capacitors.

Figure 5-20 presents the DC-side voltage of the D-STATCOM. It can be seen that the control system with the proposed D-STATCOM with BESS effectively maintained the DC-link voltage profile during the period of the voltage disturbance. The comparison of the $I_d$and $I_q$components of the D-STATCOM support current with and without battery storage are shown in Figure 5-21 and Figure 5-22 respectively. The active current output of the D-STATCOM based BESS (I_d) is quite high at the start-up time and at the beginning (t= 0.15 s) and end (t= 0.35 s) of the sag, in order to compensate for the sudden change in power demand, which then decays to its normal value. This is as expected, as it is

desirable that the battery storage acts to charge and discharge only during the disturbance. The outputs of the conventional D-STATCOM and D-STATCOM based BESS are very slightly different under steady state conditions because the internal losses of the two systems are different, the battery storage unit including the DC-DC converter has an additional loss, though this is usually small. The reactive support current I_q of the D-STATCOM based BESS system (Figure 5-22) shows a clearly damped response compared to the conventional D-STATCOM current. This is because the active power control and the voltage control are accomplished independently, and thus much more rapidly. The current and voltage magnitude of the battery storage are shown in Figure 5-23.

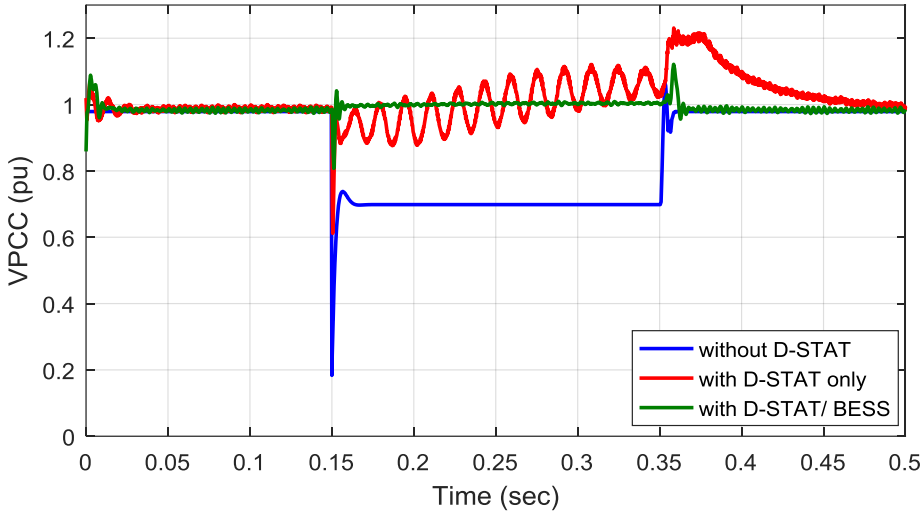

Figure 5-19 Voltage magnitude at PCC for the fault condition lasting 10 cycles

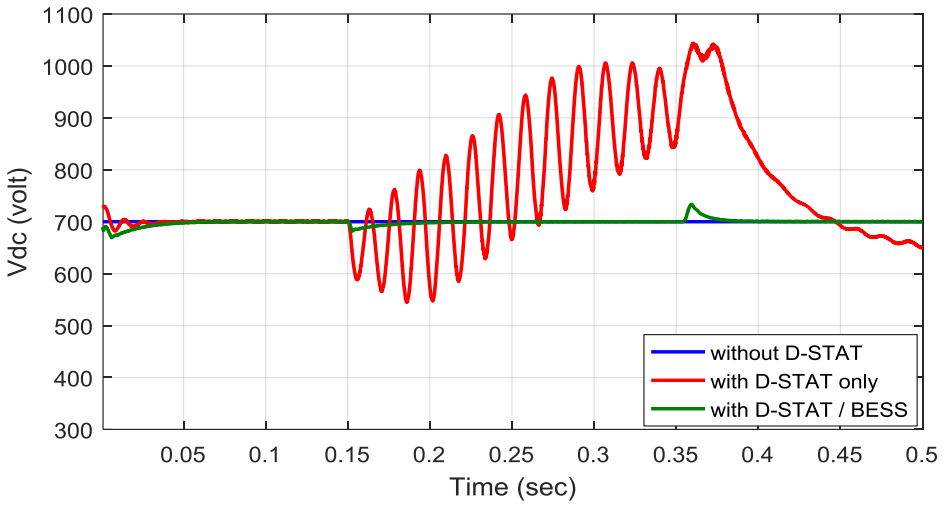

Figure 5-20 DC side voltage during the fault condition for 10 cycles

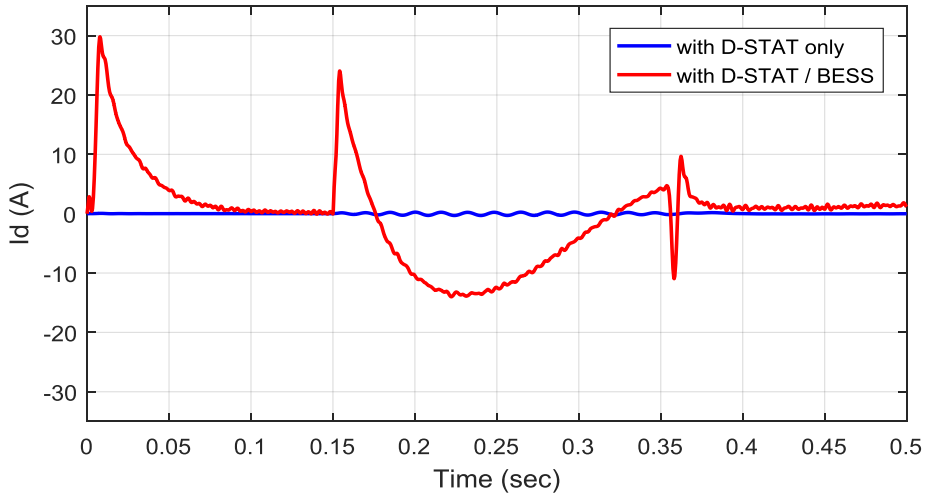

Figure 5-21 Comparison of d components of the support current

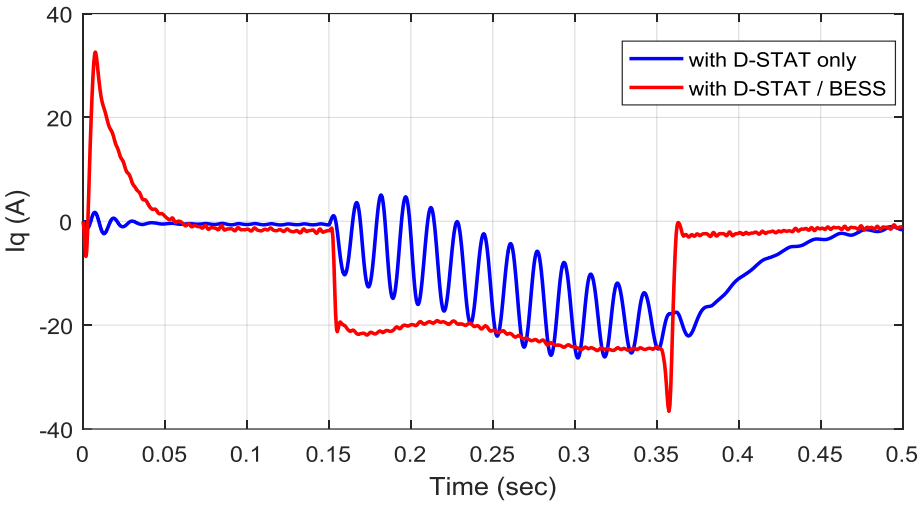

Figure 5-22 Comparison of q components of the support current

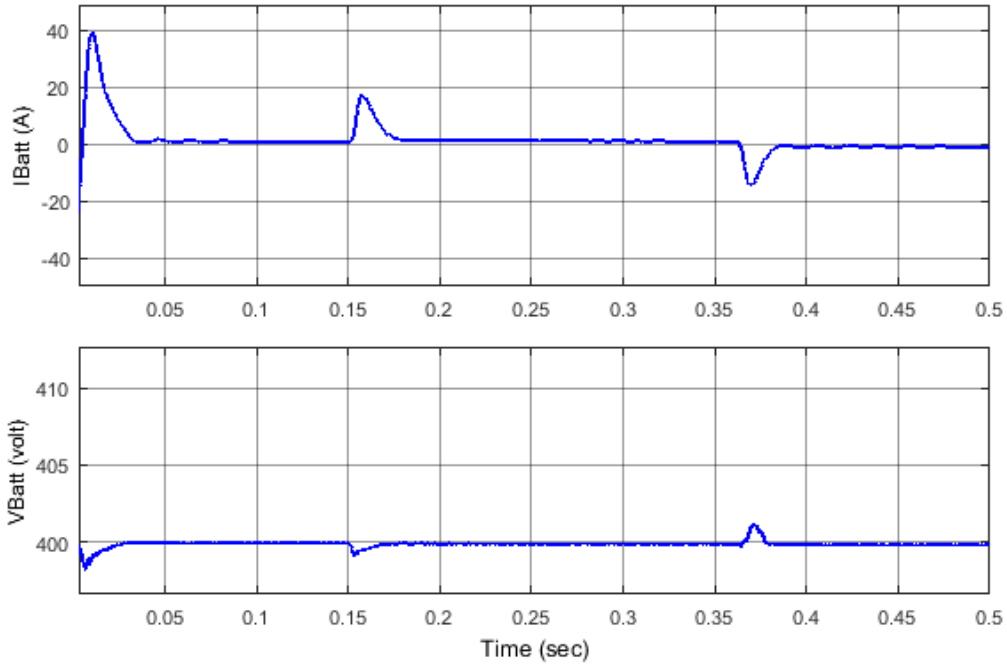

Figure 5-23 The current and voltage magnitude of the battery storage

5.4.4 Comparison between fuzzy-tuned PI controller and the standard PI controller (faults applied)

The fuzzy logic integration with the standard PI controller is modelled in a D-STATCOM based battery storage system under the fault condition described

above. Figure 5-24 shows the comparable dynamic responses of the voltage at the PCC for both controllers (the standard PI controller and adapted PI-fuzzy controller) with the fault lasting from t = 0,15 s, to t = 0.35 s. As can be seen, the magnitude of the voltage is maintained within about 1pu for both controllers. Figure 5-25 shows the voltage waveform of the DC-side with both the PI-fuzzy and conventional PI controller. It is clear from Figure 5-25 that the DC-side voltage response of the D-STATCOM with fuzzy controller is better than the response with the standard PI controller. In particular, it is seen that the values of the dips in the DC-side voltage with fuzzy application are reduced compared to the values of the dips for the voltage with PI controller. Further, the recovery time - the time taken for the dc bus voltage to return to a steady state - was significantly smaller when the fuzzy logic controller was used. This result affects the time required by the grid currents to return to steady state conditions. A summary of the comparable performances between the fuzzy -tuned PI and the standard PI controller is shown in Table 5-2. It is worth remarking that, to a certain extent the voltage response of the PCC is similar for both controllers. Both responses follow a similar pattern but the fuzzy logic controller is more effective in controlling the dynamic response of the DC voltage than the voltage response at the PCC (Figure 5-24 and 5-25). The relative responses of the I_d and I_q components of the D-STATCOM support current are shown in Figure 5-26 and Figure 5-27 respectively.

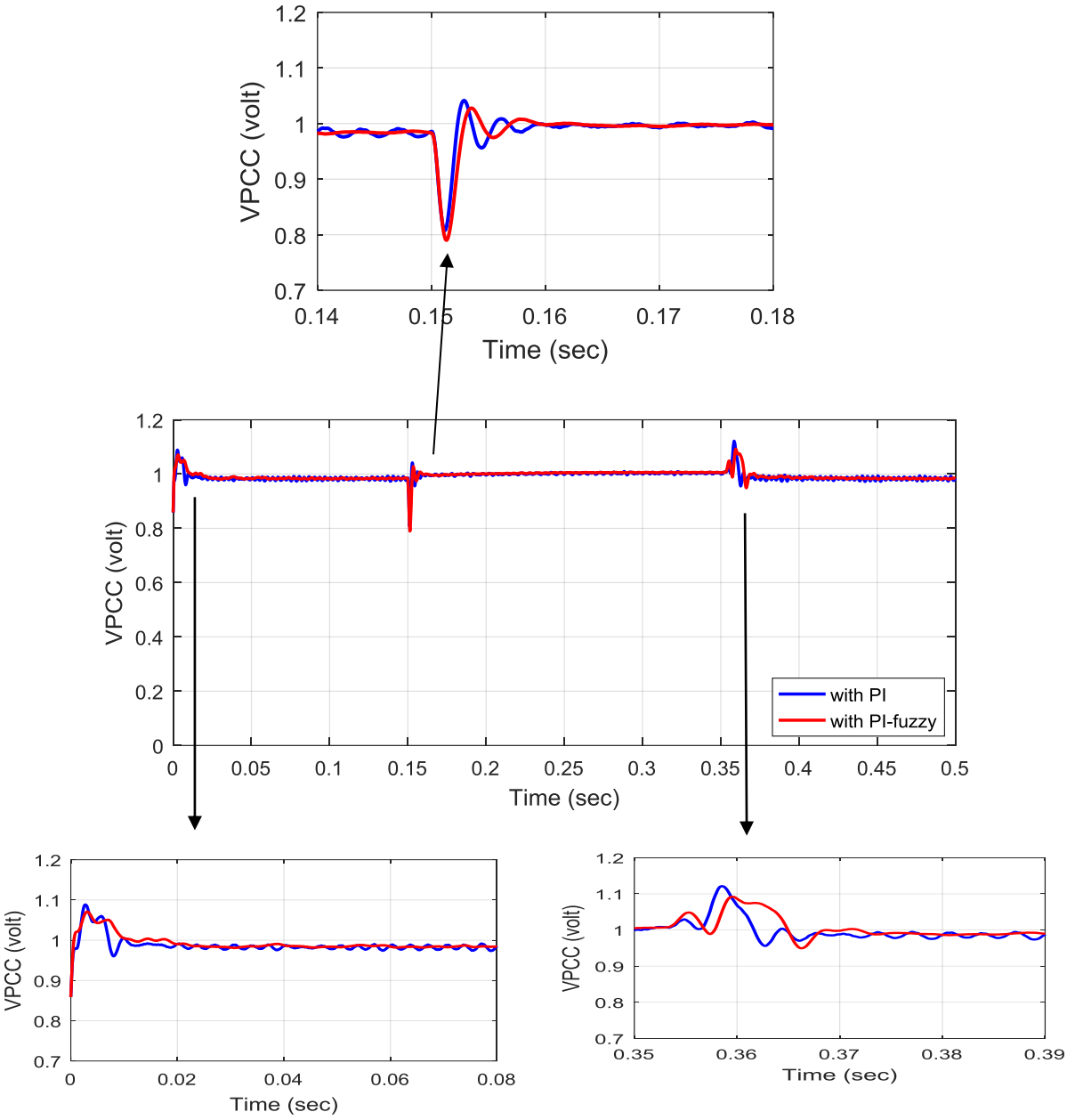

Figure 5-24 Voltage magnitude at PCC point

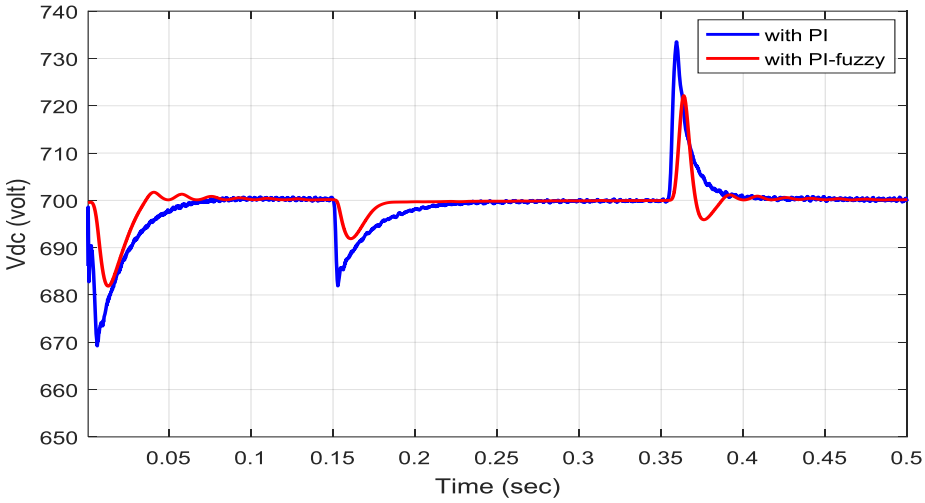

Figure 5-25 DC side voltage

Table 5-2 Comparison of the system performance

System performance		Standard PI-controller		Fuzzy -tuned PI	
		VPCC (pu)	Vdc (volt)	VPCC (pu)	Vdc (volt)
at Start-up	Max peak/Min dip (pu /volt)	1.09	669	1.07	682
	Settling time (msec)	12	70	10	50
at Fault initiation t = 0.15 s	Min dip	0.81	685	0.79	692
	Settling time (msec)	10	100	10	33
at Fault clearance t = 0.35 s	Max peak (pu /volt)	1.12	733.6	1.09	722.12
	Settling time (msec)	20	40	20	32.5

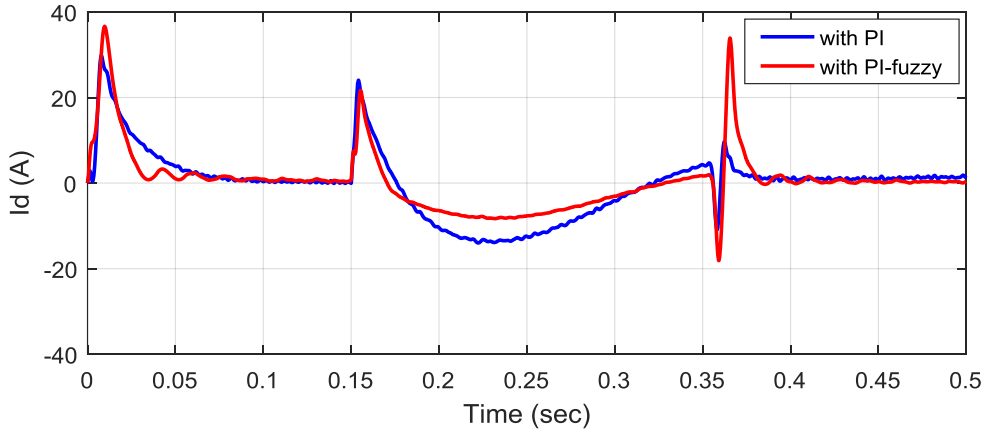

Figure 5-26 Comparison of d components of the support current

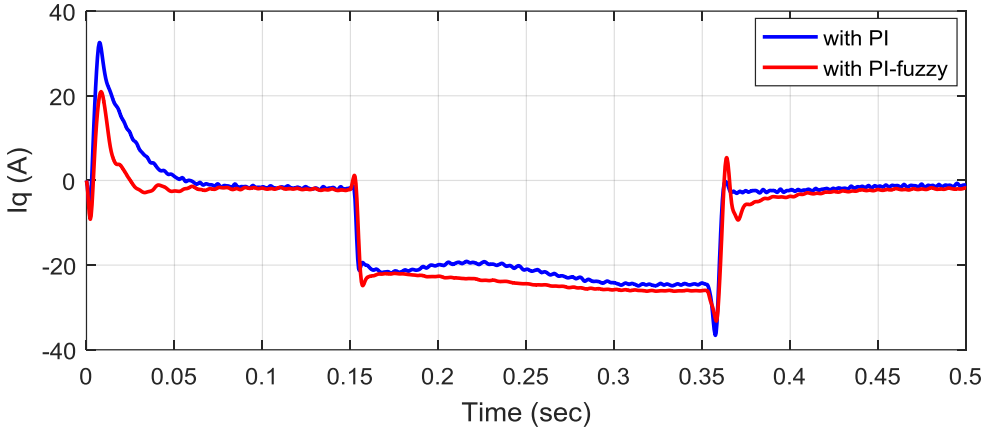

Figure 5-27 Comparison of q components of the support current

Figure 5-28 and Figure 5-29 show a comparison of control strategies for PCC voltage and DC-side voltage with fault of 2 s duration, from t = 0.5 s to t = 2.5 s. The results again demonstrate the effectiveness of D-STATCOM based BESS compensator, as the system is able to mitigate the voltage sag successfully for a longer fault period. This confirms that the D-STATCOM with BESS works very well to provide the grid a good ride through capability even when the time period of fault was as long as 2 s. A summary of the performance comparison between the fuzzy -tuned PI and the standard PI controller is shown in Table 5-3.

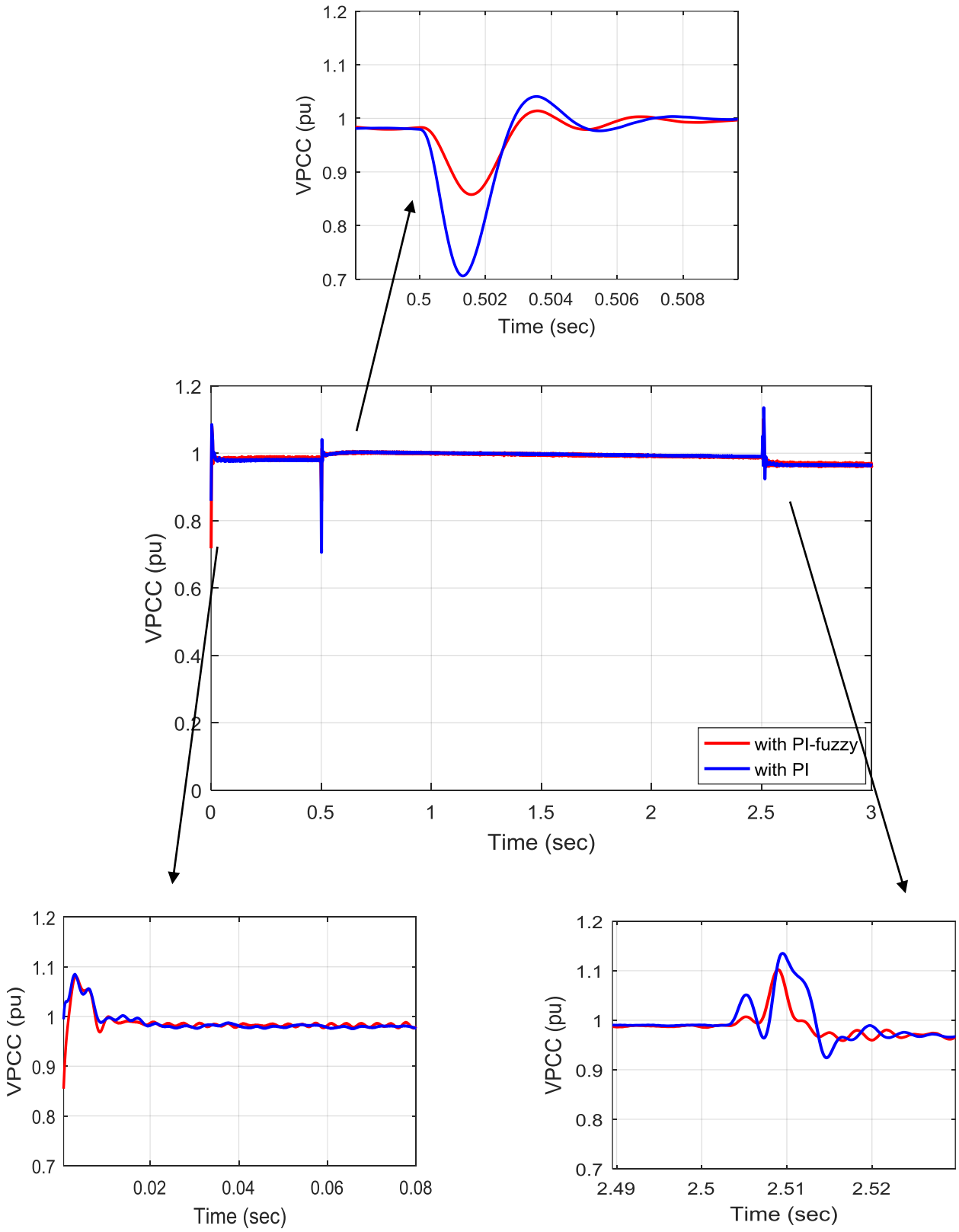

Figure 5-28 Voltage magnitude at PCC point

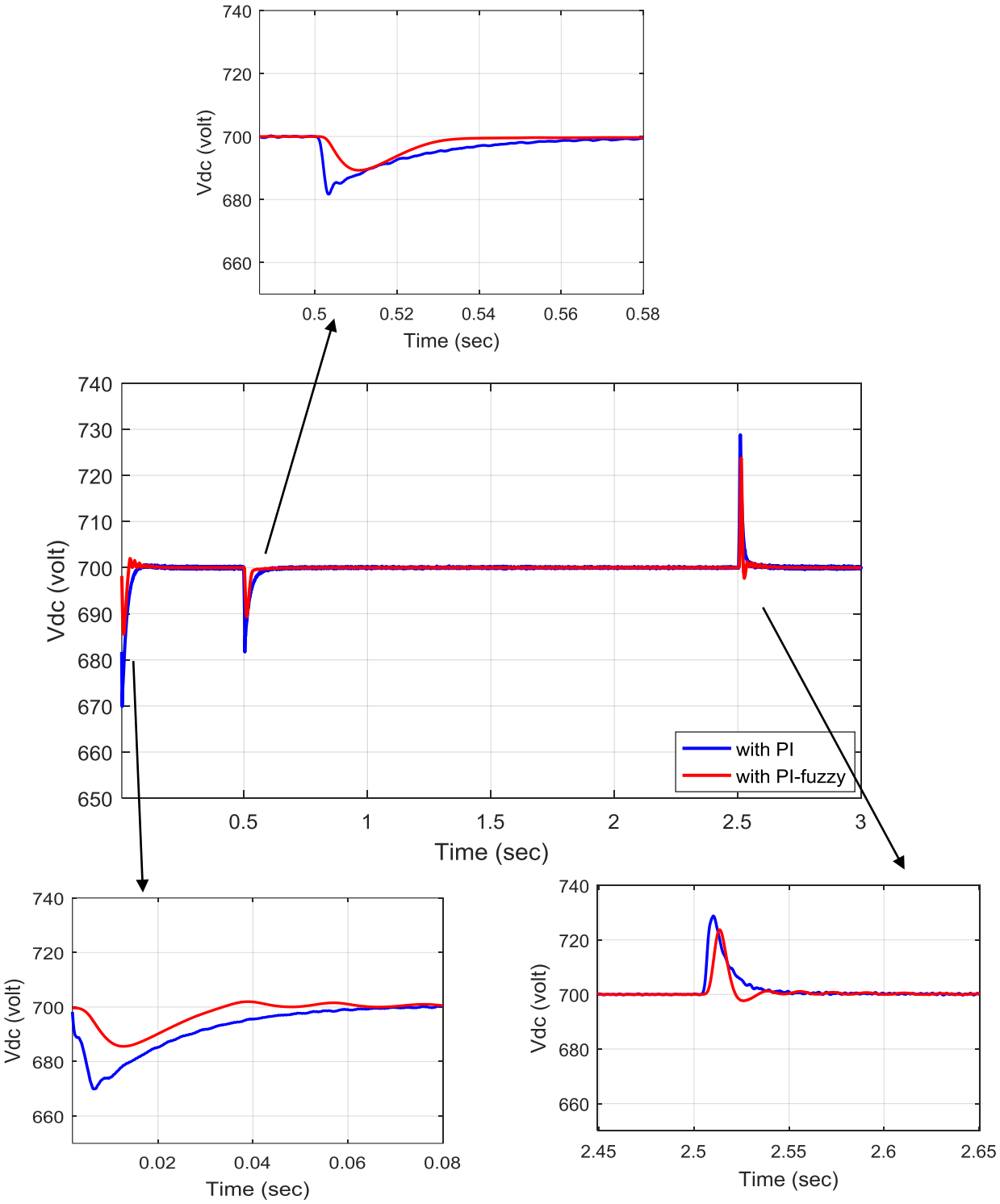

Figure 5-29 DC side voltage

Table 5-3 Comparison of system performance for fuzzy-tuned PI and standard PI controller

System performance		Standard PI-controller		Fuzzy -tuned PI	
		VPCC (pu)	Vdc (volt)	VPCC (pu)	Vdc (volt)
at Start-up	Max peak/Min dip (pu /volt)	1.085	670	1.081	685.56
	Settling time (msec)	10	80	10	45
at Fault initiation t =0.5 s	Min dip	0.7	681	0.86	689.3
	Settling time (msec)	7	80	7	38
at Fault clearance t =2.5 s	Max peak (pu /volt)	1.135	728.81	1.10	723.75
	Settling time (msec)	17	36.1	17	34

5.5 Summary

This chapter has presented a modified configuration of D-STATCOM based energy storage for three phase grids operating under balanced voltage sags. The battery storage unit, in particular the high performance high power density one used in the D-STATCOM device, acts as an effective power compensator and voltage controller at the point of common coupling of the distribution grid. Facilitated by a D-STATCOM structure, the DC-DC bidirectional charging system is able to exchange the power with grid, and therefore serves as additional resources to support the voltage stability of the distribution grid. Simulation results highlighted the ability of the energy storage system to enhance power system stability during the fault condition. D-STATCOM can avoid overcurrent tripping while mitigating adverse effects of grid faults. A performance comparison has been made of the D-STATCOM based battery storage system with fuzzy-tuned PI and standard PI controllers. The conventional linear PI controller gave acceptable results under normal conditions, but the proposed fuzzy controller allowed automated tuning that captured the nonlinearities of the microgrid and provided superior performance over varying operating conditions.

6 Chapter Six: D-STATCOM Based Hybrid Energy Storage System (HESS)

6.1 Introduction

A Microgrid is a low voltage network which connects distributed generators, and a cluster of loads that act as a single controllable entity with respect to the grid [187] [188]. With a significant proportion of distributed generation including renewable resources, there is an urgent need worldwide to speed up the implementation of energy storage unit infrastructures at the distribution level. These storages systems will help ease the integration of renewable energy into the grid and increase the momentum toward power generation by clean energy resources. On the other hand, a large increase in energy storage as an electrical load can create new challenges to the stability of the grid at distribution levels. The recent advances in smart grid technologies will enable enhanced utilization of ESS and D-FACTS devices as active and reactive power devices. If implemented appropriately, these new energy devices can become a reservoir of new resources to provide system-wide services, rather than an energy drain on the grid. With renewable energy, distributed generators and other energy storage units are now accepted as key 'players' in the next generation of electric grids at distribution level. There has been a fundamental paradigm shift from passive to active networks [9] [189]. Among these sources, battery storage units are one of the most rapidly growing technologies with D-STATCOM, as explained in Chapter Four.

The battery energy storage system (BESS) has relatively greater energy capacity but the drawback of a small rate of discharge and reduced life time when subject to high power variations [190]. The supercapacitor storage device (SC) has a high power and discharge rate that can deliver or absorb large quantities of power with a fast response time. But with low energy storage capacity compared with batteries. Thus the SC's proper application in high power demand for short periods of time [142][191]. This chapter provides a detailed analysis of a novel approach using a modified D-STATCOM converter supplied by a dual DC source (battery and SC). Based on the analysis in this chapter two control strategies, a

standard controller with low pass filter and a new sugeno-fuzzy control strategy, are proposed and tested for Hybrid Energy Storage System (HESS) management. Both strategies are designed using the concept that the SC is adapted to simultaneously inject and absorb the quantity of instantaneous power required and average power requirement is provided by the battery. This chapter explains all aspects of the procedure used for the design, which was tested using simulation.

6.2 Configurations and modelling of the HESS

The modelling and the configurations of general types of HESS topologies are presented in this section.

6.2.1 Configurations

Energy storage systems combining battery and SCs have produced effective solutions for energy management in high performance automotive and avionics systems. Various configurations of HESS, employing battery and SC have been studied[192] [193] [194]. The major battery/SC configurations: passive, semi-active, and fully active are illustrated in Figure 6-1.

In the passive type the battery and SC combinations are connected in parallel and directly to the DC side without any power electronic interface as shown in Figure 6-1(a). This type is considered as being one of the simplest and of lowest cost. However, this type cannot control the power distribution between the battery and SC. Therefore, the passive HESS performance is compromised because the energy storage units are connected in an uncontrollable manner. The semi-active HESS types are presented in Figure 6-1 (b and c) which utilize a single DC-DC converter. In Figure 6-1(b) the battery storage is connected to the DC side through the DC-DC converter and the combination connected in parallel with the SC. In Figure 6-1(c) the SC is connected in parallel with the DC-DC converter and the battery storage is connected in parallel with the combination. Thus, compared to the passive type in Figure 6-1(a), voltage stability of the DC side may be achieved. In addition, the energy stored in the battery unit in Figure 6-1(b)

and the SC unit in Figure 6-1(c) can be used more efficiently if it does not have to pass through a DC-DC converter.

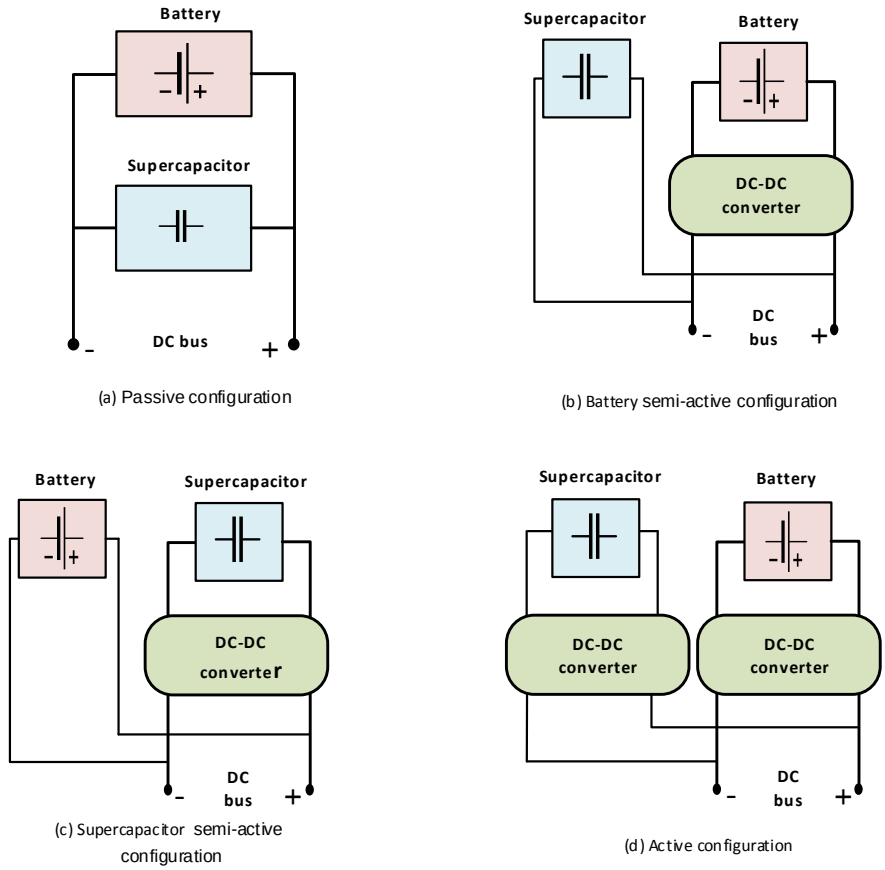

Figure 6-1 HESS topologies

However, voltage matching is required between the storage SC in Figure 6-1(b) and battery in Figure 6-1(c) and the DC side. The third configuration, shown in Figure 6-1(d), is a fully active HESS type. In this configuration two DC-DC converters are employed to connect the energy storage devices (battery and SCs) in parallel with the DC side. Although the control system complexity is increased, this type of HESS can control precisely the required power sharing between the battery and SC. This configuration could accurately manage the power distribution of the two storage devices according to the control management algorithm. Hence, a good system performance is achieved.

Generally, the recent literature [195] reports the investigated of the capability of the active HESS configuration to give better performance compared to the passive and semi-active types in the electrical vehicle sector and with microgrid

applications as explained in [196]. Thus, in this study, the active HESS configuration is proposed based on the D-STATCOM application.

6.2.2 Modelling of HESS topology

The general structure of the D-STATCOM configuration with the HESS is shown in Figure 6-2. The HESS is connected to DC side of the D-STATCOM converter through the bidirectional DC-DC converters. These converters are connected between the energy storage systems (battery and the SC) and the DC side of the converter to maintain the voltage constant on the DC side of the D-STATCOM by controlling the flowing of energy to/from the energy storage combination and grid.

Typically, the battery storage unit is the main energy storage element in the HESS configuration. “Currently, the main commercially available cell chemistries are Lead-Acid, Nickel Cadmium (NiCad), Nickel Metal Hydride (NiMH), Lithium-Ion” [197] [198]. The BESS type presented in this thesis is based on the modelling of the Lithium -Ion (Li-Ion) cell. In this chapter, the Li-Ion battery model [184] , as described in Section 5.3.2 is used to analyse the dynamic performance of the HESS with simulation of voltage regulation under different conditions.

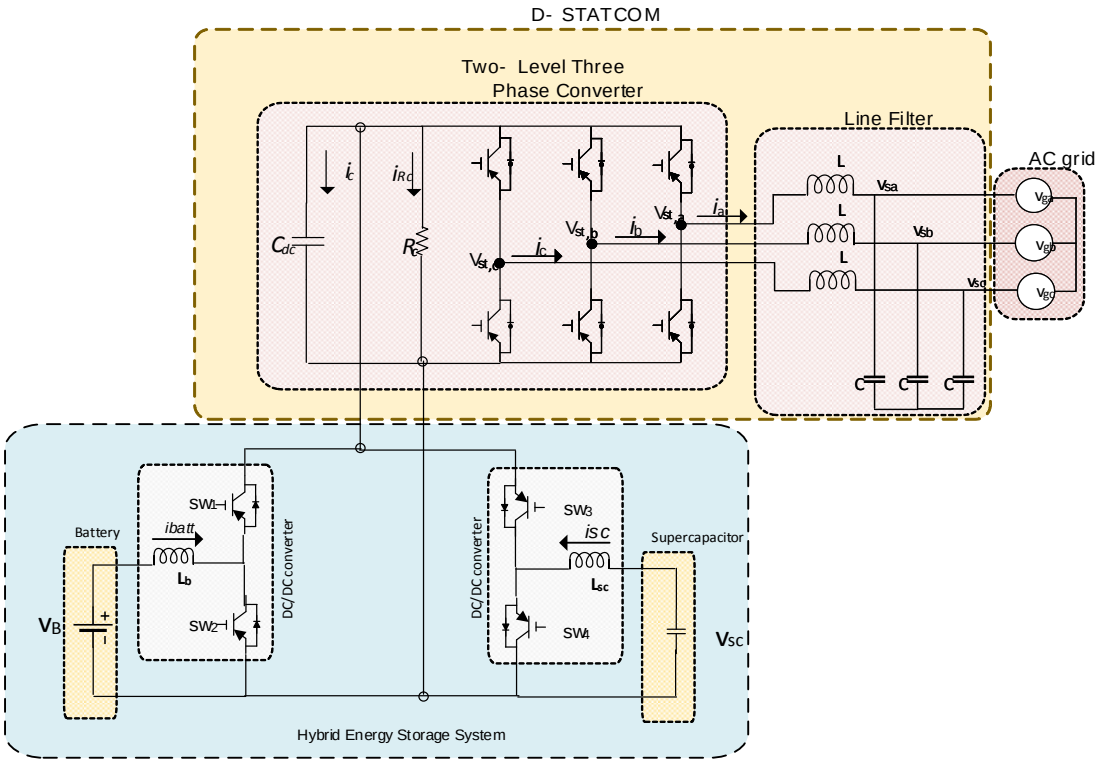

Figure 6-2 D-STATCOM with HESS configuration

To enable simulation of a battery/SC hybrid energy storage configuration, it is also necessary to model a SC storage unit. A classical SC-capacitance model is presented based on experimental findings which are supported by results reported from relevant studies [199] [200] [201] [202].

6.2.2.1 Modelling for the Supercapacitor module

A SC is an enhanced capacitor with 100 to 1000 times the capacitance per unit volume compared to a conventional electrolytic capacitor [199]. The equivalent circuit of the SC is a capacitance, C, with parallel resistance, R_p, and series resistance, R_s [201] as shown in Figure 6-3.

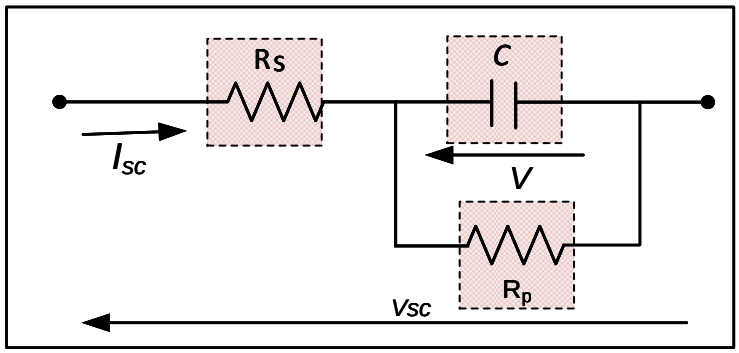

Figure 6-3 The equivalent circuit of supercapacitor

The series resistance is also known as equivalent series resistance (ESR, R_s) and affects energy loss during charging and discharging. Leakage resistance which is represented by the parallel resistance also consumes energy during self-discharge of the capacitor. In practice, the parallel resistance value is much greater than the series resistance and thus can be ignored, especially in high power applications [199].

Thus, the voltage profile of SC can be represented in two parts, a capacitive part and a resistive part. The capacitive part represents the change in voltage resulting from capacitor energy change. The voltage change due to the ESR represents the resistance part

Capacitive part is written as:

$$\frac{dV(t)}{dt} = \frac{-V(t)}{R_p\, C} + \frac{I_{sc}}{C} \quad \textbf{(6-1)}$$

The resistance part is expressed as:

$$V_R = R_s\, .\, I_{sc} \quad \textbf{(6-2)}$$

Where I_{sc} is the SC current

The total voltage change during charging or discharging of the SC can be obtained from Equations (6-12) and (6-13).

$$V_{sc}(t) = R_s . I_{sc} + V(t) \quad \textbf{(6-3)}$$

The SC voltage level is based on the state of charge (SOC) as [203]:

$$SOC = \frac{V_{sc}^2}{V_{sc,0}^2} \quad \textbf{(6-4)}$$

where:

$V_{sc,0}$ is the voltage for a fully charged SC and V_{sc} is the actual voltage of the SC.

6.2.2.2 Modelling of the parallel DC-DC converters System

The HESS with bidirectional DC-DC converters can be representing as the equivalent circuit shown in Figure 6-4. It is assumed to be a balance system and the storage units are modelled as source buses. Power losses in the switches can be represented by resistances (R_{LB} and R_{Lsc}) connected in series with the inductors of the converters (L_B and L_{sc}). The parallel capacitor represents the DC side of the D-STATCOM. Thus, the dynamic equations of the converter system can be expressed as follows:

$$L_B \frac{di_B}{dt} = V_B - (1 - d_B)V_{DC} - i_B R_{LB} \quad \textbf{(6-5)}$$

$$L_{sc} \frac{di_{sc}}{dt} = V_{sc} - (1 - d_{sc})V_{DC} - i_{sc} R_{Lsc} \quad \textbf{(6-6)}$$

$$C_{dc}\frac{dV_{DC}}{dt} = (1-d_B)i_B + (1-d_{sc})i_{sc} - i_{DC} \quad \textbf{(6-7)}$$

Where i_{DC} is the total current required by the ESS and is the difference between the main power source and load currents, d_B is duty cycle of the battery converter and d_{sc} is duty cycle of the SC converter.

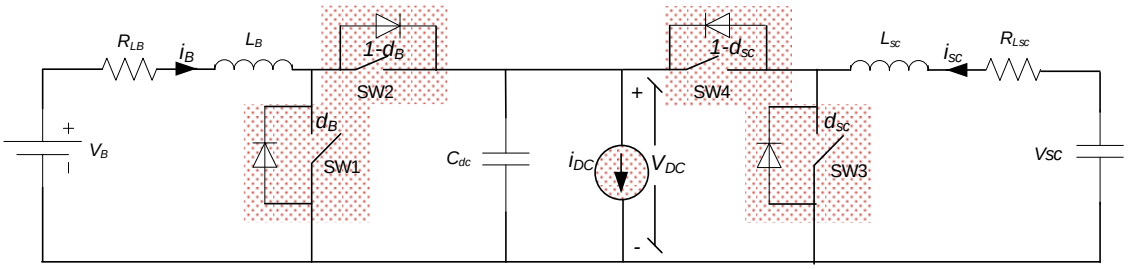

Figure 6-4 Equivalent circuit of HESS

An equivalent circuit of the DC-DC converters shown in Figure 6-4 can be represented as a time-average model, see Figure 6-5.

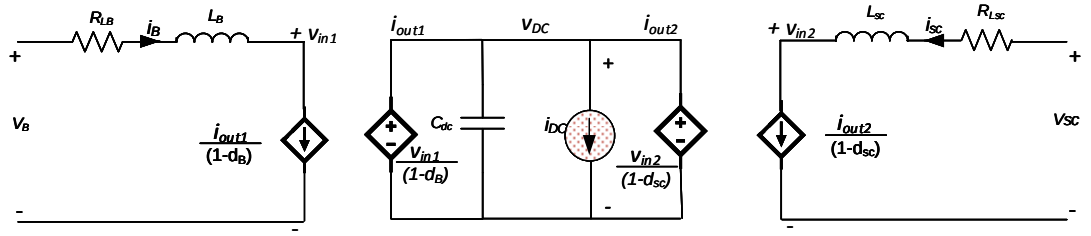

Figure 6-5 Equivalent circuit of HESS in time-average model [204]

Assuming the HESS is operating at an equilibrium operating point, Equations (6-5) to (6-7) may be subjected to linearization around an equilibrium operating point [204]. Thus, the equations for a two bidirectional converter system are:

$$L_B\frac{di_B^0}{dt} = V_B^0 - (1-D_B)V_{DC}^0 + d_B^0 V_{DC} - i_B^0 R_{LB} \quad \textbf{(6-8)}$$

$$L_{sc}\frac{di_{sc}^0}{dt} = V_{sc}^0 - (1-D_{sc})V_{DC}^0 + d_{sc}^0 V_{DC} - i_{sc}^0 R_{Lsc} \quad \textbf{(6-9)}$$

$$C_{dc}\frac{dV_{DC}^0}{dt} = (1-D_B)i_B^0 + (1-D_{sc})i_{sc}^0 - I_B d_B^0 - I_{sc}d_{sc}^0 - i_{DC}^0 \quad \textbf{(6-10)}$$

where, D_B and D_{sc} are a linearised values for d_B and d_{sc}

From Equations (6-8)(6-9) and (6-10) the state space equation has the general form of:

$$\dot{x}(t) = Ax(t) + Bu(t) + Fv(t)$$

$$y(t) = Cx(t)$$

Thus, the state space model of HESS can be formed as:

$$\frac{d}{dt}\begin{bmatrix} i_B^0 \\ i_{sc}^0 \\ V_{DC}^0 \end{bmatrix} = \begin{bmatrix} -\frac{R_{LB}}{L_B} & 0 & -\frac{(1-D_B)}{L_B} \\ 0 & -\frac{R_{Lsc}}{L_{sc}} & -\frac{(1-D_{sc})}{L_B} \\ \frac{(1-D_B)}{C_{dc}} & \frac{(1-D_{sc})}{C_{dc}} & 0 \end{bmatrix}\begin{bmatrix} i_B^0 \\ i_{sc}^0 \\ V_{DC}^0 \end{bmatrix} + \begin{bmatrix} \frac{V_{DC}}{L_B} & 0 \\ 0 & \frac{V_{DC}}{L_{sc}} \\ -\frac{I_B}{C_{dc}} & -\frac{I_{sc}}{C_{dc}} \end{bmatrix}\begin{bmatrix} d_B^0 \\ d_{sc}^0 \end{bmatrix} + \begin{bmatrix} \frac{1}{L_B} & 0 & 0 \\ 0 & \frac{1}{L_{sc}} & 0 \\ 0 & 0 & -\frac{1}{C_{dc}} \end{bmatrix}\begin{bmatrix} V_B^0 \\ V_{sc}^0 \\ i_{DC}^0 \end{bmatrix} \quad \textbf{(6-11)}$$

The LTI dynamics matrix $A = \begin{bmatrix} -\frac{R_{LB}}{L_B} & 0 & -\frac{(1-D_B)}{L_B} \\ 0 & -\frac{R_{Lsc}}{L_{sc}} & -\frac{(1-D_{sc})}{L_B} \\ \frac{(1-D_B)}{C_{dc}} & \frac{(1-D_{sc})}{C_{dc}} & 0 \end{bmatrix}$

And the corresponding input matrix $B = \begin{bmatrix} \frac{V_{DC}}{L_B} & 0 \\ 0 & \frac{V_{DC}}{L_{sc}} \\ -\frac{I_B}{C_{dc}} & -\frac{I_{sc}}{C_{dc}} \end{bmatrix}$, $F = \begin{bmatrix} \frac{1}{L_B} & 0 & 0 \\ 0 & \frac{1}{L_{sc}} & 0 \\ 0 & 0 & -\frac{1}{C_{dc}} \end{bmatrix}$

and the state vector $x^T = \begin{bmatrix} i_B^0 \\ i_{sc}^0 \\ V_{DC}^0 \end{bmatrix}$, $u^T = \begin{bmatrix} d_B^0 \\ d_{sc}^0 \end{bmatrix}$, $v^T = \begin{bmatrix} V_B^0 \\ V_{sc}^0 \\ i_{DC}^0 \end{bmatrix}$

$y = [i_B^0 \quad i_{sc}^0 \quad V_{DC}^0]^T$, $C = [1\ 1\ 1]$,

6.3 Standard HESS control strategy

The control diagram for a hybrid D-STATCOM converter with dual DC sources has been designed as shown in Figure 6-6 .The main target of this control algorithm is that the battery compensates for slow disturbances, whereas the SC compensates for fast disturbances in grid voltage. “It is assumed that state-of-charge (SOC) of energy storage components are within the acceptable limits throughout the work” [205]. Therefore, the error signal is produced by comparing the measured voltage of the DC side, V_{DC} , with a DC reference voltage, V_{DC}^*. The error drives the PI control which produces the total required current, I_{tot}^*, from the ESS. This current, I_{tot}^*, is separated into its average power value and dynamic power value by a low pass filter. The average current value is given as reference battery current, I_B^*, to the current control loop of the battery to produce the duty cycle $D_{B..}$ The duty cycle is fedforward to the PWM to generate the appropriate switching signals for the DC-DC converter battery switches. The dynamic current value is given as the reference SC current, I_{sc}^*, to the current control loop of the SC to produce the duty cycle $D_{sc..}$. The duty cycle is fedforward to the PWM to obtain the appropriate switching signals for the DC-DC converter switches of the SC.

The low-frequency component, I_{LPF}^*, of I_{tot}^* is:

$$I_{LPF}^* = F_{LPF}(I_{tot}^*) \quad \textbf{(6-12)}$$

where, $F_{LPF}(..)$ is the function of the low pass filter

I_{LPF}^* is fed to the rate limiter to control how fast the battery charges and discharges, so the reference current to the battery can be written as:

$$I_B^* = F_{limter}(I_{LPF}^*) \quad \textbf{(6-13)}$$

where $F_{limter}(..)$ is the rate limiter function

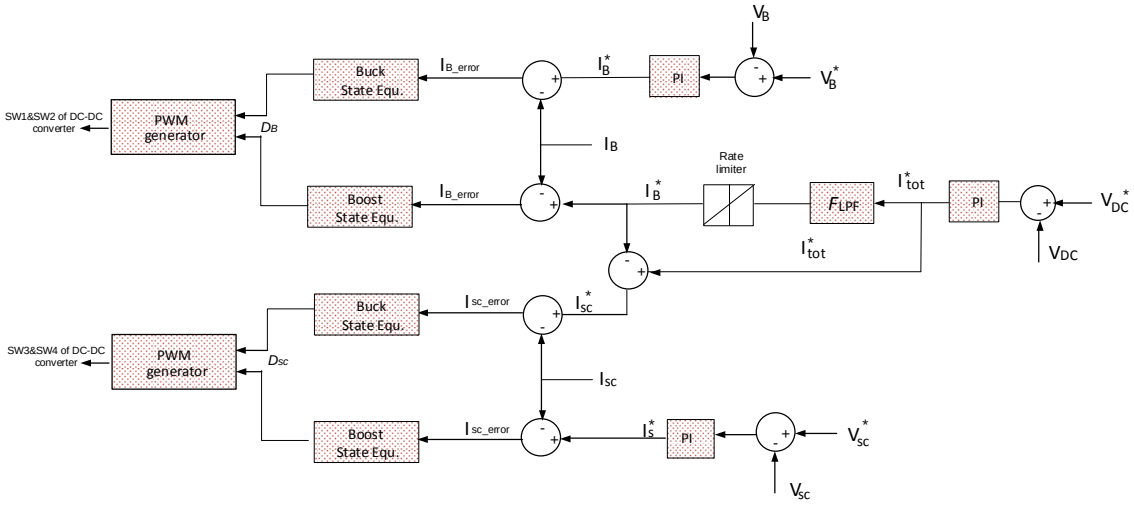

Figure 6-6 HESS controller

I_B^* and the actual battery current, I_B, are compared and the error signal drives the PI controller to obtain the duty ratio D_B which is required to produce the appropriate switching signals corresponding to the battery switches SW1 and SW2, shown in Figure 6-4. The high frequency part I_{HF}^* is represented as:

$$I_{HF}^* = I_{tot}^* - I_B^* \quad \textbf{(6-14)}$$

It may not be possible for the battery to track I_B^* instantly [205]. Thus, the uncompensated battery power, P_{uncomp}, will be:

$$p_{uncomp} = (I_{HF}^* + I_B^*) * V_B \quad \textbf{(6-15)}$$

where V_B is the battery voltage.

P_{uncomp} will be compensated for by means of the SC. In which case, the reference current of the SC will be:

$$I_{sc}^* = \frac{p_{uncomp}}{v_{sc}} = (I_{HF}^* + I_B^*) * \frac{V_B}{V_{sc}} \quad \textbf{(6-16)}$$

where V_{sc} is the SC voltage.

I_{sc}^* and the actual current I_{sc} are compared and the error signal will drive the PI controller to obtain the duty ratio D_{sc} which is required to produce the appropriate

switching signals corresponding to SC switches SW3 and SW4, shown in Figure 6-4. The overall control strategy of the HESS is presented inFigure 6-7.

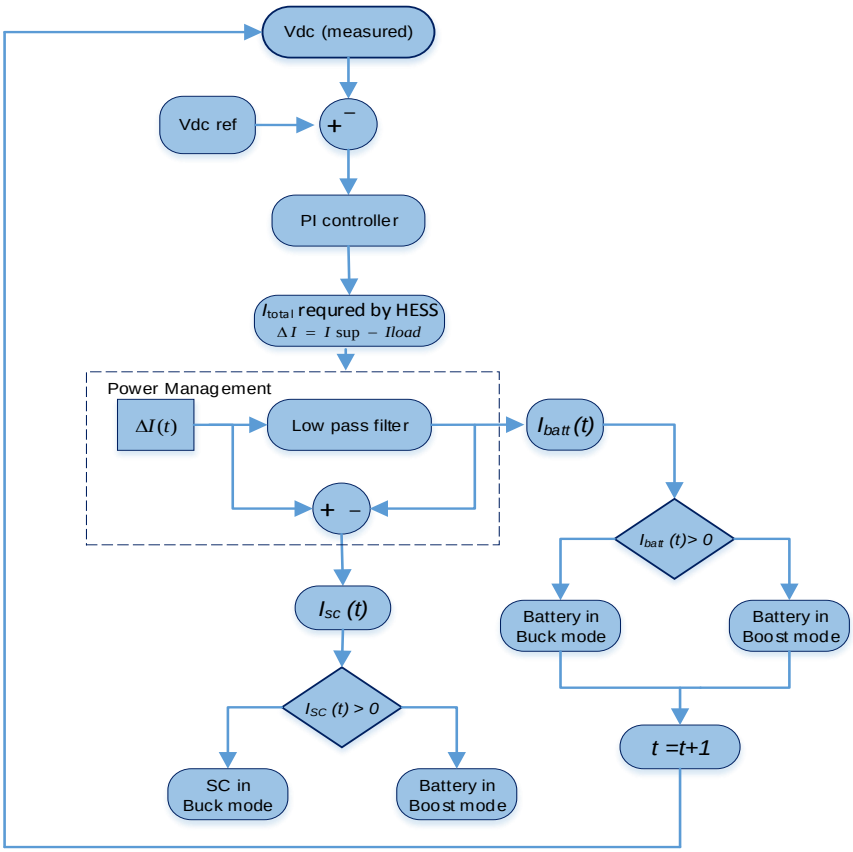

Figure 6-7 Overall control strategy of HESS

6.3.1 Constraint conditions

The above strategy for the HESS does not include the constraints on the grid and storage units, which are important when simulating the control strategy. To keep a constant DC side voltage at the setting value, the power should be balanced between the sources and loads. The system power balance constraint is:

$$P_{source} + P_{ESS} = P_{load} \tag{6-17}$$

where P_{source} is the power of the main supply in the grid, P_{ESS} represents the battery and SC power and P_{load} is the load power.

This power balance is restricted by other constraints such as minimum and maximum power flow from the battery and SC:

$$P_{Bmin} \ll P_B \leq P_{Bmax} \quad \textbf{(6-18)}$$

$$P_{scmin} \ll P_{sc} \leq P_{scmax} \quad \textbf{(6-19)}$$

where P_B and P_{sc} are the actual power of the battery and SC respectively, P_{Bmin} and P_{Bmax} are, respectively, the lower and higher power boundaries of the battery. P_{scmin} and P_{scmax} are, respectively, the lower and higher power boundaries of the SC.

Another critical constraint related to the energy storage units, is the state of charge (SOC) constraint: that the charge stored in either SC or battery should not exceed the maximum capacity nor drop below the permitted minimum limit. It is required to maintain the battery and SC units within the desired boundaries to avoid depletion or overcharging.

The SOC constraints of the battery and SC are given as:

$$SOC_{Bmin} \ll SOC_B \leq SOC_{Bmax} \quad \textbf{(6-20)}$$

$$SOC_{scmin} \ll SOC_{sc} \leq SOC_{scmax} \quad \textbf{(6-21)}$$

where SOC_B and SOC_{sc} are the actual SOC of the battery and SC respectively, SOC_{Bmin} and SOC_{Bmax} are the lower and higher SOC boundaries of the battery respectively. SOC_{scmin} and SOC_{scmax} the lower and higher SOC boundaries of the SC respectively.

The SOC limits for a battery are, typically, between 40% and 85% and for a SC within 25% and 85%. In addition, the control parameters are constrained in order to meet bus voltage restrictions. According to British Standard BS 7697 [206] [207] the bus voltage constraint is:

$$0.94pu < V_{bus} < 1.1pu \quad \textbf{(6-22)}$$

6.3.2 Control loops design for HESS

As stated in [186], the same transfer function of the DC-DC converter is valid during both charging (buck mode) and discharging (boost mode) processes.

Thus, the two modes can used in a unified controller in a complementary way by switching between the two modes. For this system of operation, the HESS controller is designed according to boost operation mode.

The control design of the HESS is included in three control loops: external voltage control loop and two internal current control loops [205] as presented in Figure 6-6. Basically, current control loops are intended to control the flow of distributed current between the battery and SCs, using the inductors of the DC-DC converters. While a voltage loop is applied to keep the variation of the constant DC side voltage within an acceptable range.

The delivery and absorption of current flow rates of the SC are faster than for battery storage [208]. Thus, the PI compensators are designed according to the SC power loop. To prevent oscillation and to distribute the transient variations to the SC, the bandwidth (B.W) of the SC current loop is kept greater than the bandwidth of the battery current loop. The B.W is $f_{sw}/6$ for the SC while the battery bandwidth is $f_{sw}/10$, where f_{sw} is switching frequency.

The current control loop response is faster than the response of the voltage control loop. So, the B.W of the outer voltage loop is kept less than for the SC current control loop. A 10kHz switching frequency is used in this design.

A. Current control loop of supercapacitor

The block diagram of current control loop design of the SC is illustrated in Figure 6-8. The reference current of the SC is produced from the outer voltage controller and the error signal between the reference and actual current values drives the current controller GPI(sc). The transfer function of the SC current to the $d_{sc}^{\sim}$ is given as [205] :

(6-23)

where $i_{sc}^{\sim}$ and $d_{sc}^{\sim}$ are small changes in the SC current and duty cycle of the SC converter.

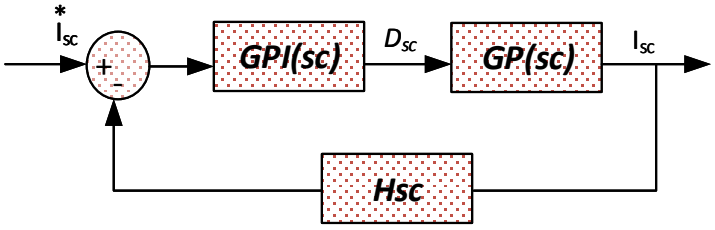

Figure 6-8 Current control loop of supercapacitor

The transfer function of the PI controller is:

$$GPI(sc) = Kp_{sc} + \frac{Ki_{sc}}{s} \tag{6-24}$$

B. Voltage control loop of HESS

Figure 6-9 presents the block diagram of the outer voltage controller. The transfer function of this loop is given as [205]:

$$GP(V) = \frac{V_{DC}^{\sim}}{i_{sc}^{\sim}} = \frac{R_C(1-D_{sc})\left(1 - \frac{L_{sc}}{R_C(1-D_{sc})^2}s\right)}{2 + R_C C_{dc} s} \tag{6-25}$$

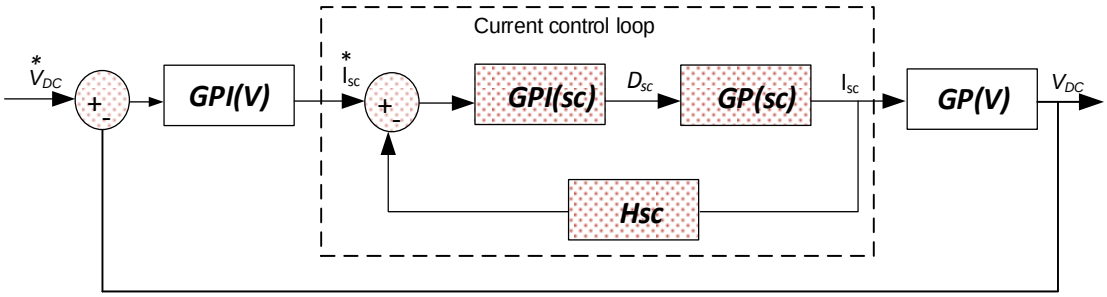

Figure 6-9 Voltage control loop of HESS

The transfer function of the PI voltage controller is [205] :as:

$$GPI(V) = Kp_V + \frac{Ki_V}{s} \tag{6-26}$$

C. Current control loop of battery

The block diagram of the current control loop of the battery is illustrated in Figure 6-10. The transfer function of the battery current to the $d_B^{\sim}$ is given as [205] :

$$GP(B) = \frac{i_B^{\sim}}{d_B^{\sim}} = \frac{V_{DC}C_{dc}\,s + 2\frac{V_{DC}}{R_C}}{L_B C_{dc} s^2 + \frac{L_B}{R_C} s + (1 - D_B)^2} \quad \textbf{(6-27)}$$

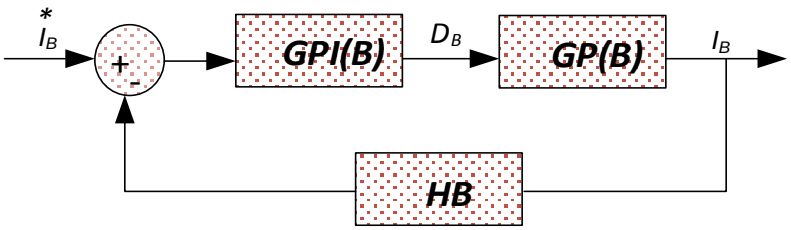

Figure 6-10 Current control loop of battery

where $i_B^{\sim}$ and $d_B^{\sim}$ are small changes in battery current and duty cycle of the battery converter. The transfer function of the PI controller is [205]:

$$GPI(B) = Kp_B + \frac{Ki_B}{s} \quad \textbf{(6-28)}$$

Connecting inductors were $L_{sc} = 10\,\mathrm{mH}$ and $L_B = 15\,\mathrm{mH}$, the resistor was $R_{dc} = 10\mathrm{K}\Omega$ and D_B=*0.3*, D_{sc}=*0.5* see Figure 6-4 are used in the design of the PI controllers. The design and tuning of the control loops are carried out following standard procedure of the MATLAB SISO tool box.

6.4 Fuzzy logic design of controller for HESS

6.4.1 The general scheme of power management

As advanced bidirectional power paradigms, microgrids require fast-online control and management of power to work instantaneously and jointly with the main utility grid in order to supply a reliable service. Generally, microgrids have used combinations of energy storage systems such as battery and SC for providing efficiency performance and smart grid operation. The lifespan of the battery is extended by the high power density of the SC [209] [152]. From other side, to meet system power requirements in microgrids, it is crucial to keep the SOC of the battery and SC within acceptable ranges because of the uncertainties

inherent in renewable energy sources. Thus, power control management is an important part of ensuring reliable and stable operation of the microgrids [210].
The hybrid system is a multisource and complex system, including a number of working modes. These modes are usually known as buck and boost modes and are responsible for producing the control signal to the switches of the DC-DC converters during power charging and discharging. To obtain accurate control of power distribution between the battery and SC, a robust control power management for HESS is required, which is able to give control decisions for suitable power flows between the storages and the grid in a fast and intelligent way.
Thus, in this section, a new approach, a sugeno-fuzzy logic controller for power management of the HESS is presented based on decision-making. “Fuzzy control is basically an adaptive and nonlinear control, which gives robust performance for a linear or non-linear plant with parameter variation” [171]. Fuzzy logic control (FLC) models the behaviour of a system by using knowledge-based rules and thus differs from classical control methods.

The key objective of the HESS controller is to manage the power exchange between the HESS and the DC side of the D-STATCOM, providing a fast response and hence improving the dynamic voltage stability of the grid. For example, a disturbance to the grid might cause the voltage at the PCC to fall, in which case the controller should be designed to stop the voltage at the PCC falling too quickly or too far, to maintain power and control power sharing on the input side. The detailed model structure of the D-STATCOM configuration with HESS based fuzzy strategy is shown in Figure 6-11.
.

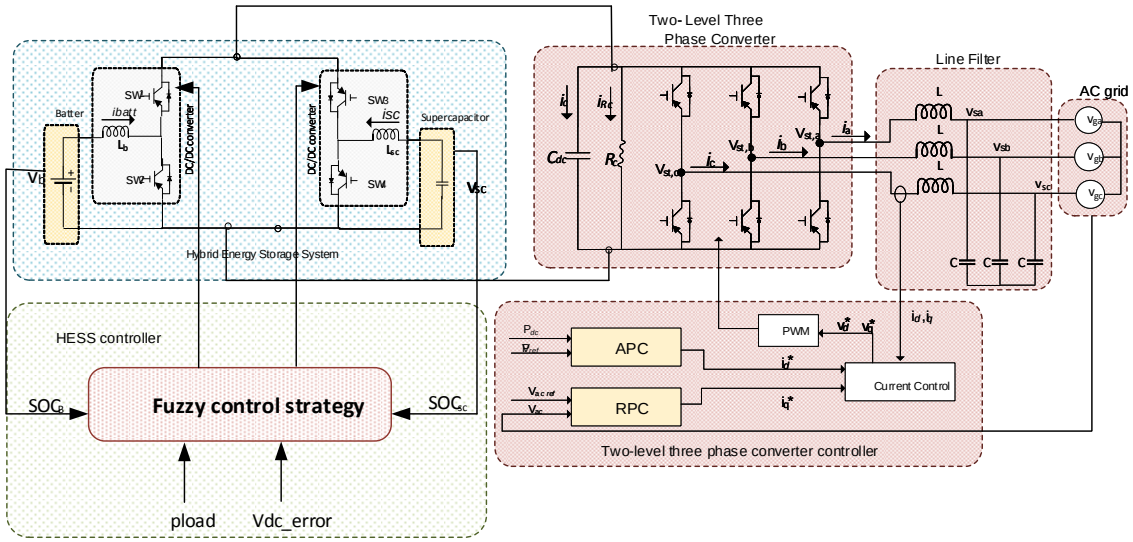

Figure 6-11 Detailed model of D-STATCOM based HESS

6.4.2 The structure of FLC

The key point behind utilizing FLC is to facilitate the overall power sharing directly between the battery and SC while keeping the $SOCs$ within permitted levels, so that the dynamic voltage response of the system is maintained. The fuzzy logic control strategy of HESS is represented in the model diagram in Figure 6-12 shows two inner current control loops (CCL) associated with two DC/DC converters. The desired output voltage of the hybrid source is maintained by the FLC. It also partitions the power to be supplied between the two energy sources according to a reference current criterion and maintains the voltage of both storage devices within the acceptable limits. The control scheme of the hybrid storage system included four input signals and two output signals as illustrated in Figure 6-12.

The inputs of the FLC are the error signal between the reference and actual voltage of the DC side of the D-STATCOM's converter, the load power, the SOC of battery and SC. The outputs variable are the reference currents of battery and SC.

The performance of the fuzzy logic based energy storage management is determined by the membership functions and fuzzy rules:

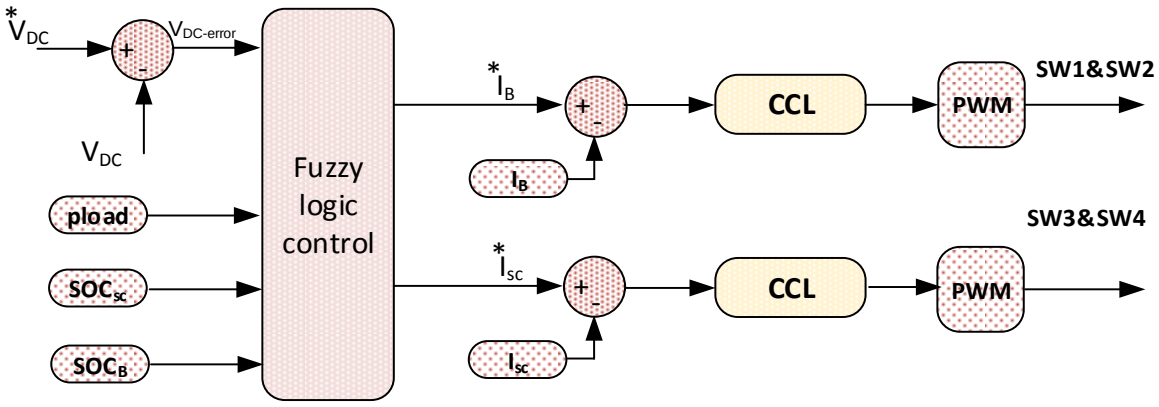

Figure 6-12 Control diagram of HESS

A. Determination of the membership functions:

As stated earlier in Section 4.6.4, the FLC includes a process whereby the real input signals are converted into a linguistic variable. Each range of the input represents by a membership function. The input membership functions are used as transitions between the different operating modes. These are given in Figure 6-13. The first input variable, the error signal of the DC side voltage (V_{DC_error}) poses a logical choice as the performance of the VSC is directly affected by the DC-side voltage, which determines the required steady state power and acts as a power buffer in transient conditions which can cause aberrations in the DC bus voltage. There are five membership functions for this input: A_1 (Negative large), A_2 (Negative small), A_3 (Zero), A_4 (Positive small) and A_5 (Positive large). The input membership functions have been tuned according to the system requirements and the membership values for each membership function ranges between (0-1). Figure 6-13 (a) shows the membership functions for the error signal. The membership functions of the second input (P_{load}) are formed on four levels to accommodate the needs of the proposed strategy, B_1 stands for low, B_2 stands for medium B_3 stands for high and B_4 stands for very high, as shown in Figure 6-13(b).

Figure 6-13 (c) and (d) show the membership functions of SOC of the battery (SOC_B) and SOC of the SC (SOC_{sc}) respectively. Four membership functions are selected for each of these two inputs: low membership represents the SOC

between zero and 25% for SC and between zero and 40% for battery, normal membership represents the SOC between 25% and 65% for SC and between the 40% and 70% for battery, high membership represents the SOC between 65% and 85% and the maximum membership function represented the SOC between 85% and 100% for both SC and battery. The variables names of all memberships functions for each of the four inputs are given in Table 6-1.

The output variables of the fuzzy control are included in the reference currents of battery and SC which were forwarded to the current control loops of the DC-DC converters.

The output memberships of the fuzzy controller are taken as constant and linear, and are represented with Neg_L= -60, Neg_s=-30, Zero =0, Pos_s= 30 and Pos_L=60 for the both battery current I_B^* and SC current I_{sc}^*.

Commonly, for a specific problem, typically a singleton output function is sufficient. Depending on the input, spikes in the values for the singleton output membership can be triggered in a linear pattern in the output domain. This allows for an efficient and compact system notation. From other side, in the case of sudden variation in the system operation condition, it used a linear function for the output membership for nonlinear mapping for each rule. In this case, as the result, the fuzzy rules are a function of the input vector which makes the control rules fairly general. For particular values of the inputs in Equations (6-29) and (6-31), the membership functions are expected to smoothly interpolate the output function. Generally, depending on the constants or linear functions, the output memberships in the sugeno systems are distinctly parameterised maps. Therefore, heuristically it is possible to use constant or linear memberships to find the best output surface to fit the system requirement, depending on the choice of parameters that would be controlled.

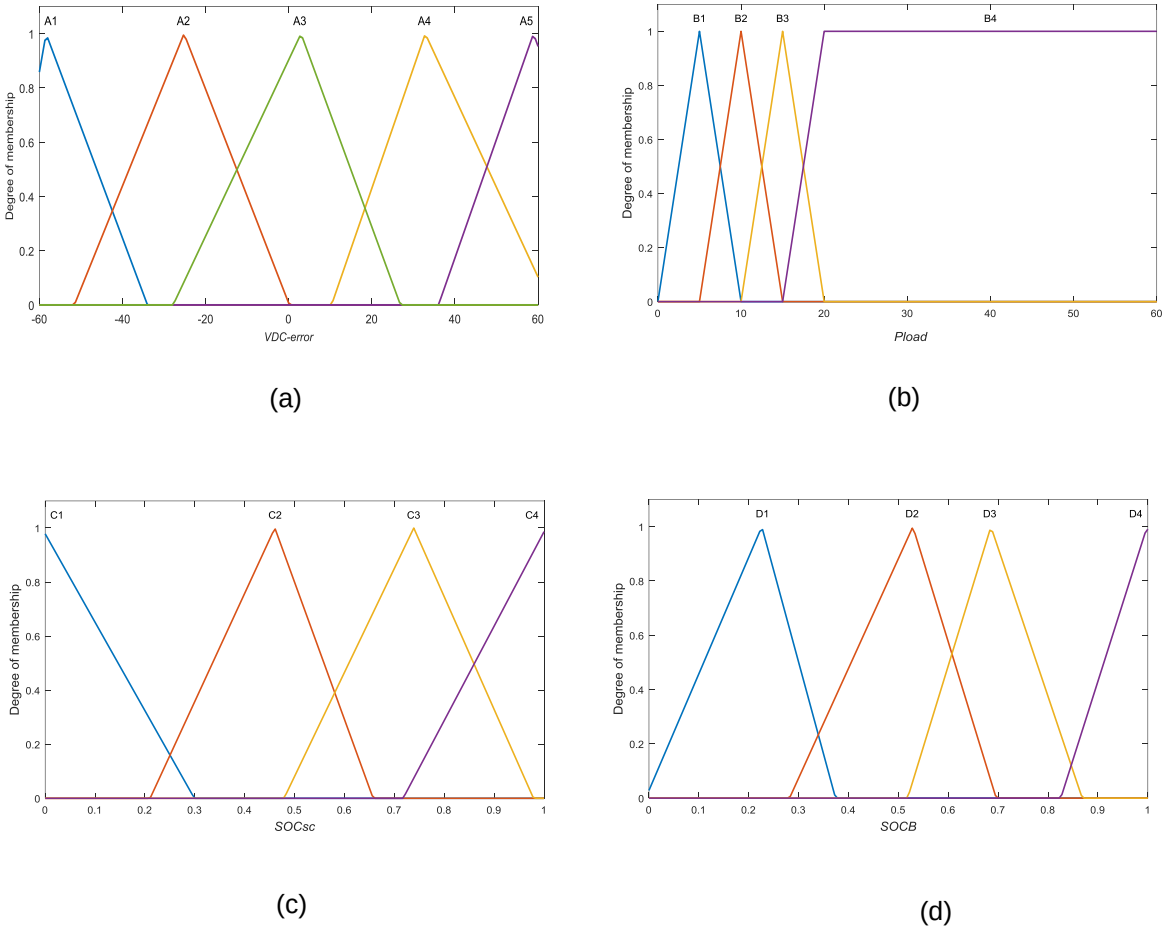

(a) (b)

(c) (d)

Figure 6-13 Membership functions of input variables

Table 6-1 The variables names of membership functions

V_{DC_error} memberships	P_{load} memberships	SOC_{sc} memberships	SOC_B memberships
A_1 = Nagative large	B_1=low	C_1 =low	D_1 =low
A_2= Negative small	B_2 =medium	C_2 = normal	D_2 = normal
A_3 = Zero	B_3 =high	C_3 = high	D_3 = high
A_4 =Positive small	B_4 = very high	C_4 = max	D_4 = max
A_5 = Positive large			

B. Fuzzy supervisor rules:

The rules for fuzzy data are normally described by the form (IF), (AND) and (THEN) statements. For example:

Rule 1:

$$IF \quad V_{DC_error} \; is \; A_1 \quad AND \quad P_{load} \; is \; B_1 \quad AND \quad SOC_{sc} \; is \; C_1 \quad AND \quad SOC_B \; is \; D_1$$

$$\text{THEN} \quad I^*_{B1} = a_{11}.V_{DC_error} + b_{11}.P_{load} + c_{11}.SOC_{sc} + d_{11}.SOC_B$$

$$I^*_{sc1} = a_{21}.V_{DC_error} + b_{21}.P_{load} + c_{21}.SOC_{sc} + d_{21}.SOC_B$$

Rule 2:

$$IF \quad V_{DC_error} \; is \; A_2 \quad AND \quad P_{load} \; is \; B_2 \quad AND \quad SOC_{sc} \; is \; C_2 \quad AND \quad SOC_B \; is \; D_2$$

$$\text{THEN} \quad I^*_{B2} = a_{12}.V_{DC_error} + b_{12}.P_{load} + c_{12}.SOC_{sc} + d_{12}.SOC_B$$

$$I^*_{sc2} = a_{22}.V_{DC_error} + b_{22}.P_{load} + c_{22}.SOC_{sc} + d_{22}.SOC_B$$

Rule k:

$$IF \quad V_{DC_error} \; is \; A_k \quad AND \quad P_{load} \; is \; B_k \quad AND \quad SOC_{sc} \; is \; C_k \quad AND \quad SOC_B \; is \; D_k$$

$$\text{THEN} \quad I^*_{Bk} = a_{1k}.V_{DC_error} + b_{1k}.P_{load} + c_{1k}.SOC_{sc} + d_{1k}.SOC_B$$

$$I^*_{sck} = a_{2k}.V_{DC_error} + b_{2k}.P_{load} + c_{2k}.SOC_{sc} + d_{2k}.SOC_B$$

So,

$$I^*_B\left(V_{DC_{error}}, P_{load}, SOC_{sc}, SOC_B\right) = \frac{\sum_{\sigma=1}^{k} \prod_{\xi} A_j\left(V_{DC_error}\right).B_h(P_{load}).C_z.(SOC_{sc}).D_w.(SOC_B).I^*_{B\sigma}}{\sum_{\sigma=1}^{k} \prod_{\xi} A_j\left(V_{DC_error}\right).B_h(P_{load}).C_z.(SOC_{sc}).D_w.(SOC_B)} \quad \textbf{(6-29)}$$

ξ represents all the membership function combinations.

j, h, z, w:represent all the membership function combinations subject to the constraints. **(6-30)**

A_j, where $j\epsilon[1,5]$

B_h, where $h\epsilon[1,4]$

C_z, where $z\epsilon[1,4]$

D_w, where $w\epsilon[1,4]$

And

$$I_{sc}^{*}\left(V_{DC_{error}}, P_{load}, SOC_{sc}, SOC_B\right) = \frac{\sum_{\sigma=1}^{k}\prod_{\xi} A_j\left(V_{DC_error}\right).B_h(P_{load}).C_z.(SOC_{sc}).D_w.(SOC_B).I_{sc\sigma}^{*}}{\sum_{\sigma=1}^{k}\prod_{\xi} A_j\left(V_{DC_error}\right).B_h(P_{load}).C_z.(SOC_{sc}).D_w.(SOC_B)} \quad \textbf{(6-31)}$$

The most important part of fuzzy logic controller design is the control rules determination. We determine the fuzzy rules by studying the characteristics of the ESSs and analysing the controller's logic process. It has been shown that successive simulations are required to confirm the reliability and robustness of the controller. On other hand, four inputs and four or five memberships for each input, as well as the nonlinearity of the system, make the total number of rules very complicated to control. So, to obtain better control execution, the number of the rules considered (80 rules) are made based on historical output information of standard HESS control management as in Section 6.3

The following are a set of rules have been applied in the fuzzy controller:

Examples of rules applied in the fuzzy controller
If V_{DC_error} is positive large, then I_B^* is Neg_L and I_{sc}^* is Neg_s
If $V_{DC_error}$is positive small, then I_B^* Neg_s and I_{sc}^* zero
If $V_{DC_error}$is zero, then I_B^* is zero and I_{sc}^* is zero
If $V_{DC_error}$is Negative small and $SOC_{sc}$is not Max, then I_B^* is zero and I_{sc}^* is Pos_s
If $V_{DC_error}$is Negative large and $SOC_{sc}$is not Max, then I_B^* is zero and I_{sc}^* is Pos_L
If $V_{DC_error}$is Negative small and $SOC_{sc}$is max, then I_B^* Pos_s and I_{sc}^* is zero
If $V_{DC_error}$is Negative large and $SOC_{sc}$is Max and SOC_B is not Max, then I_B^* is Pos_L and I_{sc}^* is zero
If P_{load} is High and $SOC_{sc}$is not low, then I_B^* is zero and I_{sc}^* Neg_L
If P_{load} is Med and SOC_B is Low and $SOC_{sc}$is not low, then I_B^* is zero and I_{sc}^* is Neg_s
If P_{load} is Low and SOC_B is low and $SOC_{sc}$is not low, then I_B^* is zero and I_{sc}^* is Neg_s

If P_{load} is High and $SOC_{sc}$is low and SOC_B is norm then I_B^* is Neg_L and I_{sc}^* is zero
If P_{load} is Med and $SOC_{sc}$is low and SOC_B is norm then I_B^* is Neg_s and I_{sc}^* is zero
If P_{load} is Low and $SOC_{sc}$is low and SOC_B is norm then I_B^* is Neg_s and I_{sc}^* is zero
If $V_{DC_error}$is Positive large, then I_B^* is Neg_L and I_{sc}^* is Neg_s
If $V_{DC_error}$is Positive small, then I_B^* Neg_s and I_{sc}^* zero

The appropriate rules for the status of the system are be decided by an inference mechanism which depended on the mapping between the membership functions of the input and output signals.

The rules are to converge the following conditions to maintain the DC side voltage at a desired level:

- When the system is in the steady state condition, the required power is supplied by the battery storage.
- The SC supplies power under a sudden load variation and provides transient power peaks to avoid the battery discharging at a high frequency and to restrict the battery discharge to relatively low currents to minimize the impact on battery life.
- When the DC side voltage is at a desired value and the load power is steady, the power distribution principle will be complex, and will depend on both SOC_B and SOC_{sc}. When SOC_B is high, the battery will always provide power to the system. When SOC_B is medium, the battery will also provide power. The SC will discharge only if SOC_{sc} is also high. If the SOC_{sc} is low, the SC will be charged. Because low SOC_B has a negative effect on battery life, when the SOC_B is low, the SC will provide power to the load. The battery will recharge only if SOC_{sc} is not low.

The surface plots shown in Figure 6-14, are used to explain rule triggering as related to the different input sets. Each of the panels presents the control surfaces for two inputs at a time with the resulting changes in I_B and I_{SC}. The intention is to gain an understanding of system behaviour to be used to plan for the D-STATCOM to better cope with sudden variations.

In Figure 6-14, the surface plots have nonlinear input-output relations whose shapes reflect the specific conditions of each application and the conflict of the different requirements.

Consider the relationship between the voltage error (V_{DC_error}) and SOC of the battery (SOC_B) with the battery reference current (I_B^*) and SC reference current (I_{sc}^*), frames (d) and (f) respectively, it can be noticed when the voltage error is zero (no power exchanging between the D-STATCOM and grid) the output reference currents of both of the battery and SC are zero. This is indicated by the areas 1 and 2 of Figure 6-15.

When the error signal of the DC side voltage (V_{DC_error}) is positive large which means that there is a sudden change in the load and therefore the D-STATCOM based HESS is required to deliver power into the grid via the discharge mode. During this time, the SC has started to discharge power until the battery has started to also deliver power as indicated in areas (3 and 4) of Figure 6-15. It is also important to note that the SOC of the two storage devices gives a priority to the SC and then the battery which results in a relatively normal level of charging. In this context, if the error signal of the DC side voltage (V_{DC_error}) is negative large that would imply the grid has a surplus of power. In this case the SC and battery have the opportunity to recharge, if the SOC for both is under the normal level then the system will give priority to charging the SC as indicated in areas (5 and 6) of Figure 6-15.

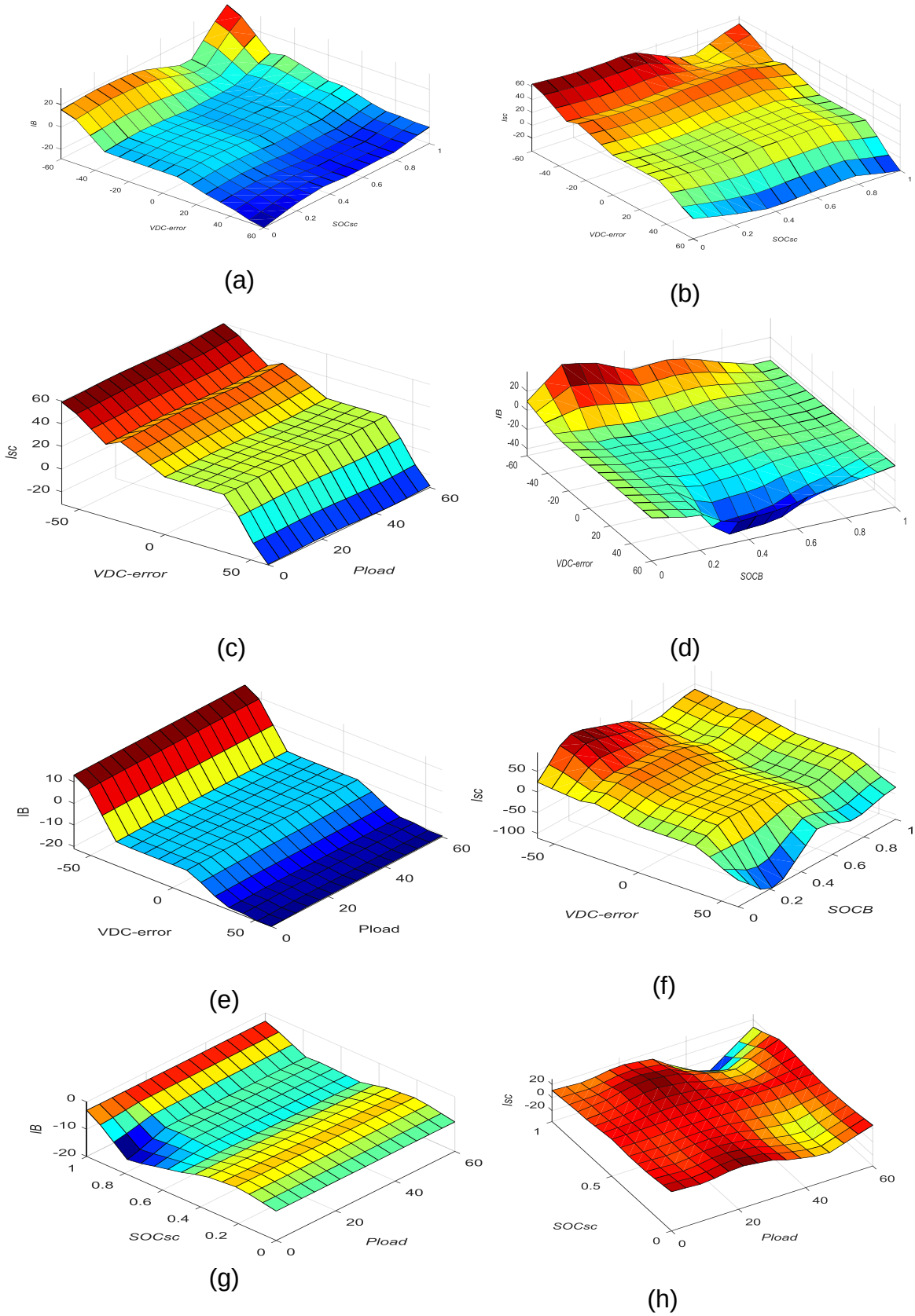

Figure 6-14 Surface plots

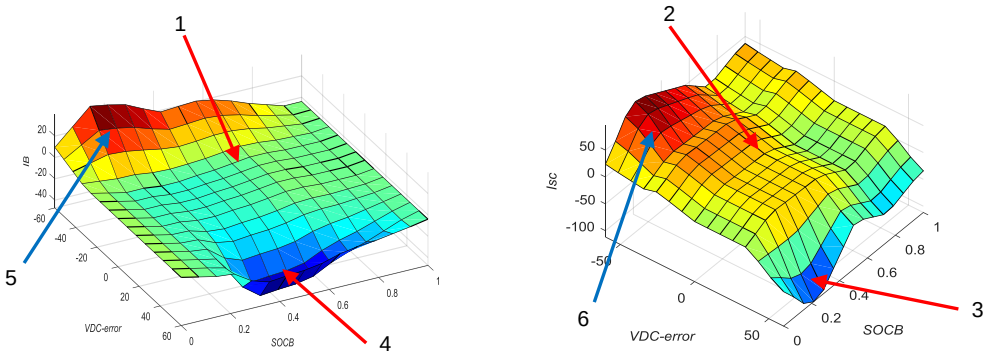

Figure 6-15 Surface description

6.5 Simulation of D-STATCOM based hybrid energy storage

Figure 6-16 shows the circuit diagram of the distribution power system connected to the D-STATCOM based HESS. Detailed simulations have been carried out in MATLAB/SIMULINK to illustrate the system performance in the context of the proposed management strategies of D-STATCOM, with dual sources (battery and SC). The rated voltage of the battery is 400 V with a capacity of 60 Ah. The auxiliary storage is a SC of 500 F with 150 V as rated voltage. The system parameters for the simulation analysis are given in Table 6-2, where the inductor and capacitor values of the power converters have been chosen after empirical investigation. In order to verify a performance of the D-STATCOM base on HESS, two study cases have been applied (with sudden load change and during fault condition).

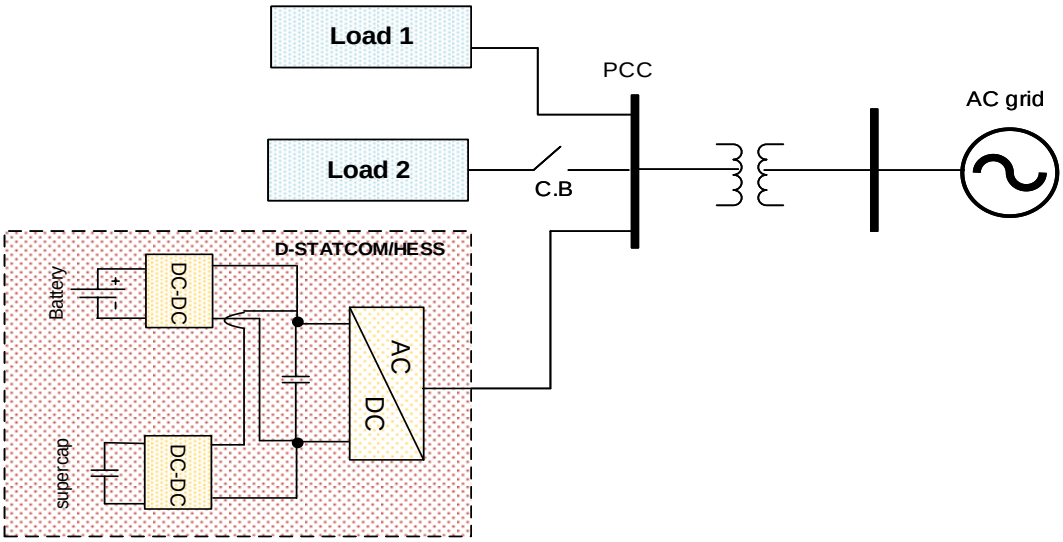

Figure 6-16 System structure of simulation model

Table 6-2 System parameters

Supercapacitor parameters	Values
Nominal voltage	150 V
Capacitance	500 F
Battery parameters	Values
Nominal voltage	400 V
Capacity	60 Ah
Converters parameters	Values
Inductance of inductors Capacitance of DC side Resistance	L_B=10 mH , L_{sc} =15 mH Cdc =2000 µF R_{dc} =10 kΩ
PI parameters	Values
Current control of Supercapacitor	Kp =0.45 Ki=30
Current control of battery	Kp=0.3 Ki=20
Voltage control loop	Kp =1.5 Ki =1.1
Power grid	Values
Main source	20 kV, 50 Hz
transformer	20 kV/380 V
DC side voltage	700 V
Loads	Values
Load 1 Load 2	380 V, 50 Hz, 25 kW 380 V, 50 Hz, 15 kW,4.6 kVR

6.5.1 Simulation of a distribution system with a sudden load change

In this case, the load power is increased at time = 0.15 second by connecting a second load to the system at the point of common coupling (PCC). The system performance is tested by using both classical and fuzzy logic control strategies. The simulation results are given below:

A. With classical control strategy

The simulation results of the D-STATCOM based HESS with a standard management scheme are shown in Figure 6-17 and Figure 6-18, 10 sec is selected as the time constant of the low pass filter to execute the simulation tests. At time t=0.15, a sudden step change in the load current occurred when a second load is switched on by closing the circuit breaker, (C.B) in Figure 6-16. The voltage response at the PCC is maintained reasonably at 1 pu as indicated in Figure 6-17. Also the DC side voltage (V_{dc}) of the D-STATCOM is displayed in the first trace in Figure 6-18, and regulated effectively to the desired value of 700 V. The second trace in the Figure 6-18 represents the total current supplied by the HESS.

It is observed in the third and fourth traces of Figure 6-18 that the maximum power demand is momentarily provided by the SC at start-up and then again at the load change, average power requirement is diverted to the battery.
It is worth noticing that the SC provides much more current than the battery during load disturbance (at start-up from 0 sec to 0.005) and when the load is increased (from 0.15 sec to 0.25 sec). After t = 0.25 seconds the current delivered from the SC dropped to zero, and the current to supply the entire load is delivered by the battery alone. This is because the total current required from the ESS is divided by the low pass filter into the instantaneous values forwarded as a reference current to the SC current control loop while the average values is a reference battery current in the battery current control loop.

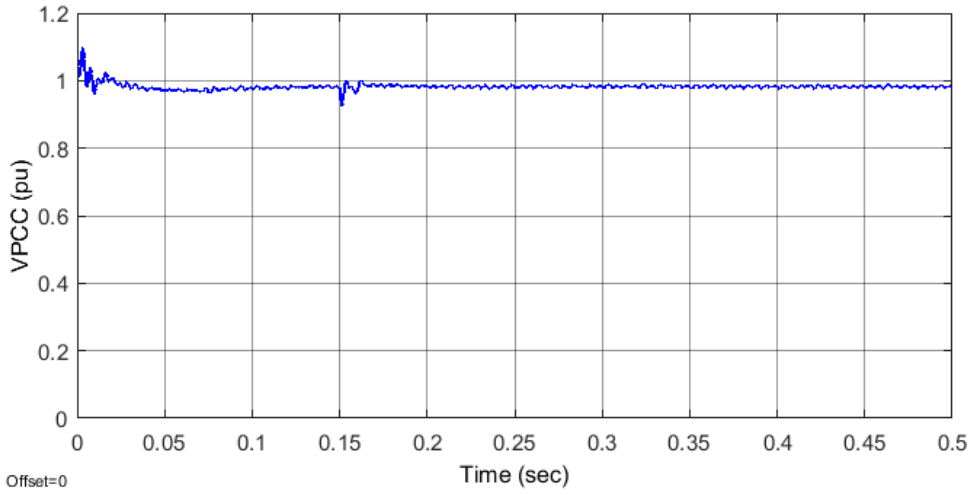

Figure 6-17 Voltage magnitude at PCC point

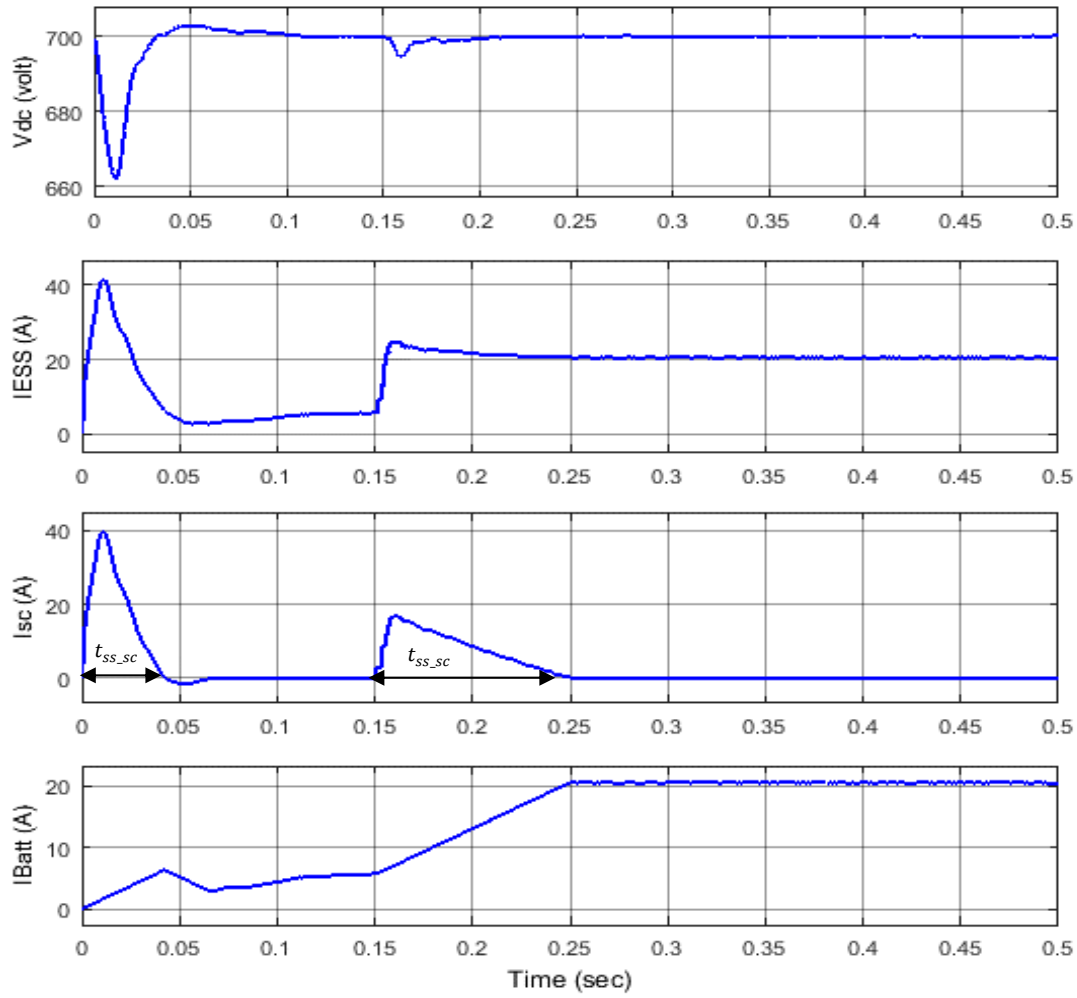

Figure 6-18 Simulation results for standard HESS management

Figure 6-19 and Figure 6-20 show the comparison of the dynamic response of the voltage at the PCC and DC side of the D-STATCOM with battery only system, and D-STATCOM based HESS. From the figures, as would be expected, it is noticed that the proposed modified D-STATCOM configuration with Dual DC Source offers a more consistent the voltage response at the PCC with significant reduction in the value of the voltage dip during the load changing condition, at time 0.15 second. The reduction is better than 50% compared to the results of the D-STACOM based battery only system (the voltage dip is reduced from 0.7877 pu to 0.9360 pu). However, there is a small oscillation in the voltage response at start-up when compared to the voltage response of the D-STATCOM based battery-only system, due to the SC charging and discharging. In addition, the voltage response of the PCC for both systems (D-STATCOM with battery only and D-STATCOM based HESS) are a slightly different in the steady state because the internal losses of both systems are different, also the SC storage unit included the DC-DC converter which has an additional loss, though this is usually small.

In addition, the maximum battery current in the proposed configuration is much lower than the maximum battery current in the D-STATCOM based battery only system (Figure 5-15), it is observed from the fourth trace of Figure 6-18 that the peak battery charge current decreased by 50% when combining the SC with the battery unit. As a consequence, the battery current stresses are reduced, and the battery life span is improved. Furthermore, as the SC is utilized to provide the transient currents, it ensures that the battery storage system is protected from high load currents and the battery unit size is reduced significantly. Hence saving in the battery life cost.

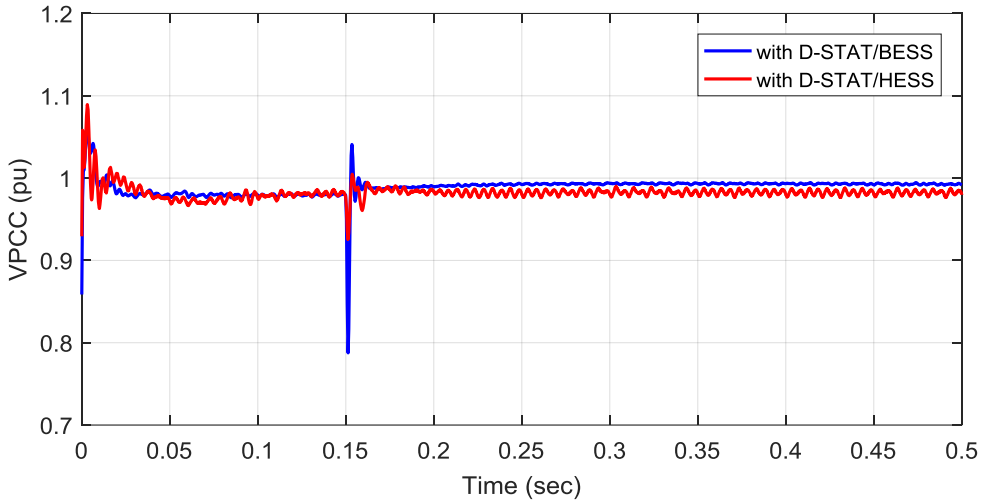

Figure 6-19 Voltage magnitude at PCC

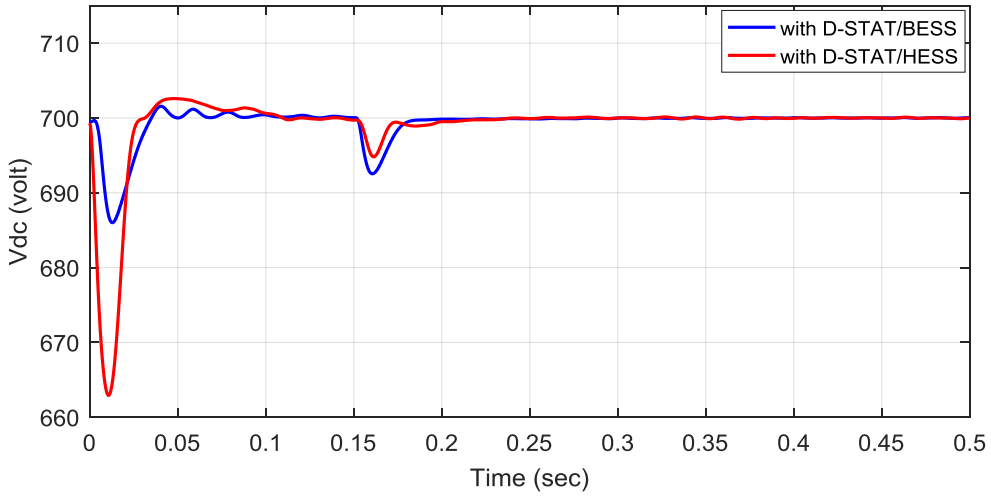

Figure 6-20 DC-side voltage

B. With fuzzy control strategy

In this section, simulation studies of the energy management strategy of the HESS with the proposed FLC method are carried out. The output results are depicted in Figure 6-21 and Figure 6-22. In FLC, the reference current of the battery and SC are determined by the set of the control rules associated with input signals which include the voltage error of the DC side and SOC of both battery and SC. The SC output current is displayed in the third trace in Figure 6-22. The SC supplied the required maximum transient current within a response time of $t_{s_sc} = 25ms$, compared to the current response of the standard control

management of $t_{s_sc} = 50ms$ (see third trace in (Figure 6-18). The remainder of the required current is delivered by the battery.

As can be seen from the fourth trace in in Figure 6-22 , from the start the battery provide more the current to regulate the voltage of the PCC, though the amount depended on the it's SOC. The output current of the battery with FLC is relatively greater than with the standard control method. However, the battery current with the proposed FLC is flatter than the output current with the standard control method. This indicates the FLC approach gave a steadier power output which is desirable to extend the lifespan of the storage unit. However, the total average battery current is the same. The DC side voltage of the D-STATCOM is displayed in the first trace, it is maintained at 700 V.

Clearly, it can be seen from Figure 6-21 the output voltage at the PCC is regulated to the desirable value with a slight oscillation though with a very fast response to the load variation.

The comparison of the voltage responses at PCC and DC side voltage between battery only system, standard HESS and the HESS based fuzzy management are seen in Figure 6-23 and Figure 6-24.

The voltage response with D-STATCOM based HESS/FUZZY shows a faster voltage response with less voltage dip at the time of the load change (t = 0.15 sec). A summary comparison of system performance between battery only system, standard HESS and the HESS based fuzzy management is shown in Table **6-3**. It can be seen that the HESS/FUZZY system can cope better with transient spikes than the other D-STATCOM models.

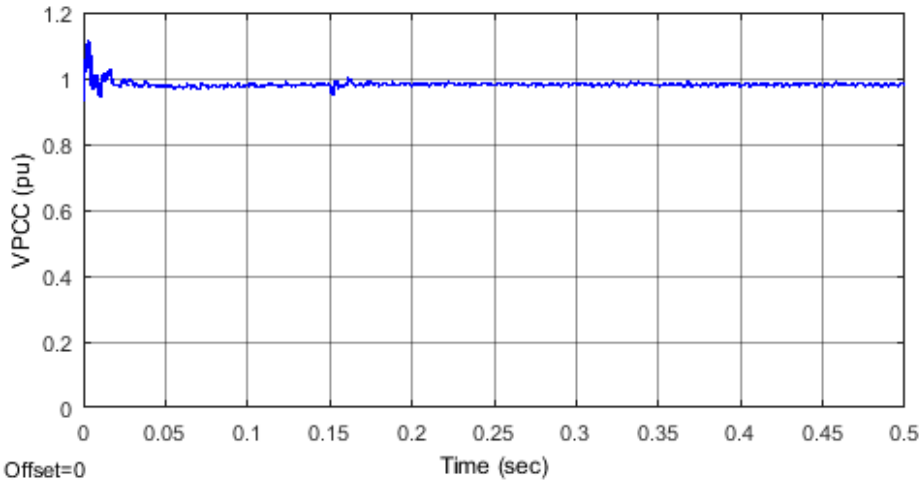

Figure 6-21 Voltage magnitude at PCC

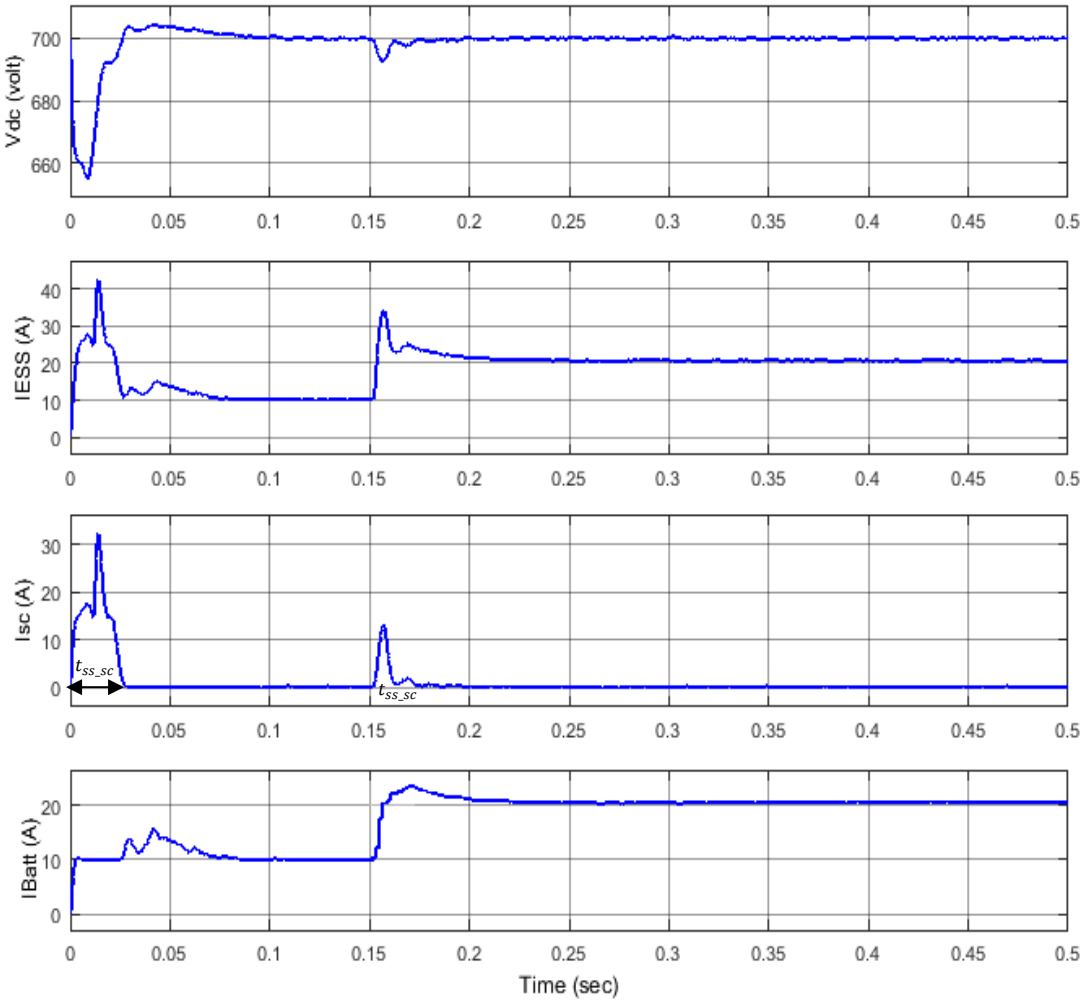

Figure 6-22 Simulation results for HESS with FLC management

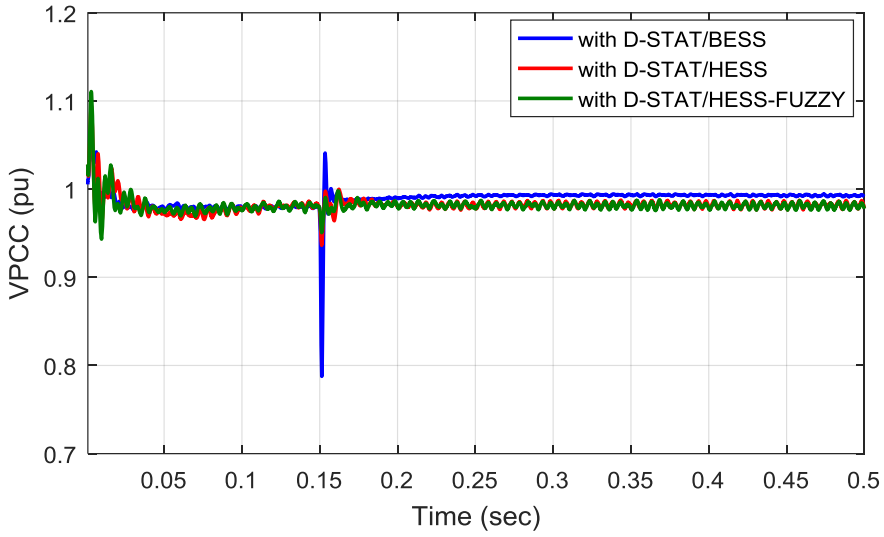

Figure 6-23 Comparison of the voltage magnitudes at PCC

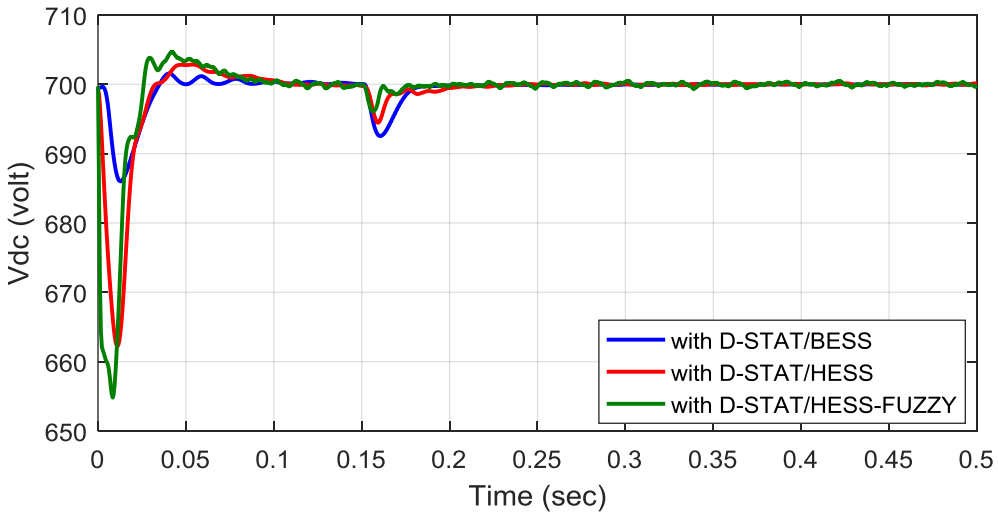

Figure 6-24 Comparison of the DC-side voltage

Table 6-3 Comparison of system performances.

System performance		Battery only system		HESS		HESS/FUZZY	
		VPCC (pu)	Vdc (volt)	VPCC (pu)	Vdc (volt)	VPCC (pu)	Vdc (volt)
at Load changing at Time =0.15	Min dip	0.787	693	0.936	694.45	0.951	696.1
	Settling time (msec)	15	50	11	20	8	12

6.5.2 Simulation of a distribution system with a three-phase fault applied at load point

A. With standard control strategy

The simulation results of the D-STATCOM based HESS with fault condition and standard control method are presented in Figure 6-25 and Figure 6-26. The results of the initial case without D-STATCOM were presented in Chapter Four.

From Figure 4-25, it is seen that the D-STATCOM converters managed, under normal condition when a balanced three phase fault is applied at the PCC at time 0.15 seconds and cleared at 0.35 seconds, the system voltage at the PCC tended to oscillate away from the desire voltage limits. The HESS provided the necessary power compensation to control the system voltage. In Figure 6-25, it is noticed that the voltage at the PCC stayed relatively stable.

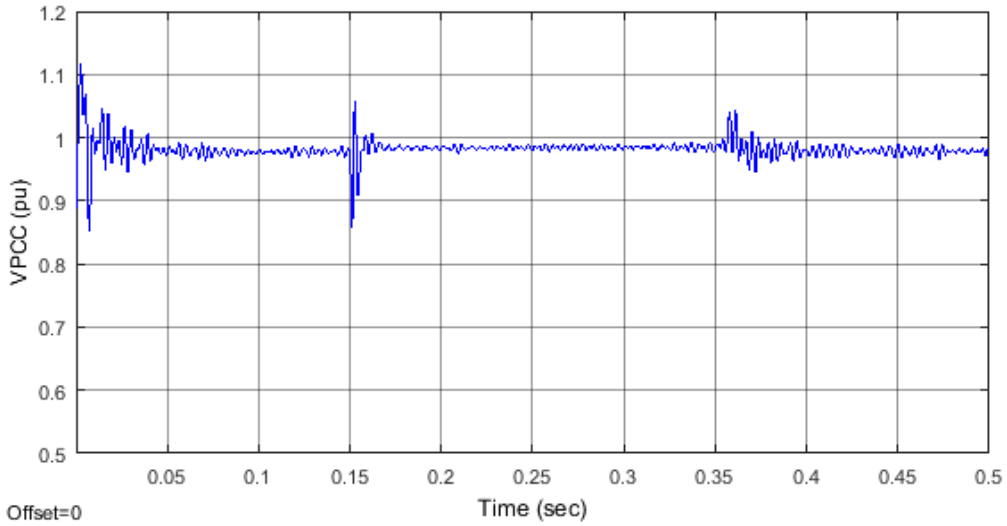

Figure 6-25 Voltage magnitude at PCC

From Figure 6-26, the SC current delivers instantly at time 0.15 seconds until the battery reacts to deliver its current. At time 0.35 seconds, it is seen that the SC can directly absorb the instantaneous rise of system currents in order to keep the system voltage constant. Thus, both energy storages shared the required current from the D-STATCOM until the system is automatically reset to the normal control.

Figure 6-27 and Figure 6-28 illustrate the comparative voltage responses at the PCC and DC side for the case of the D-STATCOM based battery only system, and D-STATCOM based HESS. The dynamic response is acceptable in both systems. The voltage response becomes more consistent by adding a HESS to D-STATCOM and nearly reached 1 pu. However, there is more oscillation in the voltage response at start-up with the D-STATCOM based HESS compared to voltage response of the D-STATCOM based battery only system. The oscillation in the system response occurs because the D-STATCOM takes energy from the DC side until both the battery and SC operate in the boost operating mode to provide the real power required by the load. The exportation of power from the DC link created an oscillation in the voltage at the PCC. It is also noticed that voltage recovery time is longer with the D-STATCOM based battery only system and shorter with the D-STATCOM based HESS. In addition, the large voltage dip in the DC side voltage at start-up, and at the instant of fault and overshoot at recovery are least with D-STATCOM /HESS and highest with D-STATCOM based BESS. This is due to the capacity of the SC to deliver high power density and it has a faster dynamic response. The SC mitigates the dip and the overshoot and keeps the voltage within the desirable range from 0.94 to 1.1 pu according to the UK voltage standard, which is based on British Standard BS 7697, i.e. ranges between - 6% and +10%. Also, the maximum battery current in the proposed configuration is much lower than the maximum battery current in the D-STATCOM based battery only system (Figure 5-23).

It is clear that the transient spikes can be coped with more efficiently with D-STATCOM based HESS than the D-STATCOM based battery only system.

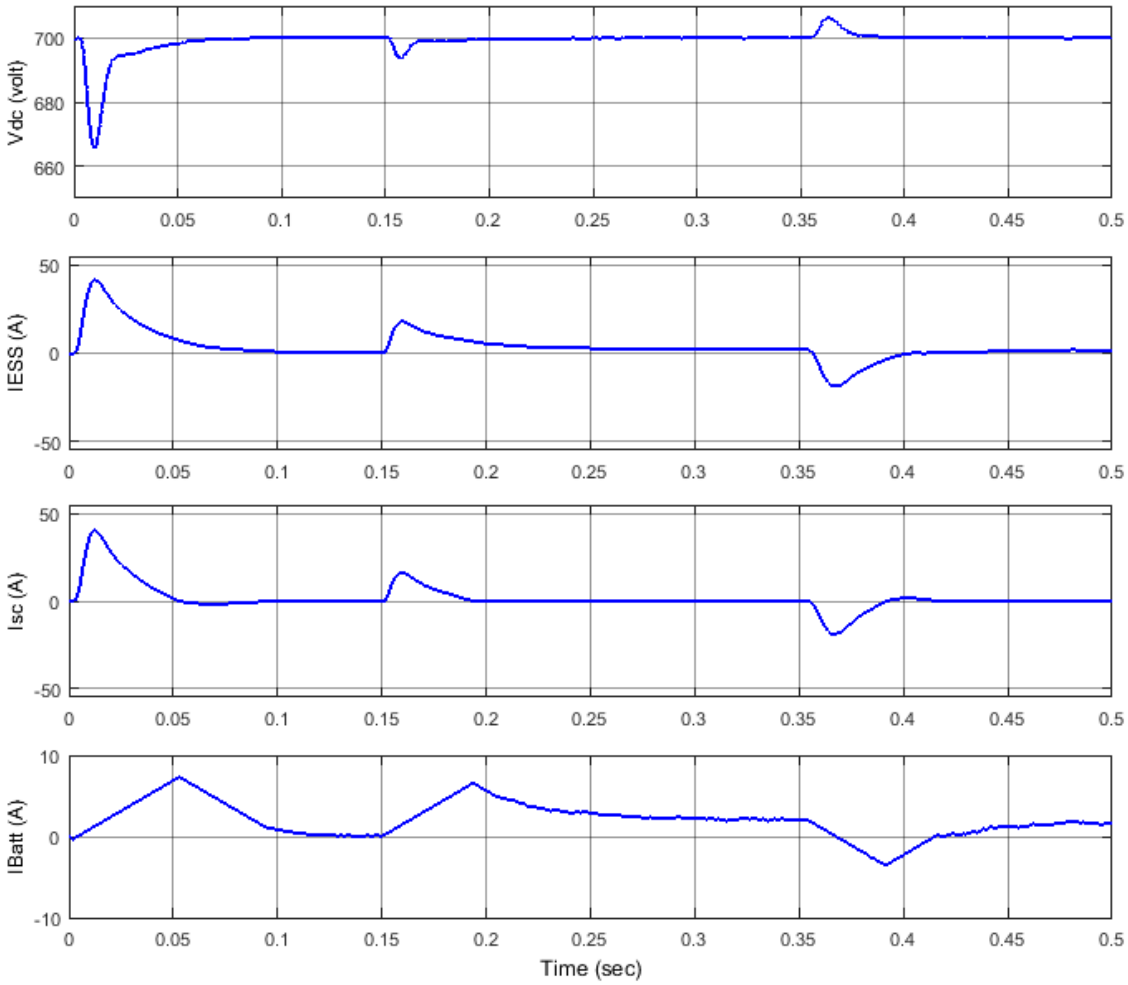

Figure 6-26 Simulation results for standard HESS management system with fault

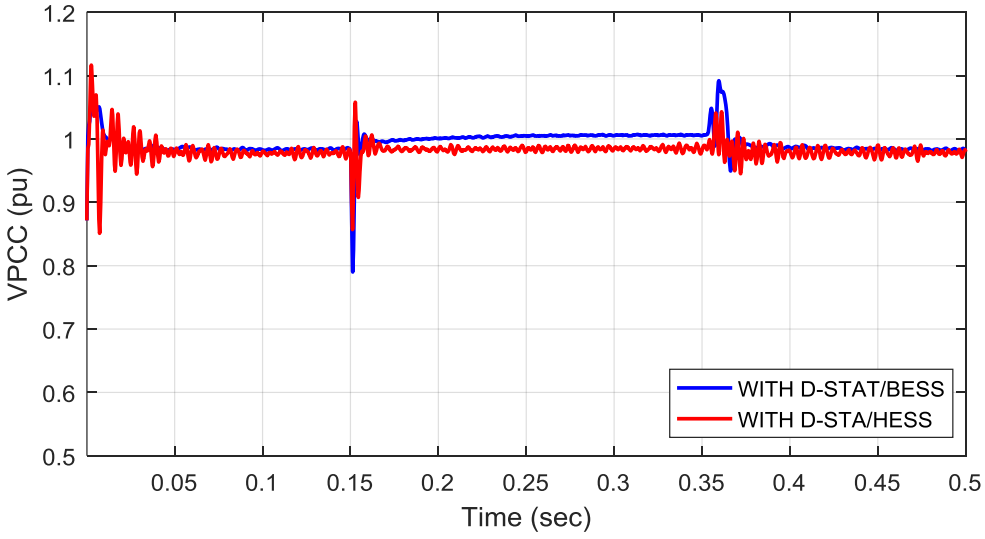

Figure 6-27 Comparison of the voltage magnitude at PCC

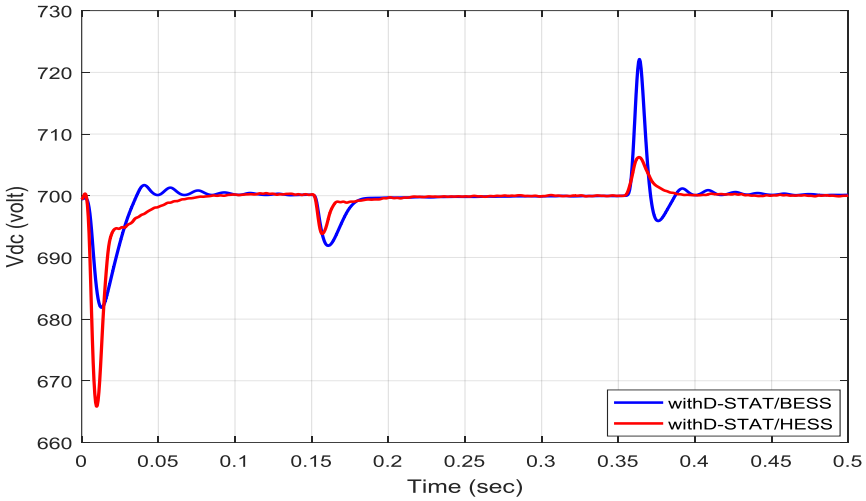

Figure 6-28 Comparison of the DC-side voltages

B. With fuzzy control strategy

In order to evaluate the performance of the proposed sugeno-fuzzy control scheme for the HESS, the simulation model of the proposed HESS with FLC have been simulated under a balanced voltage sag with magnitude 30% for 10 cycles triggered by a symmetrical fault. The output results are given in Figure 6-29 and Figure 6-30.

As mention earlier, the voltage sag begins at 0.15 sec and clears at 0.35 sec. The DC- side voltage of the D-STATCOM is displayed in the first trace of Figure 6-30 and the total current of the energy storages is displed in second trace.

According to the dataset of control rules, the output reference currents of the SC and battery are determined by the FLC with multi input signals. From the third and fourth traces of the Figure 6-30, it is obvious that the SC system and battery storage unit together provide the required system current. For the hybrid source the proposed fuzzy logic algorithm permits non-linear control of the power flow using data concerning the desired performance of the system. With this control, the suggested power flow control strategy determines the most suitable operating point for battery and SC units. Thus, the output current of the battery is provided only during the voltage disturbance.

The output of the HESS is limited to providing current during the voltage disturbance periods instantly, which improved the capacity to ride out the voltage sag. Actually, during the fault time, the current compensators restrict the output currents to within the voltage disturbance time to prevent the overloading of the converter. As a result, the DC side voltage is controlled faster, resulting in decreased voltage oscillation at the PCC as depicted in Figure 6-29.

It is interested to note from Figure 6-30 that the HESS management, by applying FLC, gives better dynamic performance in comparison to the standard filter control management. However, SC stopped providing current and the battery continued to provide the current required by the system during the disturbance time. The SC supplied the required maximum transient current for the time required to reach the steady state ($t_{s_sc} = 30ms$) compared to the response of the standard control management ($t_{s_sc} = 50ms$). Furthermore, the battery current has a faster and more consistent response with FLC compared to the battery current response using the standard control management.

Although the standard filter control management gives fairly acceptable results under fault conditions, the proposed fuzzy control management provides effective and fast voltage regulation, reducing the dips and the overshoots. Also, the fault oscillation is reduced and the ability to ride through faults is improved. Furthermore, sugeno-fuzzy control management allows automated sharing of the power between the storage units which could be used as a powerful tool in real time application and will provide superior performance in the control of varying operating conditions in microgrids.

The comparison of the voltage responses at the PCC are described in Figure 6-31. The voltage response with D-STATCOM based standard HESS shows significant change at the beginning and end of the sag. However, the ripple that occurs during the transient is less than 10% peak-to-peak, and is rapidly damped by the sugeno- fuzzy control management. The comparison of the DC side voltage responses is shown in Figure 6-32. A summary of the system performance comparison among the battery only system, standard HESS and the HESS based fuzzy management is shown in Table 6-4.

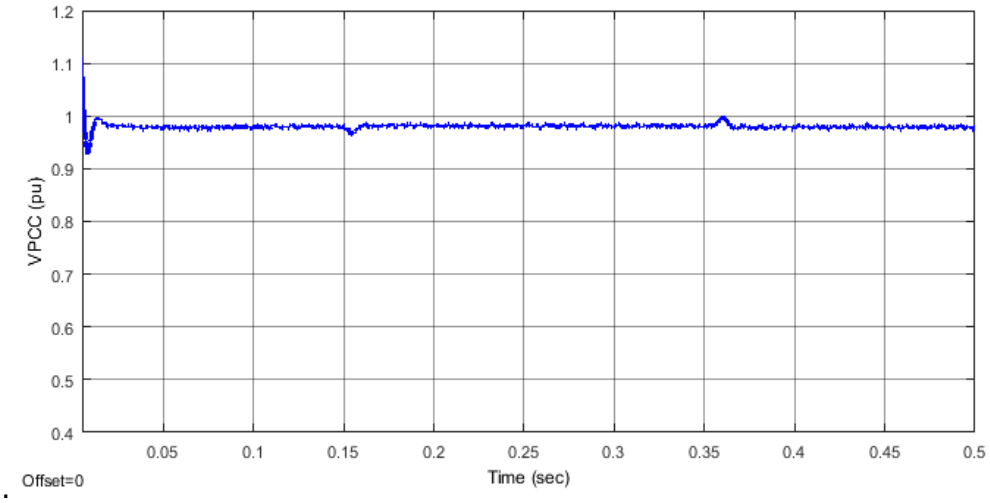

Figure 6-29 Voltage magnitude at PCC

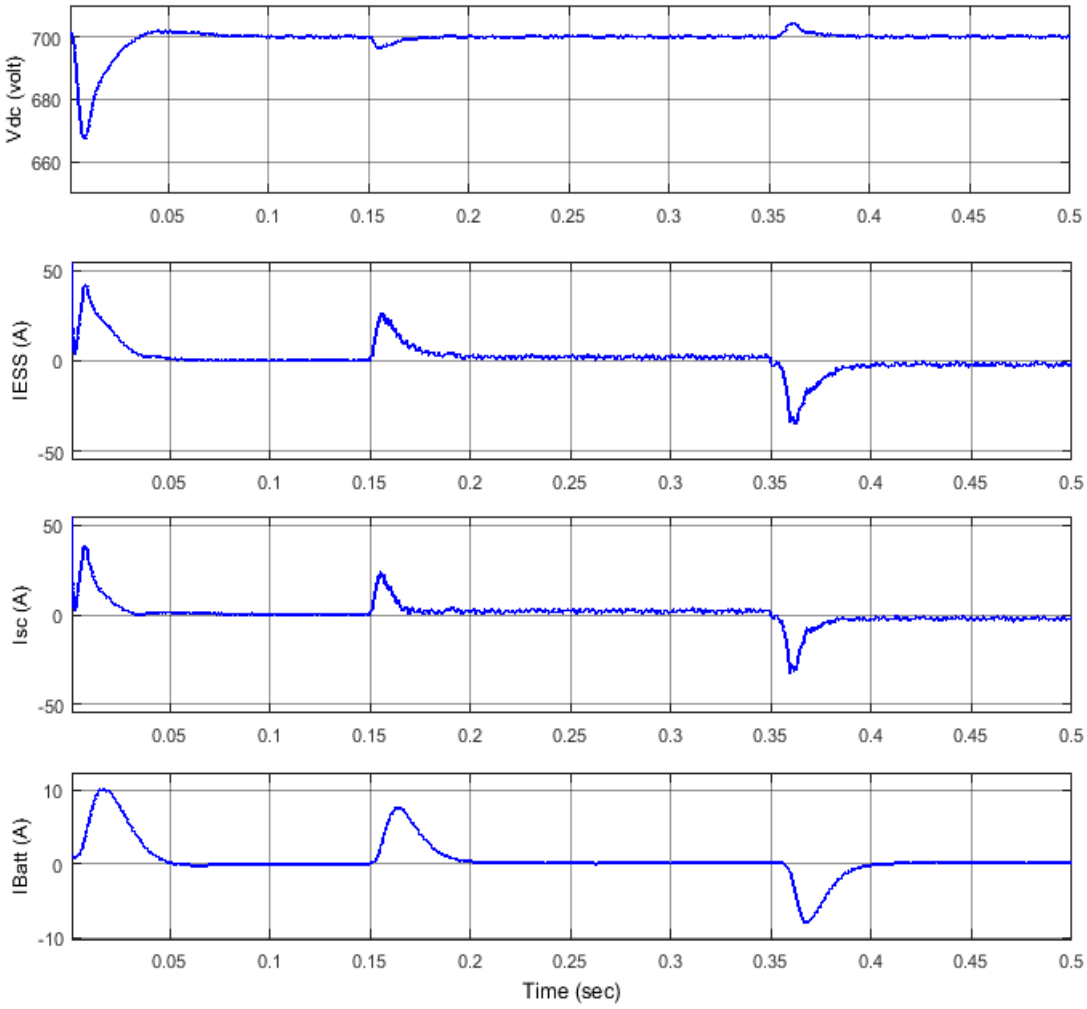

Figure 6-30 Simulation results for HESS with FLC management with fault

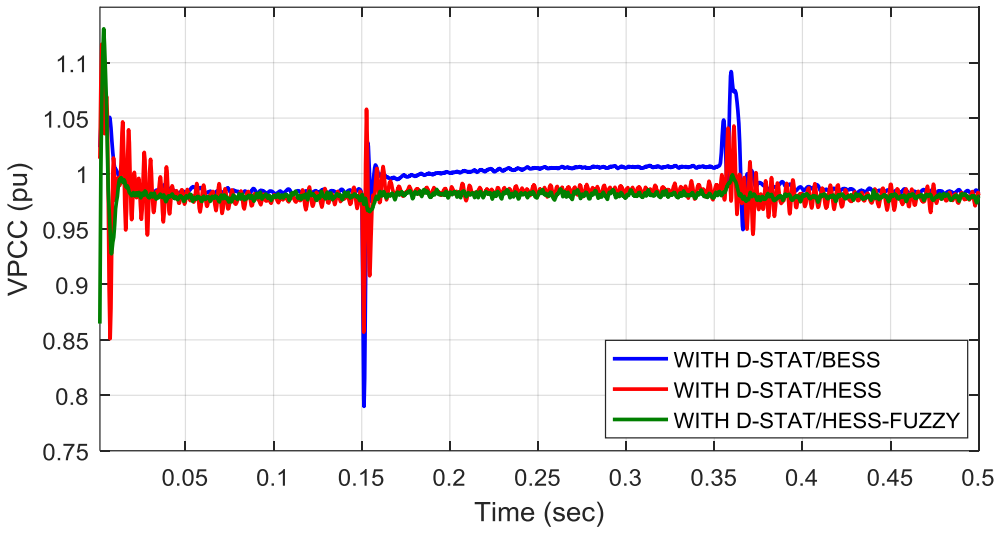

Figure 6-31 Comparison of the voltage magnitude at PCC

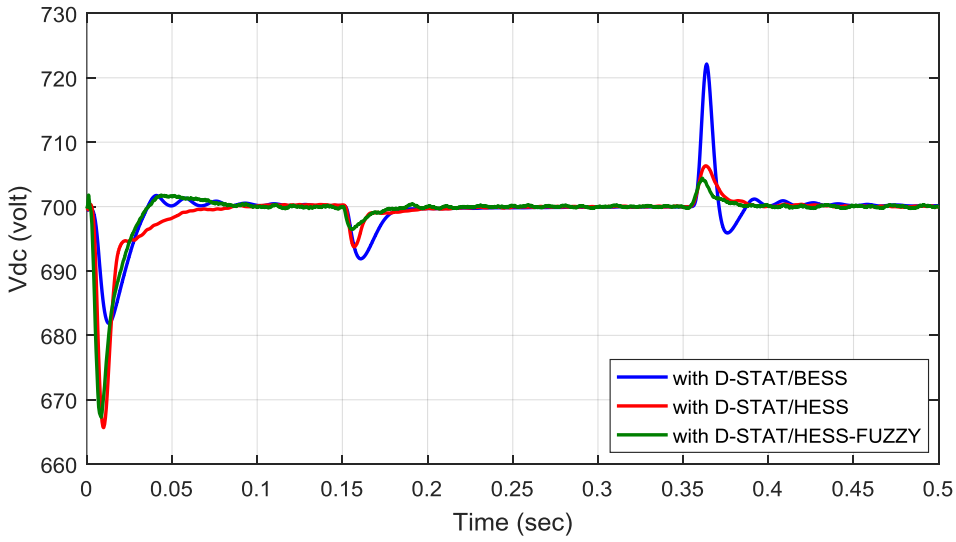

Figure 6-32 Comparison of the DC-side voltage

Table 6-4 Comparison of system performances.

System performance		Battery only system		HESS		HESS/FUZZY	
		VPCC (pu)	Vdc (volt)	VPCC (pu)	Vdc (volt)	VPCC (pu)	Vdc (volt)
At fault initiation Time =0.15	Min dip	0.79	692.0	0.857	693.7	0.966	696.5
	Settling time (msec)	10	33	16	14.5	8	12
At fault clearance Time =0.35	Max peak	1.09	722.12	1.043	706.3	-------	704.4
	Settling time (msec)	20	32.5	17.0	30	-------	24

6.6 Summary

In this chapter, considerable manipulation of energy storage technologies based on the use of FACT devices has been proposed to give better performance in microgrid operation.

The advantage of high-power storage units and high energy storage units have combined with a D-STATCOM based HESS configuration to avoid the limitations of using only one specific storage unit, which is considered to be one of the main contributions to future of energy storage technology.

The main advantages of modified D-STATCOM configuration with Dual DC Source (battery and SC) involves faster voltage regulation and reduction of battery current stresses.

Two control strategies, a standard controller with low pass filter and FLC have been designed and tested for HESS management. The strategies were designed based on the concept that the battery provides the average power requirements of the system while the SC supplies the transient power requirements. These coordinated control schemes have been shown to be able to ensure effective use of two different types of ESS (short term and long-term storage) and accomplish the followings goals:

- Successfully achieve both steady state and transient voltage stability of the distribution system.

- Improved the lifespan of the battery by minimizing the charging and discharging frequency and reducing maximum rate of battery discharge current.

The simulations results demonstrated that by managing the battery and SC combination using standard control strategy that the SC reacts swiftly to the load system requirements while the battery delivered more slowly because of the low pass filter. The difference in current between the battery and total load current required was compensated by the SC. Thus, a sugeno-fuzzy supervisor control management was proposed, to act as a fast and effective energy management system. In the supervisory HESS management strategy, a multi-input and multi-output were mapped. Thus, it was possible to implement an intelligent real-time energy management controller able to effectively distribute the required current from the ESS and provide good performance in trimming the peak battery current. The effectiveness of these proposed strategies: of maintaining a DC side voltage at 700 V and maintaining the voltage at the PCC at acceptable levels, were subsequently demonstrated by simulation.

Finally, it is concluded that the D-STATCOM based HESS configuration can efficiently minimize the maximum value of the battery current by 50% in comparison to the D-STATCOM based battery only system. Hence, it is expected that the cycle life of the battery could be extended by over 50%.

7 Chapter Seven: Experiment Design and Implementation of Real-Time Controller for a Battery-Supercapacitor Hybrid Energy Storage System

7.1 Introduction

To investigate the effectiveness of the proposed modification to the D-STATCOM based HESS, it is necessary to carry out experimental tests. Emulation of the distribution system (Figure 6-16) in real time is difficult and expensive. Reduced-scale models can offer substantial benefits for time simulation and operational testing of real systems and provide good quality estimations. The test rig is a modified version of an existing experimental platform.

This chapter, will describe the experimental testing of the scaled-down hardware prototype of the proposed energy management system presented in Chapters 5 and 6. For this part of the work the aims were:

- To show the battery current waveform in a D-STATCOM based battery only system.
- To investigate in the laboratory the current waveforms of the battery and supercapacitor (SC) for the case of a D-STATCOM based HESS.

The D-STATCOM converter based HESS used for this part of the work is a modified and extended version of an existing experimental platform. This scaled model is suitable for testing and then validating the hardware and software systems for power management, for both the HESS and battery-only system applications.

7.2 Prototype Hardware Description

The schematic of the experimental rig is shown in Figure 7-1. The rig consisted of two main parts; the combined and modified cascade inverter with a combination of energy storage systems (battery and SC) and the rig controller.

The rig design included a motor drive consisting of a 0.37 kW induction motor as a load, powered by a modified cascade inverter. The DC side of the inverter consisted of a battery bank as the main DC voltage source and a set of SC banks. The entire rig is controlled by a National Instruments CompactRIO real-time control platform using a LabVIEW FPGA module. The main elements of the hardware platform are described below:

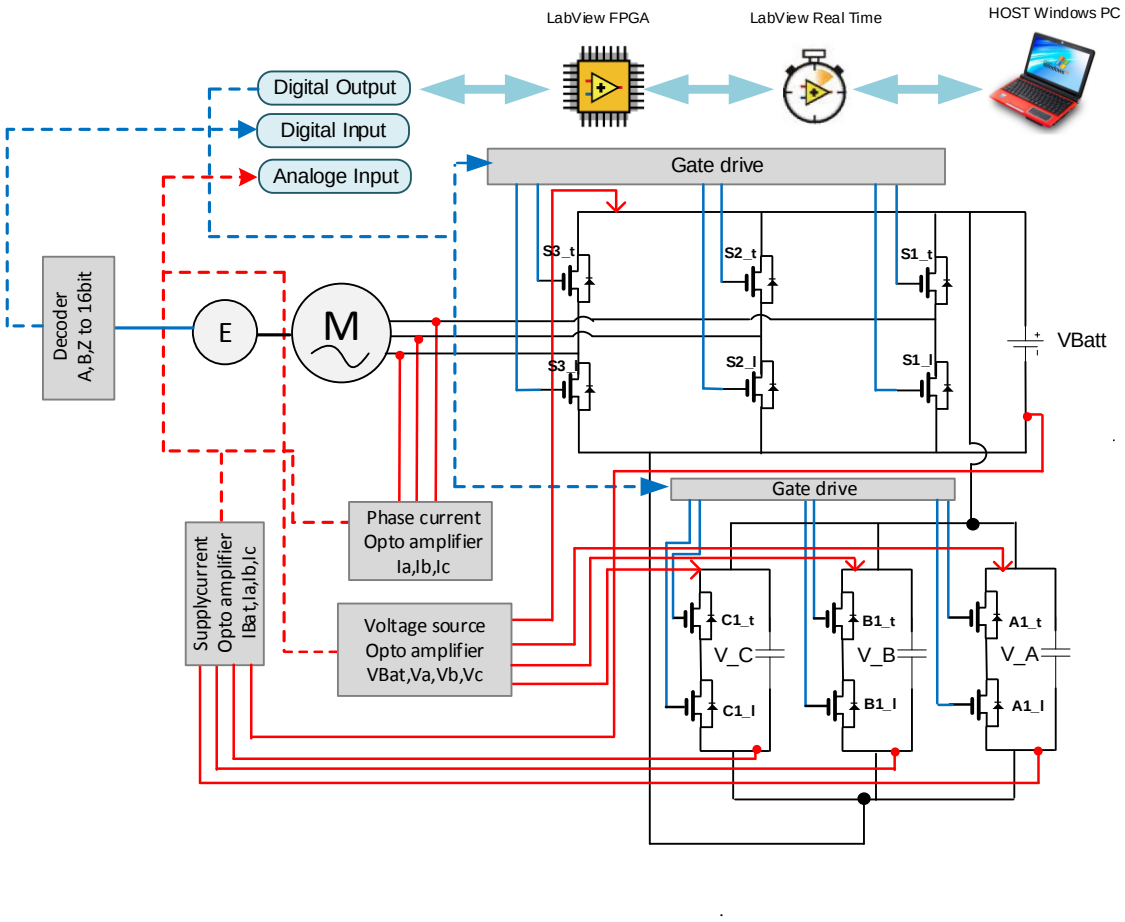

Figure 7-1: Overall schematic of experimental system

7.2.1 The Load of Platform

A KAPAK, three-phase induction motor manufactured by English Electric Machines AEI was used as the load, see Figure 7-2**.** The winding of the motor is connected in a delta configuration to meet the maximum peak voltage that is provided from the converter. A simple LC filter is connected between the three-phase terminal load and the output side of the converter to reduce the switching noise (to eliminate harmonic components of the output currents) as shown in Figure C- 1 in (Appendix C). The motor's parameters are given in Table C- 1

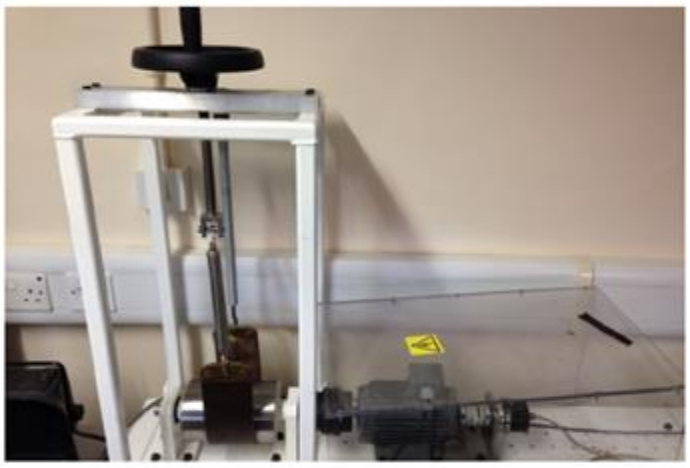

Figure 7-2 The load platform

7.2.2 Modified cascaded inverter

The configuration of the modified inverter included two sources and cascade converter, the main source is represented by the battery unit connected to the three-phase bridge converter and a combination of SC units connected to the H-bridge switches. The hardware platform of the inverter with SCs is shown in Figure **7-3**.

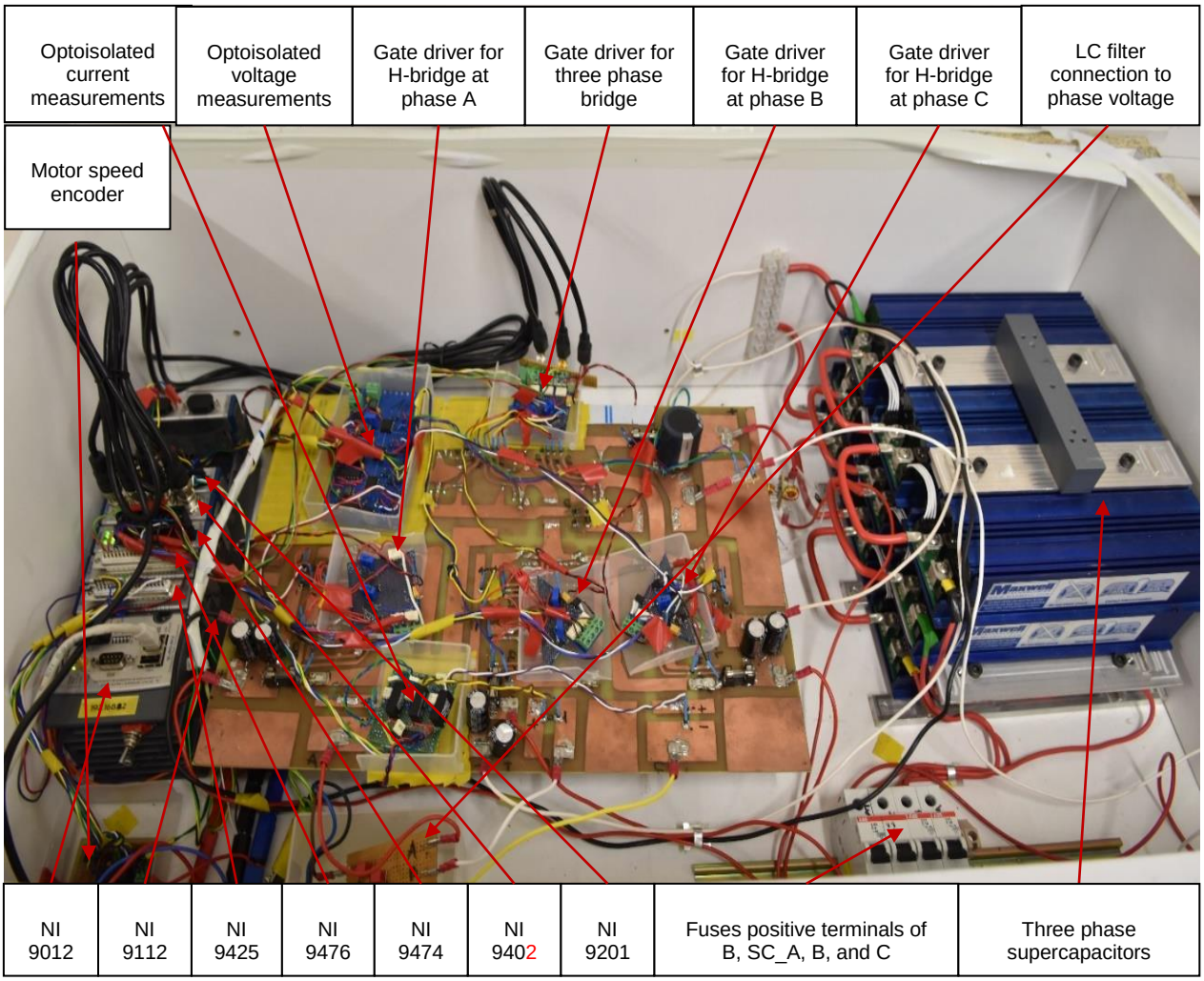

Figure 7-3 Photo showing details of inverter

7.2.3 Switch drive circuit of the inverter

Providing galvanic isolation between the sources (the battery and SC units) is one of the hardest parts in the design of the inverter. DC-DC converters (NCS6S4815C and Astec ASA00CC36-L) were used in order to provide a stable voltage supply for the switches' gates. The block diagram of the modified cascade inverter with switch drive circuits is presented in Figure C- 2 in appendix C.

The figure shows galvanically isolated low power supply units whose input voltage can be from 18 V to 75 V, and which deliver a stable and isolated auxiliary voltage from each bridge of 15 V. PSU1, PSU2, PSU3 and PSU4 are 3W and 6W universal DC/DC converters.

7.2.4 Battery bank

The battery bank is the main source that supplies the DC side of the three-phase bridge in the inverter. The battery bank contained 10 Leoch LP12-4.0 Sealed Lead Acid batteries (LAB, SLA 12 V, 4.0 Ah) connected in series with 400 mΩ total internal resistance (40 mΩ internal resistance per single battery). An LC filter element was connected between the battery bank and the three-phase bridge inverter to reduce the current ripples and help alleviate battery stress. The filter is constructed from a set of two 1 mF electrolytic capacitors and a series 80 µH inductor connected to the battery terminals. A shunt resistor with 50 mΩ was connected in series with the battery as shown in Figure 7-4. This was used to measure the battery current and is necessary to maintain battery charging and discharging within precise limits.

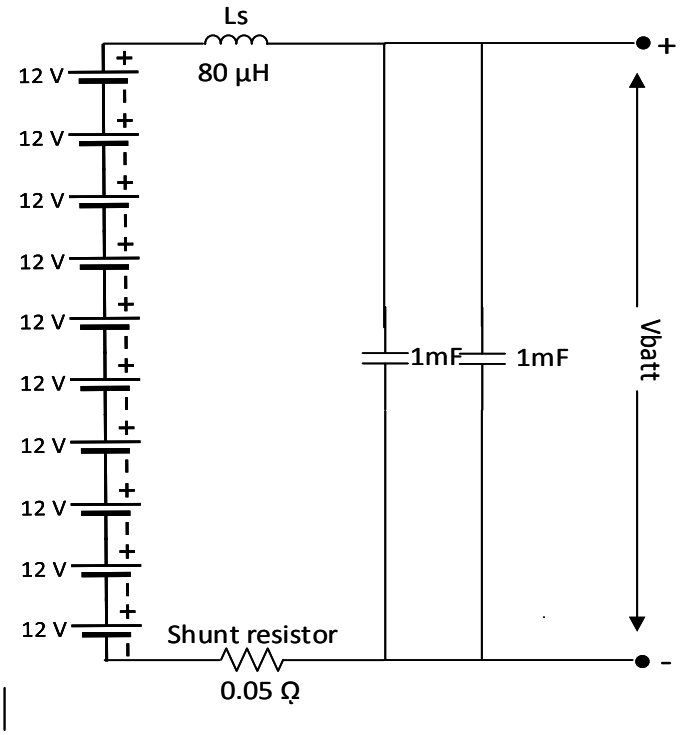

Figure 7-4 The battery voltage source

7.2.5 Supercapacitor storage unit

The second voltage source on the hardware platform is the SC. An electric double-layer boost cap UC from Maxwell Technologies (BMOD0350-15) with individually balanced cells was chosen. The pack working voltage for each cell is 15 V, so three cells are connected in series for each phase to obtain the 45 V connected to the H-bridge switches of the cascade converter. The capacitance of one module is 58 F which means the total capacitance of three connected in series in one phase is 19.33 F at 45 Volts. Thus, the maximum energy stored in each phase was 19.6 kJ. The circuit diagram for the SC compensation is presented in Figure 7-5.

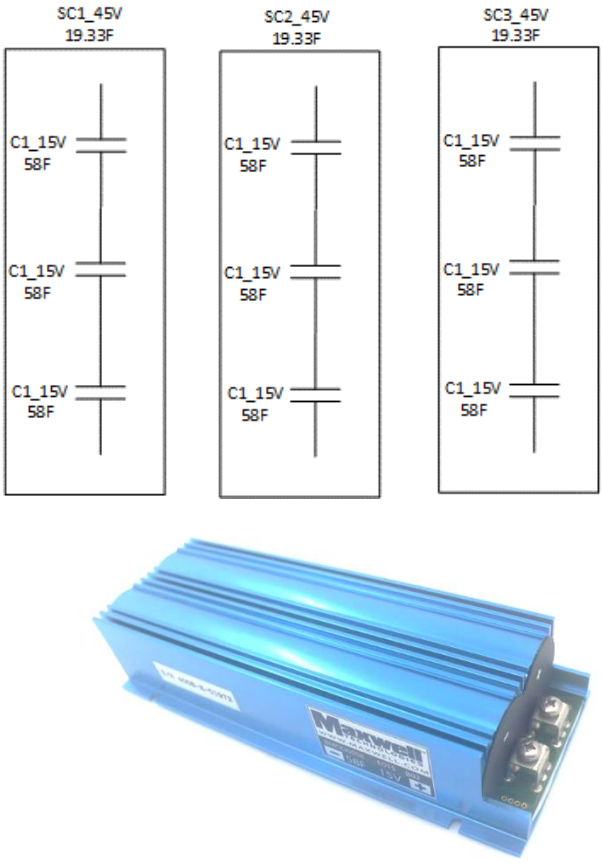

Figure 7-5 Capacitor bank and modelling circuit

7.2.6 Control platform

The National Instruments CompactRIO system embedded with a straightforward NI LabVIEW graphic interface was used as the control platform, see Figure 7-6 for the architecture of the system. A reconfigurable FPGA chip was a useful option that could be programmed using LabVIEW FPGA. This overcame the difficulty of using complicated FPGA programming languages such as VHDL. Thus, the custom timing, triggering, synchronization, control, and signal processing for analogue and digital I/Os could be achieved by exploiting the FPGA hardware embedded in CompactRIO. Details of the control system configuration is given in Appendix C. Figure 7-7 shows the physical representation of the NI CompactRIO system. Figure 7-8 show the overall hardware structure of the experimental rig.

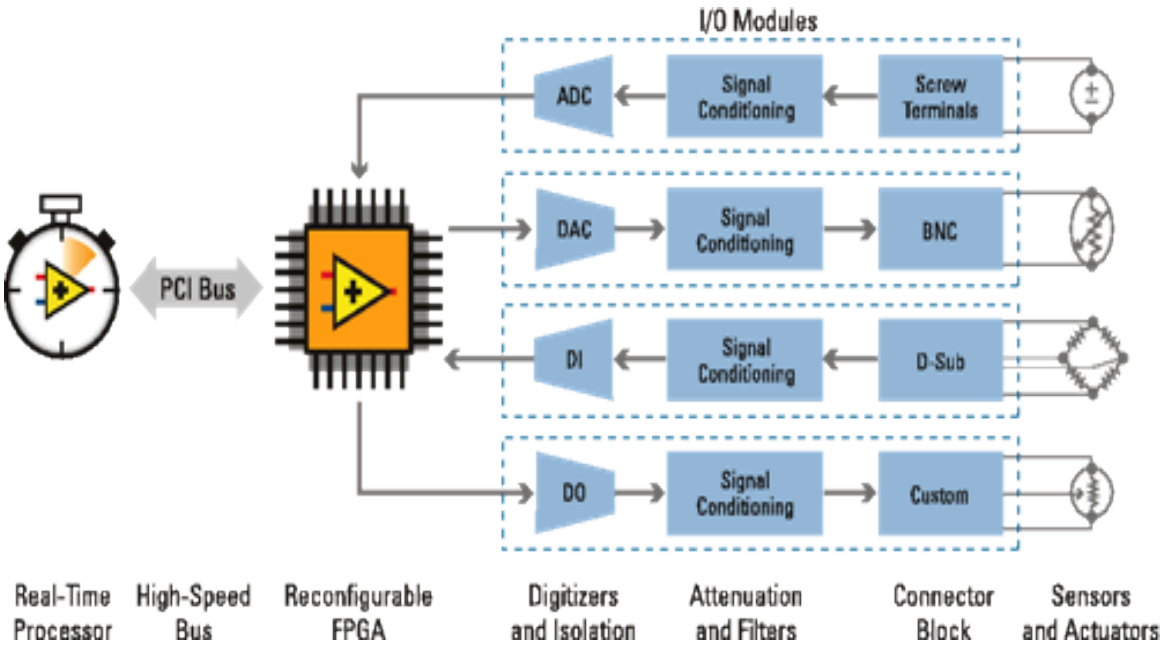

Figure 7-6: Architecture of the CompactRIO system [211]

Figure 7-7 The NI Compact RIO system with input/output allocation

7.2.7 Optoisolated digital signal interface

On the hardware platform, a high-speed logic optocoupler HCPL2601 device was used to ensure galvanic isolation between control signals from the NI system and converter gate drivers. This device has the speed and common mode rejection of 10 kV/us and 10 Mbit/s respectively. The graphic diagram of the digital optoisolator is given in Figure C- 3 in Appendix C.

7.2.8 Optoisolated voltage and current sensing circuit

Accurate feedback information of voltage and current measurements of the storage devices are essential in order to manage the maximum available energy that can be realised from the battery and SCs and to keep the voltage and current drawn from the storage devices balanced between the phases. The separate circuit constructed for each of the current sensors depended on the output of the isolation amplifiers HCPL-7840, see Figure C- 4. Also, a highly linear analogue optocoupler HCNR201 took the voltage measurement from the sources and provided isolation between each source and CRIO control system, see Figure C-5 in Appendix C. The circuit, including current and voltage measurement devices is given in Figure C- 6 in Appendix C.

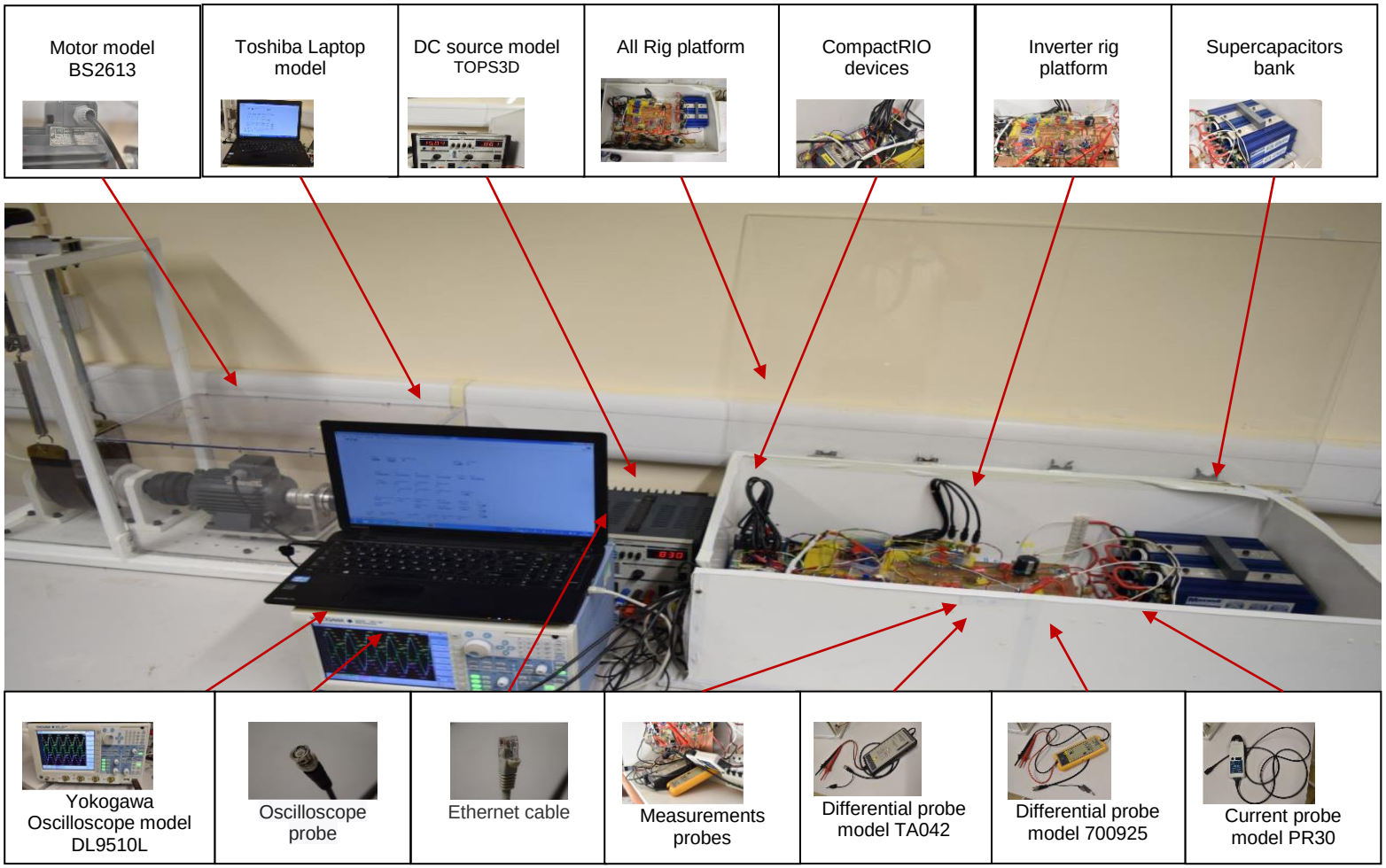

Figure 7-8: The hardware structure of the experimental rig

7.3 Experimental Setup

In order to investigate the applicability of the proposed D-STATCOM hybrid storage system, it was tested using an experimental test rig with cascade inverter-based battery and SCs. The hardware platform with dual sources (battery and SC) was tested under two modes to verify the proposed concept. Firstly, the inverter platform test was executed with the two-level three-phase bridge using the battery only system. In the second mode, the hardware platform used the hybrid storage energy system (both battery and SC). The results of the tests, the measured voltage and current for the inverter, battery current and SC current were recorded using three Picotechnology TA042 100 MHz 1400 V Differential Probes, one Yokogawa 700925 15 MHz 1000 V Differential Probe, one Techquipment LEM PR30 Oscilloscope AC/DC Current Probe and a Yokogawa DL9510L mixed signal oscilloscope.

The main purpose of the experiment was to test how the D-STATCOM's inverter with two sources, see Section 6.2.2, would operate. In this experiment, the main source provided a 60 V maximum amplitude to the three-phase bridge. Figure 7-9, 7-11, and 7-13 present the experimental results of the output waveforms of the converter based on the battery-only system supplied to the load at voltage levels of 40 V, 50 V and 60 V respectively. The system in the first mode relies on the battery current only. It can be seen from Figures that the system does not have the benefit of having the SC support the battery. The performance of the converter based on the battery only system gives a balanced output voltage with phase shift of 120^{o}.

The simulation model in chapter six has been modified and employed in this section. Figure 7-10, 7-12 and 7-14 present the simulation results of the output waveforms of the converter based on the battery-only system supplied to the load at voltage levels of 40 V, 50 V and 60 V respectively. It can be seen from the Figures that the improved simulation model still maintains the capability of the battery storage to deliver the power but with some oscillation. It can be clearly seen that experimental voltage waveforms of the three-phase bridge (yellow,

green and purple channels) of Figure 7-9, 7-11, and 7-13 and voltage waveforms of the simulation outputs captured on the control board are the same in steady state. However, a distortion is observed in experimental results. The distortion indicates that the motor voltages are not purely sinusoidal. The distortion is due to harmonic components which exist in the output voltages when the motor impedance was operated at low voltages. In terms of the time constant, the system takes longer than the designed value of the simulation. The difference in time constants between the captured value and the design is possibly due to the sample and processing delays associated with the hardware platform.

The phase current of inverter absorbed by the three-phase induction motor (load) is shown in the blue channel in (Figure 7-9, 7-11, and 7-13) was provided by the battery.

Generally, the simulation results are in good agreements with the corresponding experimental results and reasonably accurate predictions, where battery current and phase voltage and current had identical shapes.

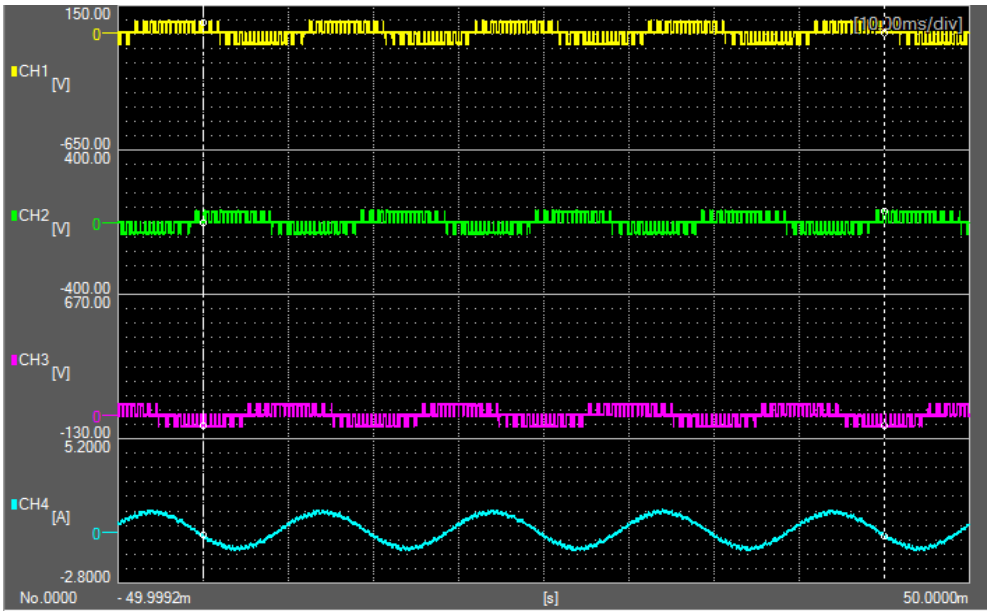

(a)

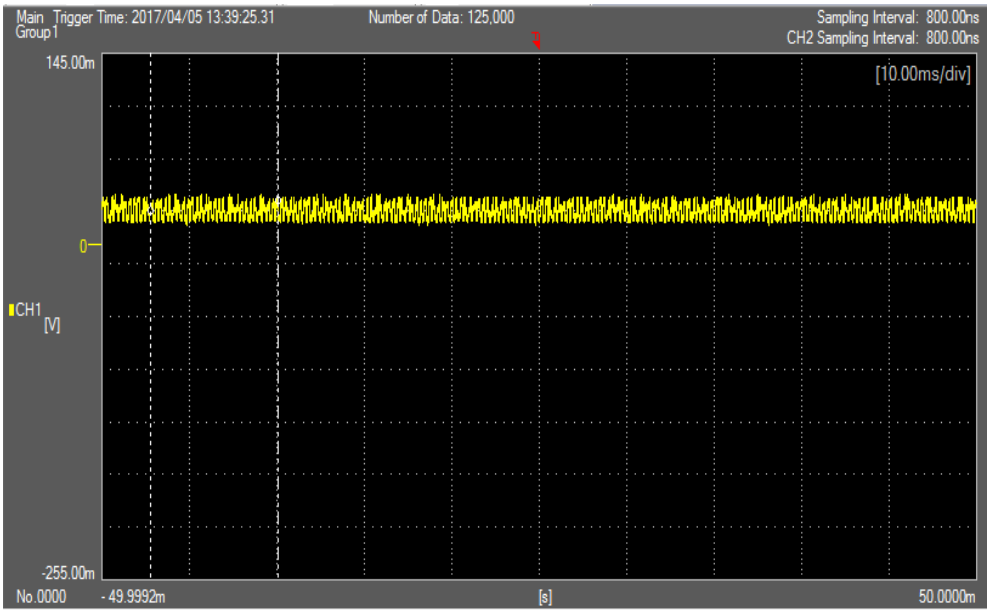

(b)

Figure 7-9 Waveforms of the three-phase bridge at output voltage 40 V (experimental results), (a) Channel 1 (yellow) voltage of inverter at line AB, channel 2 (green) voltage of inverter at line BC, channel 3 (purple) voltage of inverter at line CA, channel 4 (blue) phase current of inverter, (b) Battery current (A)

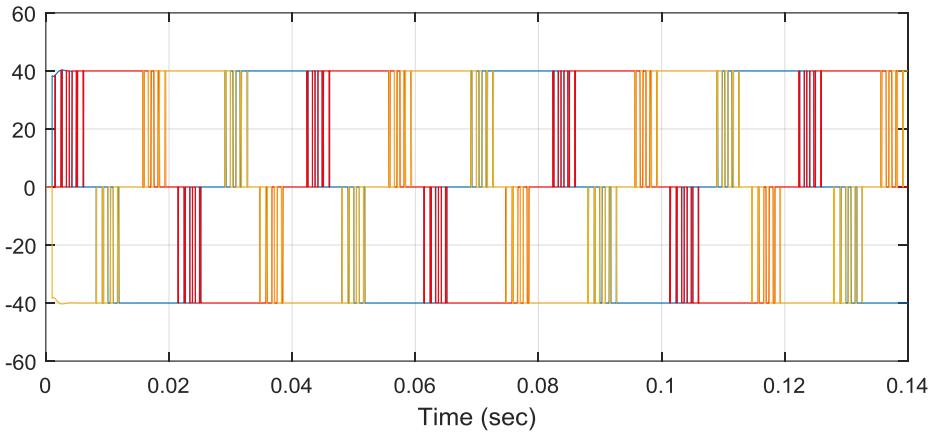

(a)

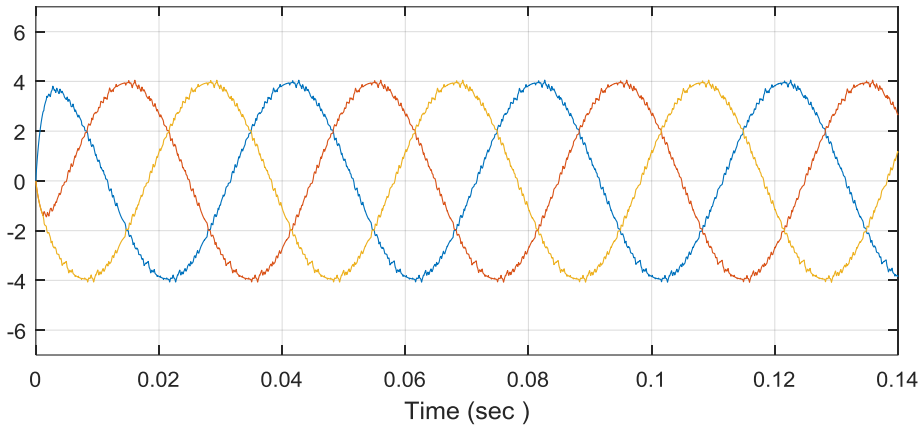

(b)

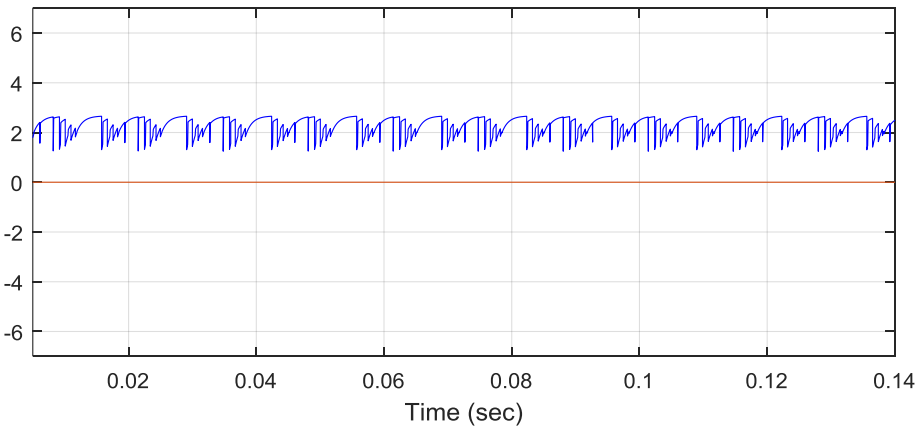

(c)

Figure 7-10 Waveforms of the three-phase bridge at output voltage 40 V (simulation results), (a) voltage waveforms of three-phase bridge, (b) three phase current of inverter, (c) Battery current (A)

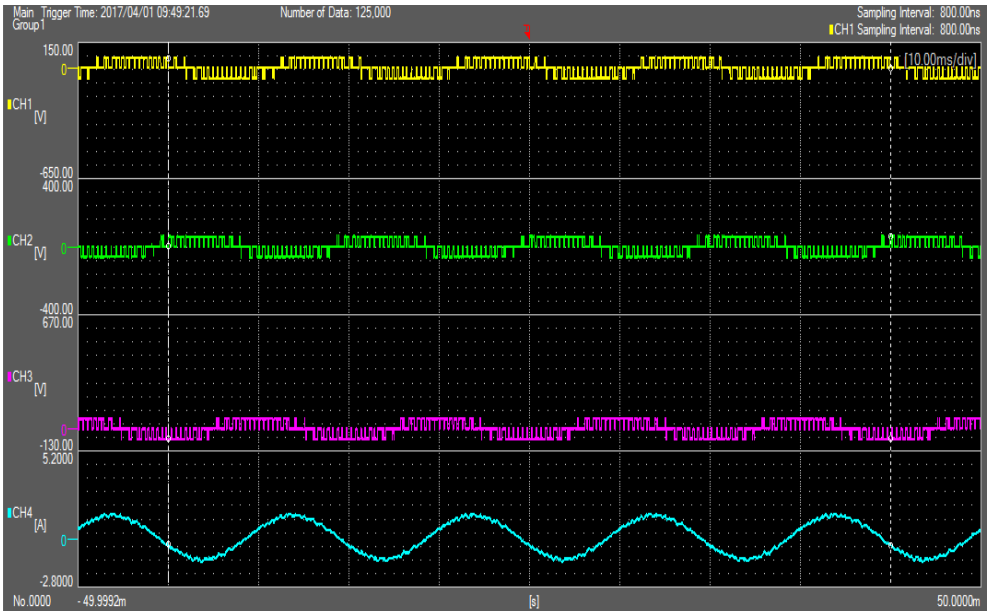

(a)

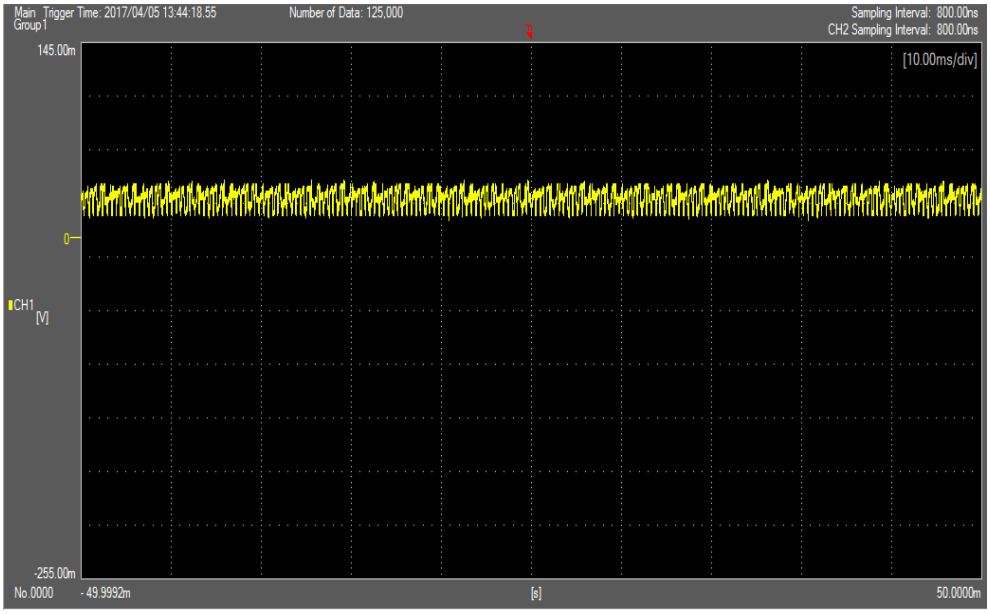

(b)

Figure 7-11 Waveforms of the three-phase bridge at output voltage 50 V (experimental results), (a) Channel 1 (yellow) voltage of inverter at line AB, channel 2 (green) voltage of inverter at line BC, channel 3 (purple) voltage of inverter at line CA, channel 4 (blue) phase current of inverter, (b) Battery current (A)

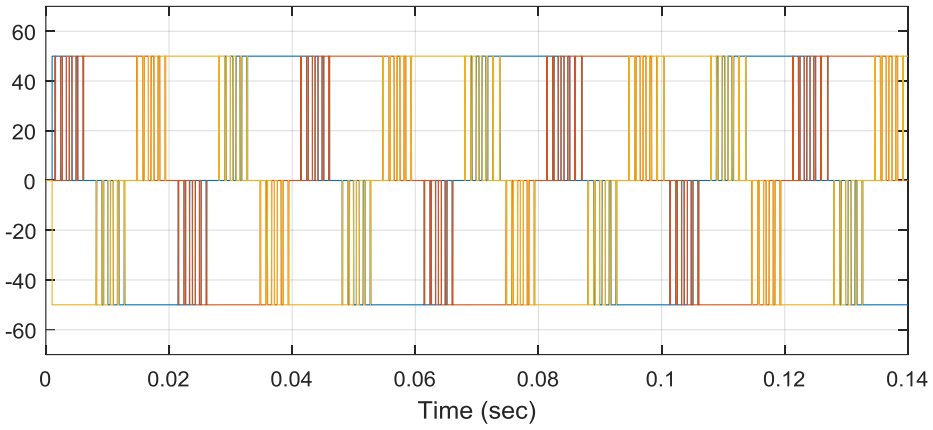

(a)

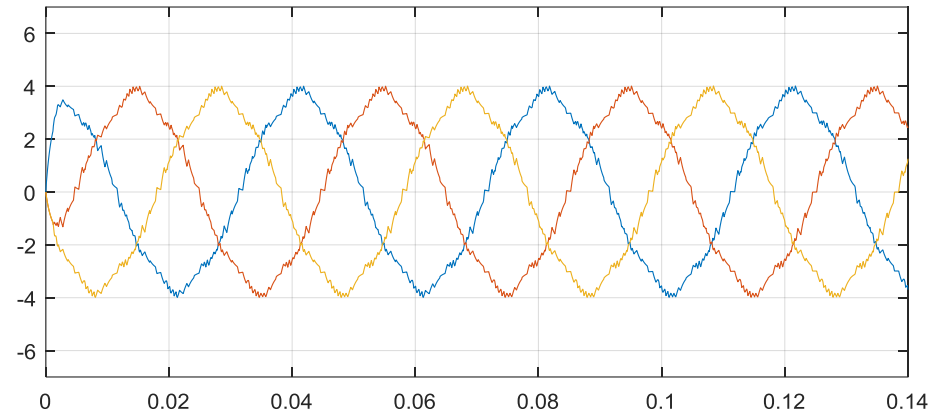

(b)

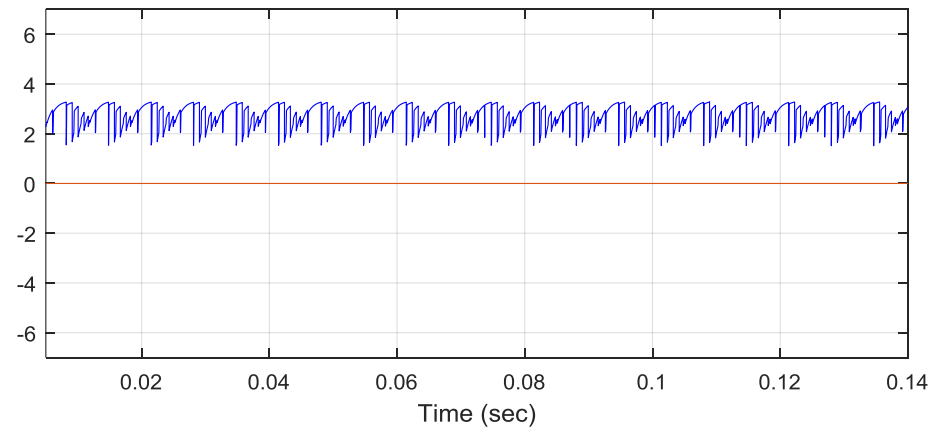

(c)

Figure 7-12 Waveforms of the three-phase bridge at output voltage 50 V (simulation results), (a) volt-age waveforms of three-phase bridge, (b) three phase current of inverter, (c) Battery cur-rent (A)

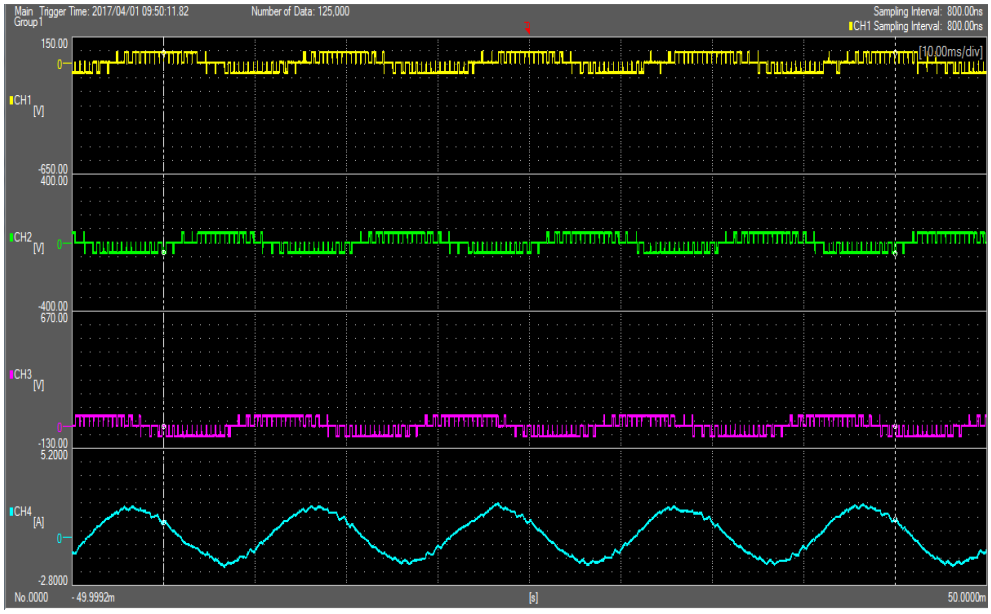

(a)

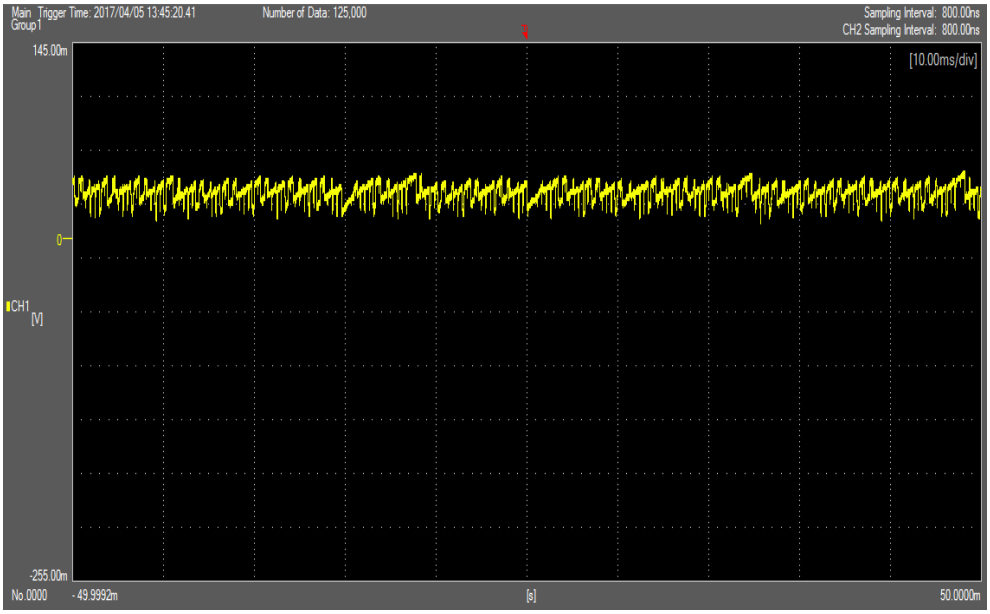

(b)

Figure 7-13 Waveforms of the three-phase bridge at output voltage 60 V (experimental results), (a) Channel 1 (yellow) voltage of inverter at line AB, channel 2 (green) voltage of inverter at line BC, channel 3 (purple) voltage of inverter at line CA, channel 4 (blue) phase current of inverter, (b) Battery current (A)

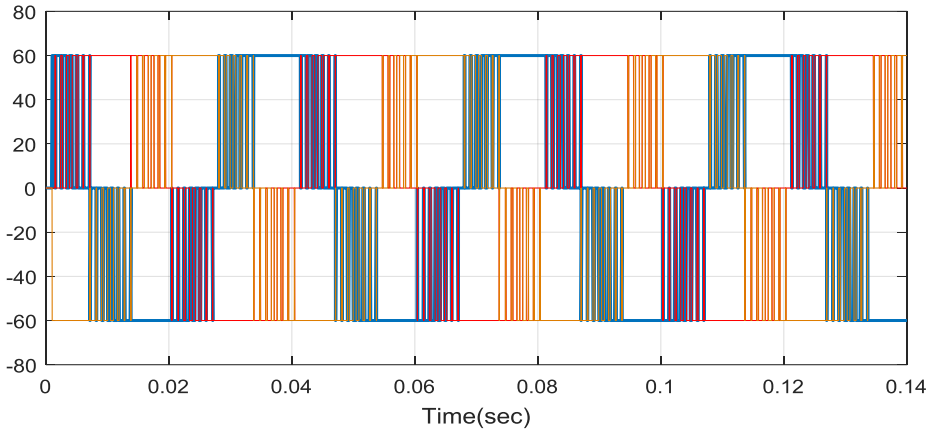

(a)

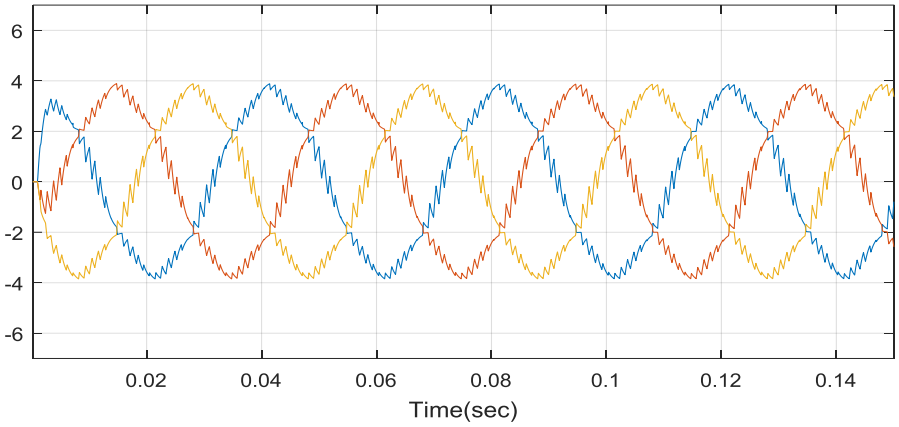

(b)

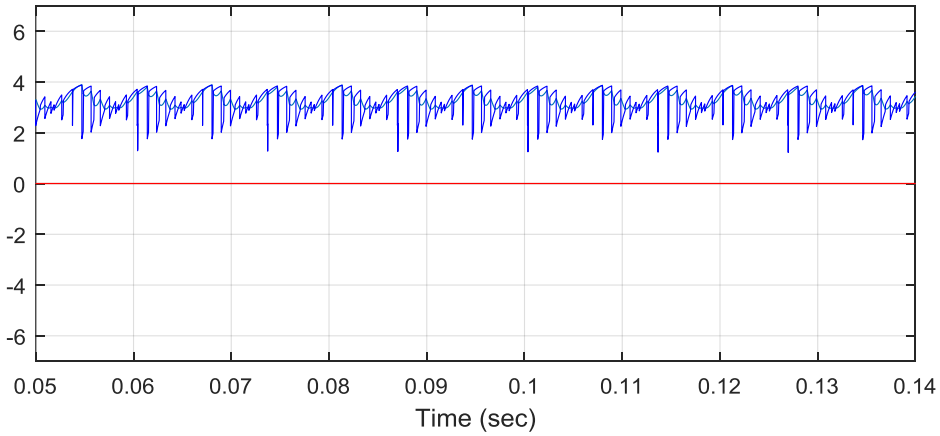

(c)

Figure 7-14 Waveforms of the three-phase bridge at output voltage 60 V (simulation results), (a) voltage waveforms of three-phase bridge, (b) three phase current of inverter, (c) Battery current (A)

Figure 7-15 to Figure 7-20 display the experimental and simulation output waveforms for distributed power sharing between the battery and SC storages units at voltage levels of 40 V, 50 V and 60 V respectively.

The main purpose of the modified D-STATCOM configuration with multisources (battery and SC) is to provide faster and better voltage regulation and reduce battery current stresses. To achieve this, in the second mode, the power demand was distributed between the two sources.

The capacity of the platform to detect sudden source current increases was verified in the second test. The battery current remained within limits while the SC reacted to sudden changes in the load and the output voltage of the converter was unchanged, as shown in Figures 7-15 (a), 7-17 (a) and 7-19 (a). Also, it can be seen that when the battery current (channel 1 in the yellow colour of Figures (b)) is at its maximum value, the SC delivered current (channel 2 in the green colour of Figures (b)).

To allow comparison of the experimental results of the second test (D-STATCOM configuration with multisources, battery and SC) with the simulations results. The modified simulation model for inverter based battery and SC at output voltage levels of 40V, 50V and 60V were performed as shown in Figure 7-16, 7-18 and 7-20. In traces (a) and (b) of the Figures an example voltage and current waveforms are presented. Trace (c) presents instantaneous current delivered by each voltage source where it is noticeable that power (blue trace) is provided by the main source almost constant current when the supercapacitor current is oscillating (red trace). In general, it is seen a close agreement between the experimental and simulation results.

Comparing the two sets of Figures it can be seen that in the first mode test the maximum battery current was higher than in the second mode test. The output phase current and voltage were not affected in either test mode; in the second mode the battery current was effectively decreased.

Figure 7-21 to Figure 7-23 give the phase-voltage waveforms of the converter at voltage levels of 40 V, 50 V and 60 V respectively.

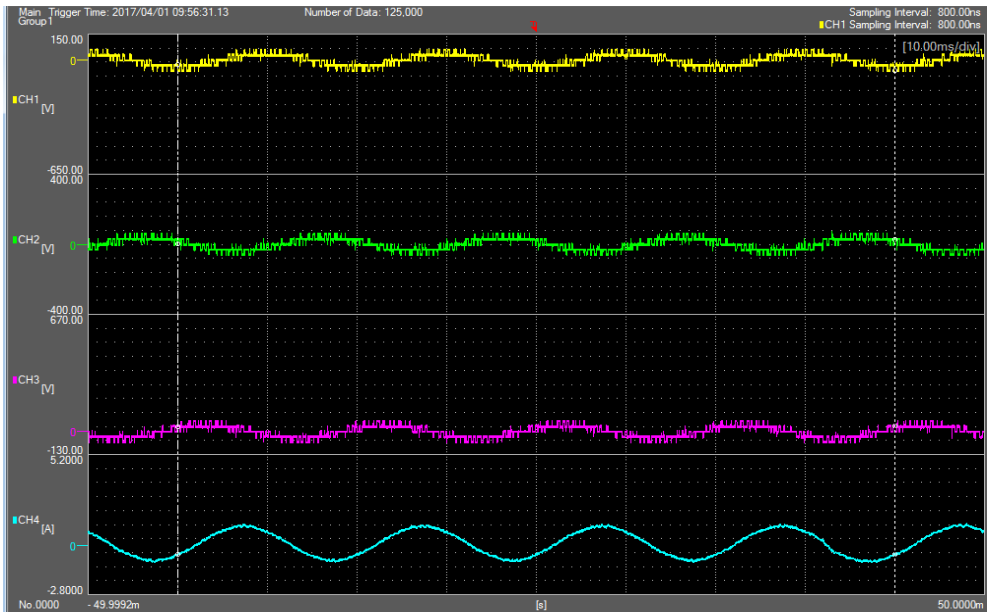

(a)

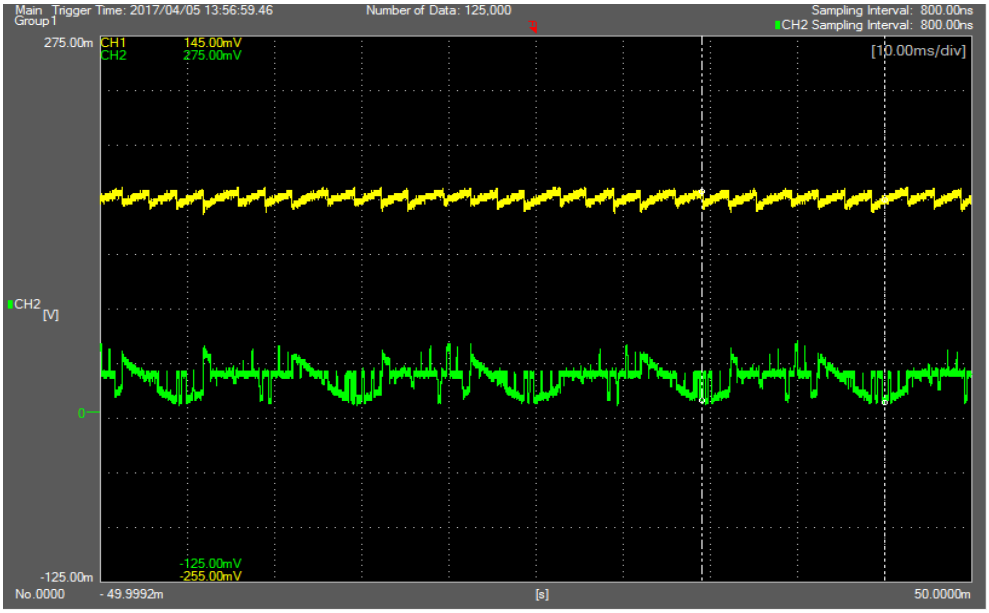

(b)

Figure 7-15 Waveforms of the inverter based battery and SC at output voltage 40 V (experimental results), (a) Channel 1 (yellow) voltage of inverter at line AB, channel 2 (green) voltage of inverter at line BC, channel 3 (purple) voltage of inverter at line CA, channel 4 (blue) phase current of inverter, (b) channel 1 (yellow) Battery current (A), channel 2 (green) SC current (A)

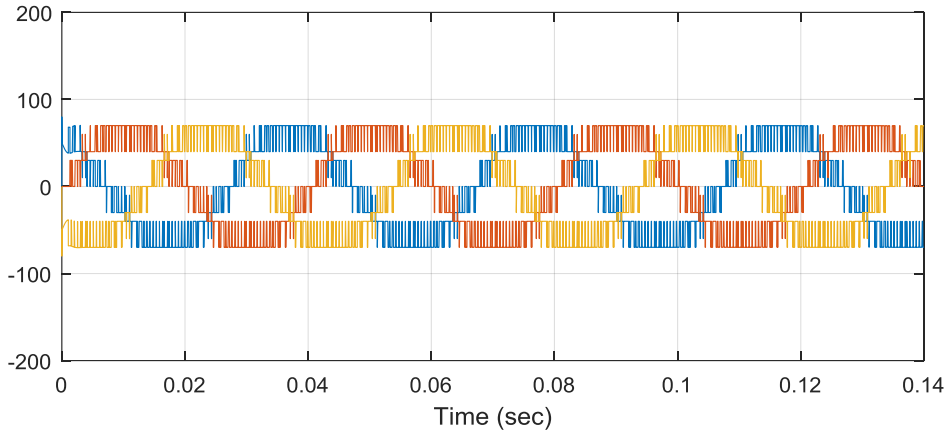

(a)

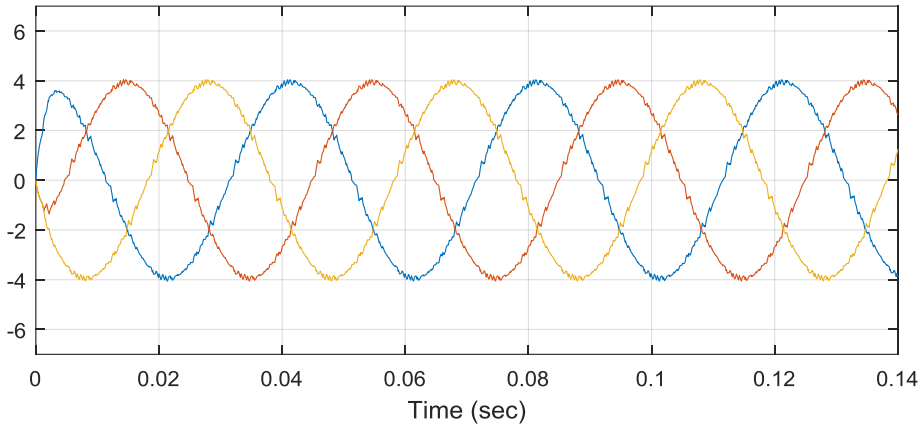

(b)

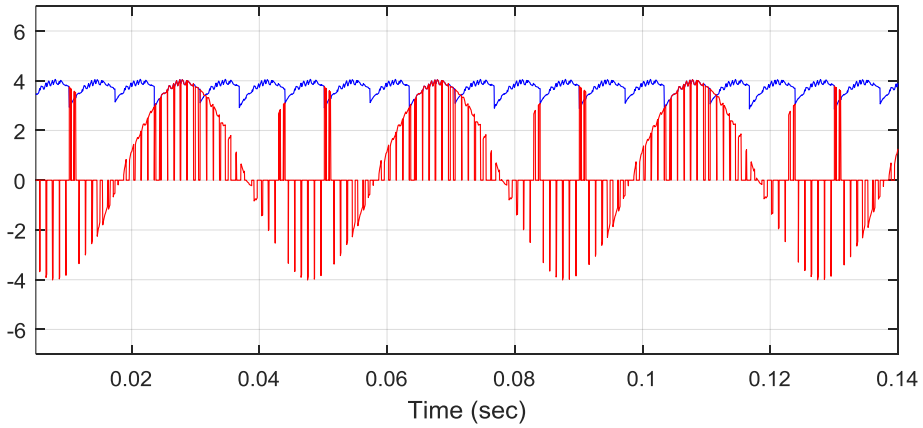

(c)

Figure 7-16 Waveforms of the inverter based battery and SC at output voltage 40 V, (simulation results), (a) voltage waveforms of three-phase bridge, (b) three phase current of inverter, (c) channel 1 (blue) Battery current (A), channel 2 (red) SC current (A)

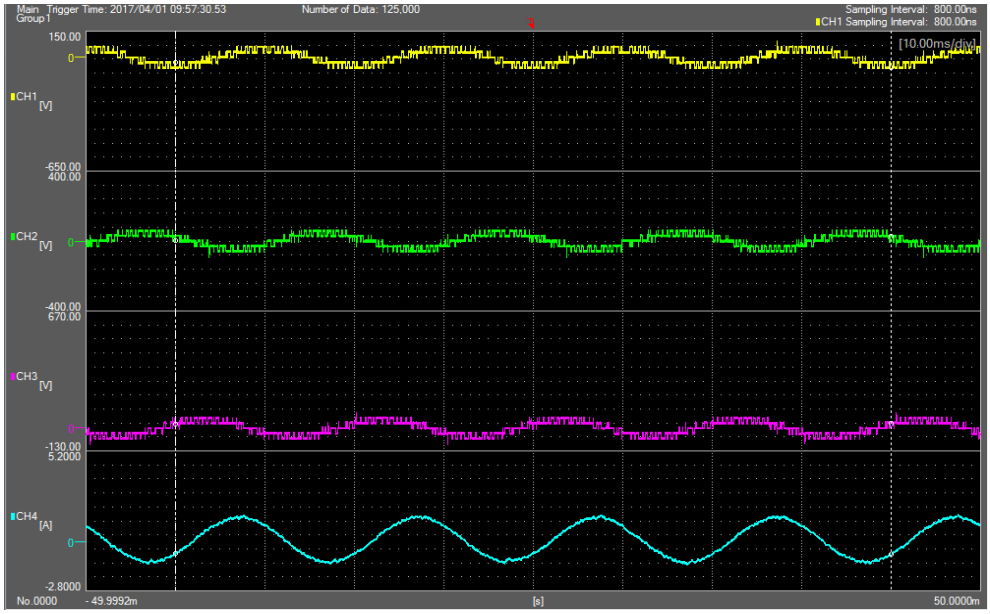

(a)

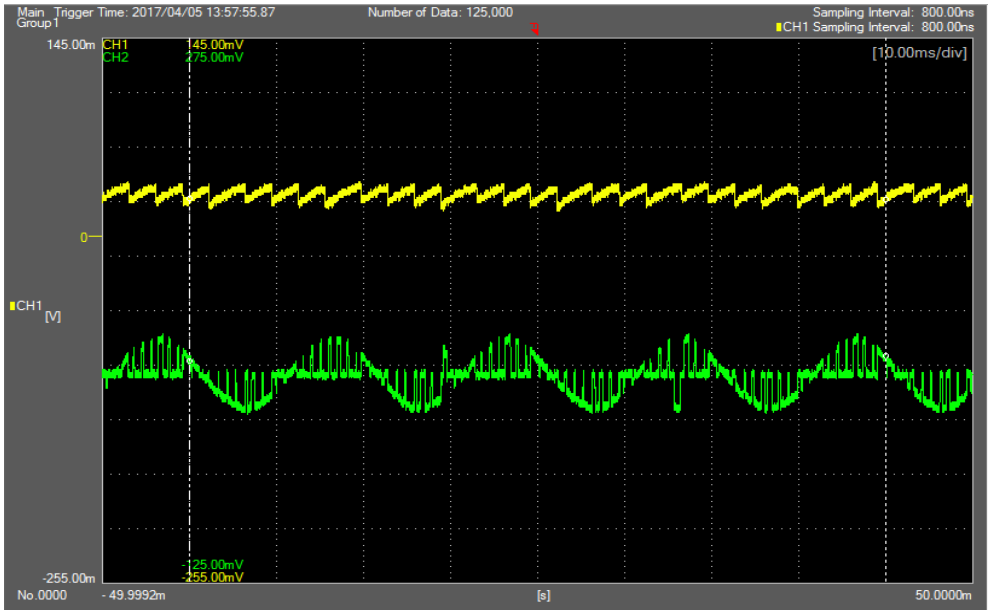

(b)

Figure 7-17 Waveforms of the inverter based battery and SC at output voltage 50 V (experimental results), (a) Channel 1 (yellow) voltage of inverter at line AB, channel 2 (green) voltage of inverter at line BC, channel 3 (purple) voltage of inverter at line CA, channel 4 (blue) phase current of inverter,(b) channel 1 (yellow) Battery current (A), channel 2 (green) SC current (A)

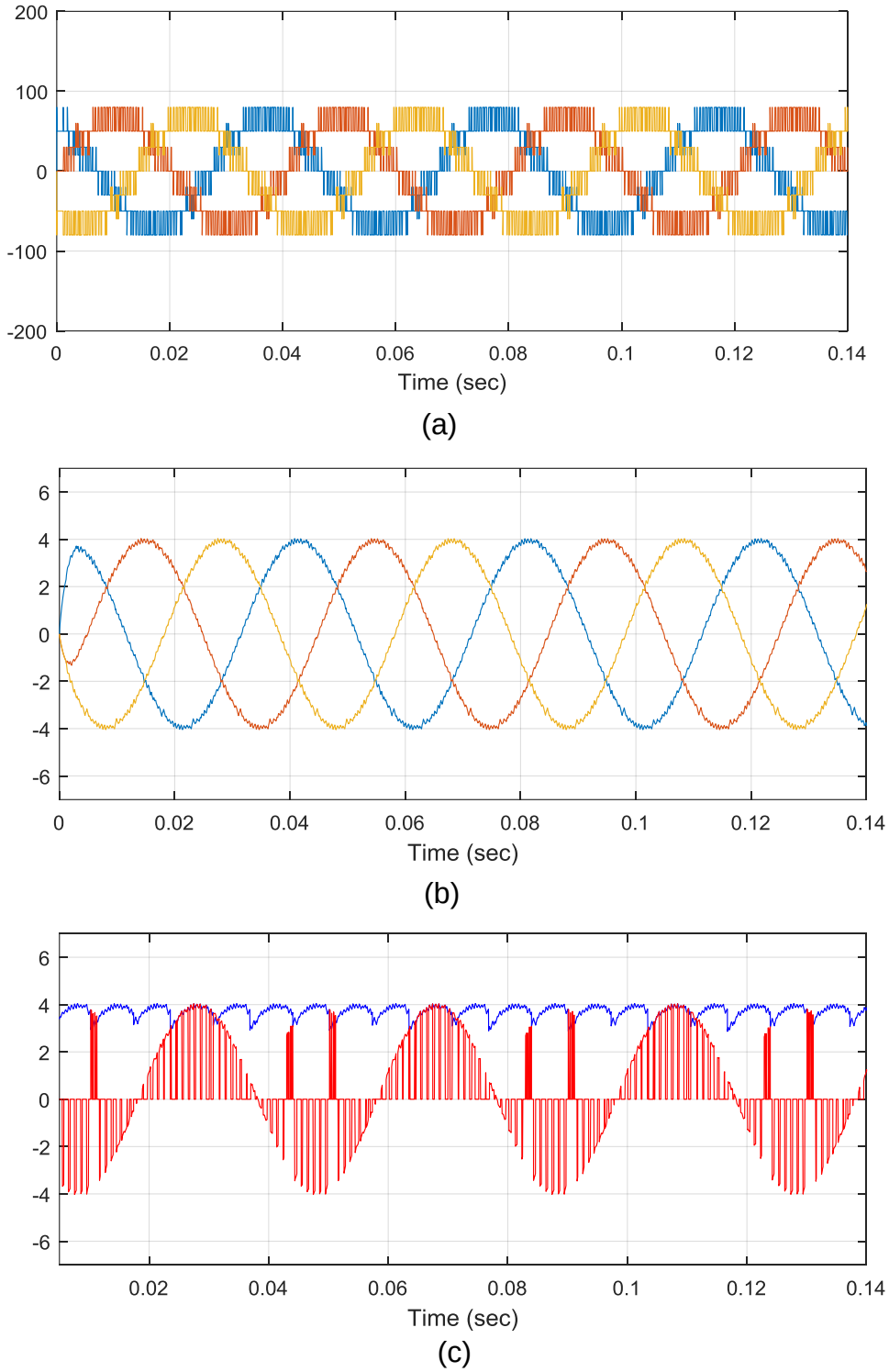

Figure 7-18 Waveforms of the inverter based battery and SC at output voltage 50 V, (simulation results), (a) voltage waveforms of three-phase bridge, (b) three phase current of inverter, (c) channel 1 (blue) Battery current (A), channel 2 (red) SC current (A)

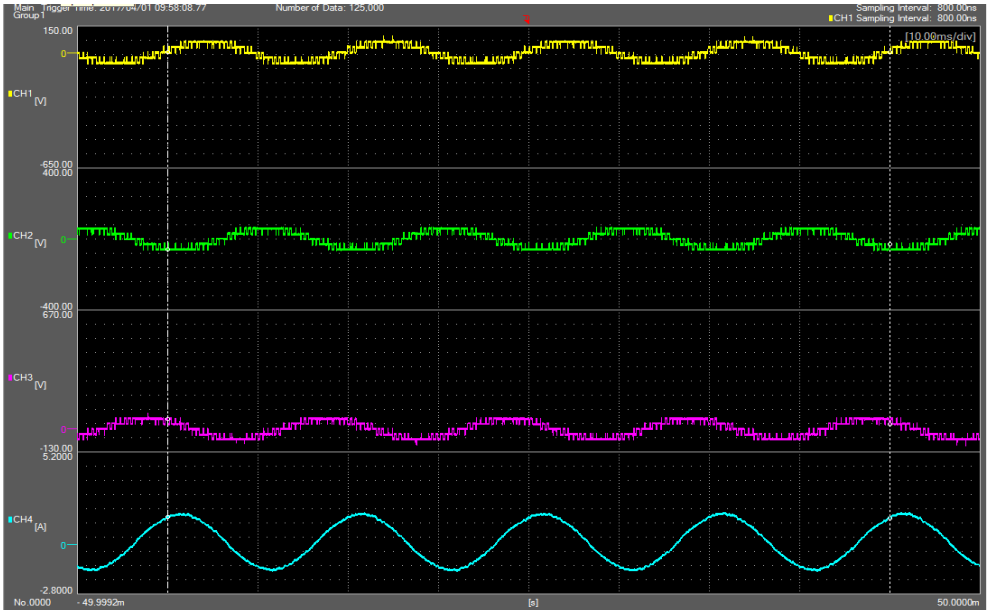

(a)

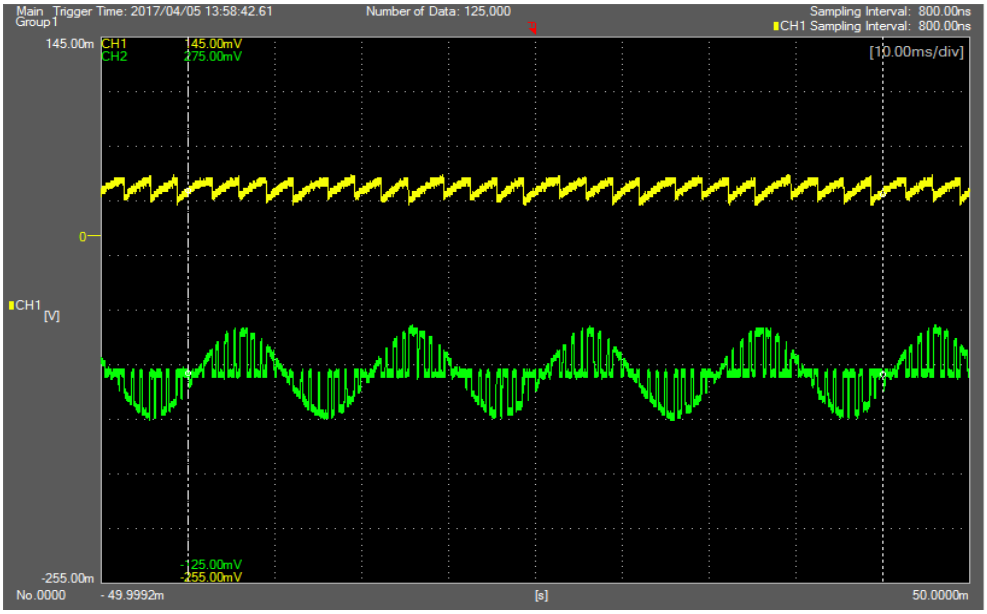

(b)

Figure 7-19 Waveforms of the inverter based battery and SC at output voltage 60 V (experimental results), (a) Channel 1 (yellow) voltage of inverter at line AB, channel 2 (green) voltage of inverter at line BC, channel 3 (purple) voltage of inverter at line CA, channel 4 (blue) phase current of inverter,(b) channel 1 (yellow) Battery current (A), channel 2 (green) SC current (A)

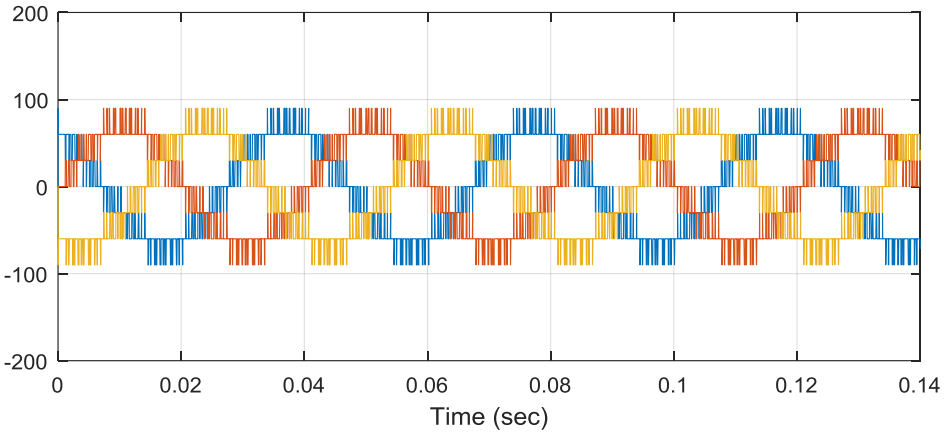

(a)

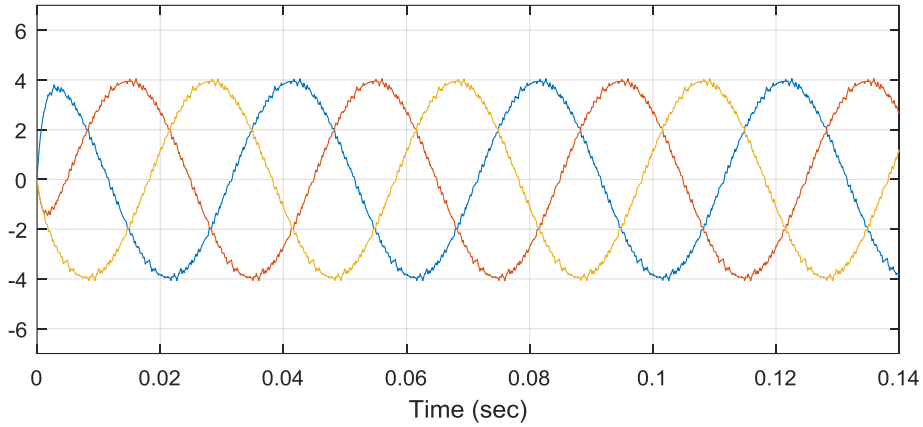

(b)

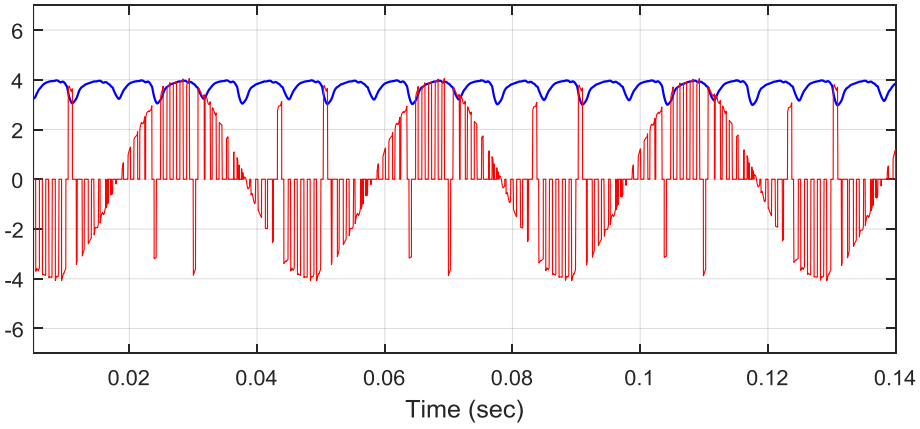

(c)

Figure 7-20 Waveforms of the inverter based battery and SC at output voltage 60 V, (simulation results), (a) voltage waveforms of three-phase bridge, (b) three phase current of inverter, (c) channel 1 (blue) Battery current (A), channel 2 (red) SC current (A)

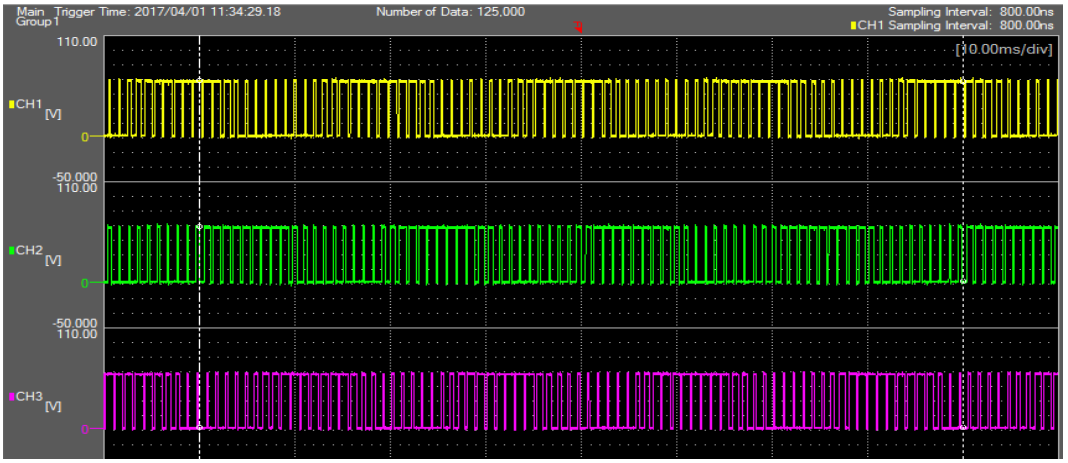

Figure 7-21 Phase waveforms of the inverter at output voltage 40 V

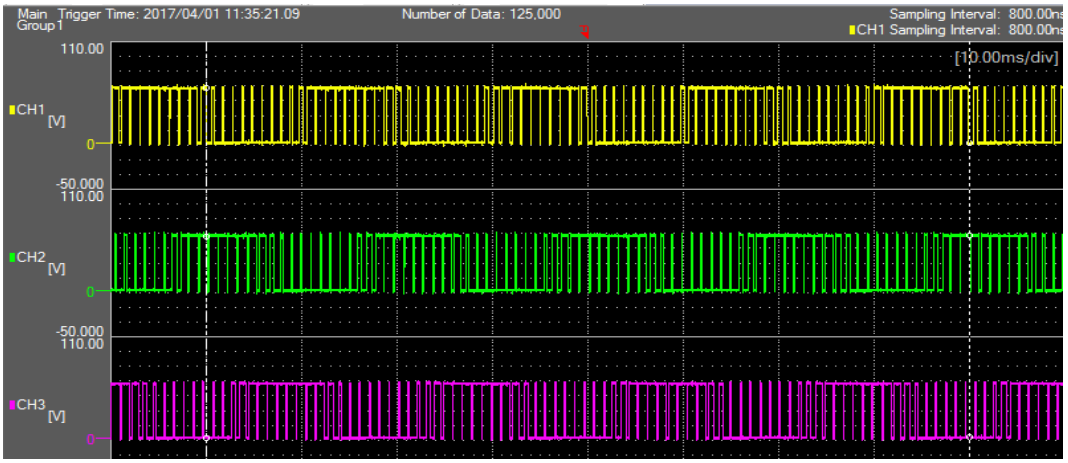

Figure 7-22 phase waveforms of the inverter at output voltage 50 V

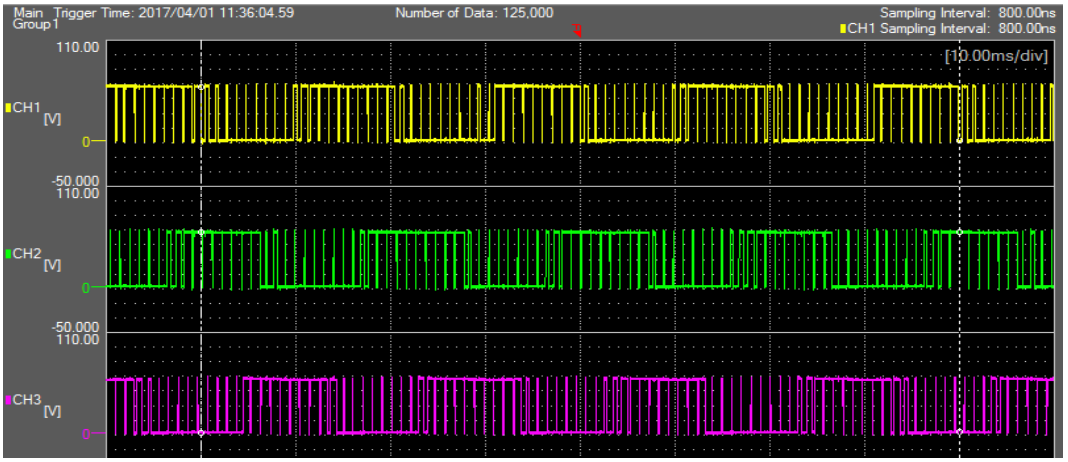

Figure 7-23 Phase waveforms of the inverter at output voltage 60 V

7.4 Summary

This chapter concentrates on the experimental validations of the D-STATCOM configuration based HESS. To develop and validate the proposed strategy of the modified D-STATCOM configuration with HESS connected with a distribution system is difficult and expensive using real systems, and to carry out those tests using model experiments are a serious challenge and will add an interesting dimension to the study. Therefore, a previous test rig was modified for these tests, this included adding a control platform consisting of FPGA processor programmed using LabVIEW software. The main purpose of the experiment was to investigate the operation of the D-STATCOM's inverter configuration with two energy sources.

Generally, the converter structure with the control platform provided a good description of the management of energy storage units used with a D-STATCOM structure. It has the capability of the experimental validation. Therefore, this prototype hardware even with its limited abilities and controlled platform acted as an effective option which gives the basis for developing other more advanced practical applications. Firstly, this chapter has presented a description of the component parts of the experimental platform to provide a good understanding of the system architecture. The system architecture consisted basically of a three-phase bridge converter, battery bank, combinations of SC and load, and other auxiliary components and measuring instruments. The chapter then reported on the two test modes that were carried out, first the inverter platform test based on the battery-only system and then the hardware platform test based on the hybrid storage energy system (battery and SC). The tests confirmed the platform with hybrid storage demonstrated the ability of the design to sense rapid source current changes and distribute the power required between the two storage units effectively. Finally, the simulation and experimental results provided very close predictions. it is reasonable to conclude that the experimental results are in very good agreements with the corresponding simulation results. Overall, the validity of the modified D-STATCOM configuration proposed has been underpinned by the experimental results.

8 Chapter Eight: Conclusions and Future Work

This chapter presents the conclusions of this study, identifying some of the limitations in the research and potential areas for future studies in this area.

8.1 Discussion and Conclusions

At the present time, across the globe, electrical power systems are undergoing serious and dramatic changes, particularly with the significant penetration of distributed generation, including renewable resources, energy storage units and smart devices. These developments should assist in reducing climate change by decreasing greenhouse gas emissions, while meeting system-level requirements for better power quality, in particularly compensating for voltage sags.

This research has integrated a number of disciplines and this has been one of its most significant challenges. Another was that there is no commonly agreed definition of what is a microgrid. This omission has been addressed by a comprehensive literature review, with a view to develop a simple description of the differences between traditional and modern power grids, particularly with respect to the allocations of new sources and power flow direction, this was done in Chapter One.

Managing these new electrical power grids is a substantial part of good grid performance, which requires the provision of solutions to current grid and voltage problems using active and reactive power compensation. Power electronics technology is an underpinning technology which can utilise the great potential of these grids even under varying operating conditions, as introduced in Chapter Two.

It is expected that in the future the development of intelligent control of advanced power electronics systems will allow electricity generated by renewable energy systems to increase grid power capacity. Additionally, the higher efficiency and greater reliability of the power conversion systems will be enhanced, hopefully reducing the cost of energy and extending the service period. Chapter Two also

summarises the current state of energy storage technology. It is shown that current energy storage uses a wide range of technologies and that by suitably combining different technologies, EES can meet most of the technical requirements for power system and network operations.

In this study, the advance in D-STATCOM application to energy storage technologies is presented as a promising option that can provide the active and reactive power support needed to give a better performance of AC grid operation. The literature survey has shown that most researchers in this field have considered the control of the power quality using only conventional D-STATCOM converters connected to distribution networks. There has been little attention given to the control and operation of D-STATCOM based energy storage systems. The main purpose of this work is to achieve voltage control and improve power quality of distribution grids by controlling the voltage at the point of common coupling using D-STATCOM combined with hybrid energy storage technology.

In Chapter Three, the modelling and analysis of a D-STATCOM connected to a distribution grid was presented in the *d-q* orientation frame. The dynamic differential equations of the distribution system were given and applied in the d-q transformation analysis and a set of steady state equations were obtained. From the plots and surface graphs resulting from the steady state analysis, it was found that the maximum load power $P_{l,max}$ decreased as the source inductance (L_s) increased, whereas increasing the time constant of the source (T_s) resulted in increasing the maximum load power $P_{l,max,desired}$. In addition, there is a linear relationship between the source voltage and the inductance and time constant of the source. The decreasing of the source time constant (T_s) results in increasing the minimum source voltage $V_{s,min}$ whilst the voltage of the source increases linearly with source inductance. Furthermore, the rating of the D-STATCOM application as a voltage regulation device corresponding to the system parameters was investigated. The rating of the $S_{D-STATCOM}$ was found to be a function of the system parameters e.g. source resistance (R_s) and source inductance (L_s).

In Chapter Four reported the investigation of the suitability of a novel control method using the sugeno-fuzzy PI controller and its fitness when used with distributed FACTS devices to mitigate problems with power quality. Firstly, the model and the control loops for a conventional D-STATCOM (without ESS) were developed based on the vector control algorithm in rotating reference frame of the (d-q). The PI control parameters (K_p and K_i) were decided on and tuned using standard procedure from the MATLAB SISO tool box. Then, an intelligent sugeno-fuzzy compensator for DC side voltage control of the D-STATCOM was developed based on the previous design of conventional linear PI compensators. Two inputs and one output for each control parameter of the PI compensator were selected to map a set of rules based on linguistic variables in an empirical way to modify the proportional and integral control parameters during different operating conditions. As a nonlinear controller, the fuzzy-tuned PI has been tested against the linear P and PI controller based D-STATCOM models. Comprehensive simulation results show that the D-STATCOM with the proposed fuzzy PI controller demonstrates significant improvements over the conventional P and PI controllers in enhancing voltage stability in distribution networks. The control approach with the PI-based sugeno-fuzzy logic supervisor gives an improved voltage response at the PCC of the AC grid, and DC side voltage response of the D-STATCOM with lower steady state error and a clear reduction in the value of the voltage dip during load changes. This was because the proportional and integral coefficients of the PI based on the fuzzy logic controller were adjusted almost instantly during the transients when the load and operating conditions changed. Since, the fuzzy supervisor is designed in such a way that the deviations in the control gains are the outputs of the fuzzy logic supervisor which are added to the reference control gains during the load changes, a good control performance can be achieved. Verification of the model and control design was implemented through MATLAB/SIMULINK. From the systematic simulation framework MATLAB/SIMULINK, it was found that the conventional D-STATCOM was limited when compensating for voltage drop under sudden load change and did not provide full voltage regulation during the fault conditions, the system tried to compensate the voltage but with a large amount of oscillation because the

conventional D-STATCOMs act only as a reactive power compensator and voltage controller at the point of common coupling by producing or absorbing reactive power, and have limited capability to support voltage stability in modern grids with high penetration of distributed generations and dynamic loads. The D-STATCOM performance can be modified by adding energy storage systems as presented in Chapters Five and Six.

Chapter Five shows that by using intelligent control on the D-STATCOM with battery energy storage integrated into its DC side, there is a marked improvement in its ability to support voltage stability. The active power exchange is made by controlling the phase of the output voltage of the D-STATCOM's converter and by adding the energy storage device to its DC part. The D-STATCOM is configured with a battery storage unit by connecting a bidirectional DC to DC (buck/boost) controller between the battery storage and the DC side of the D-STATCOM's converter. Thus, the short-term voltage stability with the D-STATCOM can be analysed based on energy storage system.

The comprehensive simulation results generally show good voltage recovery after load disturbances due to improved ability to support the grid with both active and reactive power. In particular, to provide the distribution grid a good fault ride through capability.

With the proposed FLC control, the D-STATCOM based BESS is able to absorb or inject both active and reactive power with the grid. Furthermore, a performance comparison of the D-STATCOM based BESS system with the fuzzy-tuned PI and the standard PI controller was carried out. Although the linear PI controller gives a rather acceptable result, the proposed fuzzy controller allows automated tuning that captures the nonlinearities of the grid online, and therefore provides superior performance over varying operating conditions. Thus, the nonlinear fuzzy controller is proposed for the D-STATCOM based BESS application. The active power possibilities of the D-STATCOM with BESS can be used in smart distribution grids to compensate the intermittent power of renewable energy.

Chapter Six presents a review of previous studies, this revealed a lack of quantifiable data to demonstrate the advantages of a hybrid energy storage configuration in D-STATCOM applications with respect to voltage control. The present study has succeeded in demonstrating the advantages of such a HESS strategy with a D-STATCOM device by providing new data which quantify the advantages, showing faster voltage regulation, and reduction of the battery current stresses. A novel energy management approach is suggested using two control strategies under two different conditions: standard control management and sugeno-fuzzy logic control management.

The voltage control and power management approaches are presented in this study realising effective employment of the HESS, based on the concept that the battery provides the average power requirements of the system while the SC supplies the transient power requirements. In the standard control management strategy, the error signal of the DC side of the D-STATCOM is used to produces the total required current from ESS which is divided into an average power value and dynamic power value by a low pass filter. The implementation of the D-STATCOM based HESS was tested in a distribution power grid, simulated in MATLAB/SIMULINK. The simulation data demonstrated that, compared with the D-STATCOM based battery only system, the D-STATCOM based HESS provides better voltage regulation. A further benefit of the proposed D-STATCOM configuration is that the maximum value of the battery current is reduced, and the battery is protected from high rates of charge/discharge. Hence, the battery service life is improved and extended.

As advanced bidirectional power paradigms with *renewable* and distributed resources, the fast-online power control management with HESS is required to work instantaneously and jointly with main utility grid to supply a reliable service. In this context, a D-STATCOM with multisources and non-linear system characteristics and including several working modes is complex. Therefore, a new approach; a sugeno-fuzzy logic controller based decision-making for power management of the HESS was presented. Sugeno-fuzzy control strategy based

energy management is designed by means of premise learning. It has the following important features:

(1) The rules database is described in terms of the form (IF) and (THEN) statements to formulate the conditional statements that comprise fuzzy logic.

(2) The general rule premises allow the selection of important regions of the input domain to be covered in the coding scheme.

The approach focused on developing a coordinated control strategy for a D-STATCOM based HESS (battery and SC), and concluded that:

- For a D-STATCOM with dual sources, the results demonstrated that the proposed fuzzy control management is more robust than a standard controller with low pass filter, and significantly reduces the problems associated with parameter tuning. In addition, the dips and spikes of the PCC voltage and DC-side voltage of the D-STATCOM's converter were reduced very effectively, inspiring new ideas for improving the output characteristics of the HESSs and the system's dynamic response performance.
- The fuzzy logic management approach distributes the power required almost instantaneously between the energy sources and overcame the time delay that arose with the use of a low pass filter, as in the standard method. Here, the SC supplies the required maximum transient current with a lower steady state response as compared to the current response with standard control management, approaching a 50% reduction. Furthermore, the output battery current is more steady than the current obtained using standard control management, which is desirable because it will extend the lifespan of the storage unit. However, the total average battery current is the same as the output battery current using standard control management. Hence, the fuzzy management strategy is a method that utilizes the power and energy characteristics of the battery and SC in a more effective way.
- By considering the State of Charge (SOC) levels of the battery and SC the proposed fuzzy control management protects the storage (both battery

and SC) from overcharging and under-discharging by estimating the power allocation a step ahead.

Chapter seven reports the details of the experimental rig and the results to validate the D-STATCOM configuration based HESS. Two test modes of D-STACOM operation were performed, inverter platform test based on the battery-only system and then the hardware platform test based on the hybrid storage energy system (battery and SC). The experimental platform was modified version from an existing experimental platform with control algorithm implemented on the C-Rio platform with FPGA and LabVIEW software. The proposed converter with energy storage system enhanced D-STATCOM's performance and provided the effective power sharing between the battery and supercapacitor. Thus, it will improve the voltage stability at distribution level during the transient conditions by using D-STATCOM based HESS. Simulation and laboratory results both demonstrate that HESS control strategy effectively improves the dynamic performances of the D-STATCOM device. Furthermore, a prototype rig with a modified hardware together with its control platform can present an effective option for further research in the field of converter with multiple source types

8.2 Suggestion for future work

This work has introduced a two-level, three-phase power converter configuration with multiple sources as an attractive option for D-STATCOM applications, providing a good performance in the distribution of grid voltage with fewer fluctuations and without greatly increased complexity. The work concentrated mainly on voltage regulation applications in distributed power grids, but the D-STATCOM configuration and control method could be easily employed for other applications as stated in Chapter Two. For example, to compensate for the intermittent power delivery of renewable power sources and harmonic minimisation in power distribution systems.

This work was limited mainly to the modified D-STATCOM configuration with HESS based on a two-level converter. However, there are other types of multi-level converters as mentioned in Chapter Four. So, there are many possible applications for multisource structures with multilevel inverters. The control

strategy implemented here could be scaled to be suitable to meet other specific objectives.

One other limitation of the fuzzy logic control management of HESS is determining the maximum number of control rules sets. When the upper limit is too small, no satisfactory solution can be found. But too large an upper limit in such a nonlinear system makes the total possible number of rules too large and complex to control. The fuzzy rules sets used here are limited by considering different SOC levels of the ESSs and examining the controller's analytical processes established on the historical output information obtained from the standard HESS control management. Empirical knowledge and experience play important roles in estimating the number of rules needed to achieve the desired control goal. Future work in this area research could concentrate on developing the fuzzy logic control by adding further input signals and more sets of rules incorporated without a priori information.

Although the main objectives of this study have been achieved, there are further research aspects that are worth addressing:

- An extension of energy control management to enhance the voltage stability of distribution grids with different types of sources, such as wind turbines and PV panels, and to introduce a more effective control strategy in an autonomous microgrid.
- This work has limited itself to voltage control for three-phase, balanced systems with the assumption that both the load and the supply impedance are balanced. Unbalanced load has not been addressed. It should be possible to manage the D-STATCOM to assist in the balancing of three-phase voltages and this should be part of any future work. Such work will need further development in modelling and control loop design to obtain separate d-q components for a positive and negative sequence of the voltage and current.

REFERENCES

[1] M. Vignolo and R. Zeballos, “Transmission networks or distributed generation?,” in *First International Symposium on Distributed Generation, Power System and Market Aspect, Stockholm: Royal Institute of Technology*, 2001, pp. 1–5.

[2] R. Affairs, “The United Kingdom ’ s Initial Report under the Kyoto Protocol,” UK Depertament for Environment, Food and Rural Affairs,London ,UK, 20, 2006.

[3] DECC. (2013), “UK Renewable Energy Roadmap,” Department of Energy and Climate Change, London, UK, 5,[Online].Available: https://www.gov.uk/government/uploads/system/uploads/attachment_data/file/255182/UK_Renewable_Energy_Roadmap_-_5_November_-_FINAL_DOCUMENT_FOR_PUBLICATIO___.pdf, 2013.

[4] F. Blaabjerg, Y. Yang, D. Yang, and X. Wang, “Distributed Power-Generation Systems and Protection,” *Proc. IEEE*, vol. 105, no. 7, pp. 1311–1331, 2017.

[5] IRENA. (2017), “Renewable Energy Statistics 2017 Statistiques D ’ Énergie Renouvelable 2017 Estadísticas De Energía,” International Renewable Energy Agency, [Online]. Available: http://www.irena.org/-/media/Files/IRENA/Agency/Publication/2017/Jul/IRENA_Renewable_Energy_Statistics_2017.pdf,London, UK, 2017.

[6] M. C. Falvo, L. Martirano, and D. Sbordone, “D-STATCOM with Energy Storage System for Application in SmartMicro-Grids,” in *4th International Conference on Clean Electrical Power: Renewable Energy Resources Impact, IEEE,, Alghero, Italy*, 2013, pp. 571–576.

[7] C. Source, E. Serban, E. Serban, S. Member, and H. Serban, “A Control Strategy for a Distributed Power Generation Microgrid Application With Voltage- and Current-Controlled Source Converter,” *IEEE Trans. Power Electron.*, vol. 25, no. 12, pp. 2981–2992, 2010.

[8] IET.(2013), “Electricity Networks: Handling a Shock to the System,” London, UK, [Online]. Avaliable: https://www.theiet.org/factfiles/energy/elec-shock-page.cfm, 2013.

[9] X. Luo, J. Wang, M. Dooner, and J. Clarke, “Overview of current development in electrical energy storage technologies and the application potential in power system operation,” *Appl. Energy*, vol. 137, pp. 511–536, 2015.

[10] Y. Qiu, C. Dai, and R. Jin, “Impact of power electronic device development on power grids,” in *2016 28th International Symposium on Power Semiconductor Devices and ICs (ISPSD), Prague, Czech Republic*, 2016, pp. 9–14.

[11] J. Zhang, “Power electronics in future electrical power grids,” in *2013 4th IEEE International Symposium on Power Electronics for Distributed Generation Systems (PEDG),Rogers, USA, July*, 2013, pp. 1–3.

[12] C. Greacen, R. Engel, and T. Quetchenbach (2013), “A Guidebook on Grid Interconnection and Islanded Operation of Mini-Grid Power Systems Up to 200 kW,” *[Online]. Avalible: http://cem-backup.carrespace.fr/cem-ok/www.cleanenergyministerial.org/Portals/2/pdfs/A_Guidebook_for_Mini grids-SERC_LBNL_March_2013.pdf*. .

[13] N. K. Roy, H. R. Pota, and M. J. Hossain, “Reactive power management of distribution networks with wind generation for improving voltage stability,” *Renew. Energy*, vol. 58, pp. 85–94, 2013.

[14] P. S. Subrahmanyam and S. Srikanth, “Power Quality Improvement in a pv Distribution System by Using D-STATCOM,” *Int. J. Eng. Sci. Technol.*, vol. 5, no. 12, pp. 6068–6073, 2013.

[15] M. Saradarzadeh, S. Farhangi, J. L. Schanen, P.-O. Jeannin, and D. Frey, “The benefits of looping a radial distribution system with a power flow controller,” in *2010 IEEE International Conference on Power and Energy,Kuala Lumpur, Malaysia*, 2010, pp. 723–728.

[16] M. H. J. Bollen, “What is power quality?,” *Electr. Power Syst. Res.*, vol. 66, no. 1, pp. 5–14, 2003.

[17] J. Seymour, “The seven types of power problems,” white paper 18, Revision1, Schneider Electric—Data Center, Science Center, 2011. [Online]. Available: https://www.schneider-electric.us/en/download/document/APC_VAVR-5WKLPK_EN/, 2011.

[18] V. C. Güngör *et al.*, “Smart grid technologies: Communication technologies and standards,” *IEEE Trans. Ind. Informatics*, vol. 7, no. 4, pp. 529–539, 2011.

[19] D. Francis and T. Thomas, “Mitigation of voltage sag and swell using dynamic voltage restorer,” in *International Conference on Magnetics, Machines and Drives (AICERA-2014 iCMMD), Kottayam, India*, 2014, pp. 1–6.

[20] A. Ghosh and G. Ledwich, *Power Quality Enhancement Using Custom Power Devices*. Boston: Kluwer Academic, 2002.

[21] P. M. Balasubramaniam and S. U. Prabha, “Power quality issues, solutions and standards: A technology review,” *J. Appl. Sci. Eng.*, vol. 18, no. 4, pp. 371–380, 2015.

[22] L. Zhang and M. H. J. Bollen, “Characteristic of voltage dips (sags) in power systems,” *IEEE Trans. Power Deliv.*, vol. 15, no. 2, pp. 827–832, 2000.

[23] T. Devaraju, “Role of custom power devices in Power Quality Enhancement : A Review,” *Int. J. Eng. Sci. Technol.*, vol. 2, no. 8, pp. 3628–3634, 2010.

[24] K. R. Padiyar, *Facts Controllers in Power Transmission and Distribution*. New Delhi, India: New Age Int., 2007.

[25] P. Bauer and S. W. H. De Haan, “Electronic tap changer for 500 kVA/10 kV distribution transformers:\ndesign, experimental results and impact in distribution networks,” in *Conference Record of 1998 IEEE Industry*

Applications Conference. Thirty-Third IAS Annual Meeting (Cat. No.98CH36242), Louis, MO, USA, 1998, vol. 2, pp. 1530–1537.

[26] F. Q. Yousef-Zai and D. O'Kelly, "Solid-state on-load transformer tap changer," *IEE Proc. , Electr. Power Appl.*, vol. 143, no. 6, pp. 481–491, 1996.

[27] M. Y. Cho and Y. W. Chen, "Fixed/switched type shunt capacitor planning of distribution systems by considering customer load patterns and simplified feeder model," *IEE Proc. - Gener. Transm. Distrib.*, vol. 144, no. 6, p. 533, 1997.

[28] L. A. Gallego and A. Padilha-Feltrin, "Voltage regulator modeling for the three-phase power flow in distribution networks," in *2008 IEEE/PES Transmission and Distribution Conference and Exposition: Latin America, Bogota, Colombia*, 2008, pp. 1–6.

[29] S. A. Dolli and S. H. Jangamshetti, "Modeling and optimal placement of voltage regulator for a radial system," in *2012 International Conference on Power, Signals, Controls and Computation, Kerala, India*, 2012, pp. 1–6.

[30] J. a P. Lopes, N. Hatziargyriou, J. Mutale, P. Djapic, and N. Jenkins, "Integrating distributed generation into electric power systems: A review of drivers, challenges and opportunities," *Electr. Power Syst. Res.*, vol. 77, no. 2007, pp. 1189–1203, 2007.

[31] J. H. Choi and J. C. Kim, "Advanced voltage regulation method of power distribution systems interconnected with dispersed storage and generation systems (revised)," *IEEE Trans. Power Deliv.*, vol. 16, no. 2, pp. 329–334, 2001.

[32] M. Pikulski and H. Nielsen, "Controlled Sources of Reactive Power Used for Improving Voltage Stability," Electrical Power Systems and High Voltage Engineering, Aalborg University , Aalborg,Sci Rep. EPSH10-1012, 2008.

[33] A. Mahendra, "Novel Control of PV Solar and Wind Farm Inverters as

STATCOM for Increasing Connectivity of Distributed Generators," M.Sc. thesis, Department of Electrical and Computer Engineering, The University of Western Ontario, London, Ontario, Canada, 2013.

[34] M. a. Mahmud, M. J. Hossain, H. R. Pota, and a. B. M. Nasiruzzaman, "Voltage control of distribution networks with distributed generation using reactive power compensation," in *in Proc. 37th Annual Conf. IEEE Industrial Electronics Society, Melbourne, Australia*, 2011, pp. 985–990.

[35] R. M. Mathur and R. K. Varma, *Thyristor-Based FACTS Controllers for Electrical Transmission Systems*. USA: A JOHN WILEY & SONS, INC., 2002.

[36] J. M. Carrasco *et al.*, "Power-Electronic Systems for the Grid Integration of Renewable Energy Sources : A Survey," *IEEE Trans. Ind. Electron.*, vol. 53, no. 4, pp. 1002–1016, 2006.

[37] F. Blaabjerg, F. Iov, T. Terekes, R. Teodorescu, and K. Ma, "Power Electronics - Key Technology for Renewable Energy Systems," in *2011 2nd Power Electronics, Drive Systems ans Technologies Conference, Tehran, Iran*, 2011, pp. 445–466.

[38] M. Noroozian, N. a. Petersson, B. Thorvaldson, A. B. Nilsson, and C. W. Taylor, "Benefits of SVC and STATCOM for electric utility application," in *2003 IEEE PES Transmission and Distribution, Dallas, TX, USA*, 2003, vol. 3, pp. 1–8.

[39] E. E. C. Moraes, S. J. De Mesquita, R. P. S. Leão, M. B. M. Neto, K. Q. Silva, and R. M. C. Correa, "The Application of D-STATCOM in Smart Distribution Grid with Wind Power Plants," in *International Conference on Industry Applications (INDUSCON), 10th IEEE/IAS , Fortaleza, Brazil)*, 2012, pp. 1–6.

[40] S. Mohammadi, "Impacts of D-STATCOM on Voltage Stability," *African J. Comput. ICT*, vol. 6, no. 2, pp. 121–128, 2013.

[41] M. G. Molina, "Distributed energy storage systems for applications in future

smart grids," in *Sixth IEEE/PES Transmission and Distribution: Latin America Conference and Exposition (T&D-LA), Montevideo, Uruguay*, 2012, pp. 1–7.

[42] B. Singh, A. Adya, A. P. Mittal, J. R. P. Gupta, and B. N. Singh, "Application of DSTATCOM for mitigation of voltage sag for motor loads in isolated distribution systems," in *IEEE International Symposium on Industrial Electronics, Montreal, Canada*, 2006, vol. 3, pp. 1806–1811.

[43] G. Shahgholian and Z. Azimi, "Analysis and design of a DSTATCOM based on sliding mode control strategy for improvement of voltage sag in distribution systems," *Electron.*, vol. 5, no. 3, 2016.

[44] K. L. Anaya and M. G. Pollitt, "Integrating distributed generation: Regulation and trends in three leading countries," *Energy Policy, Publ. by Elsevier*, vol. 85, pp. 475–486, 2015.

[45] M. Moghaddam, "On the Performance of Distributed and Cloud-Based Demand Response in Smart Grid," *IEEE Trans. Smart Grid*, vol. pp, no. 99, 2017.

[46] Q. Sun, J. Wu, Y. Zhang, N. Jenkins, and J. Ekanayake, "Comparison of the development of Smart Grids in China and the United Kingdom," in *Innovative Smart Grid Technologies Conference Europe (ISGT Europe), Gothenberg, Sweden*, 2010, pp. 1–6.

[47] A. T. Agbedahunsi, "Frequency Control for Microgrids using Enhanced Storage," Ph.D. Thesis, Department of Electrical and Electronic Engineering, The university of Nottingham, Nottingham, UK, 2013.

[48] S. Fankhauser and F. Jotzo, "Economic growth and development with low-carbon energy," *Grantham Research Institute on Climate Change and the Environment*, 2017. [Online]. Available: http://doi.wiley.com/10.1002/wcc.495.

[49] V. S. Bhadoria, N. Singh, and V. Shrivastava, "A Review on Distributed Generation Definitions and DG Impacts on Distribution System," in

International Conference on Advanced Computing and Communication Technologies (ICACCT™), 2013.

[50] F. Gonzalez-Longatt and C. Fortoul, “Review of Distributed Generation Concept: Attempt of Unification,” in *International Conference on Renewable Energies and Power Quality (ICREPQ´05), España*, 2005, vol. 1, no. 3, pp. 1–4.

[51] J. Mitra and S. Suryanarayanan, “System analytics for smart microgrids,” in *Power and Energy Society General Meeting, 2010 IEEE, Providence, USA*, 2010, pp. 1–4.

[52] C. Huang, D. Yue, S. Deng, and J. Xie, “Optimal scheduling of microgrid with multiple distributed resources using interval optimization,” *Energies*, vol. 10, no. 3, pp. 1–23, 2017.

[53] W. Kramer, S. Chakraborty, B. Kroposki, and H. Thomas, “Advanced Power Electronic Interfaces for Distributed Energy Systems Part 1 : Systems and Topologies,” Department of Energy Office of Energy Efficiency and Renewable Energy, National Renewable Energy Laboratory, Golden, Colorado, NREL/TP-581-42672, 2008.

[54] P. F. Ribeiro, B. K. Johnson, P. F. Ribeiro, S. Member, and B. K. Johnson, “Energy storage systems for advanced power applications,” *Proc. IEEE*, vol. 89, no. 12, pp. 1744–1756, 2001.

[55] E. Cavanagh, K. Ward, J. K. Behrens, S. Bhatt, A. I. Ratnam, E. L. Oliver and J. Hayward, “Electrical Energy Storage : Technology Overview and Applications,” CSIRO, Australia. EP154168, 2015.

[56] M. G. Molina (2010), “Dynamic Modelling and Control Design of Advanced Energy Storage for Power System Applications,” Dynamic Modelling, Alisson V. Brito (Ed.), ISBN: 978-953-7619-68-8, InTech,[Online]. Available : http://www.intechopen.com/books/dynamic-modelling/dynamic-modelling-and-control-design- of-advanced-energy-storage-for-power-system-applications.

[57] H. Chen, T. N. Cong, W. Yang, C. Tan, Y. Li, and Y. Ding, “Progress in electrical energy storage system: A critical review,” *Prog. Nat. Sci.*, vol. 19, no. 3, pp. 291–312, 2009.

[58] H. Douglas and P. Pillay, “Sizing ultracapacitors for hybrid electric vehicles,” in *31st Annual Conference of IEEE Industrial Electronics Society*, 2005, pp. 1599–1604.

[59] F. Blaabjerg, Y. Yongheng, and M. Ke, “Power electronics - Key technology for renewable energy systems - Status and future,” in *Electric Power and Energy Conversion Systems (EPECS), 2013 3rd International Conference on, Istanbul, Turkey*, 2013, pp. 1–6.

[60] J. M. Maza-Ortega, E. Acha, S. García, and A. Gómez-Expósito, “Overview of power electronics technology and applications in power generation transmission and distribution,” *J. Mod. Power Syst. Clean Energy*, vol. 5, no. 4, pp. 499–514, 2017.

[61] Z. Chen, J. M. Guerrero, F. Blaabjerg, and S. Member, “A Review of the State of the Art of Power Electronics for Wind Turbines,” *IEEE Trans. Power Electron.*, vol. 24, no. 8, pp. 1859–1875, 2009.

[62] G. L. M. Tolbert, T. J. King, B. Ozpineci, J. B. Campbell and D. T. R. Muralidharan et al., “Power Electronics for Distributed Energy Systems and Transmission and Distribution Applications,” Eng. Sci. Technol. Div., Oak Ridge Nat. Lab., Oak Ridge, ORNL/TM-2005/230, 2005.

[63] R. P. Singh, S. K. Bharadwaj, and R. K. Singh, “Flexible AC Transmission System Controllers : A State of Art,” *Int. J. Electron. Electr. Eng.*, vol. 7, no. 8, pp. 843–850, 2014.

[64] L. G. Narain G. Hingori, *Understanding FACTS Concepts and Technology of Flexible AC Transmission Systems*. M. El-Hawary, New York: IEEE press, 2000.

[65] N. G. Hingorani, “FACTS-flexible AC transmission system,” in *International Conference on AC and DC Power Transmission, London, UK*, 1991, pp. 1–

7.

[66] A. A. Edris *et al.*, “Proposed terms and definitions for Flexible AC Transmission System (FACTS),” *IEEE Trans. Power Deliv.*, vol. 12, no. 4, pp. 1848–1853, 1997.

[67] E. Mahdiyeh, S. Hussain, M. Azah, and K. Mohammad, “A Survey on Flexible AC Transmission Systems (FACTS),” *Prz. Elektrotechniczny (Electr. Rev.)*, vol. 88, no. 1, pp. 1–11, 2012.

[68] V. Kakkar and N. K. Agarwal, “Recent trends on FACTS and D-FACTS,” in *In modern electric power systems (MEPS), proceedings of the international symposium IEEE, Wroclaw, Poland*, 2010, pp. 1–8.

[69] V. Hamidi, K. S. Smith, and R. C. Wilson, “Smart Grid technology review within the Transmission and Distribution sector,” in *Innovative Smart Grid Technologies Conference Europe (ISGT Europe), 2010 IEEE PES, Gothenberg, Sweden*, 2010, pp. 1–8.

[70] M. Vaziri, M. Afzal, M. Zarghami, A. Yazdani, S. Vadhva, and F. Tavatli, “Voltage impacts of DG on Distribution Grid with Voltage Regulators and SVCs,” in *IEEE Green Technologies Conference, Denver, CO, USA*, 2013, pp. 322–329.

[71] M. Karimi and P. Farhadi, “Selecting the Best Compatible SVC Type in Power Systems for transient Stability,” *Int. J. Green Energy*, vol. 12, no. 1, pp. 87–92, 2015.

[72] M. Karimi, P. Farhadi, M. B. Ahmadi, T. Sojoudi, and D. Mostafa, “Statistical Analysis of Shunt-FACTS Devices Impact on Power Flow Control,” *Res. J. Appl. Sci. Eng. Technol.*, vol. 4, no. 6, pp. 675–685, 2012.

[73] T. TSUNEDOMI, Kunihiko TAMURA, Shigeru OMORI, “Effectiveness of D-SVC on Rural Networks,” in *22nd International Conference and Exhibition on Electricity Distribution (CIRED 2013), Stockholm, Sweden*, 2013, pp. 10–13.

[74] K. Kahle, F. R. Blanquez, and C. M. Genton, “The Design and Performance of Static Var Compensators for Particle Accelerators,” in *17th European Conference on Power Electronics and Applications (EPE’15 ECCE-Europe), Geneva, Switzerland*, 2015, pp. 7–10.

[75] M. V. W. Chandrakar, V K, “Static Synchronous Compensator (STATCOM) for the improvement of the Electrical System performance with Non Linear load,” *Int. J. Power Syst.*, vol. 1, pp. 27–32, 2016.

[76] B. Singh, P. Jayaprakash, D. P. Kothari, A. Chandra, and K. Al Haddad, “Comprehensive Study of DSTATCOM Configurations,” *IEEE Trans. Ind. INFORMATICS*, vol. 10, no. 2, pp. 854–870, 2014.

[77] S. H. Hosseini, A. Nazarloo, and E. Babaei, “Application of D-STATCOM to improve distribution system performance with balanced and unbalanced fault conditions,” in *IEEE Electrical Power and Energy Conference (EPEC), Halifax, NS, Canada*, 2010, pp. 1–6.

[78] K. Al-Haddad, R. Saha, A. Chandra, and B. Singh, “Static synchronous compensators (STATCOM): a review,” *IET Power Electron.*, vol. 2, no. 4, pp. 297–324, 2009.

[79] P. Srithorn, “Control of a Statcom With Supercap Acitor Energy,” Ph.D thesis, Department of Electrical and Electronic Engineering, University of Nottingham, Nottingham, UK, 2009.

[80] A. F. Obando-montaño, C. Carrillo, J. Cidrás, and E. Díaz-dorado, “A STATCOM with Supercapacitors for Low-Voltage Ride-Through in Fixed-Speed Wind Turbines,” *Energies*, vol. 7, pp. 5922–5952, 2014.

[81] A. Chakraborty, S. K. Musunuri, A. K. Srivastava, and A. K. Kondabathini, “Integrating STATCOM and battery energy storage system for power system transient stability: A review and application,” *Adv. Power Electron.*, vol. 2012, pp. 1–12, 2012.

[82] N. Goel, R. Patel, and S. Chacko, “Genetically Tuned STATCOM for Voltage Control and Reactive Power Compensation,” *Int. J. Comput.*

Theory Eng., vol. 2, no. 3, pp. 345–351, 2010.

[83] R. J. Lee, P. Pillay, R. G. Harley, and K. G. V Avenue, “D, Q Reference Frames for the Simulation of Induction Motors,” *Electr. Power Syst. Res.*, vol. 8, no. 1, pp. 15–26, 1984.

[84] W.-N. Chang and K.-D. Yeh, “Design of D-STATCOM for fast load compensation of unbalanced distribution systems,” in *4th IEEE International Conference on Power Electronics and Drive Systems. Denpasar, Indonesia*, 2001, vol. 2, pp. 801–806.

[85] A. Shukla, A. Ghosh, and A. Joshi, “A Hysteresis Current Controlled Flying Capacitor Multilevel Inverter based DSTATCOM,” in *IEEE Power Engineering Society General Meeting, San Francisco, USA*, 2005, vol. 1, pp. 857–864.

[86] M. H.Rashid, *POWER ELECTRONICS HANDBOOK*, 3rd ed. USA: Elsevier Inc., 2011.

[87] A. Banerji, S. K. Biswas, and B. Singh, “DSTATCOM control algorithms: A review,” *Int. J. Power Electron. Drive Syst.*, vol. 2, no. 3, pp. 285–296, 2012.

[88] S. P. Gawande and S. kha. & M.R.Ramteke, “Design Consideration for Configuration , Topology & Control Schemes of DSTATCOM Implemented on Distribution Systems,” *Lect. Notes Inf. Theory*, vol. 1, no. 3, pp. 89–94, 2013.

[89] D. Srinivas, M. Z. Lazarus, and K. P. Satsangi, “Comparative Study of Different Control Strategies for Dstatcom,” *Int. J. Adv. Res. Electr. Electron. Instrum. Eng.*, vol. 1, no. 5, pp. 362–368, 2012.

[90] R. S. Herrera, P. Salmerón, H. Kim, P. Salmeron, and H. Kim, “Instantaneous reactive power theory applied to active power filter compensation: Different approaches, assessment, and experimental results,” *IEEE Trans. Ind. Electron.*, vol. 55, no. 1, pp. 184–196, 2008.

[91] B. Singh and J. Solanki, “A Comparison of Control Algorithms for

DSTATCOM," *IEEE Trans. Ind. Electron.*, vol. 56, no. 7, pp. 2738–2745, 2009.

[92] J. L. Willems, "A new interpretation of the Akagi-Nabae power components for nonsinusoidal three-phase situations," *IEEE Trans. Instrum. Meas.*, vol. 41, no. 4, pp. 523–527, 1992.

[93] A. Kumar, V. K. Dwivedi, S. Maity, and M. Bajaj, "Performance Comparison of Control Algorithms for Load Compensation Using D-STATCOM under Abnormal Source Voltage," *J. Autom. Control Eng.*, vol. 2, no. 1, pp. 54–58, 2014.

[94] T. Zaveri, B. Bhavesh, and N. Zaveri, "Control Techniques for Power Quality Improvement in Delta Connected Load using DSTATCOM," in *IEEE International Electric Machines & Drives Conference*, 2011, pp. 1397–1402.

[95] K. J. Lee, J. P. Lee, D. Shin, D. W. Yoo, and H. J. Kim, "A novel grid synchronization PLL method based on adaptive low-pass notch filter for grid-connected PCS," *IEEE Trans. Ind. Electron.*, vol. 61, no. 1, pp. 292–301, 2014.

[96] B. B. Bukata and Y. Li, "Reviewing DSTATCOM for smart distribution grid applications in solving power quality problems," in *Proceedings of 17th International Conference on Automation and Computing, Huddersfield, UK*, 2011, pp. 294–299.

[97] A. Timbus and R. Teodorescu, "Linear and nonlinear control of distributed power generation systems," in *Conference Record of the 2006 IEEE Industry Applications Conference Forty-First IAS Annual Meeting, Tampa, FL, USA*, 2006, pp. 1015–1023.

[98] D. Rajasekaran, S. S. Dash, A. B. Mayilvaganan, C. Subramani, and S. Krishnan, "Artificial Neural Network Controller Based Distribution Static Compensator for Voltage Sag Mitigation," *Am. J. Appl. Sci.*, vol. 10, no. 7, pp. 688–695, 2013.

[99] N. M. G. Kumar, P. S. Raju, and P. Venkatesh, “Control of DC Capacitor Voltage In a D StATCOM Using Fuzzy Logic Controller,” *Int. J. Adv. Eng. Technol.*, vol. 4, no. 1, pp. 679–690, 2012.

[100] G. Zhu, D. Yang, and Q. Zhu, “Fuzzy PI Control Based on the Instantaneous Power Balance for the DSTATCOM,” in *Advances in Computer Science, Intelligent System and Environment. Advances in Intelligent and Soft Computing*, D. Jin and S. Lin, Eds. Berlin, Heidelberg: Springer, 2011, pp. 487–491.

[101] N. A. Rahim and J. Selvaraj, “Implementation of Hysteresis Current Control for Single- Phase Grid Connected Inverter,” in *7th International Conference on Power Electronics and Drive Systems, Bangkok, Thailand*, 2007, pp. 1097–1101.

[102] A. Rohani and M. Joorabian, “Modeling and Control of DSTATCOM using adaptive hysteresis band current controller in Three - Phase Four -Wire Distribution systems,” in *IEEE International Conference on Power Electronics, Drives and Energy Systems (PEDES), Tehran, Iran*, 2014, pp. 291–297.

[103] Y. Xiao-ping, Z. Yan-ru, and W. Yan, “A Novel Control Method for DSTATCOM Using Artificial Neural Network,” in *2006 CES/IEEE 5th International Power Electronics and Motion Control Conference, Shanghai, China*, 2006, pp. 1–4.

[104] Y. Lei, Z. Jianhua, and J. Cheng, “D-STATCOM Control Based on Self-Tuning PI with Neural Networks,” in *China International Conference on Electricity Distribution (CICED), Shanghai, China*, 2012, pp. 1–4.

[105] P. Mitra and G. K. Venayagamoorthy, “A DSTATCOM controller tuned by Particle Swarm Optimization for an electric ship power system,” in *IEEE Power and Energy Society General Meeting - Conversion and Delivery of Electrical Energy in the 21st Century, Pittsburgh, USA*, 2008, pp. 1–6.

[106] H. Wang, X. Meng, L. Zhao, and T. Zhao, “Controlling Study of D-

STATCOM Based on Hybrid Genetic Optimization PID Algorithm," in *24th Chinese Control and Decision Conference (CCDC), Taiyuan, China*, 2012, pp. 2762–2766.

[107] N. Farokhnia, R. Khoraminia, and G. B. Gharehpetian, "Optimization of PI Controller Gains in Nonlinear Controller of STATCOM Using PSO and GA," *Int. Conf. Renew. Energies Power Qual. (ICREPQ), Granada , Spain*, pp. 1–6, 2010.

[108] H. Chen, J. Li, and X. Zhou, "PSO-based self-tuning PI control for STATCOM," in *IEEE 7th International Power Electronics and Motion Control Conference - ECCE Asia, IPEMC, Harbin, China*, 2012, pp. 2710–2715.

[109] A. Ounissa, A. Djamal, and L. A. Narimen, "Voltage Regulation of Wind Farm Connected to Distribution Network Using Fuzzy Supervisory Control," *Int. J. Sci. Eng. Res.*, vol. 4, no. 11, pp. 1410–1416, 2013.

[110] G.W.Moon, "Predictive Current Control of Distribution Static Compensator for Reactive Power Compensation," *IEE Proc. - Gener. Transm. Distrib.*, vol. 146, no. 5, pp. 515–520, 1999.

[111] E. Monmasson, L. Idkhajine, C. Marcian N, I. Bahri, A. Tisan, and M. Naouar, "FPGAs in Industrial Control Applications," *IEEE Trans. Ind. INFORMATICS*, vol. 7, no. 2, pp. 224–243, 2011.

[112] N. Mariun, S. Member, H. Masdi, S. M. Bashi, A. Mohamed, and S. Yusuf, "Design of a Prototype D-Statcom using DSP Controller for Voltage Sag Mitigation," in *International Conference on Power Electronics and Drives Systems, Kuala Lumpur, Malaysia*, 2006, pp. 6–11.

[113] M. K. Mishra, K. Karthikeyan, P. K. Linash, and S. Member, "A Development and Implementation of DSP Based DSTATCOM to Compensate Unbalanced Non- linear Loads," in *IIEEE Power India Conference, New Delhi, India*, 2006, pp. 319–322.

[114] K. Murugesan, R. Muthu, S. Vijayenthiran, and M. Jb, "Prototype Hardware

Realization of The DSTATCOM for Reactive Power Compensation," *Int. J. Electr. Power Energy Syst.*, vol. 65, pp. 169–178, 2015.

[115] V. Dinavahi, R. Iravani, and R. Bonert, "Design of a Real-Time Digital Simulator for a D-STATCOM System," *IEEE Trans. Ind. Electron.*, vol. 51, no. 5, pp. 1001–1008, 2004.

[116] C. A. Sepúlveda, J. A. Muñoz, J. R. Espinoza, M. E. Figueroa, and P. E. Melín, "All-on-Chip dq -Frame Based D-STATCOM Control Implementation in a Low-Cost FPGA," *IEEE Trans. Ind. Electron.*, vol. 60, no. 2, pp. 659–669, 2013.

[117] N. K. Roy, M. J. Hossain, S. Member, and H. R. Pota, "Voltage Profile Improvement for Distributed Wind Generation using D-STATCOM," in *IEEE Power and Energy Society General Meeting, Detroit, USA*, 2011, pp. 1–6.

[118] C. K. Vasoya, K. Khatua, and N. Yadav, "Analysis of D-STATCOM Control in Low Voltage Distribution System with Wind Power Generation," in *International Journal of Engineering Development and Research*, 2014, pp. 1–10.

[119] R. S. Bajpai and R. Gupta, "Voltage and Power Flow Control of Grid Connected Wind Generation System Using DSTATCOM," in *IEEE Power and Energy Society General Meeting - Conversion and Delivery of Electrical Energy in the 21st Century, Pittsburgh, PA, USA*, 2008, pp. 1–6.

[120] S. Devi and M. Geethanjali, "Optimal location and Sizing Determination of Distributed Generation and DSTATCOM using Particle Swarm Optimization Algorithm," *Int. J. Electr. Power Energy Syst.*, vol. 62, pp. 562–570, 2014.

[121] C. Kumar, M. V. M. Kumar, and M. K. Mishra, "A control scheme to enhance DSTATCOM operation in power distribution system," in *IEEE 6th International Symposium on Power Electronics for Distributed Generation Systems, PEDG, Aachen*, 2015, pp. 1–6.

[122] K. Anuradha, B. P. Muni, and A. D. Rajkumar, "Cascaded Multilevel

Converter Based DSTATCOM Using p-q Theory with DC Link Voltage Balancing," in *International Conference on Power and Energy Systems, Chennai, India*, 2011, pp. 1–6.

[123] J. G. P. Reddy and K. R. Reddy, "Design and Simulation of Cascaded H-Bridge Multilevel Inverter Based DSTATCOM for Compensation of Reactive Power and Harmonics," in *1st International Conference on Recent Advances in Information Technology (RAIT), Dhanbad, India*, 2012, pp. 737–743.

[124] M. Goyal, B. John, and A. Ghosh, "Harmonic Mitigation in an Islanded Microgrid using a DSTATCOM," in *IEEE PES Asia-Pacific Power and Energy Engineering Conference (APPEEC)*, 2016, pp. 1–5.

[125] S. R. Arya, B. Singh, A. Chandra, and K. Al-Haddad, "Power Factor Correction and Zero Voltage Regulation in Distribution System Using DSTATCOM," in *IEEE International Conference on Power Electronics, Drives and Energy Systems, Bengaluru, India Power*, 2012, pp. 1–6.

[126] S. R. Arya and B. Singh, "CTF Control Algorithm of DSTATCOM for Power Factor Correction and Zero Voltage Regulation," in *IEEE Third International Conference on Sustainable Energy Technologies (ICSET), Kathmandu, Nepal*, 2012, pp. 157–162.

[127] E. E. C. Moraes, S. J. de Mesquita, R. P. S. Leao, M. B. M. Neto, K. Q. da Silva, and R. M. C. Correa, "The application of D-STATCOM in smart distribution grid with wind power plants," in *International Conference on Industry Applications (INDUSCON), 10th IEEE/IAS , Fortaleza, Brazil*, 2012, pp. 1–6.

[128] M. F. Farias, M. G. Cendoya, and P. E. Battaiotto, "Wind Farms in Weak Grids Enhancement of Ride-Through Capability Using Custom Power Systems," in *IEEE/PES Transmission and Distribution Conference and Exposition: Latin America, Bogota, Colombia*, 2008, pp. 1–5.

[129] C. H. Appalanarayana, D. V. N. Ananth, K. D. S. Prasad, C. H. Saibabu, S.

Saikiran, and T. Papinaidu, “Application of STATCOM for Transient Stability Improvement and Performance Enhancement for a Wind Turbine Based Induction Generator,” *Int. J. Soft Comput. Eng.*, vol. 2, no. 6, pp. 158–163, 2013.

[130] G. R. F. Q. Mafra, W. Uturbey, and B. J. Cardoso Filho, “Analysis of the Operation of a D-STATCOM in Unbalanced Distribution Systems Under Voltage Disturbances,” in *IEEE/PES Transmission and Distribution Conference and Exposition: Latin America, Sao Paulo, Brazil*, 2011, pp. 629–634.

[131] N. Mariun, S. Aizam, H. Hizam, and N. Abd Wahab, “Design of Pole Placement Controller in D- STATCOM for Unbalanced Faults Mitigation,” in *International Power Engineering Conference, Singapore, Singapore*, 2005, pp. 504–509.

[132] M. C. Falvo, L. Martirano, and D. Sbordone, “D-STATCOM with Energy Storage System for Application in SmartMicro-Grids,” in *4th International Conference on Clean Electrical Power: Renewable Energy Resources Impact, IEEE,, Alghero, Italy*, 2013, pp. 571–576.

[133] P. F. Ribeiro, B. K. Johnson, M. L. Crow, A. Arsoy, and Y. Liu, “Energy Storage Systems for Advanced Power Applications,” *Proc. IEEE*, vol. 89, no. 12, pp. 1744–1756, 2001.

[134] A. Nazarloo, S. H. Hosseini, and E. Babaei, “Flexible D-STATCOM Performance as a Flexible Distributed Generation in Mitigating Faults,” in *2nd Power Electronics, Drive Systems and Technologies Conference, PEDSTC , Tehran, Iran*, 2011, pp. 568–573.

[135] M. Molina and P. E. Mercado, “Dynamic Modeling and Control Design of DSTATCOM with Ultra-Capacitor Energy Storage for Power Quality Improvements,” in *IEEE/PES Transmission and Distribution Conference and Exposition: Latin America, Bogota, Colombia*, 2008, pp. 1–8.

[136] M. Yibre and M. A. Abido, “Supercapacitors for Wind power Application,” in

International Conference on Renewable Energy Research and Application, Madrid, Spain, 2013, pp. 418–422.

[137] M. K. Döşoğlu, A. Basa Arsoy, and U. Güvenç, “Application of STATCOM-Supercapacitor for Low-Voltage Rride-Through Capability in DFIG-Based Wind Farm,” *Neural Comput. Appl.*, vol. 28, no. 9, pp. 2665–2674, 2017.

[138] E. B. Seyed Hossein Hosseini, Amin Nazarloo, “Super-Capacitor Based D-STATCOM Applied in 13-Bus Industrial Distribution System,” in *The 8th Electrical Engineering/ Electronics, Computer, Telecommunications and Information Technology (ECTI) Association of Thailand - Conference, Khon Kaen, Thailand*, 2011, pp. 715–718.

[139] P. Srithorn, M. Sumner, L. Yao, and R. Parashar, “Power system stabilisation using STATCOM with supercapacitors,” in *IEEE Industry Applications Society Annual Meeting, Edmonton, Canada*, 2008, pp. 1–8.

[140] M. Mangaraj, A. K. Panda, and T. Penthia, “Supercapacitor Supported DSTATCOM for Harmonic Reduction and Power Factor Correction,” in *IEEE Students’ Conference on Electrical, Electronics and Computer Science, SCEECS, Bhopal, India*, 2016, pp. 1–6.

[141] K. Sahay and B. Dwivedi, “Supercapacitors Energy Storage System for Power Quality Improvement : An Overview,” *J. Electr. Syst.*, vol. 10, pp. 1–8, 2009.

[142] A. Nazarloo, S. H. Hosseini, E. Babaei, M. Bagher, and B. Sharifian, “Integrated D-STATCOM with Supercapacitor Used in IEEE Industrial Distribution System,” *ECTI Trans. Electr. ENG, Electron. Commun.*, vol. 10, no. 1, pp. 130–137, 2012.

[143] M. Zarghami, M. Y. Vaziri, A. Rahimi, and S. Vadhva, “Applications of Battery Storage to Improve Performance of Distribution Systems,” in *IEEE Green Technologies Conference, Denver, CO, USA*, 2013, pp. 345–350.

[144] P. Gupta, Ravi Sharma, N K Tiwari, A. Gupta, N. Nigam, and A. Gupta, “Application of energy storage devices in power systems,” *Int. J. Eng. Sci.*

Technol., vol. 3, no. 1, pp. 289–297, 2011.

[145] a Goikoetxea, M. Rodríguez, H. Bindner, and A. Milo, “Design of control strategies to improve grid integration in fixed speed wind energy systems with battery storage,” in *International Conference on Renewable Energies and Power Quality, ICREPQ 08 Santander*, 2008.

[146] H. T. Le and S. Santoso, “Analysis of Voltage Stability and Optimal Wind Power Penetration Limits for a Non-radial Network with an Energy Storage System,” in *IIEEE Power Engineering Society General Meeting, Tampa, FL, USA*, 2007, pp. 1–8.

[147] suman B. S. Alka, “Load Compensation with DSTATCOM and BESS,” in *Power Electronics (IICPE)*, 2012, pp. 1–6.

[148] V. Virulkar and M. Aware, “Analysis of DSTATCOM with BESS for mitigation of flicker,” in *International Conference on Control, Automation, Communication and Energy Conservation, Perundurai, Tamilnadu, India*, 2009, pp. 1–7.

[149] A. Valderrábano and J. M. Ramirez, “DStatCom regulation by a fuzzy segmented PI controller,” *Electr. Power Syst. Res.*, vol. 80, no. 6, pp. 707–715, 2010.

[150] D. Amoozegar, “DSTATCOM modelling for voltage stability with fuzzy logic PI current controller,” *Int. J. Electr. Power Energy Syst.*, vol. 76, pp. 129–135, 2016.

[151] J. Shi, A. Noshadi, and P. Kalam, Akhtar Shi, “Fuzzy Logic Control of DSTATCOM for Improving Power Quality and Dynamic Performance,” in *Power Engineering Conference (AUPEC)*, 2015, pp. 2–7.

[152] A. M. Zhou, Haihua Bhattacharya, Tanmoy Tran, Duong Siew, Tuck Sing Terence Khambadkone, “Composite Energy Storage System Involving Battery and UltracapacitorWith Dynamic Energy Management in Microgrid Applications,” *IEEE Trans. Power Electron.*, vol. 26, no. 3, pp. 923–930, 2011.

[153] H. Yashuai, X. Yonghai, and L. Yangfan, “Research on Application of STATCOM / HESS in Wind Power Integrated to the Grid,” in *IEEE 2nd International Future Energy Electronics Conference (IFEEC), Taipei, Taiwan*, 2015, pp. 1–6.

[154] S. Singh, “An Extensive Survey on Distribution Static Compensator (DSTATCOM),” *Int. J. Emerg. Technol. Advanved Eng.*, vol. 4, no. 3, pp. 669–673, 2014.

[155] K. Somsai, T. Kulworawanichpong, and N. Voraphonpiput, “Steady-State Performance of D-STATCOM for Load Voltage Regulation,” in *Asia-Pacific Power and Energy Engineering Conference, Shanghai, China*, 2012, pp. 1–4.

[156] H. Saadat, *POWER SYSTEM ANALYSIS*. New Delhi: Tata McGraw - Hill, 1999.

[157] M. H. Haque, “Compensation of Distribution System Voltage Sag by DVR and D-STATCOM,” in *IIEEE Porto Power Tech Proceedings, Porto, Portugal*, 2001, vol. 1, pp. 264–268.

[158] K. Somsai, “Control Design and Application of D-Statcom for Load Voltage Control,” Ph.D. Thesis, Department of Electrical Engineering, Suranaree University of Technology, 2012.

[159] K. Somsai, N. Voraphonpiput, and T. Kulworawanichpong, “Symmetrical Optimum Design of Compensating Current and DC Voltage Controllers for D-STATCOM,” *Int. J. Control Autom.*, vol. 6, no. 2, pp. 65–80, 2013.

[160] B. Singh, S. S. Murthy, and S. Gupta, “Analysis and Design of STATCOM-Based Voltage Regulator for Self-Excited Induction Generators,” *Trans. Energy Convers.*, vol. 19, no. 4, pp. 783–790, 2004.

[161] J. Dixon, L. Moran, J. Rodriguez, and R. Domke, “Reactive Power Compensation Technologies: State-of-the-Art Review,” *Proc. IEEE*, vol. 93, no. 12, pp. 2144–2164, 2005.

[162] R. Yazdani, Amirnaser Iravani, *Voltage-Sourced Converters in Power Systems Modeling, Control and Applications*. Hoboken, New Jersey: John Wiley & Sons, Inc, 2010.

[163] J. Hossain and H. R. Pota, *Robust Control for Grid Voltage Stability: High Penetration of Renewable Energy*. Singapore: Springer, 2014.

[164] G. P. Adam, K. H. Ahmed, N. K. Singh, S. J. Finney, and B. W. Williams, "A Hybrid Multilevel Converter for Medium and High Voltage Applications," in *IEEE PES Trondheim PowerTech , Trondheim, Norway*, 2011.

[165] A. A. Gebreel, "Simulation and Implementation of Two- Level and Three-Level Inverters By Matlab and Rt-Lab," MSc Thesis, Electrical and Computer Science, The Ohio State University, Columbus, USA, 2011.

[166] M. Hagiwara, R. Maeda, and H. Akagi, "Control and Analysis of the Modular Multilevel Cascade Converter Based on Double-Star Chopper-Cells (MMCC-DSCC)," *IEEE Trans. Power Electron.*, vol. 26, no. 6, pp. 1649–1658, 2011.

[167] O. Anaya-Lara, D. Campos-Gaona, E. Moreno-Goytia, and G. Adam, *Offshore wind energy generation, Control, Protection, and Integration to Electrical Systems*. Chichester, UK: JohnWiley & Sons, Ltd Registered, 2014.

[168] N. M. Shah, V. K. Sood, and V. Ramachandran, "Modeling, Control and Simulation of A chain Link STATCOM in EMTP-RV," *Electr. Power Syst. Res.*, vol. 79, no. 3, pp. 474–483, 2009.

[169] C. Schauder and H. Mehta, "Vector Analysis and Control of Advanced Static VAR Compensators," *IEE Proc. Gener. Transm. Distrib.*, vol. 140, no. 4, pp. 299–306, 1993.

[170] S. Phinit, "Conrol of A STATCOM with Supercapacitor Energy Storage .," Ph.D. Thesis, Department of Electrical and Electronic Engineering, The university of Nottingham, Nottingham, UK, 2009.

[171] K. M. Passino and S. Yurkovich, *Fuzzy Control*. Menlo Park, California: Addison Wesley Longman, Inc, 1998.

[172] M. G. Simoes, “Introduction to Fuzzy Control,” Engineering Division, Colorado School of Mines, USA, 80401-1887, 2003.

[173] G. A. Tsengenes and G. A. Adamidis (2012, sep27th), “Performance Evaluation of PI and Fuzzy Controlled Power Electronic Inverters for Power Quality Improvement,” [Online]. Available: Https://www.intechopen.com/books/fuzzy-controllers-recent-advances-in-theory-and-applications/performance-evaluation-of-pi-and-fuzzy-controlled-power-electronic-inverters-for-power-quality-improv, Ed. .

[174] C. C. Lee, “Fuzzy Logic in Control Systems: Fuzzy Logic Controller-Part I,” *IEEE Trans. Syst. Man, Cybern.*, vol. 20, no. 2, pp. 404–417, 1990.

[175] H. Suryanarayana and M. K. Mishra, “Fuzzy Logic based Supervision of DC link PI Control in a DSTATCOM,” in *Annual IEEE India Conference, Kanpur, India*, 2008, pp. 1–6.

[176] A. Saepullah and S. W. Romi, “Comparative Analysis of Mamdani , Sugeno And Tsukamoto Method of Fuzzy Inference System for Air Conditioner Energy Saving,” *J. Intell. Syst.*, vol. 1, no. 2, pp. 143–147, 2015.

[177] T. Takagi and M. Sugeno, “Fuzzy Identification of Systems and Its Applications to Modeling and Control,” *IEEE Trans. Syst. Man. Cybern.*, vol. 15, no. 1, pp. 116–132, 1985.

[178] F. Iov, A. D. Hansen, P. Sørensen, and N. A. Cutululis, “Mapping of grid faults and grid codes,” Risø National Laboratory, Technical University of Denmark, Roskilde, Denmark, Risoe-R; No. 1617(EN), 2007.

[179] and S. C. Alejandro D. Dominguezz-Garc ıa, Christoforos N. Hadjicostis, Philip T. Krein, “Small Inverter-Interfaced Distributed Energy Resources for Reactive Power Support,” in *Twenty-Sixth Annual IEEE Applied Power Electronics Conference and Exposition (APEC), Fort Worth, TX, USA*, 2011, pp. 1616–1621.

[180] X. Wang, J. M. Guerrero, F. Blaabjerg, and Z. Chen, “A Review of Power Electronics Based Microgrids,” *Int. J. Power Electron.*, vol. 12, no. 1, pp. 181–192, 2012.

[181] J. Hossain, A. Mahmud, F. Milano, S. Bacha, and A. Hably, “Design of Robust Distributed Control for Interconnected Microgrids,” *IEEE Trans. Smart Grid*, vol. 7, no. 6, pp. 2724–2735, 2016.

[182] M. G. Molina and P. E. Mercado, “Controlling A Static Synchronous Compensator With Superconducting Magnetic Energy Storage For Applications On Primary Frequency Control,” *Lat. Am. Appl. Res.*, vol. 126, pp. 119–126, 2004.

[183] C. Shen, Z. Yang, M. L. Crow, and S. Atcitty, “Control of Statcom with Energy Storage Device,” in *IEEE Power Engineering Society Winter Meeting. Conference Proceedings, Singapore, Singapore*, 2000, pp. 2722–2728.

[184] O. Tremblay and L.-A. Dessaint, “Experimental Validation of a Battery Dynamic Model for EV Applications,” *World Electr. Veh. J.*, vol. 3, pp. 289–298, 2009.

[185] O. Tremblay, L. Dessaint, and A. Dekkiche, “A Generic Battery Model for the Dynamic Simulation of Hybrid Electric Vehicles,” in *IEEE Vehicle Power and Propulsion Conference, Arlington, TX, USA*, 2007, pp. 284–289.

[186] J. Zhang, J. S. Lai, and W. Yu, “Bidirectional DC-DC Converter Modeling and Unified Controller with Digital Implementation,” in *Twenty-Third Annual IEEE Applied Power Electronics Conference and Exposition, Austin, TX, USA*, 2008, pp. 1747–1753.

[187] J. A. P. Lopes, C. L. Moreira, and A. G. Madureira, “Defining Control Strategies for MicroGrids Islanded Operation,” *IEEE Trans. Power Syst.*, vol. 21, no. 2, pp. 916–924, 2006.

[188] J. W. Simpson-Porco, Q. Shafiee, F. Dorfler, J. C. Vasquez, J. M. Guerrero, and F. Bullo, “Secondary Frequency and Voltage Control of Islanded

Microgrids via Distributed Averaging," *IEEE Trans. Ind. Electron.*, vol. 62, no. 11, pp. 7025–7038, 2015.

[189] T. J. Hammons, "Greenhouse Gas Emissions From Power Generation in Europe," in *39th International Universities Power Engineering Conference, UPEC, Bristol, UK*, 2004, pp. 837–844.

[190] A. M. Van Voorden, L. M. Ramirez Elizondo, G. C. Paap, J. Verboomen, and L. Van Der Sluis, "The Application of Super Capacitors to Relieve Battery-Storage Systems in Autonomous Renewable Energy Systems," in *IEEE Lausanne Power Tech, Lausanne, Switzerland*, 2007, pp. 1–6.

[191] C. Banos, M. Aten, P. Cartwright, and T. C. Green, "Benefits and Control of STATCOM with Energy Storage in Wind Power Generation," in *The 8th IEE International Conference on AC and DC Power Transmission, London, UK*, 2006, pp. 230–235.

[192] X. Zhang, Z. Dong, and C. Crawford, "Hybrid Energy Storage System for Hybrid and Electric Vehicles: Review and a New Control Strategy," in *Proceeding of the ASME 2011 International Mechanical Engineering Congress and Exposition, Denver, Colorado, USA*, 2011, pp. 91–101.

[193] C. Xiang, Y. Wang, S. Hu, and W. Wang, "A New Topology and Control Strategy for a Hybrid Battery-Ultracapacitor Energy Storage System Changle," *Energies*, vol. 7, pp. 2874–2896, 2014.

[194] S. Zhang, R. Xiong, and X. Zhou, "Comparison of the Topologies for A Hybrid Energy-Storage System of Electric Vehicles Via A Novel Optimization Method," *Sci. China Technol. Sci.*, vol. 58, no. 7, pp. 1173–1185, 2015.

[195] J. M. Miller and G. Sartorelli, "Battery and Ultracapacitor Combinations - Where should the Converter Go?," in *IEEE Vehicle Power and Propulsion Conference, Lille, France*, 2010, pp. 1–6.

[196] A. Etxeberria, I. Vechiu, H. Camblong, J. M. Vinassa, and H. Camblong, "Hybrid Energy Storage Systems for renewable Energy Sources Integration

in microgrids: A review," in *Conference Proceedings IPEC, Singapore, Singapore*, 2010, pp. 532–537.

[197] D. Noréus, "Substitution of Rechargeable NiCd Batteries," Arrhenius Laboratory, Stockholm University, Stockholm, Sci Rep. 106 91, 2000.

[198] D. R. Wilburn, "Material Use in the United States--Selected Case Studies for Cadmium, Cobalt, Lithium, and Nickel in Rechargeable Batteries," U.S. Geological Survey, Reston, Virginia, Sci Rep. 2008–5141, 2008.

[199] A. B. Cultura and Z. M. Salameh, "Performance Evaluation of a Supercapacitor Module for Energy Storage Applications," in *IEEE Power and Energy Society General Meeting - Conversion and Delivery of Electrical Energy in the 21st Century, Pittsburgh, PA, USA*, 2008, pp. 1–7.

[200] D. B. Murray, M. G. Egan, J. G. Hayes, and D. L. O. Sullivan, "Applications of Supercapacitor Energy Storage for a Wave," in *Proceedings of the Eighth European Wave and Tidal Energy Conference, Uppsala, Sweden*, 2009, pp. 786–795.

[201] A. Mansour, C. M. Hedi, and B. Faouzi, "Experimental Study of a Pack of Supercapacitors Used in Electric Vehicles," *Sci. World J.*, vol. 2017, pp. 1–8, 2017.

[202] H. S. Khalil and K. N. Faris, "Ultracapacitor : Modelling and Characterization for Electric Vehicle Application," *Int. J. Eng. Res.*, vol. 5, no. 8, pp. 681–686, 2016.

[203] J. Timmermans, P. Zadora, Y. Cheng, J. Van Mierlo, and P. Lataire, "Modelling and Design of Super Capacitors as Peak Power Unit for Hybrid Electric Vehicles," in *IEEE Vehicle Power and Propulsion Conference, Chicago, IL, USA*, 2005, pp. 701–708.

[204] Z. J. Yu, Zhang and Y. Xunwei, "Small-Signal Modeling and Analysis of Battery- Supercapacitor Hybrid Energy Storage Systems," in *IEEE Power & Energy Society General Meeting, Calgary, Canada*, 2009, pp. 1–8.

[205] S. K. Kollimalla, M. K. Mishra, and N. L. Narasamma, “Design and Analysis of Novel Control Strategy for Battery and Supercapacitor Storage System,” *IEEE Trans. Sustain. Energy*, vol. 5, no. 4, pp. 1137–1144, 2014.

[206] C. Zhao, C. Gu, F. Li, and M. Dale, “Understanding LV Network Voltage Distribution- UK Smart Grid Demonstration Experience,” in *IEEE Power & Energy Society Innovative Smart Grid Technologies Conference (ISGT), Washington, USA*, 2015, pp. 1–6.

[207] “Nominal voltages for low voltage public electricity supply systems,” BS 7697:1993, ed. London: British Standards Institution, 2003.

[208] A. Shrivastava and S. Gupta, “Review on Super Capacitor-Battery based Hybrid Energy Storage System for PV Application,” *Int. J. Adv. Eng. Manag. Sci.*, vol. 3, no. 4, pp. 378–381, 2017.

[209] G. Wang, M. Ciobotaru, and V. G. Agelidis, “Power Smoothing of Large Solar PV Plant Using Hybrid Energy Storage,” *IEEE Trans. Sustain. Energy*, vol. 5, no. 3, pp. 834–842, 2014.

[210] K. Nikhil, M. K. Mishra, and S. Kotra, “Power Management Based on the Operating Conditions of Grid, Mircogrid and Hybrid Storage,” in *4th International Conference on Renewable Energy Research and Applications, Palermo, Italy*, 2015, pp. 1437–1441.

[211] N.I(2009), “CompactRIO Developers Guide,” *[Online]. Availaible: http://www.juxingyiqi.com/download/dailichanpin/criodevgudfull.pdf*. .

Appendix A Small Signal Modelling of the PCC Control loop design

According to the chapter three, the D-STATCOM device can be represented as a controllable current source as shown in Figure A-1.

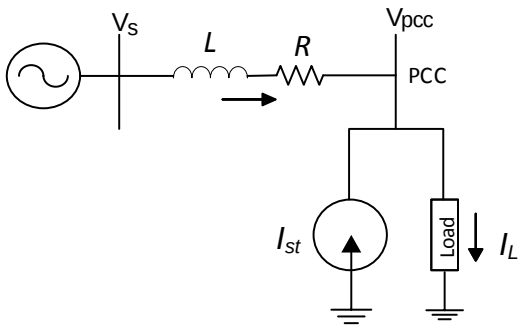

Figure A-1 Modelling circuit for D-STATCOM with AC grid

where

V_s is the voltage of the source

V_{PCC} is the voltage at the point of common coupling

I_L is the current of the main load

I_{st} is the current of the D-STATCOM

L is the inductance between the AC source and the PCC

R is the resistance between the AC source and the PCC

According to the circuit diagram shown in the Figure A-1, the three phase voltage and current relationship can be formulated as given:

$$\begin{bmatrix} V_{s,a} - V_{PCC,a} \\ V_{s,b} - V_{PCC,b} \\ V_{s,c} - V_{PCC,c} \end{bmatrix} = L\frac{di}{dt}\begin{bmatrix} i_a \\ i_b \\ i_c \end{bmatrix} + R\begin{bmatrix} i_a \\ i_b \\ i_c \end{bmatrix} \quad \textbf{(A-1)}$$

The d-q transformation analysis applied to above equations, gives the voltage formulas in a d-q reference frame as:

$$V_{s,d} - V_{PCC,d} = L\frac{dI_d}{dt} + RI_d - \omega LI_q \quad \textbf{(A-2)}$$

$$V_{s,q} - V_{PCC,q} = L\frac{dI_q}{dt} + RI_q + \omega LI_d \quad \textbf{(A-3)}$$

In the d-q orientation frame the d-component is aligned to the voltage of PCC, the q- component of the voltage at PCC becomes zero, voltage $V_{PCC,q=0}$.

The load current is the summation of the source current and D-STATCOM current, therefore the load current representation in the d-q reference frame given as:

$$I_{L,d} = I_d + I_{st,d} \quad \textbf{(A-4)}$$

$$I_{L,q} = I_q + I_{st,q} \quad \textbf{(A-5)}$$

As the DC link capacitor has a limited energy, the D-STATCOM supports the grid with reactive power only. Thus, $I_{st,d} = 0$, therefore after substituting Equation (A-4) and (A-5) into Equation (A-2) and (A-3), results the Equations as:

$$V_{s,d} - V_{PCC,d} = L\frac{dI_{L,d}}{dt} + RI_{L,d} - \omega L(-I_{st,q} + I_{L,q}) \quad \textbf{(A-6)}$$

$$V_{s,q} = L\frac{d(-I_{st,q} + I_{L,q})}{dt} + R(-I_{st,q} + I_{L,q}) + \omega LI_{L,d} \quad \textbf{(A-7)}$$

The perturbing and Laplace transformation applied to Equation (A-6) and (A-7), gives:

$$\Delta V_{s,d} - \Delta V_{PCC,d} = (SL + R)\Delta I_{L,d} - \omega L(-\Delta I_{st,q} + \Delta I_{L,q}) \quad \textbf{(A-8)}$$

$$\Delta V_{s,q} = (SL + R)(-\Delta I_{st,q} + \Delta I_{L,q}) + \omega L \Delta I_{L,d} \quad \textbf{(A-9)}$$

Assuming the voltage of the three-phase power source is constant at all time, therefore

$\Delta V_{s,d}$ and $\Delta V_{s,q}$ equal zero. If the load being the active power component, the load current on the q-axis will assume constant compared to the variation in the d-axis, thus $\Delta I_{L,q}$ equal zero. Equation (A-8) and (A-9) can be represented as:

$$-\Delta V_{PCC,d} = (SL + R)\Delta I_{L,d} - \omega L(-\Delta I_{st,q}) \quad \textbf{(A-10)}$$

$$0 = (SL + R)(-\Delta I_{st,q}) + \omega L \Delta I_{L,d} \quad \textbf{(A-11)}$$

Equation (A-11) can be rewritten,

$$\Delta I_{L,d} = \frac{(SL+R)}{\omega L} \Delta I_{st,q} \quad \textbf{(A-12)}$$

From Equation (A-10) and (A-12) the variation of the voltage magnitude at the PCC to the variation in the reactive current component of the D-STATCOM given as:

$$\frac{\Delta V_{PCC}}{\Delta I_{st,q}} = \frac{(SL + R)^2}{\omega L} + \omega L \quad \textbf{(A-13)}$$

The term $(SL + R)^2/\omega L$ in above Equation can be ignored because the value of the impedance connected between the AC source and the point of the common coupling is very small [170].

Appendix B State equation for buck and boost controller

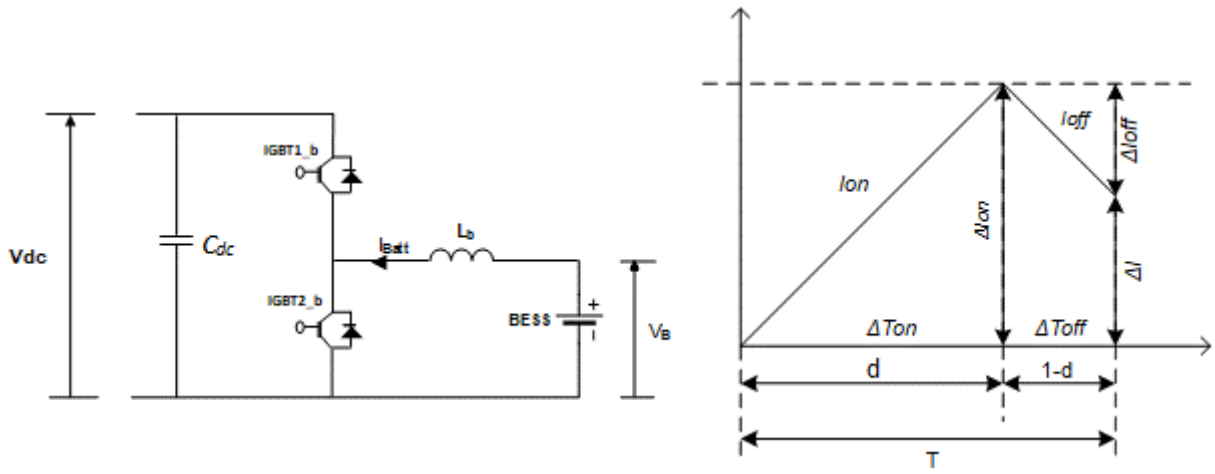

A-Converter schematic diagram **B- one sample period for inductor**

Figure B 1 Inductor current during one sample for DC-DC converter topology

For buck operation (IGBT1_b) is on and (IGBT2_b) is off and represented with $u_1 = 1\,, u_2 = 0$

Applying current and voltage for Kirchhoff

$$L_b \frac{di}{dt} = V_{dc} - V_B \quad \textbf{(B-1)}$$

$$C \frac{dv}{dt} = i_c - \frac{1}{R} V_B \quad \textbf{(B-2)}$$

$$V_l = L_b \frac{di}{dt} = L_b \frac{\Delta I_{on}}{\Delta t_{on}} = V_{dc} - V_B \quad \textbf{(B-3)}$$

$$\Delta I_{on} = \frac{d}{L_b}(V_{dc} - V_B) \quad \textbf{(B-4)}$$

For buck operation $u_2 = 0,\ u_1 = 0$

Applying current and voltage for Kirchhoff

$$L_b \frac{di}{dt} = -V_B \quad \textbf{(B-5)}$$

$$V_L = V_{Batt} = L_b \frac{\Delta I_{off}}{\Delta t_{off}} \quad \textbf{(B-6)}$$

$$\Delta I_{off} = \frac{1-d}{L_b} V_B \quad \textbf{(B-7)}$$

Referring to the Figure B 1 (b), the overall change in the inductor current during one sampling period is given:

$$\Delta I = \Delta I_{on} - \Delta I_{off} = \frac{1}{L_b}(dV_{dc} - V_B) \quad \textbf{(B-8)}$$

$$d_{buck} = \frac{L_b \Delta I + V_B}{V_{dc}} \quad \textbf{(B-9)}$$

For boost operation $u_1 = 0,\ u_2 = 1$

Applying current and voltage for Kirchhoff

$$L_b \frac{di}{dt} = V_B \quad \textbf{(B-10)}$$

$$C \frac{dv}{dt} = -\frac{V_{dc}}{R} \quad \textbf{(B-11)}$$

$$V_L = V_B = L_b \frac{\Delta I_{on}}{\Delta t_{on}} \quad \textbf{(B-12)}$$

$$\Delta I_{on} = \frac{dV_B}{L_b} \quad \textbf{(B-13)}$$

For boost operation $u_1 = 0,\ u_2 = 0$

$$L_b \frac{di}{dt} = V_B - V_{dc} \quad \textbf{(B-14)}$$

$$V_L = V_{dc} - V_B = L \frac{\Delta I_{off}}{\Delta t_{off}} \quad \textbf{(B-15)}$$

$$\Delta I_{off} = \frac{1-d}{L_b}(V_{dc} - V_B) \quad \textbf{(B-16)}$$

The change in the inductor current is given as

$$\Delta I = \Delta I_{on} - \Delta I_{off} \quad \textbf{(B-17)}$$

$$\Delta I = \frac{1}{L}(V_B - (1-d)V_{dc}) \quad \textbf{(B-18)}$$

$$d_{boost} = 1 + \frac{L\Delta \mathrm{I} - V_B}{V_{dc}} \quad \textbf{(B-19)}$$

Appendix C Graphic Description of the Laboratory setup

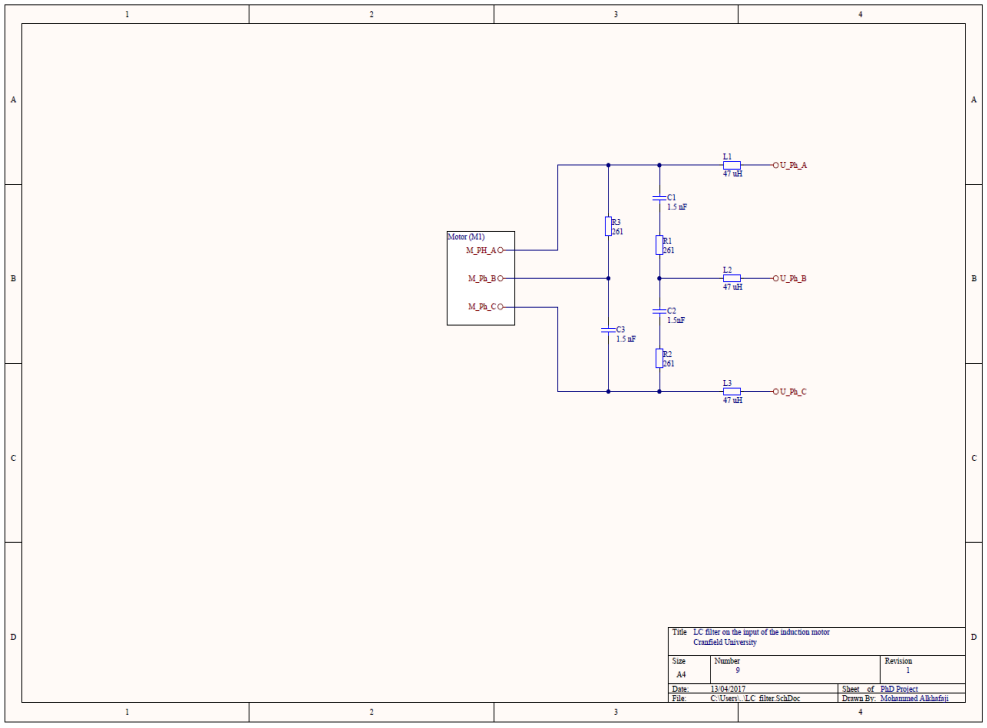

Figure C- 1 Schematic diagram of input LC_filter for induction motor

Table C- 1 Induction motor parameters

Parameter	Value
Power	0.37 kW
Voltage	220/250 V, Delta configuration 380/440 V, Star configuration
Current	1.5 A, Delta configuration 0.9 A, Star configuration
Number of phases	Three, 50 Hz
Speed	2840 rev/min
Regime	Continuous work
Winding resistance	21 Ω, Delta configuration, 30 Ω, Star configuration

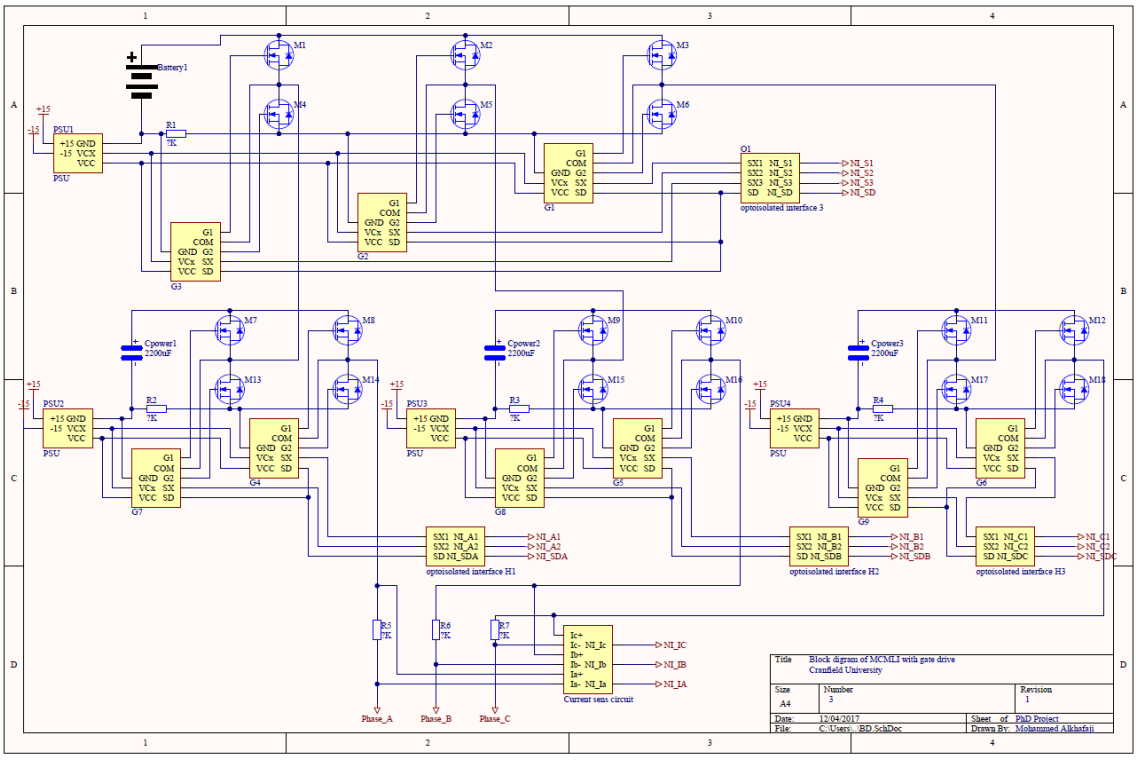

Figure C- 2 Modified cascade inverter with switch drive circuits

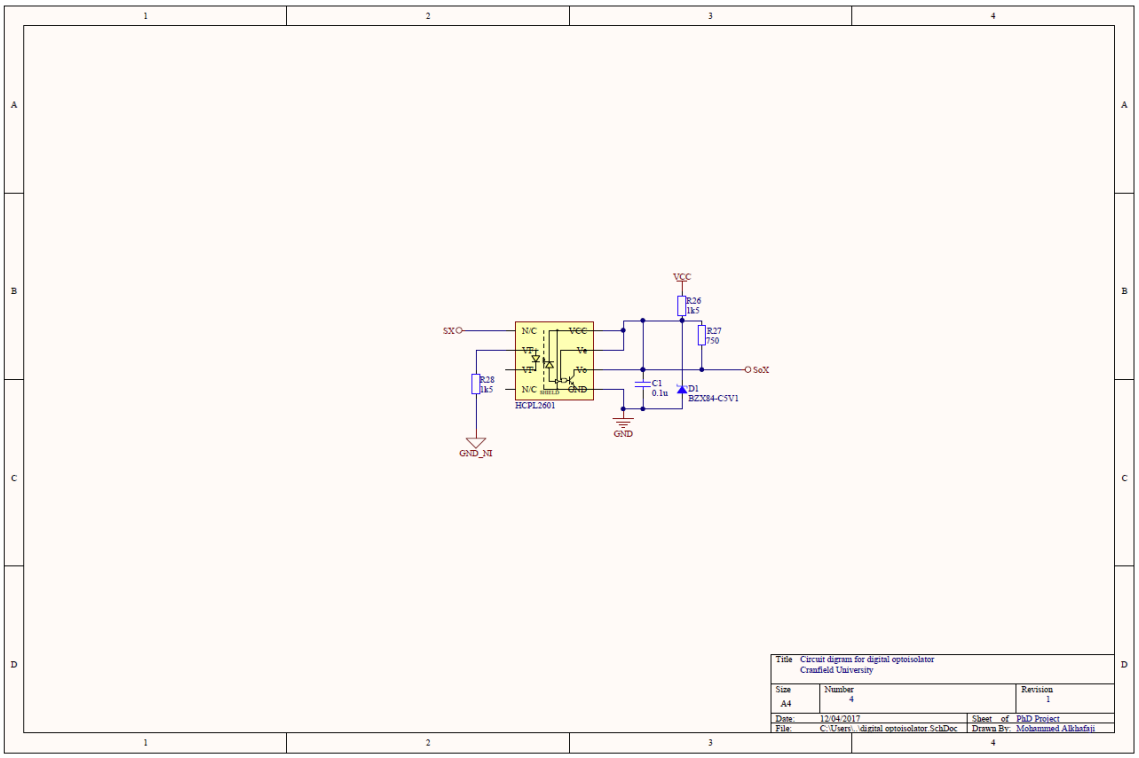

Figure C- 3 Simplified diagram of the HCPL2601 optocoupler

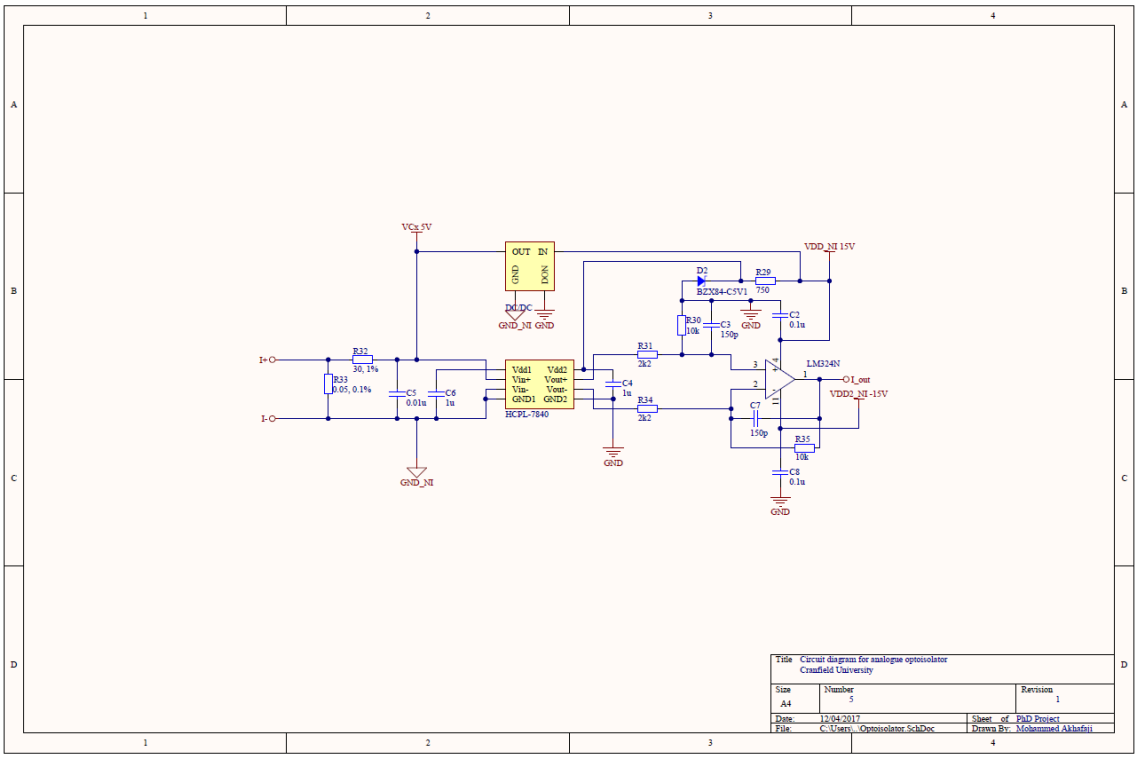

Figure C- 4 Schematic diagram of analogue optoisolator

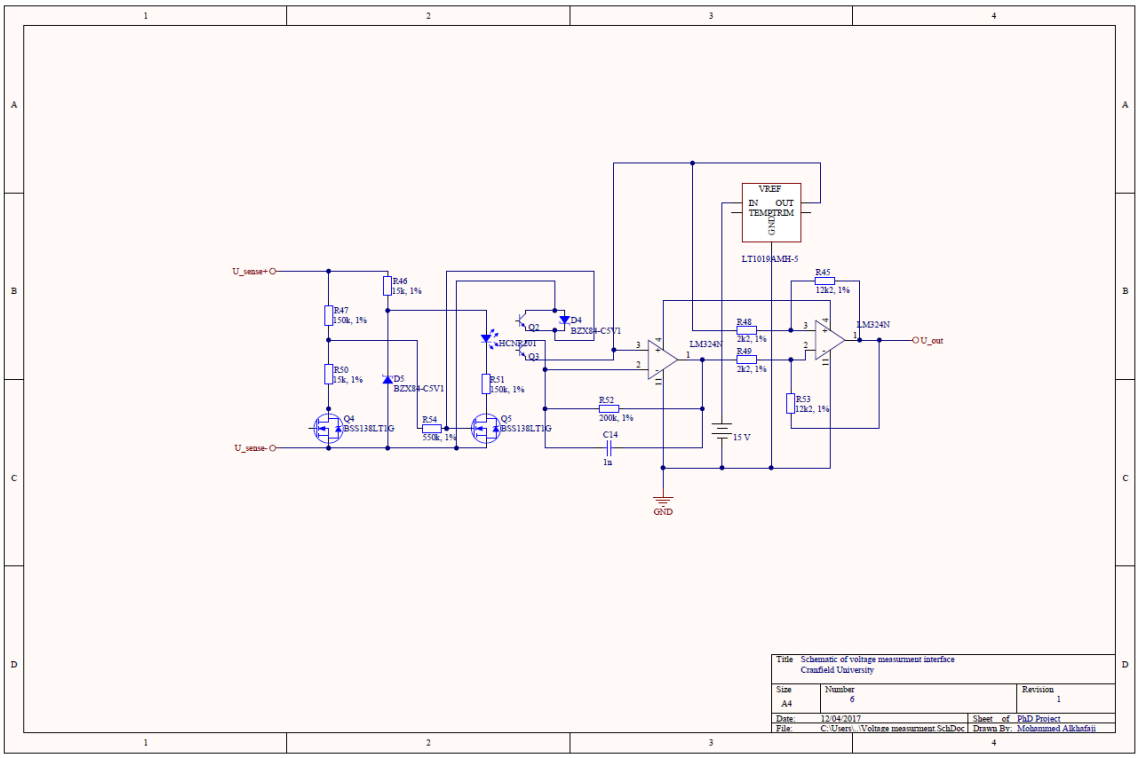

Figure C- 5 Schematic diagram of voltage measurement interface

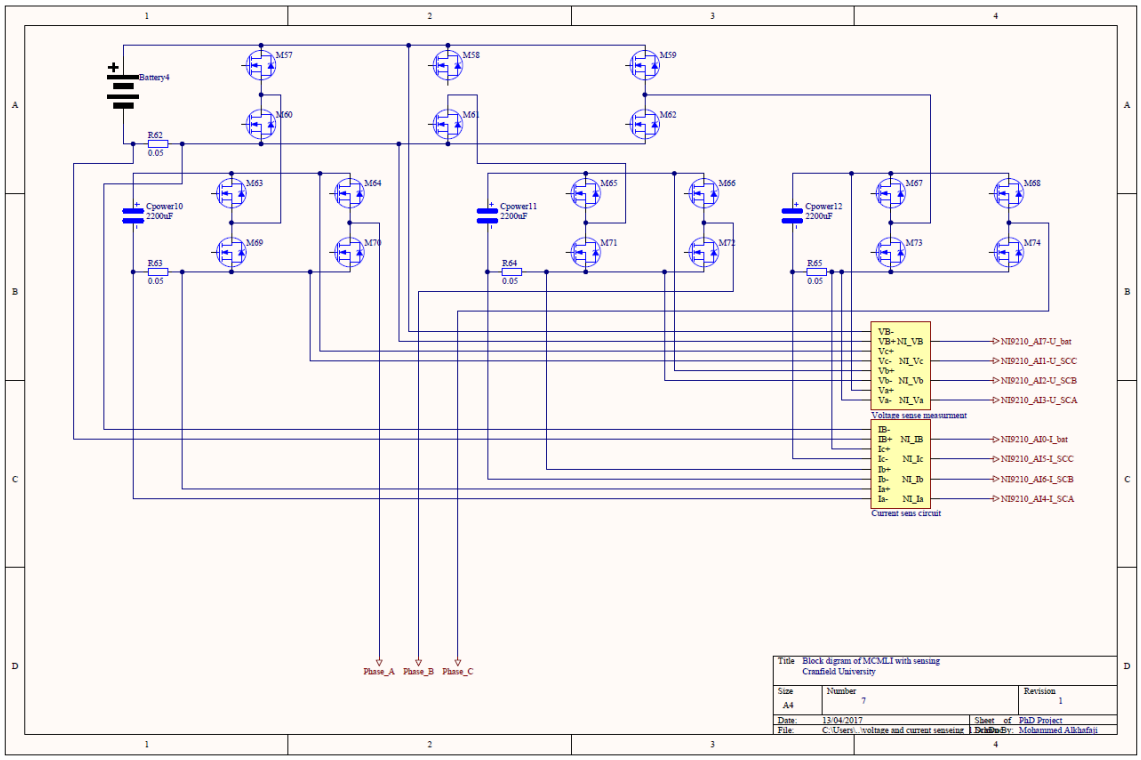

Figure C- 6 Schematic diagram of including voltage and current sensing

Control Platform detiales

NI CRIO 9012: it is an embedded real-time controller that is suitable for advanced control and monitoring the operation of proposed inverter. The specification of this device is 400 MHz CPU, 64 MB DRAM, and 128 MB of storage. This controller features accept one Ethernet, one USB, and one serial connectivity ports. The configuration of the cRIO-9012 is shown in the Figure C- 7.

NI CRIO 9112: it is a rugged programmable FPGA CRIO chassis that can be used to add C series I/O modules to the controller. It consists of eight Xilinx Virtex 5 LX30 FPGA slots with 19200 flip-flops and 1152 kbit embedded RAM. It operates at an internal clock frequency of 40 MHz. The chassis is connected to the compatible CRIO controller to communicate with the modules installed in the chassis as illustrated in Figure C-8.

NI 9425: it is input series digital model with 32 channels and 7 µs resolution. It works to read decoded information from position encoder as shown in Figure C-9.

NI 9476: it is a source of low-speed digital output model with 500µs resolution. It is used to control shutdown function of gate drivers. D01 to D0 4 that are used to enable switching of the manual switch, three phase bridge, H-bridge phase A, H-bridge phase B, and H-bridge phase C respectively. The configuration of the model is shown in Figure C-10.

NI 9474: it is eight high-speed digital output channels module with 1 µs resolution. Six channels outputs are used to control H- bridge converters in each phase. D02 and D03 control gate signals of H-bridge converter connected at phase A. D04 and D05 control gates signals of H-bridge converter connected at phase B. D06 and D07 control gates signals of H-bridge converter connected at phase C (Figure C-11).

NI 9402: it is high speed four bidirectional channels model with 4 µs resolution. The first three channels (DIO0-DIO2) are used to control gate signals of the three-phase bridge while digital input DIO3 is used to detect full rotation from the encoder. The signal level of DIO0 to DIO2 is amplified from 5V to 15V for the optoisolated circuit (Figure C-12).

NI 9201: it is the eight analogue input channels model with ±10 V input range, 12-Bit resolution, and 500 KS/s sampling frequency. It is used to measure voltage and current feedback signals. The channel is distributed as below:

AI0 is occupied to measure three phase bridge inverter supply current (IBatt)

AI1 is occupied to measure H-bridge converter supply voltage connected to phase C (SC)

AI2 is occupied to measure H-bridge converter supply voltage connected to phase B (SCb)

AI3 is occupied to measure H-bridge converter supply voltage connected to phase A (SCa)

AI4 is occupied to measure inverter current at phase A (Ia)

AI5 is occupied to measure inverter current at phase C (Ic)

AI6 is occupied to measure inverter current at phase B (Ib)

AI7 is occupied to measure three phase bridge inverter supply voltage (Vbat).

The current in AI0, AI4, AI5, and AI6, the voltage in AI1, AI2, and AI3, and the voltage in AI7are converted by external hardware from ±6 A to ±10 V, from floating 0-65 V to 0-10 V, and from floating 0-160 V to 0-10 V respectively (see Figure C-13).

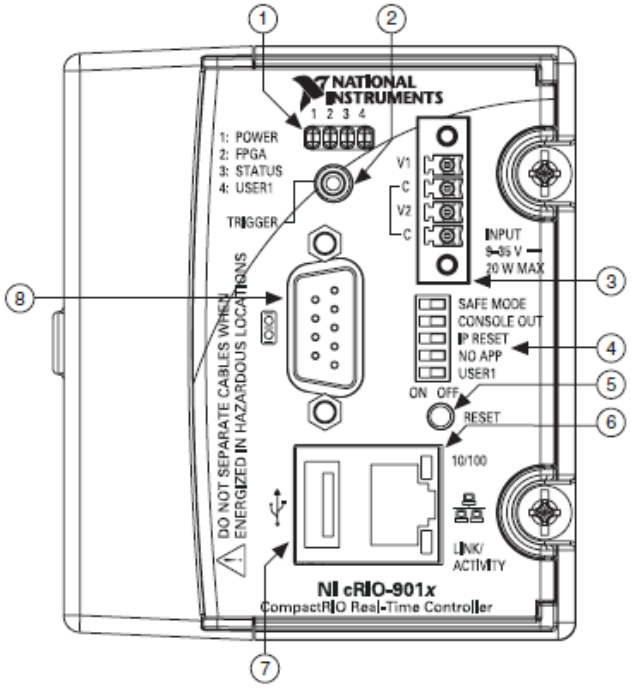

1	LEDs	5	Reset Button
2	SMB Connector	6	RJ-45 Ethernet Port
3	Power Connector	7	USB Port
4	DIP Switches	8	RS-232 Serial Port

Figure C- 7 : Compact RIO cRIO-9012 configuration

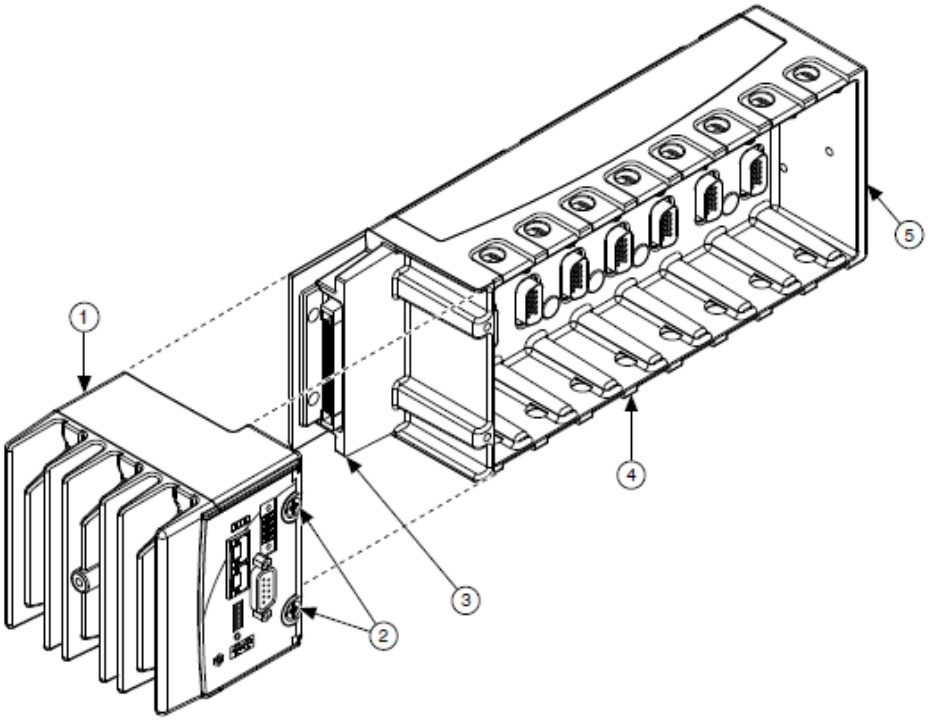

1. Controller
2. Captive Screws
3. Controller Slot
4. Reconfigurable Embedded Chassis
5. Grounding Screw

Figure C-8 : CRIO chassis connection to CRIO controller

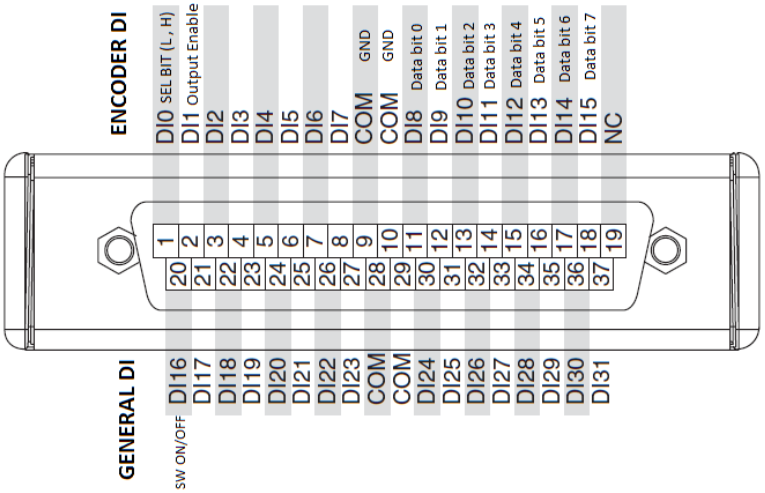

Figure C- 9 : NI 9425 model configuration

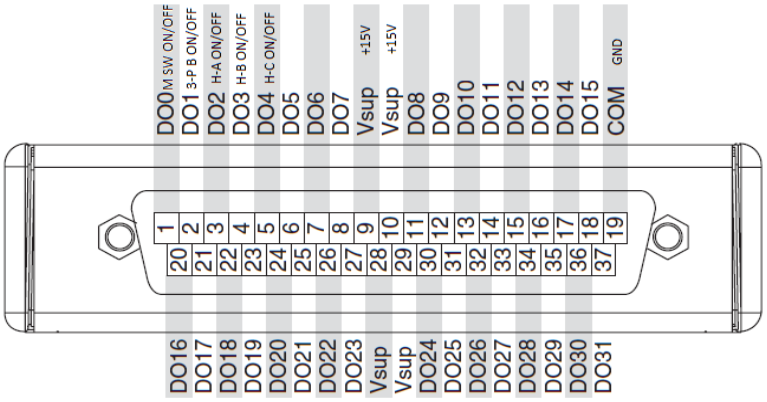

Figure C-10: NI 9476 model configuration

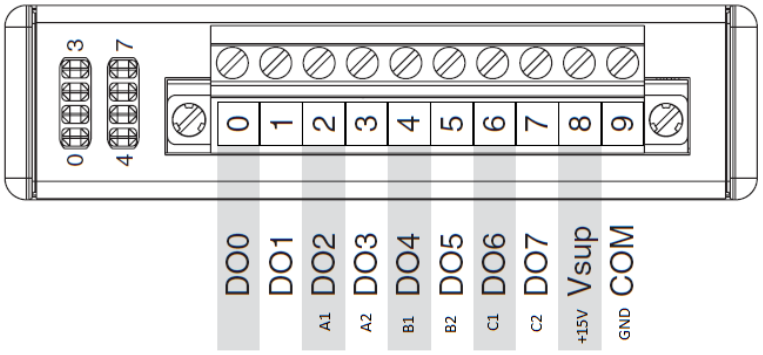

Figure C-11: NI 9474 model configuration

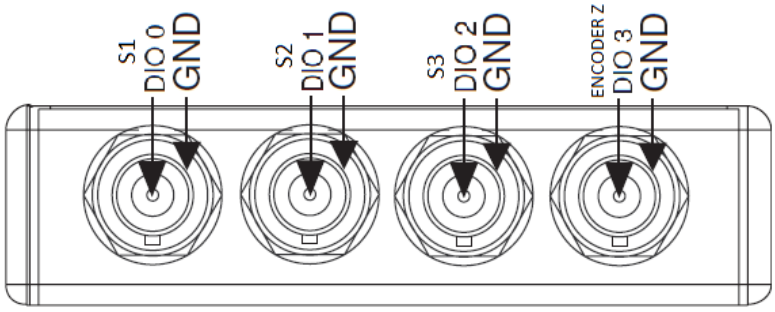

Figure C-12: NI 9402 model configuration

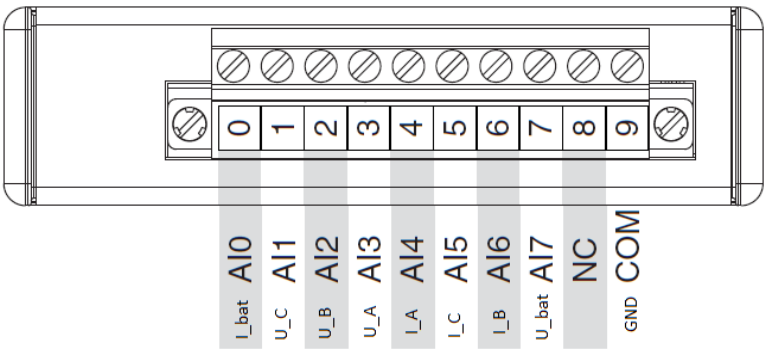

Figure C-13: NI 9201 model configuration